UNIVERSITY OF CALIFORNIA SAN DIEGO

Characterizing the Impact Dynamics of Small Particles: The Aerosol Impact Spectrometer

A dissertation submitted in partial satisfaction of the requirements for the degree Doctor of Philosophy

in

Nanoengineering

by

Morgan E.C. Miller

Committee in charge:

Professor Robert E. Continetti, Chair
Professor Olivia A. Graeve
Professor Vicki H. Grassian
Professor Ping Liu
Professor Clifford M. Surko

2020

The Dissertation of Morgan E.C. Miller is approved and it is acceptable in quality and form for publication on microfilm and electronically:

_____

_____

_____

_____

_____

Chair

University of California San Diego

2020

DEDICATION

I dedicate this dissertation to my parents, David and Susan, without whom this dissertation would not be possible; their loving support and assistance has facilitated this work as much as any experiment.

In recognition of my advisor and mentor Bob whose guidance and support has enabled my scientific adventures at UCSD.

In recognition of my loving girlfriend Ashley for the support and encouragement, both intellectual and emotional, in closing this chapter of my life.

In recognition of my friends and family whose support I always rely on when work becomes challenging.

In recognition of all the talented colleagues and collaborators that have assisted me into becoming the scientist I am today.

TABLE OF CONTENTS

Signature Page iii

Dedication iv

Table of Contents v

List of Figures ix

List of Tables xii

Acknowledgements xiii

Vita xv

Abstract of the Dissertation xvi

Chapter 1: Introduction 1

1.1. Impact Dynamics of Particles 1

1.2. Particle Generation Techniques 7

1.3. Particle Characterization Techniques 8

1.4. Particle Energetic Control 11

1.5. Structure of Dissertation 12

1.6. References 13

Chapter 2: Experimental Methods and Data Analysis 17

2.1. Overview of Experimental Apparatus 17

2.1.1. Particle Source 19

2.1.2. Energy Selection 25

2.1.3. Image Charge Detection 29

2.1.4. Charge Detection Mass Spectrometry 33

2.1.5. Linear Accelerator 37

2.1.6. Impact Measurements 43

2.2. Vacuum System 51
2.3. Data Acquisition System 53
2.3.1. System Control 53
2.3.2. Data Storage 59
2.4. Data Analysis Software 60
2.4.1. In-situ Analysis 60
2.5. Spectrometer Calibration 65
2.6. Conclusion 67
2.7. References 68
Chapter 3: Coefficient of Restitution Studies of Polystyrene Latex Spheres 70
3.1. Introduction 70
3.2. Experimental Methods 71
3.3. Results and Discussion 78
3.4. Conclusions 81
3.5. References 82
Chapter 4: Impact Dynamics Studies with a Tapered Image Charge Detector 84
4.1. Introduction 84
4.2. Experimental Methods 86
4.3. Calibration and Analysis 94
4.4. Conclusions 107
4.5. References 108
Chapter 5: Impact Dynamics of Submicron Tin Particles 110
5.1. Introduction 110
5.2. Experimental Methods 112
5.3. Results 113

5.4. Discussion 118
5.4.1. Modeling of CoR Data 118
5.4.2. Scaling Particle Rebound Angular Measurements 127
5.5. Conclusions 132
5.6. References 134
Chapter 6: Bombardment of Freestanding Thin Films 137
6.1. Introduction 137
6.2. Experimental Methods 139
6.2.1. Film Provenance 144
6.2.2. Film Installation 144
6.3. Results and Discussion 145
6.4. Conclusions 154
6.5. References 155
Chapter 7: Particle Beam Characterization with Microchannel Plate Detector 157
7.1. Introduction 157
7.2. Experimental 158
7.3. Results and Discussion 161
7.4. Conclusion 173
7.5. References 174
Chapter 8: Enceladus Ice Particle Analog Production 176
8.1. Introduction 176
8.2. Experimental Methods 178
8.3. Results and Discussion 181
8.3.1. Reaching Desired Ice Particle Velocity 181
8.3.2. Impact Dynamics of Ice Particles 184

8.4. Conclusions 194

8.5. References 195

Appendix A: Circuit Diagrams 198

A.1. Apparatus Control 198

A.2. NET Circuitry 201

A.3. LINAC High Voltage Circuitry 203

A.4. LINAC Logic Circuit 205

A.5. Remote FET Configuration for Image Charge Detector 208

LIST OF FIGURES

Figure 1.1: Coefficient of restitution curve 4

Figure 2.1: General apparatus layout with key components labeled 18

Figure 2.2: Enclosed electrospray ionization source exterior 20

Figure 2.3: Enclosed electrospray ionization source interior 22

Figure 2.4: Breakout of aerodynamic lens 24

Figure 2.5: Design of quadrupole deflector 26

Figure 2.6: Particle production arm overview 28

Figure 2.7: Image charge detection tube axial slice 30

Figure 2.8: Image charge detection signal 32

Figure 2.9: Diagram of NET optics rail 35

Figure 2.10: Particle oscillation in NET square wave 36

Figure 2.11: Diagram of LINAC and injection optics 38

Figure 2.12: LINAC electric field calculation 42

Figure 2.13: Single ICD CoR measurement setup 44

Figure 2.14: Measurement setup for thin film bombardment 46

Figure 2.15: CCD images of thing film mounted in beamline 47

Figure 2.16: Tapered image charge detector 49

Figure 2.17: MCP detector setup 50

Figure 2.18: AIS pumping system diagram 52

Figure 2.19: AIS timing diagram 54

Figure 2.20: Various QD program histograms 58

Figure 2.21: Cross-correlation filter example signal 64

Figure 3.1: PSL quadrupole deflector charge distribution 73
Figure 3.2: PSL CDMS spectra 74
Figure 3.3: ICD and target diagram for PSL CoR 76
Figure 3.4: Average rebound velocity of PSLs on silicon 77
Figure 3.5: Comparison of PSL CoR to previous study 80
Figure 4.1: Expanded view of tapered ICD 87
Figure 4.2: Expanded view of collision analysis target 89
Figure 4.3: Configuration of TICD for scattering measurements 91
Figure 4.4: Axial geometry of TICD with key parameters 92
Figure 4.5: Example waveforms of TICD 95
Figure 4.6: Signature waveforms of particle impact on CAT and TICD 99
Figure 4.7: Geometry for measuring CoR with TICD and CAT 101
Figure 4.8: CoR comparison of TICD and single ICD data 104
Figure 4.9: Analysis of tin particle rebound trajectories at 150 m/s 106
Figure 5.1: CoR measurements of different diameter tin particles 115
Figure 5.2: Measurements of tin particle rebound trajectories 116
Figure 5.3: Tin CoR trend fits with Hertzian model 124
Figure 5.4: Size dependent fit of particle yield strength 126
Figure 5.5: Comparison of rebound behavior of 300 nm and 500 nm tin 128
Figure 5.6: Empirical normalization of size dependent CoR and rebound data .. 131
Figure 6.1: Pellicle impact region setup 140
Figure 6.2: Pellicle with scaffolding mounted in ICD3 chuck 142
Figure 6.3: Pellicle impact region setup 143

Figure 6.4: Pellicle bombardment dataset 146
Figure 6.5: Comparison of CoR for pellicle and bulk targets 148
Figure 6.6: Destruction velocity of pellicle films 152
Figure 7.1: Experimental setup of MCP impact measurements 160
Figure 7.2: Overlay of phosphor screen images of open face MCP 162
Figure 7.3: Overlay of phosphor screen images for MCP with mesh 164
Figure 7.4: Centroid image of Figure 7.3 colorized by event count 165
Figure 7.5: Electric field contour lines of open face MCP 167
Figure 7.6: MCP configuration with half face covering 168
Figure 7.7: Overlay of phosphor screen images for MCP with half-face cover .. 170
Figure 8.1: Ice particle diameter distributions 179
Figure 8.2: Average CoR for 1700 nm and 850 nm ice particles 185
Figure 8.3: TICD and CAT signals of ice particle impact and fragmentation 186
Figure 8.4: Post-impact behavior of 850 nm ice particles 190
Figure 8.5: Thresholds of fragmentation extracted from previous work 193
Figure A.1: Diagram of digital port buffer 199
Figure A.2: PCB of custom buffer circuit 200
Figure A.3: Diagram of the NET circuit 202
Figure A.4: Diagram of the high voltage LINAC circuit 204
Figure A.5: Simplified diagram of LINAC logic circuit 206
Figure A.6: Circuit diagram of LINAC logic circuit 207
Figure A.7: Circuit diagram of remote FET configuration for ICDs 209

LIST OF TABLES

Table 4.1: List of parameters used for TICD characterization 93

Table 4.2: Example CoR calculations for Figure 4.7 102

Table 5.1: Results of model fit to tin CoR data 123

Table 6.1: Pellicles tested in AIS impact experiments 153

Table 7.1: Statistics of MCP efficiency for different detector configurations ... 171

ACKNOWLEDGEMENTS

Chapter 2 uses a figure (2.10) as it appears in Adamson, B.D.; Miller, M.E.C.; Continetti, R.E. The aerosol impact spectrometer: a versatile platform for studying the velocity dependence of nanoparticle-surface impact phenomena. *European Physical Journal, Techniques and Instrumentation*, 2017, 4 (2). The dissertation author is coauthor and the dissertation advisor is the corresponding author.

Chapter 3 uses figures (3.1 and 3.2) as they appear in Adamson, B.D.; Miller, M.E.C.; Continetti, R.E. The aerosol impact spectrometer: a versatile platform for studying the velocity dependence of nanoparticle-surface impact phenomena. *European Physical Journal, Techniques and Instrumentation*, 2017, 4 (2). The dissertation author is coauthor and the dissertation advisor is the corresponding author.

Chapter 4, in full, is a reprint of the material as it appeared in Miller, M.E.C.; Mezher, M.; Continetti, R.E., Tapered image charge detector for measuring velocity distributions of submicrometer particle scattering. *Review of Scientific Instruments* **2020,** 96 (6), 063305. The dissertation author is the primary author and the dissertation advisor is the corresponding author.

Chapter 5 is a manuscript in preparation with authors Miller, M.E.C.; Mezher, M.; De Dea, S.; Continetti, R.E., with the working title Size-dependent Coefficient of Restitution Phenomena for Submicron Tin Particles. The dissertation author is the primary author and the dissertation advisor is the corresponding author.

Chapter 8 is a manuscript in preparation with authors Miller, M.E.C.; Burke, S.; Continetti, R.E., with the working title Impact Studies of Hypervelocity Micron Water-Ice. The dissertation author is the primary author and the dissertation advisor is the corresponding author.

VITA

2014	Bachelor of Science, Physics, University of California San Diego
2013-20	Research Assistant, University of California San Diego
2016	Master of Science, Nanoengineering, University of California San Diego
2020	Doctor of Philosophy, Nanoengineering, University of California San Diego

PUBLICATIONS

Miller, M.E.C., Burke, S., Continetti, R. E., "Impact Studies of Hypervelocity Micron Water-Ice", *In preparation*

Belousov, A., Miller, M. E. C., Simcic, J., Nikolic, D., Hodyss, R., Malaska, M., Hofmann, A., Waller, S. E., Lambert, J., Madzunkov, S., Darrach, M., Jaramillo-Botero, A., Continetti, R. E., Cable, M. L., "Sampling Accelerated Micron Scale Ice Particles with a Quadrupole Ion Trap Mass Spectrometer", *In preparation*

Miller, M.E.C., Mezher, M., De Dea, S., Continetti, R. E., "Size-dependent Coefficient of Restitution Phenomena for Submicron Tin Particles", *In preparation*

Miller, M. E. C., Mezher, M., Continetti, R. E., "Tapered Image Charge Detector for Measuring Velocity Distributions of Submicron Particle Scattering", *Review of Scientific Instruments*, 2020, 91 (6), 063305.

Adamson, B. D., Miller, M. E. C., Continetti, R. E., "The aerosol impact spectrometer: a versatile platform for studying the velocity dependence of nanoparticle-surface impact phenomena", *European Physical Journal, Techniques and Instrumentation*, 2017, 4 (1), 2

ABSTRACT OF THE DISSERTATION

Characterizing the Impact Dynamics of Small Particles: The Aerosol Impact Spectrometer

by

Morgan E.C. Miller

Doctor of Philosophy in Nanoengineering

University of California San Diego, 2020

Professor Robert E. Continetti, Chair

Small particle interactions with surfaces dominate processes from industrial manufacturing to micrometeorite impacts in space. For particles that are optically visible a wide range of modeling and studies exist to characterize the mechanical behavior and material properties that govern these interactions. The properties of materials at smaller scales, below microns in size, can differ from bulk measurements and the body of literature examining these smaller interactions lacks the same variety of experimental data. Presented herein is a new tool,

the Aerosol Impact Spectrometer (AIS), for the characterization of submicron particles impacting on surfaces.

The AIS is composed of a particle source, particle mass spectrometer, linear accelerator, impact target, and post impact detectors. Highly charged particles are generated using an electrospray ionization source before being injected into vacuum through an aerodynamic lens. A subset of the particle beam is selected using a quadrupole deflector and individual particles are injected into a linear electrostatic trap. As particles oscillate in the trap, charge detection mass spectrometry is performed to determine individual particle mass and charge before being ejection into a linear accelerator. A series of high voltage elements either accelerates or decelerates each particle to a select final energy before impacting a target surface. The subsequent behavior of the particle is examined with a variety of charge sensitive detectors including measurements of particle sticking and rebound velocity.

Rebound velocities over a wide range of initial energies have been measured for polystyrene latex spheres, tin metal particles, and frozen water-ice. Additionally, investigations of post-impact behavior including velocity angular distributions and fragmentation limits have been performed for tin and ice particles. The behavior of each species is distinct and further analysis of the tin metal particles shows behavior consistent with non-bulk material properties of the metal. Evidence for water ice melting and fragmentation have also been observed with high impact energies. Finally, the techniques employed to examine particle behavior after impact have also been applied to examine durability in freestanding ultrathin films under particle bombardment and measure the efficacy of large particle detection using a microchannel plate detector.

Chapter 1. Introduction

1.1 Particle Impact Dynamics

From bullets to atomic bombardment, understanding the processes and properties that govern interactions between bodies striking surfaces has been an area explored across a continuum of sizes. Foundational understanding of these interactions is often attributed to Newton's Law of Restitution[1] which notes that the speed of objects after a collision is dependent on the composition of these objects. Speed, in this statement, represents many factors coming together to affect the dynamics of a collision. Understanding the depth of this statement is intertwined with centuries of research still ongoing. With the advancement of understanding into these interactions, the scales at which we are able to examine and characterize behavior has decreased. Small particle interactions, those that occur for particles less than a micron in size, can be found across a wide range of studies and applications, and understanding the behavior of these interactions is an ongoing in scientific research. In additive industrial manufacturing, small particles are used to make durable coatings after being sprayed onto a surface and bonded.[2,3] Understanding the capture mechanisms of these particles after impact with a surface is required to make manufacturing technology more efficient. In other industrial settings, small particle contaminants threaten clean processes such as photolithography and containment/capture of these particles is of the utmost importance.[4,5] Design of contaminant mitigation strategies is aided by an understanding of the behavior of particles interacting with a surface. Environmental studies examining aerosols collected in situ must be able to efficiently capture and sample small particles.[6–8] The design of efficient collectors is aided by

understanding the adhesion mechanisms of the aerosol particles to a collector surface. Outside of Earth's atmosphere, sampling and collection of small particles from comets[9] and other solar sources[10,11] are accomplished with significantly higher energy interactions. Costly instruments designed to undertake these often decades-long studies need to be proven effective with terrestrial experiments, specifically in how they are able to capture and analyze particles. These are instances where a small particle-surface interaction plays a key role in the design and implementation of devices and processes.

When describing the impact dynamics of a particle striking a surface, a commonly used descriptor comes from Newtonian physics: the coefficient of restitution (e or CoR). The CoR of a collision is defined as the ratio of the post-impact velocity (v_f) to the impact velocity (v_i):

$$e = \frac{v_f}{v_i} \tag{1.1}$$

This is used to describe collisions where no mass loss occurs in the particle, and therefore will also represent the inelasticity of that collision. Many factors affect the CoR of a particle, but broadly, CoR represents how much energy the particle was able to retain after impact. When the CoR of a particle is zero, that particle has lost all of its energy during the impact and has a final kinetic energy of zero. When the CoR of a particle is one, the particle has lost none of its energy during the impact and the collision is perfectly elastic. These two limits are generally examined as a function of v_i, and the dominant processes that occur at different impact velocities dictate the CoR behavior. Generally, at very low impact velocities, surface energy interactions dominate, leading to particles sticking to the surface (a CoR of zero).[12] At higher velocities, while these surface energy interactions are still fairly strong relative to the incident

energy, CoR rapidly increases until reaching a maximum value (usually very near to one). In this regime, collisions are very elastic with few loss mechanisms affecting the particle and the surface.[13] At even higher velocities CoR begins to decrease until zero CoR is again reached as rebounds from the surface cease. The energy loss mechanisms at these high velocities cause particles to adhere to a surface or can be associated with other mass-loss phenomena such as fragmentation and vaporization of material.[14,15] A graphic representation of CoR as a function of incident velocity is shown in Figure 1.1.

Understanding the processes that affect particle-surface interaction at different impact velocities is the subject of a myriad of different studies with each attempting to mathematically model the post impact behavior of a particle as a function of material properties. For the work presented here, understanding the processes that affect particle-surface interactions for velocities greater than the 'peak elasticity' point is primarily of interest. In this region, permanent deformation of the particle and target (plasticity) is the primary energetic loss process.[16] For different materials, the onset of plasticity, when that material is under stress and strain, is denoted as that material's yield strength.[16] This denotes where permanent deformation of the material occurs. For CoR, this is correlated to the onset of collision inelasticity.

In order to quantify the effect of inelastic processes, it is possible to model the behavior of different materials and relate that to experimentally measurable data. The CoR is a convenient metric for examining the plasticity of a collision because all energetic factors affect this single measure. Many past efforts to model particle-surface interactions are paired with experiments where CoR is the primary measurement performed.

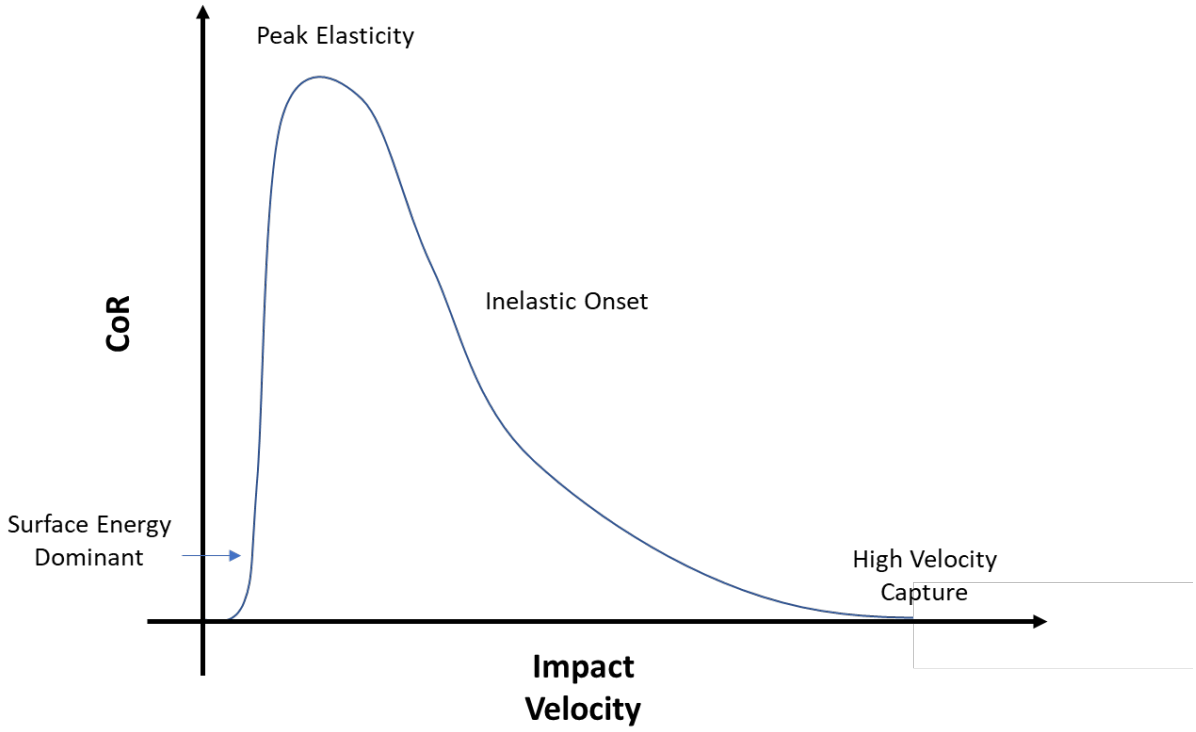

Figure 1.1: *Graphic representation of a CoR curve as a function of incident velocity. Curve shape is not to scale, and roughly approximates the behavior of particles studied in Chapter 3. Low velocity behavior is modeled from Dahneke [12].*

However, these measurements are typically done with only a few different materials[17] and there exists no large database of CoR characterizations, particularly for particles less than one micron in size. The often cited and foundational work of Dahneke[12,13,18] is an example of an experimental data set used for comparison with predictive modeling.[19] Developing a platform to examine the impact dynamics of small particles is the primary focus of the work presented here. The techniques used in development of this characterization tool are presented here and in Chapter 2.

Existing modeling of the processes in materials that affect the elasticity of a collision has advanced from Hertz who considered the mechanics of two spheres interacting.[20,21] Many models use this approach to describe the elastic interaction and add additional effects for various inelastic processes. Early work adapting the purely elastic description of Hertz to include inelastic processes can be found in Bitter.[16] This description classifies the particle-surface interaction into plastic and elastic energies, dependent on key material properties of the particle and impact surface. These properties include: the Young's modulus of the materials, a measure of how the material reacts to stress and strain; the Poisson ratio, a measure of material behavior under compression; and yield strength, a measure of stress required to deform the material. These properties and the assumptions made in most models concerning particle-surface interaction are constructed using continuum mechanics. A potential limitation is that the material properties used as inputs to these models tend to be directly measurable quantities assumed to be static, in this case concerning stress and strain.

Beyond the basic concept that energies in the particle-surface interaction can be divided into categories of elastic and inelastic plastic behavior, modeling can be used to predict the

onset of inelastic phenomena. The Johnson, Kendall, and Roberts (JKR)[22] model describes how Hertz's elastic contact theory applies to surface energies and adhesion, particularly in lower energy cases where this effect is most significant. This model was experimentally examined with large (> 1cm) rubber spheres. Tsai et al.[19] expanded the application of surface energies with effects of surface roughness over a wide range of energies by the inclusion of plastic deformation of the material. This model was experimentally validated by comparison to the dataset collected by Dahneke[13] of micron polystyrene latex spheres. More recently, Hassani-Gangaraj[23] has developed modeling of higher energy impact adhesion where plasticity is accounted for as a thermodynamic process. This model was examined experimentally using ~10 μm tin metal particles. A thorough review of models in the aerosol community is presented in Cai et al.[8] with particular attention paid to low velocity interactions.

Models dependent on material properties can only be applied when accurate measures of those properties are available. This becomes an added complication in studies of small particles where these material properties can differ from bulk values significantly.[24,25] In addition to potential size-dependent effects, materials simulations and experimental observations have demonstrated that the assumed static nature of yield strength in many models is incomplete, as this parameter dynamically changes during the high strain-rates experienced during impact.[26,27]

In order to understand existing/future models and the effects for smaller particles, further experimental observations of particle dynamics need to performed to provide sets of experimental observables for a range of systems. Creating a platform that allows the collection acquisition of this type of data is the prime motivation for the work presented in the following

chapters. In order to develop this platform, a variety of techniques have been integrated to allow experimental observation of particle impact dynamics, primarily measurements of particle CoR for different sizes, velocities, and material compositions.

1.2 Particle Generation Techniques

In order to study interactions with a surface, particles, either individually or as an ensemble, need to be generated in a controlled manner. Creating particles that are microns in size or less (small particles) can be done with a wide variety of techniques depending on the particle composition and desired charge state. As with atomic and molecular species, a convenient control mechanism for small particles with charge is thus of electric fields. An array of control mechanisms such as electrostatic lenses, energy selective filters,[28] electrodynamic accelerators,[29] and electrostatic ion traps[30] are useful for working with charge carriers and make the generation and manipulation of charged particles favorable. Because of their ready control, many methods for producing charged particles exist. Some of these methods include contact charging of bare dust particles,[31,32] liquid metal ion sources,[33] and laser ablation.[34]

One particularly useful method for generating charged particles is electrospray ionization (ESI). ESI is commonly used in mass spectrometry to generate molecular ions and has the flexibility to work with very large ions.[35–37] In ESI, a solution of interest is fed through a needle held at high potential. The needle aerosolizes and creates ions within the solution which can be used to deposit large amounts of charge onto particles.[38] This method is particularly flexible because the ions generated are initially created as a solution that can be

customized to fit the experimental needs. For particle generation, a colloidal suspension of the particles of interest is used and each particle is generated within a droplet of solution that subsequently evaporates, depositing charge onto the particle within. Alternatively, particles can be produced directly from droplets of solution that are frozen after being created. The charge carrier in ESI is the solution that particles are either suspended in or composed of. Non-conductive particles can be generated with high amounts of charge, as long as the carrier solution used to make the colloidal suspension is capable of carrying charge. This makes ESI an ideal source for the generation of a wide variety of highly charged particles. Its use with a variety of particle compositions and sizes is described in the following chapters.

1.3 Particle Characterization Techniques

Characterizing size-dependent impact phenomena requires a method for measuring particle size before impact. Additionally, kinetic energy measurements are most readily performed with particle mass and velocity information. With larger particles, this has often been done with imaging of the particle diameter and optical measurements of the particle traveling through space. This allows the particle's size and velocity to be determined. However, with smaller particles (< 1 μm) it becomes increasingly difficult to rely on traditional imaging techniques. Because of the useful control mechanisms that are accessible when working with charged particles, detection technologies specific to charged particles are also commonly used. Charge-sensitive detectors can supply the critical information for much smaller particle sizes as do optical techniques for larger particles.

Characterization of particle velocity is required for measuring particle CoR. This measurement is most easily performed by detecting a particle at two different locations and times. With knowledge of the distance between the two locations (Δx), and the time difference between the detections (Δt), velocity (v) can be calculated:

$$v = \frac{\Delta x}{\Delta t} \tag{1.2}$$

Image charge detectors are devices capable of measuring when a charge carrier passes near the charge-sensitive detection element. The charge carrier induces a small current in the detection element which is amplified by the detector and converted to a voltage signal. A commonly used type of detector is a cylindrical detection element where signal is induced when a charge carrier passes through the axis of the cylinder.[39] A unique signal is produced when the carrier enters the tube, and exits the tube. Velocity measurements of a charged particle can be made by using multiple image charge detectors with a known distance between them and calculating the time between the two induced signals. Additionally, a single image charge detection tube can be used to calculate particle velocity by comparing the length of the cylindrical detection element to the time between the entrance and exit signal. This velocity measurement is non-destructive and does not interfere with the particle flight path making it well suited for repeated measurements of a single particle.

In conjunction with velocity measurements, measuring the mass of individual particles allows the calculation of particle kinetic energy. Mass measurements with homogenous material, or materials of known compositions can be used to calculate particle diameter as well. Non-destructive mass measurements of charged particles can be performed using the same detector (image charge detector) used for performing velocity measurements. Particles made

to oscillate through an image charge detector using a set of two electrostatic mirrors produce a regular signal with a signature frequency. Each peak from this signal can be used to calculate the particle velocity described previously, while the frequency of the oscillation signal can be related to the particle mass-to-charge ratio. This method of particle characterization using an electrostatic trap was pioneered by Benner[30] and is known as charge detection mass spectrometry. This built on the techniques of Fourier Transform Ion Cyclotron Resonance Mass Spectrometry for studying large ions and applied them to species with mass in excess of MDa. The electrostatic potential used to trap the particle must be well characterized so that modeling of this potential allows the relationship of mass-to-charge ratio and oscillation frequency to be established for a particular potential geometry. In addition to frequency and velocity, the amplitude of the signal produced on the image charge detector can be calibrated to determine the amount of charge on a particle passing through the detector. This capability, paired with an electrostatic trap, allows repeated measurement of particle charge (each oscillation) and measurement of the particle mass-to-charge ratio. From these measurements the particle mass can be determined, and from particle material density a particle diameter can be assigned. With the measurement capabilities described above, the charged particle velocity, mass, charge, and diameter can be determined. A more detailed description of the measurements made in this work can be found in Chapter 2.

1.4 Control of Particle Kinetic Energy

In order to examine particle impact dynamics at different velocities/energies, control over single particle kinetic energy is required. Previous experimental studies have used a variety of techniques to generate energy-selected particles including aerodynamic accelerators,[18,40] laser-based accelerators,[41,42] and Van de Graaff accelerators.[43] In order to energetically control charged particles, another convenient acceleration technique is the linear accelerator (LINAC). A LINAC is operated by repeatedly switching high voltage across pairs of electrodes such that the charged particle is repeatedly accelerated by each electrode. Precision high voltage switching in a LINAC allows electrodynamic acceleration to be operated at lower voltages (~10 kV) than the static megavolt potentials required in Van de Graaff acceleration facilities, while still being capable of achieving greater than megavolt total potentials across the accelerator. This technique was originally applied to heavy molecular ions by Hendell and Even[29] who used a series of coaxial tubes to repeatedly accelerate ions. Each gap between tubes applies additional potential to the ion by re-referencing the potential on each LINAC element as the particle passes through the tube. This technique is used to create high kinetic energy molecular ions and can be used on particles of masses in excess of terradaltons. The variable potential that can be applied to the LINAC also allows variable acceleration of particles where higher potentials are used to achieve higher final energies. Particles with sufficient charges for their size can achieve high velocities with a LINAC, much like those achieved with Van de Graff accelerators, without requiring the high voltage operating environment of a megavolt acceleration stage. Experimental implementation of a LINAC for particle acceleration is presented in Chapter 2 and Chapter 8.

1.5 Structure of Dissertation

The techniques described in the proceeding sections can all be combined to create an instrument well suited for characterizing the impact dynamics of small particles: the Aerosol Impact Spectrometer. The instrument description and function are presented in Chapter 2. Uses of the device for characterizing different particle impact dynamics are described in Chapter 3, Chapter 5, and Chapter 8. In Chapter 3 Polystyrene latex spheres used to calibrate the mass spectrometer are impacted onto a target and CoR measurements taken and compared to previous work. In Chapter 5 and Chapter 8 previously unexplored sizes of submicron tin and water-ice particles are impacted onto target with CoR information collected in addition to new impact dynamics data. Additional experimental capabilities are presented in Chapters 4, Chapter 6, and Chapter 7. Chapter 4 introduces a new image charge detector design used to measure rebound angular distributions after particle impact. Chapter 6 explores the use of ultrathin film targets to measure resilience under particle bombardment. Chapter 7 demonstrates the use of microchannel plate detectors to measure submicron particle impacts.

1.6 References

(1) Newton, I. *Newton's Principia : The Mathematical Principles of Natural Philosophy*; First American edition, carefully revised and corrected / with a life of the author, by N. W. Chittenden. New-York : Daniel Adee, 1846., 1846.

(2) Klinkov, S. V.; Kosarev, V. F.; Rein, M. Cold Spray Deposition: Significance of Particle Impact Phenomena. *Aerosp. Sci. Technol.* **2005**, *9* (7), 582–591. https://doi.org/10.1016/j.ast.2005.03.005.

(3) Fauchais, P.; Montavon, G. Thermal and Cold Spray: Recent Developments. *Key Eng. Mater.* **2008**, *384*, 1–59. https://doi.org/10.4028/www.scientific.net/KEM.384.1.

(4) Bakshi, V. EUV Source Technology. *EUV Lithogr.* **2009**, 103–131. https://doi.org/10.1117/3.769214.ch3.

(5) van de Kerkhof, M. A.; van Empel, T.; Lercel, M.; Smeets, C.; van de Wetering, F.; Nikipelov, A.; Cloin, C.; Yakunin, A.; Banine, V. E. Advanced Particle Contamination Control in EUV Scanners. In *Proceedings of SPIE*; 2019; p 27. https://doi.org/10.1117/12.2514874.

(6) Rao, A. K.; Whitby, K. T. Non-Ideal Collection Characteristics of Inertial Impactors-I. Single-Stage Impactors and Solid Particles. *J. Aerosol Sci.* **1978**, *9* (2), 77–86. https://doi.org/10.1016/0021-8502(78)90069-1.

(7) Miyakawa, T.; Matsuzawa, R.; Katayama, M.; Takegawa, & N. Reconsidering Adhesion and Bounce of Submicron Particles Upon High-Velocity Impact. *Aerosol Sci. Technol.* **2013**, *47* (5), 472–481. https://doi.org/10.1080/02786826.2013.763895.

(8) Cai, Y.; Tay, K.; Zheng, Z.; Yang, W.; Wang, H.; Zeng, G.; Li, Z.; Keng Boon, S.; Subbaiah, P. Modeling of Ash Formation and Deposition Processes in Coal and Biomass Fired Boilers: A Comprehensive Review. *Appl. Energy* **2018**, *230*, 1447–1544. https://doi.org/10.1016/j.apenergy.2018.08.084.

(9) Burch, J. L.; Gombosi, T. I.; Clark, G.; Mokashi, P.; Goldstein, R. Observation of Charged Nanograins at Comet 67P/Churyumov-Gerasimenko. *Geophys. Res. Lett.* **2015**, *42* (16), 6575–6581. https://doi.org/10.1002/2015GL065177.

(10) Albers, N.; Hörning, M.; Kempf, S.; Krivov, A. V.; Makuch, M.; Schmidt, J.; Seiß, M.; Miodrag Sremčević. E Ring Dust Sources: Implications from Cassini's Dust Measurements. *Planet. Space Sci.* **2006**, *54* (9–10), 1024–1032. https://doi.org/10.1016/J.PSS.2006.05.022.

(11) Yaroshenko, V. V.; Ratynskaia, S.; Olson, J.; Brenning, N.; Wahlund, J.-E.; Morooka, M.; Kurth, W. S.; Gurnett, D. A.; Morfill, G. E. Characteristics of Charged Dust

Inferred from the Cassini RPWS Measurements in the Vicinity of Enceladus. *Planet. Space Sci.* **2009**, *57* (14–15), 1807–1812. https://doi.org/10.1016/J.PSS.2009.03.002.

(12) Dahneke, B. The Capture of Aerosol Particles by Surfaces. *J. Colloid Interface Sci.* **1971**, *37* (2), 342–353. https://doi.org/10.1016/0021-9797(71)90302-X.

(13) Dahneke, B. Further Measurements of the Bouncing of Small Latex Spheres. *J. Colloid Interface Sci.* **1975**, *51* (1), 58–65. https://doi.org/10.1016/0021-9797(75)90083-1.

(14) Hassani-Gangaraj, M.; Veysset, D.; Nelson, K. A.; Schuh, C. A. In-Situ Observations of Single Micro-Particle Impact Bonding. *Scr. Mater.* **2018**, *145*, 9–13. https://doi.org/10.1016/J.SCRIPTAMAT.2017.09.042.

(15) Hassani-Gangaraj, M.; Veysset, D.; Nelson, K. A.; Schuh, C. A. Impact-Bonding with Aluminum, Silver, and Gold Microparticles: Toward Understanding the Role of Native Oxide Layer. *Appl. Surf. Sci.* **2019**, *476*, 528–532. https://doi.org/10.1016/j.apsusc.2019.01.111.

(16) Bitter, J. G. A. A Study of Erosion Phenomena Part I. *Wear* **1963**. https://doi.org/10.1016/0043-1648(63)90003-6.

(17) Brach, R. M.; Dunn, P. F.; Li, X. Experiments and Engineering Models of Microparticle Impact and Deposition. *J. Adhes.* **2000**, *74* (October), 227–282. https://doi.org/10.1080/00218460008034531.

(18) Dahneke, B. Measurements of Bouncing of Small Latex Spheres. *J. Colloid Interface Sci.* **1973**, *45* (3), 584–590.

(19) Tsai, C.-J.; Pui, D. Y. H.; Liu, B. Y. H. Capture and Rebound of Small Particles Upon Impact with Solid Surfaces. *Aerosol Sci. Technol.* **1990**, *12* (3), 497–507. https://doi.org/10.1080/02786829008959364.

(20) Hertz, H. R. On the Contact of Elastic Solids 1881. In *Miscellaneous Papers*; Macmillan and Co.: London, 1896; p 146.

(21) Hertz, H. R. On the Contact of Rigid Elastic Solids and on Hardness 1882. In *Miscellaneous Papers*; Macmillan and Co.: London, 1896; p 163.

(22) Johnson K. L.; Kendall K.; Roberts A. D. Surface Energy and the Contact of Elastic Solids. *Proc. R. Soc. A* **1971**, *324*, 301–313.

(23) Hassani-Gangaraj, M.; Veysset, D.; Nelson, K. A.; Schuh, C. A. Melt-Driven Erosion in Microparticle Impact. *Nat. Commun.* **2018**, *9* (1), 5077. https://doi.org/10.1038/s41467-018-07509-y.

(24) Nowak, J. D.; Beaber, A. R.; Ugurlu, O.; Girshick, S. L.; Gerberich, W. W. Small Size Strength Dependence on Dislocation Nucleation. *Scr. Mater.* **2010**, *62* (11), 819–822.

https://doi.org/10.1016/j.scriptamat.2010.01.026.

(25) Kim, J. Y.; Greer, J. R. Tensile and Compressive Behavior of Gold and Molybdenum Single Crystals at the Nano-Scale. *Acta Mater.* **2009**, *57* (17), 5245–5253. https://doi.org/10.1016/j.actamat.2009.07.027.

(26) Chen, Q.; Alizadeh, A.; Xie, • Wanting; Wang, X.; Champagne, V.; Gouldstone, • Andrew; Lee, J.-H.; Sinan, •; Ftü, M.; Müftü, S.; Edu, M. High-Strain-Rate Material Behavior and Adiabatic Material Instability in Impact of Micron-Scale Al-6061 Particles. *J Therm Spray Tech* **2018**, *27*, 641–653. https://doi.org/10.1007/s11666-018-0712-4.

(27) Xie, W.; Alizadeh-Dehkharghani, A.; Chen, Q.; Champagne, V. K.; Wang, X.; Nardi, A. T.; Kooi, S.; Müftü, S.; Lee, J.-H. Dynamics and Extreme Plasticity of Metallic Microparticles in Supersonic Collisions. *Nat. Sci. Reports* **2017**. https://doi.org/10.1038/s41598-017-05104-7.

(28) Zeman, H. D. Deflection of an Ion Beam in the Two-Dimensional Electrostatic Quadrupole Field. *Rev. Sci. Instrum.* **1977**, *48*, 1079. https://doi.org/10.1063/1.1135188.

(29) Hendell, E.; Even, U. Tabletop Linear Accelerator for Massive Molecules. *Rev. Sci. Instrum.* **1995**, *66* (7), 3901–3902. https://doi.org/10.1063/1.1145390.

(30) Benner, W. H. A Gated Electrostatic Ion Trap To Repetitiously Measure the Charge and m/z of Large Electrospray Ions. *Anal. Chem* **1997**, *69* (20), 4162–4168.

(31) Stübig, M.; Schäfer, G.; Ho, T. M.; Srama, R.; Grün, E. Laboratory Simulation Improvements for Hypervelocity Micrometeorite Impacts with a New Dust Particle Source. *Planet. Space Sci.* **2001**, *49* (8), 853–858. https://doi.org/10.1016/S0032-0633(01)00035-6.

(32) Beaty, N. Pulsing Characteristic Effects on the Charging of Iron Dust Sources, University of Colorado Boulder, 2013.

(33) Clampitt, R. Advances in Molten Metal Field Ion Sources. *Nucl. Instruments Methods Phys. Res.* **1981**, *189* (1), 111–116. https://doi.org/10.1016/0029-554X(81)90132-4.

(34) Fujii, T.; Inoue, S.; Kannari, F. Measurements of Charged Particles in the Laser Ablation Plume of Polymers. *J. Appl. Phys.* **1995**, *78* (5), 3401–3407. https://doi.org/10.1063/1.359968.

(35) Aksyonov, S. A.; Williams, P. Impact Desolvation of Electrosprayed Microdroplets - A New Ionization Method for Mass Spectrometry of Large Biomolecules. *Rapid Commun. Mass Spectrom.* **2001**, *15* (21), 2001–2006. https://doi.org/10.1002/rcm.470.

(36) Doussineau, T.; Kerleroux, M.; Dagany, X.; Clavier, C.; Barbaire, M.; Maurelli, J.;

Antoine, R.; Dugourd, P. Charging Megadalton Poly(Ethylene Oxide)s by Electrospray Ionization. A Charge Detection Mass Spectrometry Study. *Rapid Commun. Mass Spectrom.* **2011**, *25* (5), 617–623. https://doi.org/10.1002/rcm.4900.

(37) Cai, Y.; Peng, W.-P.; Kuo, S.-J.; Lee, Y. T.; Chang, H.-C. Single-Particle Mass Spectrometry of Polystyrene Microspheres and Diamond Nanocrystals. *Anal. Chem.* **2002**, *74* (1), 232–238. https://doi.org/10.1021/ac010776y.

(38) Daly, R. T.; Kerby, J. D.; Austin, D. E. Electrospray Charging of Minerals and Ices for Hypervelocity Impact Research. *Planet. Space Sci.* **2013**, *75* (1), 182–187. https://doi.org/10.1016/j.pss.2012.11.012.

(39) Shelton, H.; Hendricks, C. D.; Wuerker, R. F. Electrostatic Acceleration of Microparticles to Hypervelocities. *J. Appl. Phys.* **1960**, *31*, 1243. https://doi.org/10.1063/1.1735813.

(40) Rennecke, S.; Weber, A. P. The Critical Velocity for Nanoparticle Rebound Measured in a Low Pressure Impactor. *J. Aerosol Sci.* **2013**. https://doi.org/10.1016/j.jaerosci.2012.12.007.

(41) Willem Visser, C.; Tagawa, Y.; Sun, C.; Lohse, D. Microdroplet Impact at Very High Velocity. https://doi.org/10.1039/c2sm26323h.

(42) Veysset, D.; Sun, Y.; Kooi, S. E.; Lem, J.; Nelson, K. A. *Laser-Driven High-Velocity Microparticle Launcher In Atmosphere And Under Vacuum*.

(43) Burchell, M. J.; Cole, M. J.; McDonnell, J. a. M.; Zarnecki, J. C. Hypervelocity Impact Studies Using the 2 MV Van de Graaff Accelerator and Two-Stage Light Gas Gun of the University of Kent at Canterbury. *Meas. Sci. Technol.* **1999**, *10*, 41–50. https://doi.org/10.1088/0957-0233/10/1/011.

Chapter 2. Experimental Methods and Data Analysis

Characterization of small particle impact dynamics has proven a challenge in modern research. Most experimental examinations of the particle-surface impact system have been confined to optically accessible particle sizes, readily characterized by direct imaging and post-impact examinations. Experiments that are able to examine smaller particle sizes often do so by measuring ensemble behavior without single particle discrimination. The ability to probe single particle interactions with a surface at smaller size regimes is important to understanding the dynamics of these interactions and the effect that material property differences from bulk has on these interactions.

2.1 Overview of Experimental Apparatus

The development and operation of the Aerosol Impact Spectrometer is the primary advancement described in this dissertation. A detailed description of its components and operations is explored in the following sections and a partial summary of its basic operation can be found in Adamson et. al.[1] The apparatus core functionality relies on the application of both commonly used and novel techniques to small particle systems creating a unique capability matched by no other device in the world. The general operation of the apparatus consists of a particle source to generate single highly charged particles in vacuum, a spectrometer to analyze the properties single particles, an energetic control mechanism to fix the final energy of single

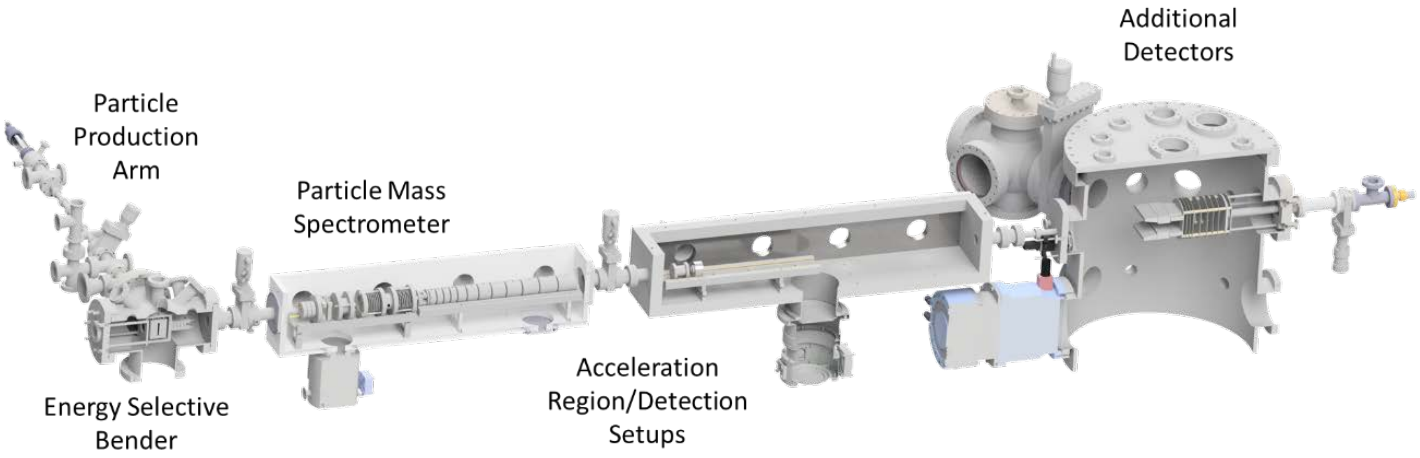

Figure 2.1: *General apparatus layout with key components labeled.*

particles, and a variety of detectors/targets to examine single particle interactions with a surface. An overview of the apparatus construction is shown in Figure 2.1.

Generation of highly charged particles was chosen as the basis of these measurements as it permits electrostatic control of particle trajectories and energies, and the use of charge-sensitive measurement techniques employed in both the mass spectrometry and collisional analysis detectors. Although originally envisioned to examine the heterogeneity of laboratory-produced environmental aerosol analogs, the features of the apparatus allow production, characterization, and impact evaluation of a wide variety of aerosol species including particles from colloidal suspensions and ices. The production methodology and characterization of the individual particle species will be explored for different experiments in Chapters 3, 5, 6, and 7, as well as the different detection mechanisms used in each experiment.

2.1.1 Particle Source

The primary function of the ion source in the apparatus is the generation of particles with sufficient charge to be controlled and detected. Multiple techniques exist for producing single highly charged particles[2–4] and the most reliable approach found to work with the AIS is electrospray ionization (ESI). Electrospray ionization sources are commonly used in mass spectrometry as a simple and consistent soft ionization technique for molecular species solutions that might otherwise be prone to fragmentation upon ionization. In addition to its more common functionality for molecular ion production, colloidal solutions can be used to produce highly charged single particle aerosols.[5] This method works by passing a colloidal solution of particles through a capillary or needle held at high potential resulting in an aerosolizing spray

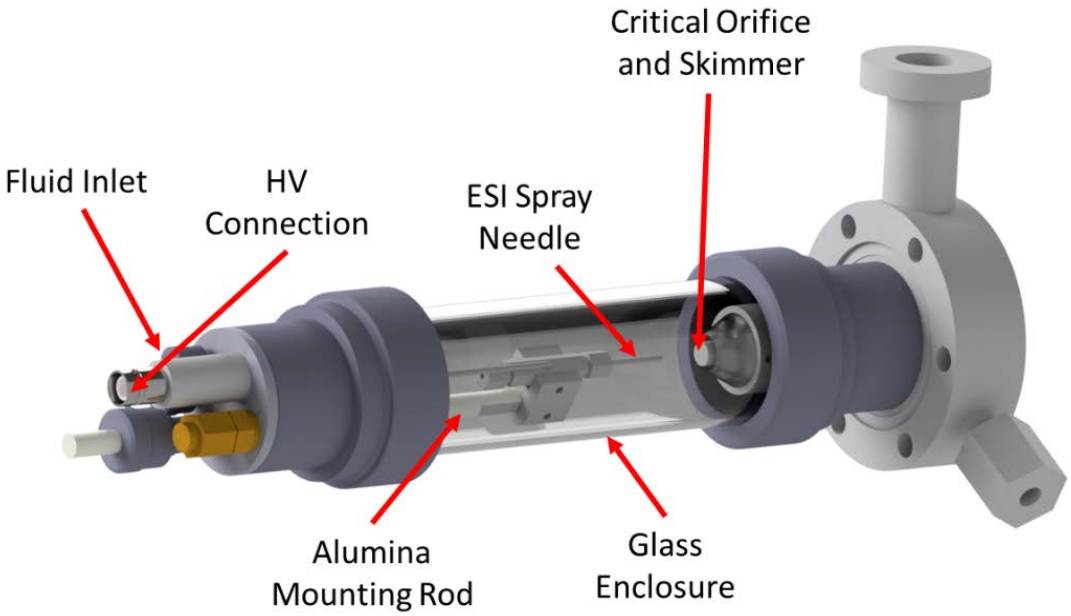

Figure 2.2: *Enclosed electrospray ionization source with major components labeled.*

at the outlet. The liquid of the colloidal solution acts to carry charge from the needle into the aerosolized cloud where smaller and smaller droplets are created as the liquid particles evaporate and coulombically explode.[6] Droplets carrying a single particle from the colloidal suspension can sufficiently dry and deposit the initial liquid droplet charge onto the surface of the particle. This way, even non-conductive particle species are capable of being charged using an ESI source. ESI aerosolized plumes are typically sprayed into a grounded capillary or pinhole interface to vacuum.

The source consists of an enclosed-atmosphere chamber with a suspended needle through which solution is pumped and sprayed. A diagram of this setup is detailed in Figure 2.2. The present needle assembly consists of a square cut metal tube (100 µm ID, 229 µm OD) fit into a ValCo union (250 µm joint). The solution is supplied to the union through 250 µm Teflon resin tubing from a 5 mL syringe driven by a syringe pump (typical operation 0.01-0.2 mL/hr). The union is held in place using a custom aluminum mounting block on an alumina rod. The needle is held ~ 5 mm from the critical orifice, a pinhole of 150-200 µm in size. Voltage is supplied from a high voltage power supply to the aluminum mounting block and the entire assembly is operated at 1.5-5.5 kV depending on solution, flow rates, and needle position.

When operating with a colloidal solution, drying of the particles post-spray is critical to operation. This is performed in two stages: a heated counter flow and high temperature drift region. A counterflow gas (typically pure nitrogen) is released through a skimmer aperture surrounding the critical orifice (Figure 2.2). Before entering the skimmer the nitrogen passes through a commercial gas heater that heats the inlet region to 60-100°C (Omega, T-type process heater). Gas flow rates through the heater are regulated with a dual-gas mixing flow regulator

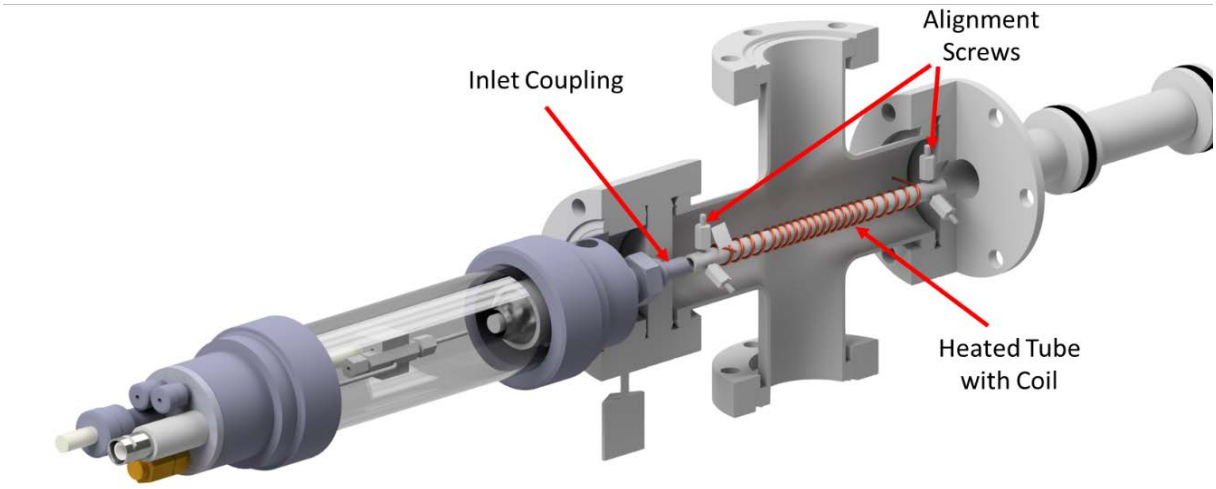

Figure 2.3: *Enclosed electrospray ionization source coupled with heating region.*

(Matheson, 7372-T) with typical flows of 12.4 SCCM. The skimmer assembly and outside chamber are resistively heated with heating tape to provide a high temperature environment at the ESI inlet (~100°C). The critical orifice of the ESI is mounted using a SS316 tube that couples to a flow tube within the first vacuum chamber. The flow tube is wrapped in thermal coaxial wire, as seen in Figure 2.3, and supported on each end by a set of welded alignment screws. Power is supplied to the thermal coaxial wire from a high current feedthrough mounted to the chamber and the pressure of the chamber is monitored with a capacitance gauge. The flow tube allows the initial beam to pass through additional heating that can be readily operated to achieve temperatures > 500°C. The operating pressure in this chamber is 1-10 Torr with higher pressures localized in the heating tube that is directly exposed to the inlet orifice. When liquid solutions (water, heptanol (aq)) have been used for the purpose of creating ices, the heated region is removed to promote rapid cooling and solidification of the droplets in vacuum.

After generation and introduction into partial vacuum, the particle beam is passed into a series of apertures ranging from 2-6 mm in diameter that form an aerodynamic lens (ADL). The lens typically used was modeled after the works of Liu et. al.[7] but constructed in a custom form using the tools published by Wang and McMurry.[8] A series of KF-16 tubes have been precision machined to mount aluminum aperture plates on one end of each tube (Figure 2.4). The aperture sits where the o-ring retainer typically slots into the tube, requiring custom retainers to be made for the construction of the lens. Progressively smaller apertures (5.89 mm, 5.31 mm, 4.60 mm, 3.40 mm, and 3.10 mm) are mounted in a series of 4 of KF-16 tubes forming the body of the lens with a conflat (CF) adapter at the lens start and a KF-16 cross at the end to facilitate vacuum connection. The entire assembly is aligned using a custom SS316 mandrel made to center the progressive apertures onto a single axis. The pumping for the aerodynamic

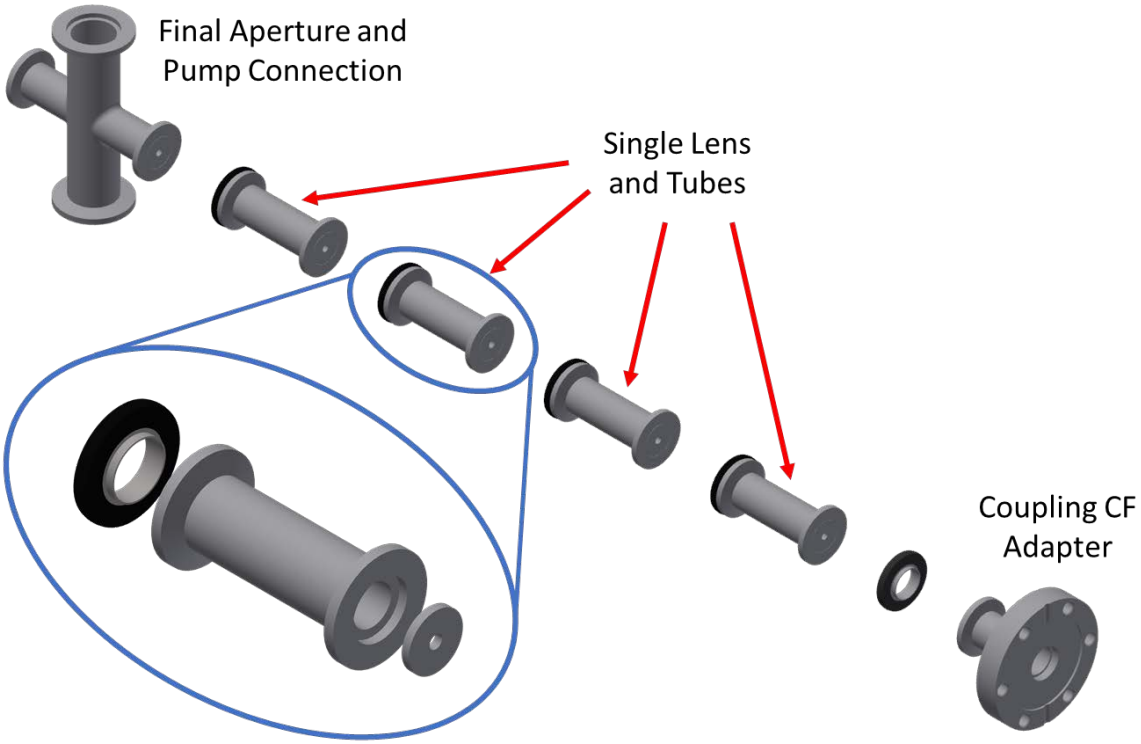

Figure 2.4: *Breakout of aerodynamic lens design. Individual KF tubes contain different aperture sizes to form the lens.*

lens is supplied after the final aperture with an Osaka ER100D dry pump. The operating pressure after the lens is typically ~100 mTorr.

A series of differentially pumped CF crosses using a Alcatel RSV 350 with a Leybold D65BCS roots blower backing pump and Pfeiffer TMH064 allow the final chamber of the particle production beam line to operate at ~1e-5 Torr when open to the critical orifice. In addition to providing differential pumping stages, these chambers house particle detectors (see particle detector section). The resultant particle beam has a narrow velocity distribution, typically with a full-width-half-max of < 6m/s, based on the operating pressure at each end of the ADL and this beam can be efficiently steered into an energy selective filter (detailed in the following section).

2.1.2 Energy Selection

The mass spectrometry performed on particles within the beam requires a form of energy selection to get accurate mass information. A particularly sensitive method to perform this selection is accomplished by using a quadrupole deflector that bends an energetic subset of the particle beam down the secondary axis of the apparatus. The quadrupole deflector (QD) used in AIS is modeled after the work of Zeman,[9] which was adapted here to create a deflector with four SS316 quarter-cylinder rods mounted squarely and perpendicular to the plane of the apparatus held at equal and opposite potentials (Figure 2.5). The potential applied to the rods deflects particles at different angles depending on their energy-per-charge. When the energy-per-charge of a particle is equal to the potential applied to the deflector the particles are

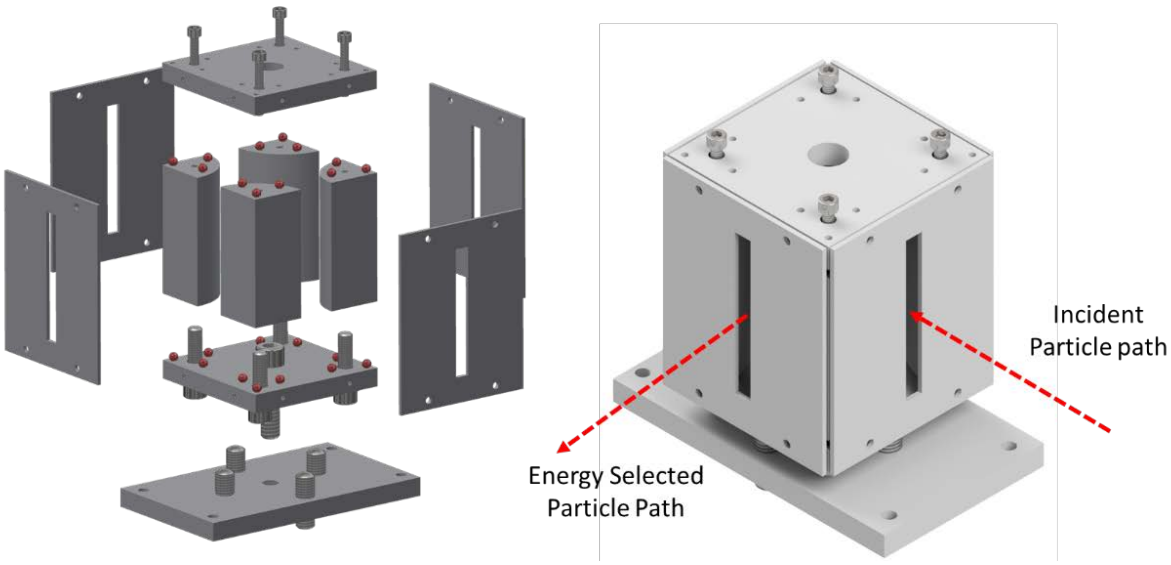

Figure 2.5: *Quadrupole deflector design. Blowup of QD components (left) and QD assembly (right)*

deflected 90° from their original trajectory. This allows for a single set of energy-per-charge particles to be transmitted into the mass spectrometer. To prevent transmission of non-selected energies, all sides of the deflector are equipped with a rectangular skimming plate. This plate prevents off-axis particles from continuing down the beamline and helps to set the resolution of this deflector. SIMION simulations of the deflector in use with a 10 mm wide skimming plate aperture have shown the energy-per-charge selection to be within 10% of the voltage applied to the QD when operating at hundreds of Volts. Immediately before and after the deflector assembly, the chamber is equipped with sets of electrostatic deflectors, einzel lenses, and particle detectors. These facilitate steering the particle beam into and out of the QD. An overview of the position of these optics and the particle production arm of the apparatus is presented in Figure 2.6.

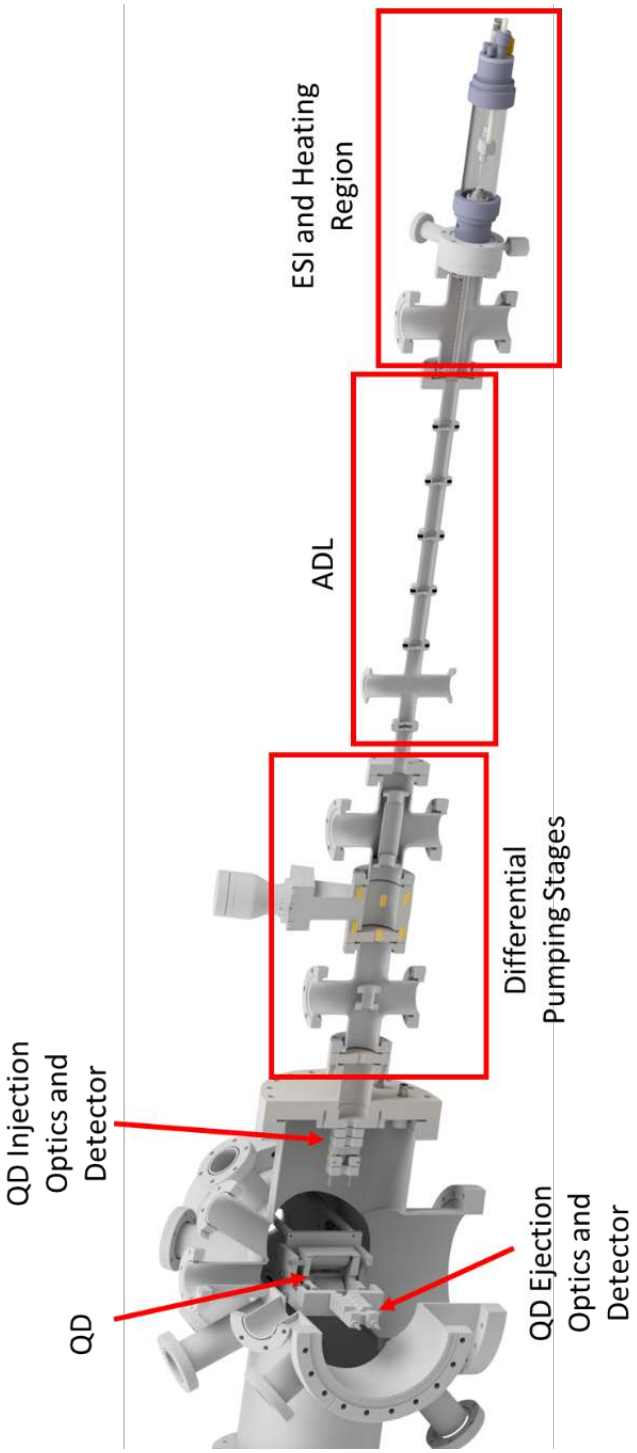

Figure 2.6: *Overview of particle production arm*

2.1.3 Image Charge Detection

Image charge detection techniques are used to make a wide variety of measurements in the apparatus including measurements of particle position, velocity, oscillation frequency in a trap, and rebound trajectory. The technology to measure small highly charged particles with electronic detection was first pioneered by Shelton et. al.[10] and was used to measure velocities of hypervelocity iron dust particles produced in a van de Graaf accelerator. Significant improvements and new applications of image charge detection have been developed in more advanced velocity measurement devices[11] and new fields of mass spectrometry.[12,13] The measurements performed in the AIS to date have been carried out primarily using one geometry of image charge detector (ICD), with the notable exception of the device described in Chapter 4 – the ICD tube.

The basic functionality of an ICD is to measure the induced charge produced from a charged species interacting with a conductive tube. As the charged species approaches the detector, a small current is produced by charge flow in the conductive tube. This current can be amplified and converted into a voltage signal with the appropriate circuitry (detailed in Appendix A). For the ICD tube geometry, particles pass axially along the centerline of the tube. The signal produced has a distinct square shape with an edge associated with the particle entering the tube and a matching edge of the particle leaving the tube (Figure 2.7).

The square wave signal produced by an ICD can be used to obtain various information. By looking at the width of the ICD signal in time, the transit time of the particle through the tube can be measured (Figure 2.8). When paired with the known length of the ICD, this allows

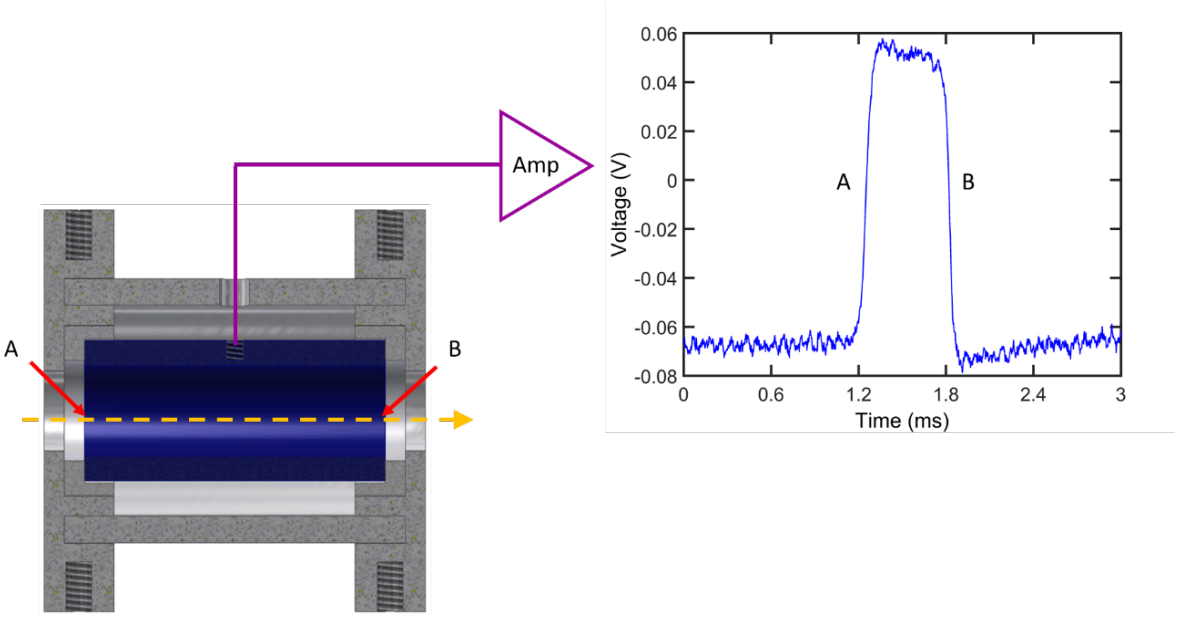

Figure 2.7: *Image Charge Detection Tube (ICD). The detection electrode is highlighted in blue, supported in a shielded casing (axial slice). A) Particle enters the tube which produces the rising edge of the signal. B) Particle leaves the tube which produces the falling edge of the signal.*

for the determination of the axial velocity of the particle. The exact points in time that correspond to the physical dimensions of the detector are dependent on the response time of the circuitry used and the geometry of the shielding around the detection electrode. These can be calibrated using multiple image charge detectors of similar geometries to make redundant velocity measurements (using the leading edge of each detector). The velocity calculated by the transit time between detectors' leading edges can then be compared to measurements performed on a single square waveform to determine where along the peak true transit time measurements can be made. Using the calibration procedure above and with modeling of induced charge in SIMION it was deduced that the optimal points in time for measuring velocities of the ICDs used in the AIS is at ~60% the maximum height of the waveform (for both the rising and falling edges).

Additionally, the amplitude of the induced voltage signal can be measured (Figure 2.8) and calibrated to the charge of the particle inducing the signal. This amplitude measurement and calibration of particle charge detection is more thoroughly explained in Section 2.5. It is apparent in Figure 2.8 that the baseline of the detector signal is not even from the rising edge to the falling edge, potentially obscuring the true signal amplitude. This asymmetry is caused by the feedback resistor and capacitor discharging while the particle transits the ICD. The top of the signal is not flat due to this discharge, and the drop in amplitude leads to an over correction to baseline on the falling edge. Although the baseline directly on either side of the detector is not symmetric, the total rise/fall of the signal is equal on both sides. In addition to measuring the charge and axial velocity of particles, ICDs can be used to measure the oscillation frequencies of particles within a trap, a technique used in charge detection mass spectrometry, as described in the next section.

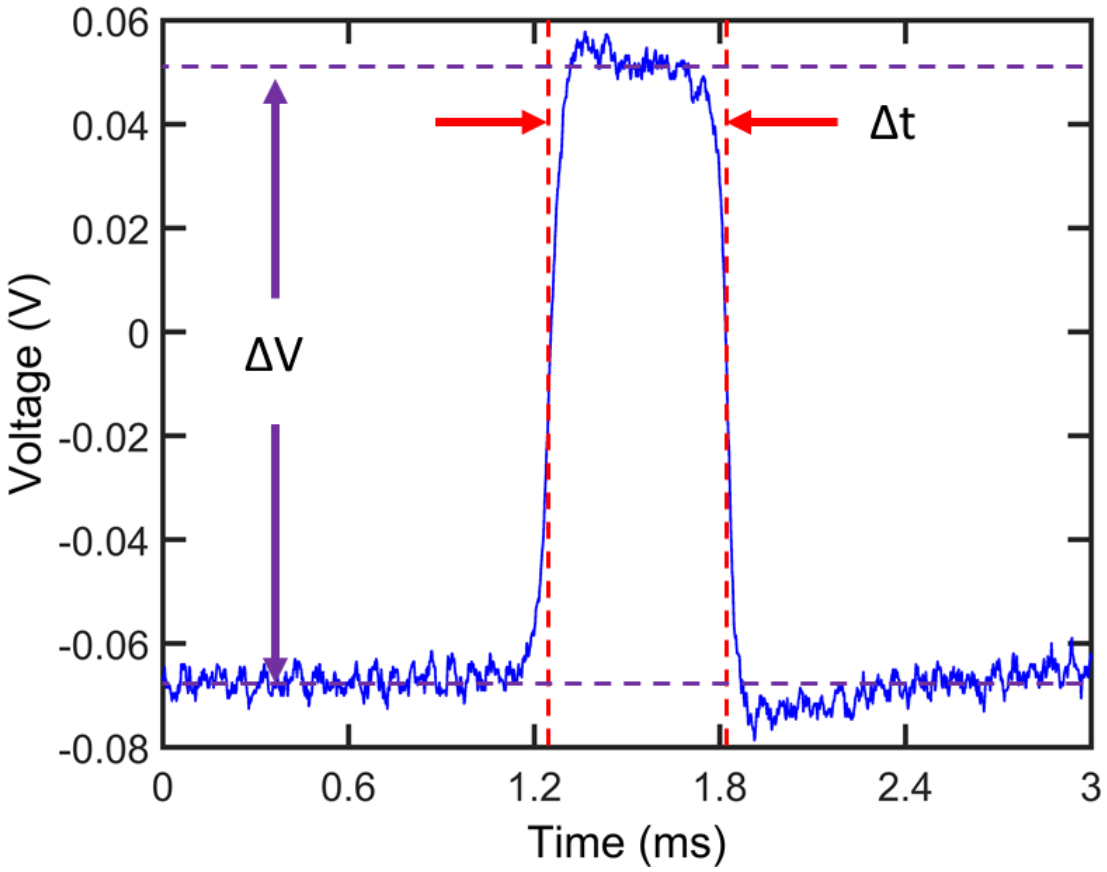

Figure 2.8: *ICD signal labeled with width in time (Δt) and height (ΔV)*

2.1.4 Charge Detection Mass Spectrometry

Charge detection mass spectrometry (CDMS) allows the characterization of extremely large (> MDa) species capable of carrying large amounts of charge. Using the image charge detector design detailed in section 2.1.3 and an electrostatic trap, the oscillation frequency of a single particle in the linear electrostatic trap can be converted into both mass and charge information.

In the AIS, single particles are introduced into an electrostatic trap (Nanoparticle Electrostatic Trap, NET) based on the linear electrostatic trap design of Benner.[12] This trap consists of two stacks of seven SS316 disc electrodes held in place and aligned with grounded aluminum discs onto an alignment rail (Figure 2.9). These electrodes are configured with both an electrostatic einzel lens and a switched high voltage potential ramp (mirror). The two stacks are arranged with mirror symmetry around a central ICD held in between the two stacks. The wiring of these electrodes is detailed in Appendix A. The mirrors are capable of trapping a particle by switching the high voltage potential on when a particle enters the trapping region. This operates with the entrance-side mirror initially being kept at ground until a particle is detected in the intra-trap ICD (called ICD2). Upon detection, a high voltage switch raises the potential of the entrance mirror to voltages greater than the energy-per-charge of the particle. The exit mirror is held at the same high potential during the entire particle loading phase of operation. The particle then oscillates repeatedly through ICD2 creating a regular square wave signal (Figure 2.10). This square wave signal is used to perform CDMS by measuring the particle's oscillation frequency, the particle's intra-ICD transit time, and the amplitude of the

induced image charge signal. The particle's mass-to-charge ratio is calculated from the oscillation frequency by using a model in SIMION to fit the equation below:[1]

$$\frac{m}{z} = \frac{C_{frequency}}{f^2} \tag{2.1}$$

Where m is the particle mass, z is the particle charge, $C_{frequency}$ is calibration factor used to relate frequency to mass-t0-charge ratio, and f is the oscillation frequency. The model uses the potentials from the trap (the mirror potential and the two einzel lens potentials) and the initial energy of the injected particles to scan through a wide range of mass-to-charge particles. For each particle mass-to-charge ratio in this trapping simulation an oscillation frequency is calculated. The group of calculated oscillation frequencies is then fit to the above equation and the factor ($C_{frequency}$) that relates the two is used to calculate the mass-to-charge ratio of a single trapped particle from a given oscillation frequency. The transit time of the particle through the ICD tube is used to determine the particle velocity. Finally, the amplitude of the induced signal on ICD2 is linearly proportional to the charge on the individual particle trapped within the NET. This proportionality is determined by calibrating the response from ICD2 with a known amount of capacitively coupled induced charge in real time, after each particle trapping cycle. Both the velocity and charge measurement of a particle within the trap is calculated from an averaged waveform produced by stacking multiple oscillations of the same particle within the trap. This is done within the data acquisition program in parallel with the frequency measurement and mass-to-charge ratio calculation (as detailed in the data acquisition section below).

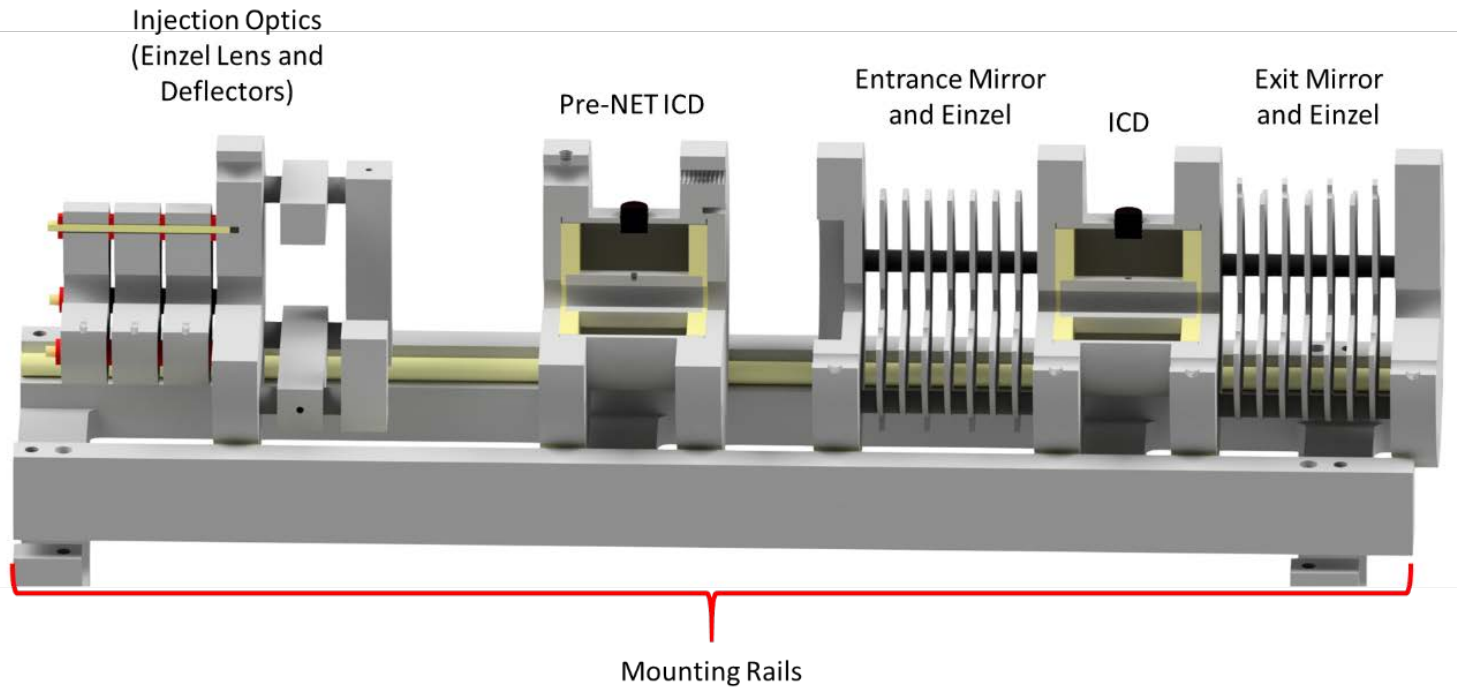

Figure 2.9: *Diagram of the NET optics rail*

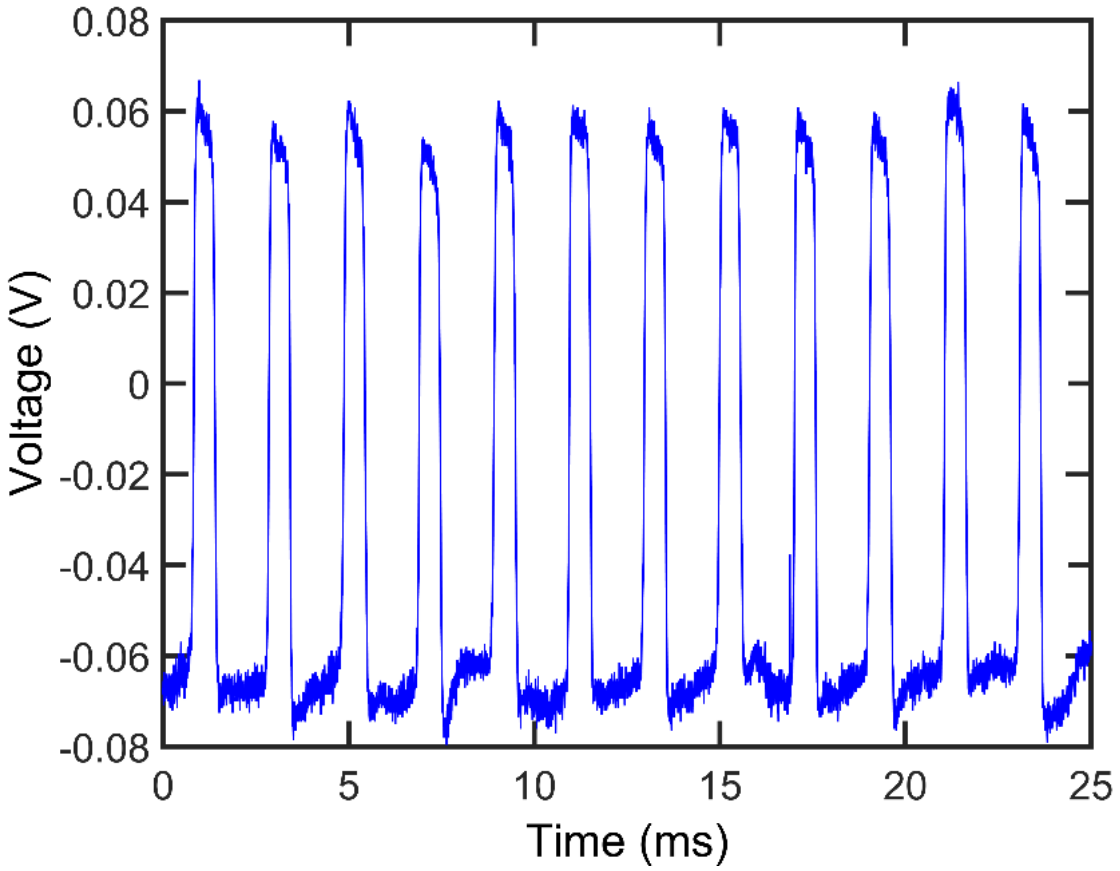

Figure 2.10: *Example square wave produced by particle oscillations in the NET (~20000 e^- charges on a 1 micron diameter polystyrene latex sphere). This figure has been reproduced from ref. 1.*

Mass spectrometric information can be collected for a number of single particles and averaged over the ensemble to produce distributions of information such as: initial velocity, charge, mass, and in the case of homogeneous material particles, size. Most importantly, these data are collected non-destructively and calculated on-the-fly. This enables direct use of the measured mass and velocity of a single particle for calculations needed in acceleration and deceleration.

2.1.5 Linear Accelerator

After passing through the NET, particles are injected into a linear accelerator or LINAC, a series of electrodes that when switched can accelerate or decelerate particles to a final controlled energy. The LINAC electrodes are mounted on an insulated rail system similar to that used for the NET and interconnected to form two circuits: one for the even-numbered elements and one for the odd-numbered elements. By applying potentials to each of these circuits in a specific pulse sequence, a single particle can experience a constant push/pull forward to accelerate to high velocities, or with a retarding potential, the particle can be decelerated. Depending on the number of electrodes used and the potential applied to each electrode a wide range of final velocities (energies) can be achieved. A 12 element LINAC is shown in Figure 2.11. Different configurations have been employed depending on the desired experimental geometry and energies, including a 9 element, 20 element, and 41 element stack. Potential is applied to the electrodes using two high voltage switches (Behlke HTS 301-03-GSM switches) connected in parallel to a high voltage power supply (Glassman

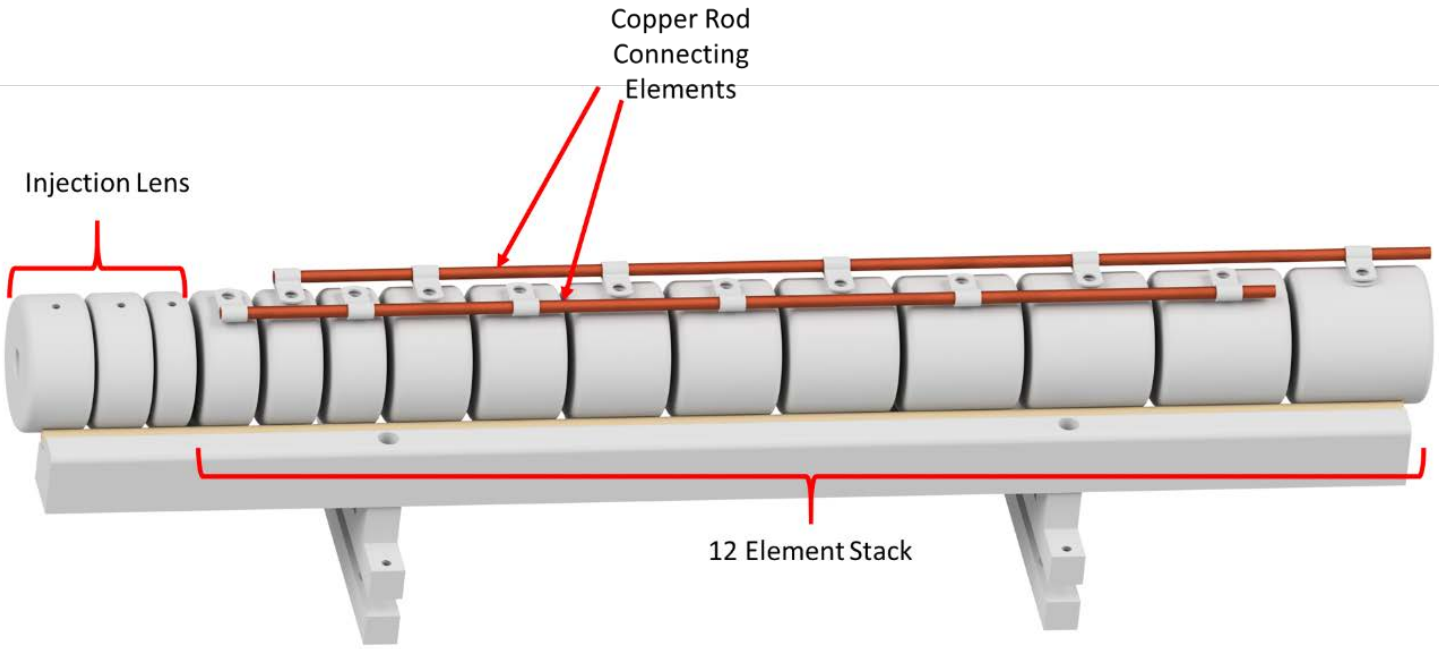

Figure 2.11: *Diagram of the LINAC and injection optics on a mounting rail*

PS/FR20R15.0). The circuit used in this switching process is detailed in Appendix A. Deceleration of polystyrene latex spheres has been demonstrated down to ~10 m/s, and acceleration of ice grains in excess of 2 km/s has been achieved to date.

Acceleration or deceleration requires a specific pulse sequence to be applied to the LINAC elements. The pulse sequence is calculated a single particle using the velocity and mass-to-charge ratio information determined in the NET in conjunction with a SIMION (SIMION 8.1) simulation of the electric fields in the LINAC assembly. With the following steps, this calculation can be performed in real time for individual particles trapped in the NET. This model determines, in the transit time for a given particle mass-to-charge ratio through each element. Once the SIMION model of the electric fields in the LINAC has been created for a given electrode geometry, a repetitive fixed potential is applied across the LINAC elements. A particle of mass and charge in the range of those under mass spectrometric study in the NET (~5e-16 kg with ~20000 e in the initial study of polystyrene latex spheres reported in ref EPJTI) is then flown through the LINAC simulation. The simulation logs and outputs the position of the particle and the axial electric field (along the cylindrical axis of symmetry of the LINAC, x) experienced by the particle at every time point during the simulation. The specific mass and charge of the test particle used will not affect the output of the simulated electric field as long as the values selected do not accelerate the particle faster than the simulation can smoothly step (Δx of each time step should be kept < 0.01 mm). Once this numerical simulation of the axial trajectory has been generated, the data is imported into MATLAB for processing. The trajectory is generated in the time-steps of the simulation, but the simulation of interest is the axial-position-dependent electric field on an evenly spaced linear sequence (array) in “x”. The information in MATLAB is run through a spline-interpolation algorithm to find the electric

field at every axial step on a 0.01 mm grid. The size of the grid was chosen as 0.01 mm to balance the amount of information needed to capture the electric field shape of the LINAC with the ease of working with a large dataset. Once produced, this grid of electric field information is saved to a file and loaded into a LabVIEW-based code that is used to calculate the specific pulse sequence required by the LINAC, in real time for each single particle. The calculation used to generate the pulse sequence steps the particle across the electric field in an "n" number of steps in "x". At each step in x, for a particle with a given mass-to-charge ratio and velocity, the velocity and time are calculated as follows:

$$t_n = t_{n-1} + (dx/v_{n-1}) \tag{2.2}$$

$$v_n = v_{n-1} + \left(\left(\frac{E_{n-1}}{mz}\right) * (t_n - t_{n-1})\right) \tag{2.3}$$

here t_n is the time at the nth step (along x), dx is the step size along x, v_n is the velocity at the nth step, and E_{n-1} is the electric field at the $n-1$ step. The initial time (t_0) is taken to be 0 and the initial velocity is taken to be the velocity calculated while trapped in the NET. After this calculation has been performed the time at the center of each LINAC element is extracted and the pulse sequence is generated by calculating the time of flight between each element center.

The electric field generally takes the form of Figure 2.12 with distinct peaks corresponding to the small region between LINAC elements. The elements of the LINAC each contain a field-free region near the axial center, allowing element-specific scaling of the electric field. The electric field array is separated into distinct regions, each corresponding to the center-to-center axis between elements in the LINAC. Each region is then scaled relative to the

potential being used on the LINAC. The SIMION simulation is originally done with a known amount of potential between each element. The ratio of the potential actually applied to the LINAC and the potential applied in SIMION can be multiplied to scale each electric field region. This is possible because the electric field of the LINAC scaling linearly with the applied potential and each region does not interact strongly. In addition to scaling the electric field by the potential applied to the high voltage switches, the electric field for a given LINAC element can be scaled by a 0-1 value to account for the voltage drop across the switching sequence. High voltage capacitors buffer the output of the high voltage switches, but at high acceleration potentials the voltage output of the switches drops across the sequence by as much as 15%.

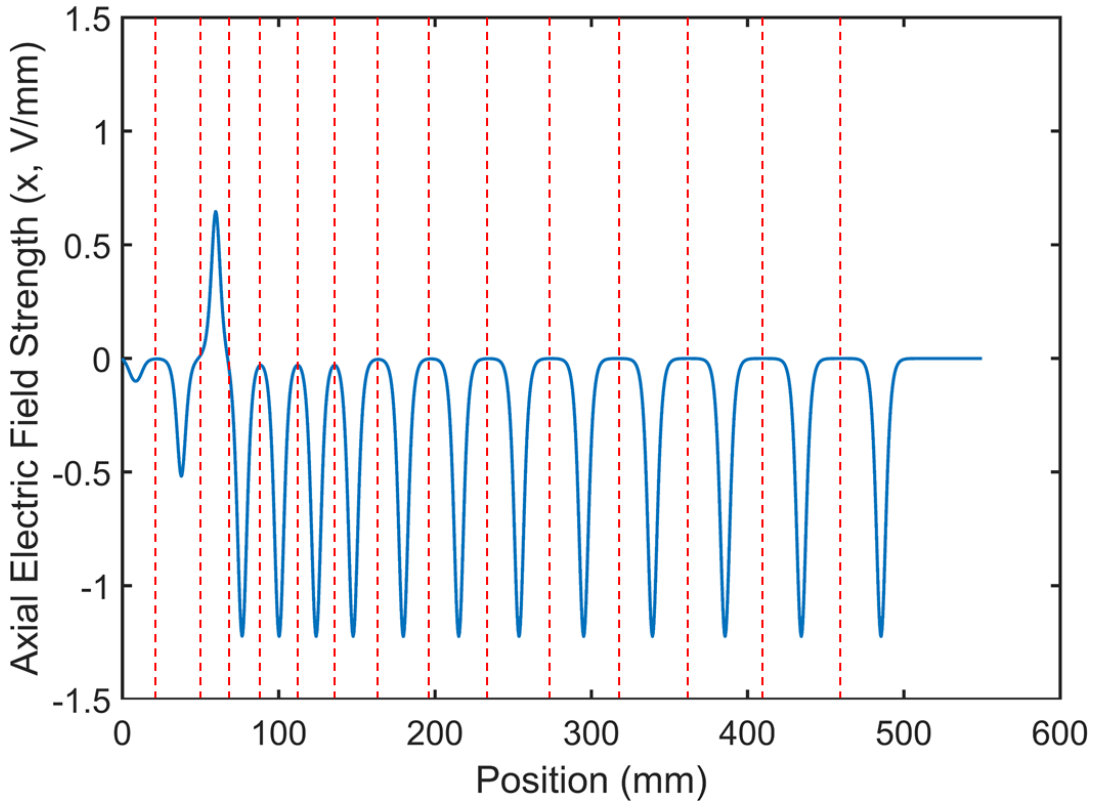

Figure 2.12: *Example electric field calculations for the LINAC configuration pictured in Figure 2.11. Axial electric field created by each element is isolated and scaled by the ratio of the potential applied to that elements and the original potential from the simulation.*

2.1.6 Impact Measurements

After acceleration, particles are impacted onto a variety of targets/detectors to measure different impact-dynamic-related quantities. The form and function of these detectors is briefly described below and detailed in each of the following experimental chapters. The simplest of impact experiments performed in AIS allows the measure of a particle impact velocity onto a target surface and subsequent axial rebound velocity (if any) from that surface. This is performed by placing an impact target normal to the beamline with a cylindrical ICD (of the same geometry and design as the one used in the NET) directly in front of the target (Figure 2.13). As in the NET, this ICD can measure the velocity of a particle passing through it if it that has sufficient charge to produce an image charge signal. If a particle passing through the detector hits the target and rebounds directly back through the same detector, this velocity measurement is performed twice. Both the incoming and rebounding velocity of the particle can be calculated using a single detector in this manner. When compared, these velocity measurements constitute a direct measurement of the coefficient of restitution (CoR) of the particle, where CoR is defined as:

$$e = \frac{v_r}{v_i} \tag{2.4}$$

In equation 2.4, e is the CoR, v_r is the rebound velocity, and v_i is the incident velocity. When no mass loss occurs, the CoR is a measurement of the loss in energy (inelasticity) of the collision. Using the variable energy of the LINAC to accelerate particles to different initial velocities allows the measurement of particle CoR over a range of incident velocities.

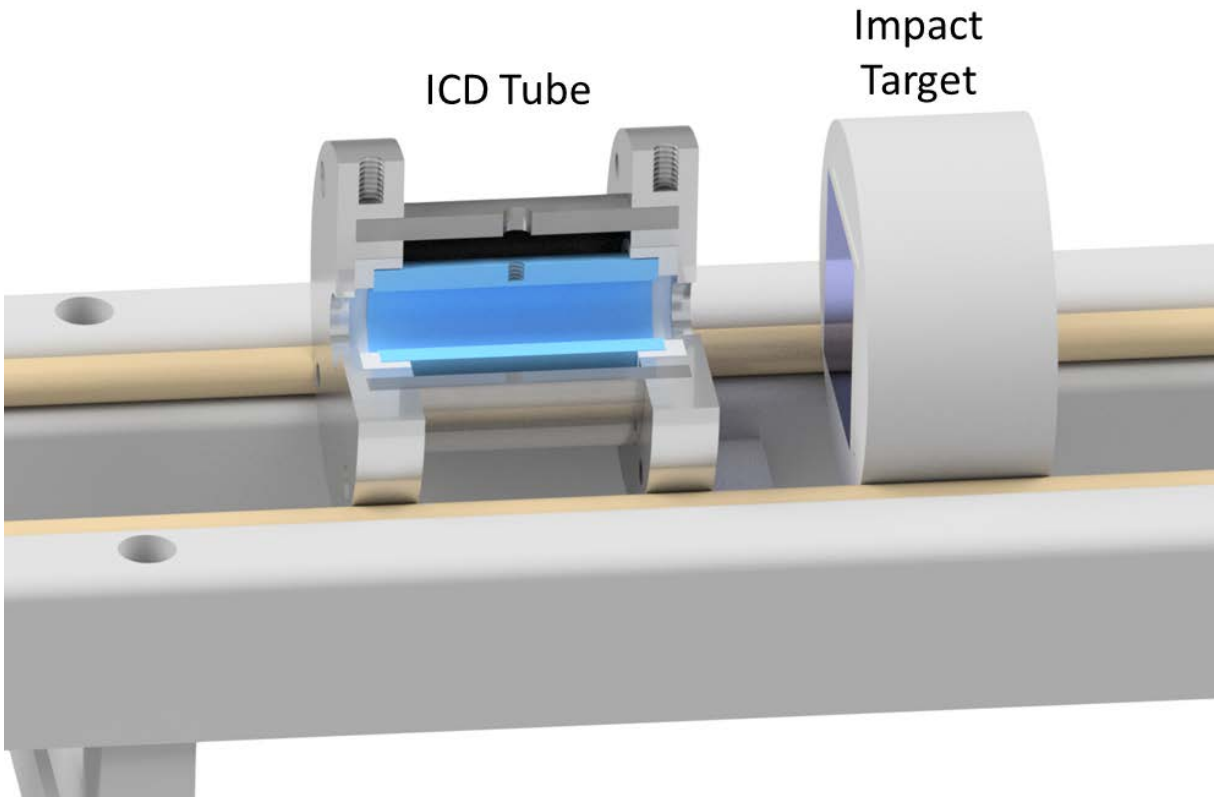

Figure 2.13: *Basic CoR measurement setup: a single ICD and impact target mounted normal to the axis of the ICD (and particle beam line).*

In addition to a hard target that allows the measurement of particle rebound velocities, the use of a fragile target can allow the measurement of target destruction under particle bombardment. In order to measure target destruction, an ultrathin (<100 nm) free standing film is mounted normal to the centerline of the incident particle path in the same configuration as the hard target (Figure 2.14). This film can then be tested for durability under repeated impact by particles of a fixed energy. Due to the mass spectrometric characterization capabilities of the NET and the control of incident energy provided by the LINAC, single impacts of a fixed energy can be repeatedly applied to the target. Film destruction can be done with progressively higher energies until destruction of the film occurs. In order to measure the incident velocity of particles a single ICD tube is placed directly in front of the film target. In order to capture any penetration of the film by a particle without film destruction, the film is mounted on a post-target ICD tube where the active area of the detector is behind the film, allowing detection of anything that passes through the film. To monitor target condition, a CCD camera is trained through a window onto the film in vacuum. An image from the camera is taken for each particle impact. The stressed nature of the film allows easy identification of film failure which is generally catastrophic (Figure 2.15). Further details of this experiment are found in Chapter 6.

The single tube ICD only measures particles that rebound nearly directly back through the detection tube. However, for cases where the post-impact trajectory is outside of the acceptance angle of the detector (usually small), information is lost. This acceptance angle can be increased by creating a “tapered” detector geometry. A functional detector with this geometry has been developed and incorporated into the AIS (Figure 2.16). In addition to the wider acceptance angle achievable with this detector design, individual steps of the detector can be configured with individual image charge detectors to allow angular resolution of the

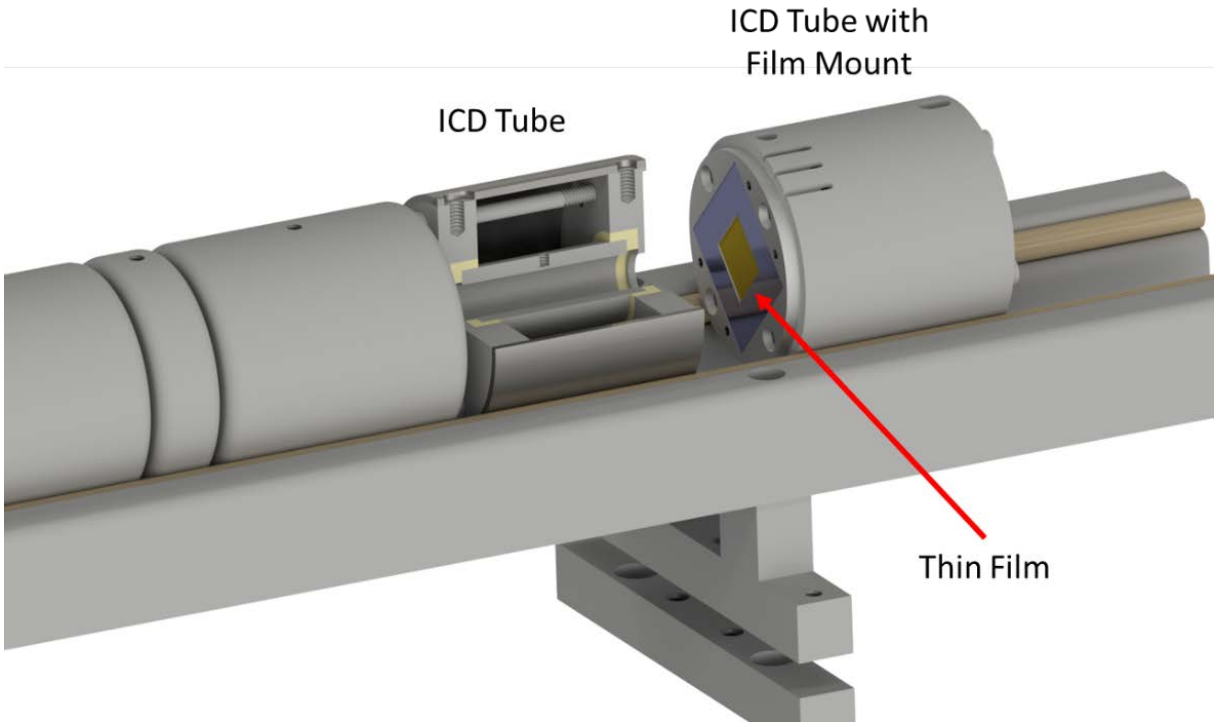

Figure 2.14: *Measurement setup for thin film bombardment. Thin film is pictured in gold.*

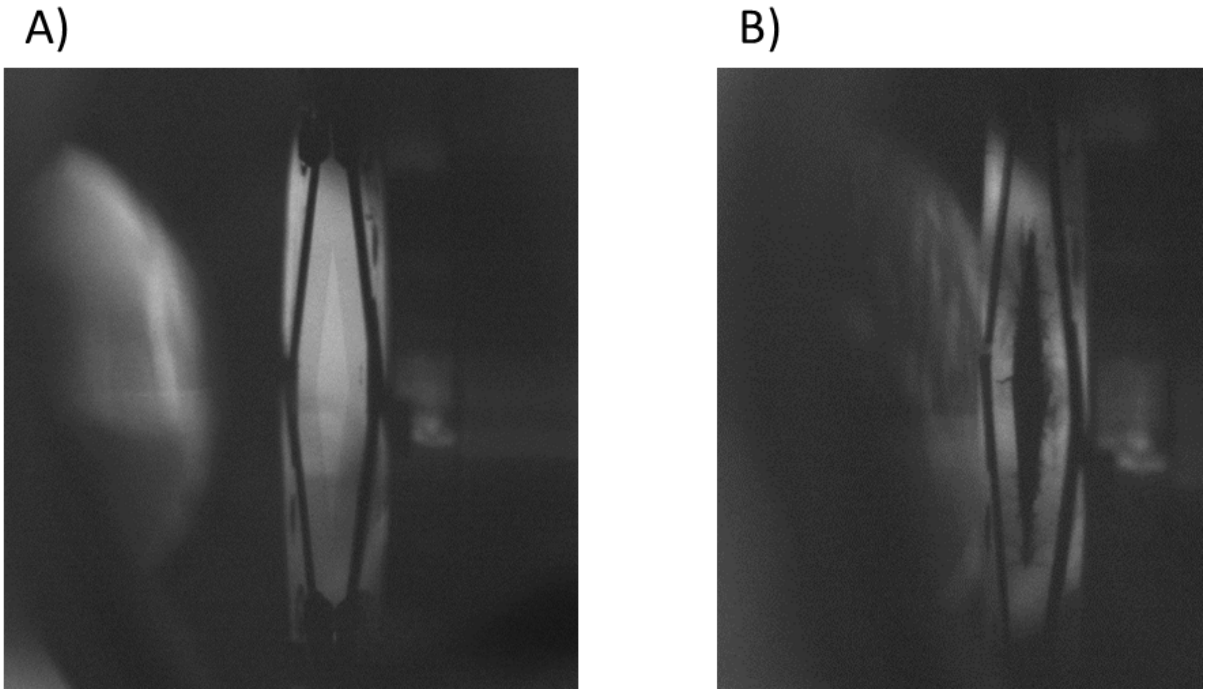

Figure 2.15: *CCD images of thin film mounted in beamline. A) Intact thin film in vacuum (bright diamond in image center). B) Thin film after catastrophic failure (complete destruction of film).*

particle's post-impact trajectory. In order to aid in the angular analysis of trajectories, knowledge of the impact site of the particle is important. Reduction of the uncertainty associated with the impact site can be achieved with a smaller target and particle impacts can be recorded using an image charge detector connected to the target. Together this configuration forms the 4-element detector seen in Figure 2.16, where three elements are collecting information about the rebound behavior of the particle and the fourth is connected to the impact target.

Finally, impact-position-sensitive detectors can be placed in-line with the particle beam to allow the measure of either instrument functionality or additional particle behavior analysis. The simplest of these measurements is the placement of a microchannel plate (MCP) based detector with phosphor screen normal to the particle beam (Figure 2.17). Contemporary work has demonstrated that measurements of very high mass to charge ratio species is possible with MCPs,[14,15] an observation also noted with the AIS. Measurement of not only the direct impact of particles, but also the resulting fragments, when paired with center of mass analysis of the produced spots, allows for a coarse measurement of impact location for a given particle. Therefore, at high incident energies and sensitive detection settings, fragment patterns can be recorded repeatedly for a particle beam to determine approximate beam waist.

More complicated separate detectors can also be utilized in concert with particle bombardment supplied by the AIS. Installation of a time-of-flight mass spectrometer to the end of the apparatus is ongoing. This will allow interrogation of molecular ejecta after particle collision with a surface by accelerating released molecules and other low mass species back across the chamber into a time- and position- sensitive MCP-based detector.

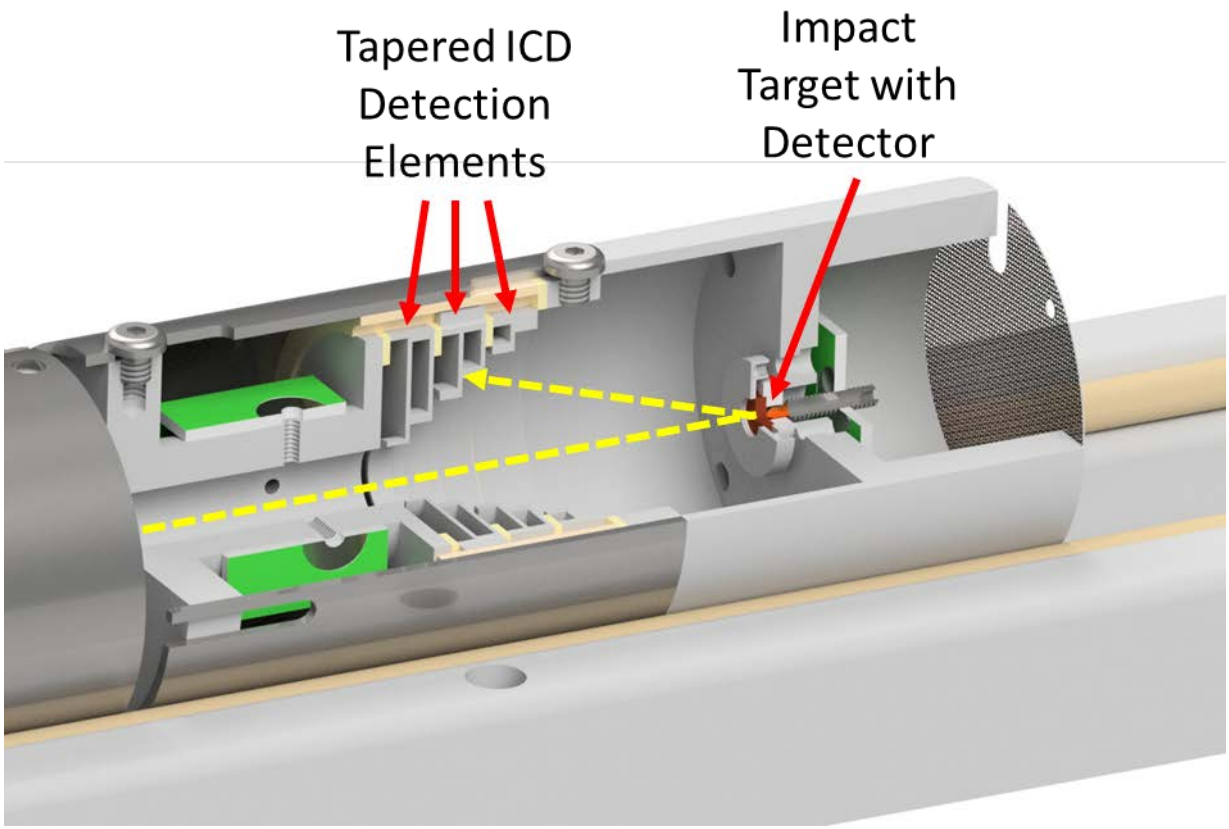

Figure 2.16: *Tapered ICD (tapered image charge detector, TICD) with instrumented impact target (collision analysis target, CAT). Sample particle trajectory shown in yellow.*

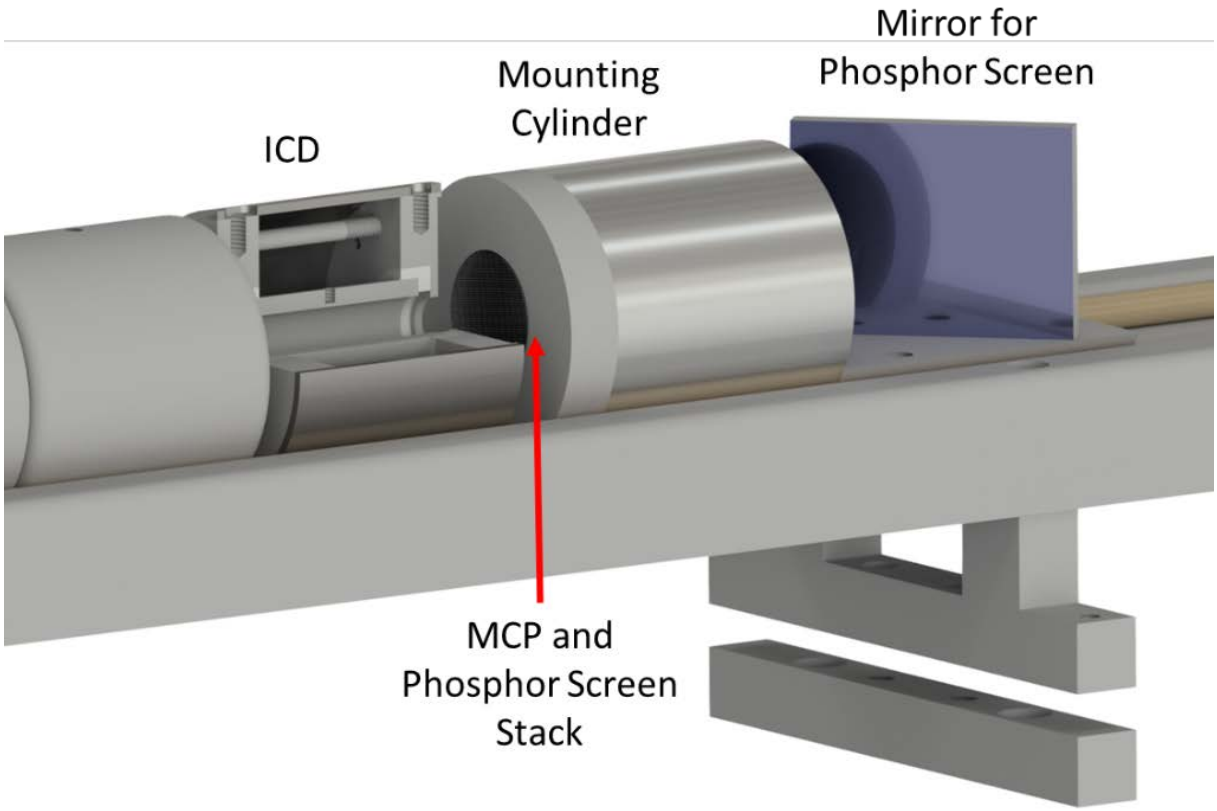

Figure 2.17: *MCP detector setup. Mirror allows for CCD camera (outside of chamber) observation of the phosphor screen within the mounting cylinder.*

2.2 Vacuum System

In order to facilitate the gradual transition from atmospheric pressure to pressures as low as 1e-8 Torr, a robust differential pumping system has been implemented on the apparatus. The vacuum gradient is established with differential pumping apertures separating the initial vacuum stages beginning with direct exposure to atmosphere through the ESI inlet orifice. A description of the various aperture locations and types of pumps is outlined in Figure 2.18

The critical pumping system pressure of the ADL is made adjustable using a precision leak valve attached to the post-ADL dry pump. This valve can be opened and closed to artificially raise the pressure on the pumping side of the ADL. This changes the particle flux transported through the ADL by changing the pressure conditions of the lens. This permits selection of different sized species depending on pressure and, when paired with variability in ESI voltage and needle position can produce a range of different particle sizes for a single electrospray solution.

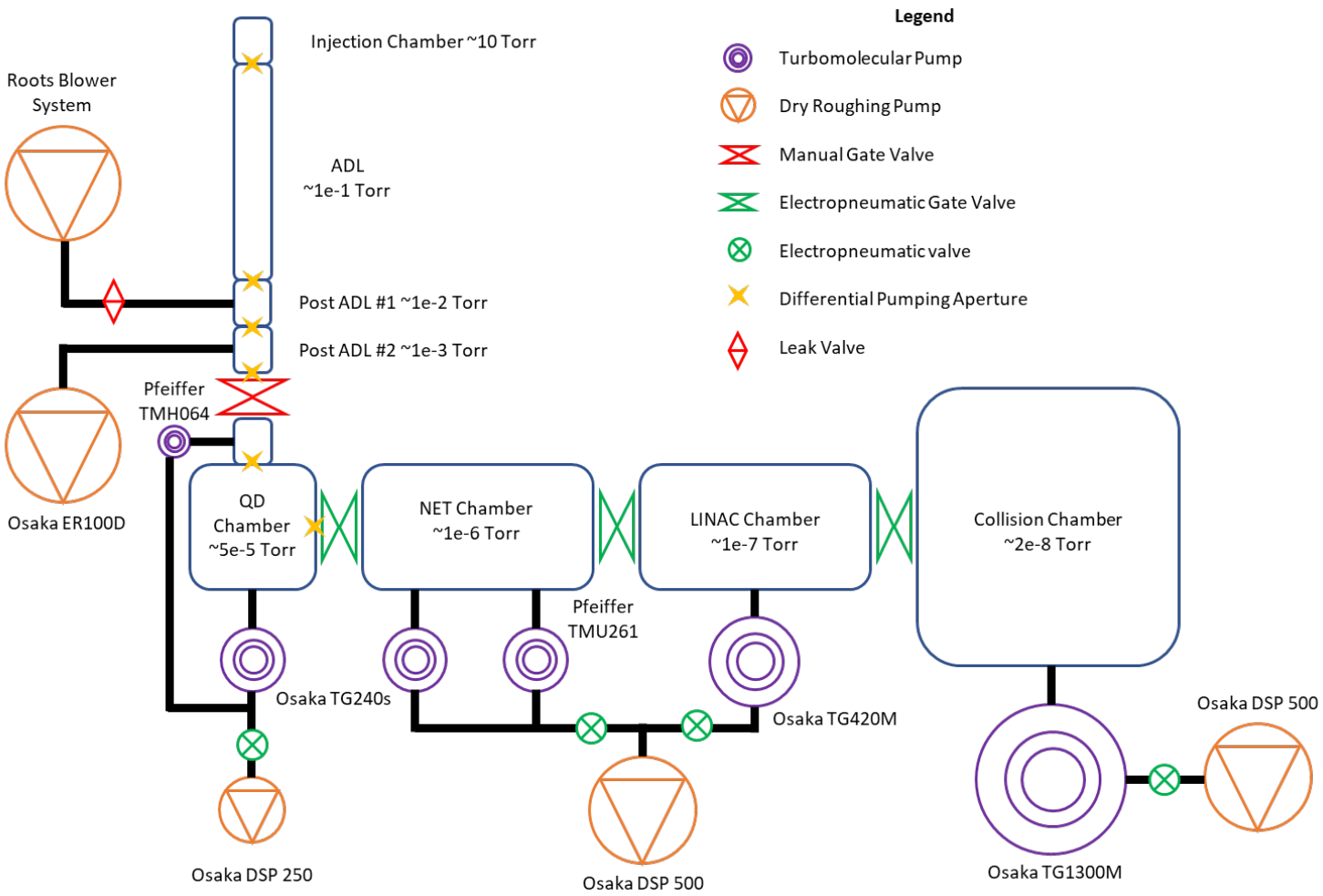

Figure 2.18: *AIS pumping system with valves and critical apertures labeled. The relative size of the individual components is roughly indicative of relative pumping speeds.*

2.3 Data Acquisition System

The primary data generated from the AIS is produced from image charge detection traces and images captured with a CCD camera. In order to acquire these data and electronically control different aspects of the apparatus a robust data acquisition system has been developed primarily in LabVIEW (LabVIEW 2015, National Instruments). The programs developed allow communication with various components of the apparatus including power supplies, high voltage switches, detectors, and pressure gauges through both analog and digital interfaces. Most system control and data acquisition occurs with National Instruments digitizers instrumented with field programmable gate-arrays (FPGA). The form and function of these communications is explained in the following sections.

2.3.1 System Control

The control system developed in LabVIEW 2015 runs through a host computer (DAQ1), and remote FPGA/digitizer module (National Instruments PXI-7952R and National Instruments NI 5731). For additional digitization capabilities a secondary host computer (DAQ2) with separate FPGA/digitizer/high-speed digitizer is used (National Instruments PXIe-7961R, National Instruments NI 5751B, and National Instruments PXI-5154). The main functions of this control system is to first trap particles in the NET, accelerate particles using the LINAC, and digitize the data from the various detector configurations. The sequence of operation for a typical experiment is shown in Figure 2.19. A simple experiment contains the following steps: (1) digitized signal from ICD2 measures single particle initial injection into the trap; (2) the

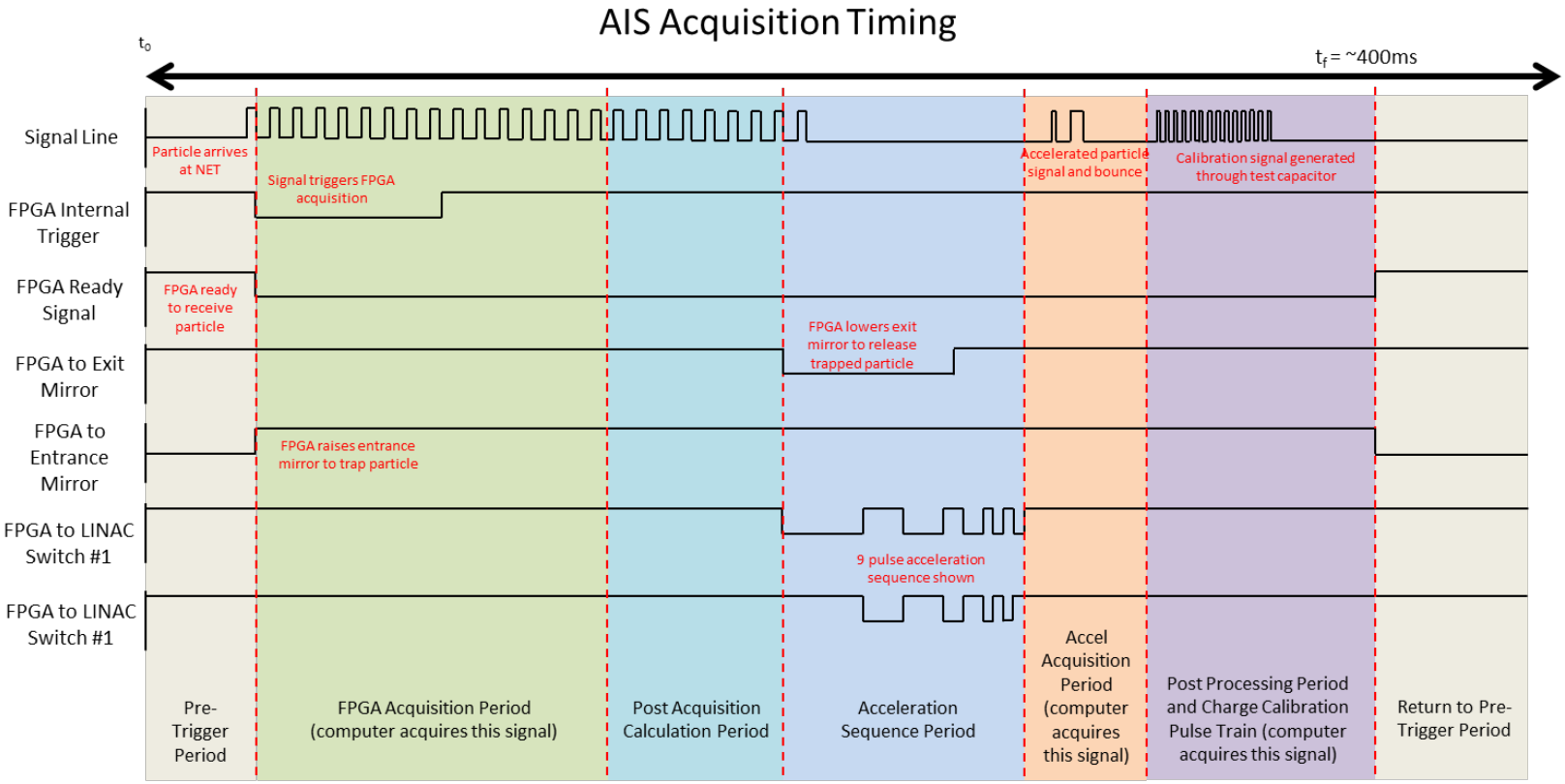

Figure 2.19: *Timing diagram for AIS acquisition system.*

mirrors of the trap close (potential is applied); (3) repeated oscillation signal from ICD2 is digitized and transmitted to the host computer (DAQ1) for analysis; (4) a LINAC timing sequence is developed on the host computer and loaded to the FPGA; (5) a particle is released from the NET and the LINAC accelerates the particle; (6) after the LINAC has fired the signal from a post-LINAC ICD tube is digitized on the DAQ2; (7) this signal is analyzed for particle velocity (incident and rebound velocities) and saved to a waveform datafile. Expansions of the experimental setup usually require additional digital triggers (for hardware such as cameras) or digitization of additional signals that can be accommodated in the two FPGA systems.

A key feature of the data acquisition system is the interface between the spectrometric characterization of the particle and the subsequent acceleration of that particle. When accelerating or decelerating, the LINAC can be operated in two distinct modes: per-particle analysis mode (PPAM) and distribution mode (Mode-D). When operating in PPAM, particles are trapped within the NET as detailed above and spectrometrically analyzed. Once the velocity and mass-to-charge ratio have been calculated the timing sequence for the LINAC is generated. This is done while the particle is still within the trap and allows the LINAC sequence to be tailored to specific particle properties (m/z and velocity). Once the sequence is developed the particle is ejected from the NET. This ejection event is used to inject the particle into the LINAC and also serve as the trigger for initiation of the LINAC pulse sequence. Due to the significant time required to trap the particle (periods of oscillation ~ms) and analyze the data this mode of operation currently takes > 200 ms per-particle. PPMA mode has been used for the majority of experiments performed measuring particle CoR and angular distributions. Due to the full analysis performed per-particle, this data acquisition mode allows the CoR of individual particles to be correlated with the spectrometric properties of the particle such as

mass or charge. When all of this information is not needed and a higher event rate is required, particles can be accelerated using a computationally simpler approach: Mode-D. In this mode of operation, first a representative set of particles with a distribution of mass, charge, and velocity are trapped and analyzed in the NET (without acceleration). Analysis of this ensemble provides the average initial velocity and mass-to-charge ratio for particles produced under given ion source conditions, ADL, and quadrupole deflector energy settings.. With this information, a single LINAC pulse sequence is calculated to fit the averaged spectrometric characteristics (mass-to-charge ratio and velocity) of the particles under study. This sequence can then be used to accelerate particles with minimal computational input. In Mode-D, an oscilloscope (Tektronix MSO54) is used to detect individual particles passing through a pre-LINAC ICD. The trigger from this scope sends a logic pulse that triggers the generalized LINAC pulse sequence from a simplified program. Because no computations are required and no trapping required, this program is capable of operating significantly faster than PPAM (< 10 ms per-particle). Mode-D has primarily been used to accelerate particles to maximal velocity at the highest rate possible when individual spectrometric information is not required.

In addition to the main experiment run on the apparatus, the voltages applied to the quadrupole deflector on the AIS is optimized with using a separate program. When operating, this program allows the characterization of particle flux being transmitted with the QD as well as coarse identification of particle charge and velocity for each transmission setting. The potentials (positive and negative) of the deflector rods in the QD are controlled with two programmable high voltage power supplies and typically operate between 100-1000 V. A LabVIEW program has been created to scan the potentials applied to the deflector and measure the flux of particles transmitted at each applied potential. This is accomplished by remotely

interfacing DAQ1 with the power supplies and the ICD located directly after the QD. For each voltage setting this program acquires fixed durations of signal (~100 ms) from the post-QD ICD multiple times. Each record is examined and the following is determined: number of peaks (particles) in the trace, width of each peak (velocity), and height of each peak (charge). Histograms of particle fluxes can then be created measuring each of these statistics (Figure 2.20). The QD setting can be optimized by selecting voltages with a high rate of flux and the peak height/velocity information can be used to compare between different ESI settings.

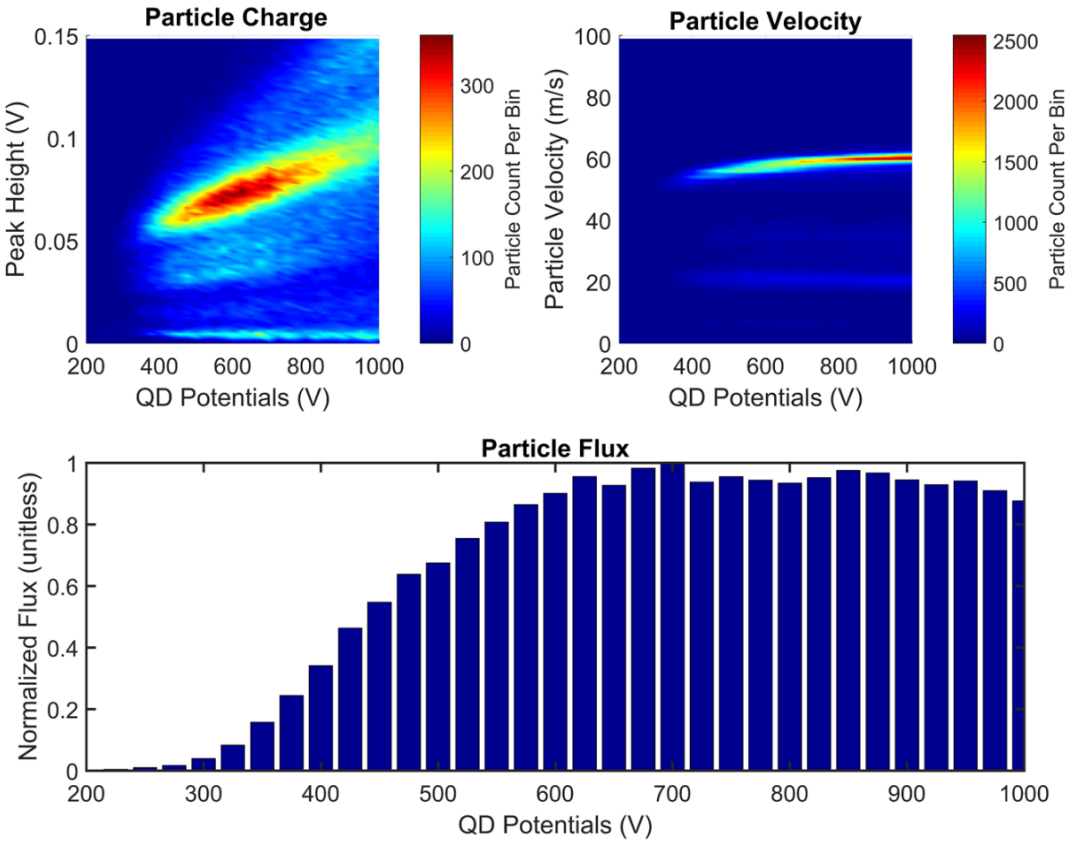

Figure 2.20: *Various QD program histograms. Particle charge is measured by individual signal heights, velocity by individual signal widths, and flux by signal count in a set time span. This information is collected by cycling through QD voltage settings repeatedly and adding the measurements together. The particle charge data presented here are not calibrated, so only a voltage value of the signal is represented (rather than a value expressed in units of charge).*

2.3.2 Data Storage

A variety of parameters, timings, digitized traces, and other information gets produced for every particle that is analyzed by the apparatus. This information is generally collected/produced from the LabVIEW programs running on DAQ1 and DAQ2 and stored in different data files for analysis. Most experimental data are analyzed on secondary computers using custom programs written in MATLAB. In order to facilitate the transfer of the information collected on DAQ1 and DAQ2 storing the data quickly and efficiently is important.

The data generated by DAQ1 is written directly from LabVIEW into a binary file for each experimental run of the DAQ1 experimental control program. These files are given a unique identifier (number) and organized by calendar date. Individual data gets written to the binary file using a single byte header, followed by the information being recorded. The header of each piece of information contains a number that corresponds to a master list of data types maintained for all the different data produced during an experiment. This header and its comparison to the master list allows import of the binary files from DAQ1 into MATLAB with the data already identified. Automatic backup of collected data is performed daily with copies of important data folders and code transferred to a variety of cloud-based platforms.

The data generated by DAQ2 is written directly from LabVIEW into a text file. Most run-specific information is recorded by DAQ1 automatically or manually on the DAQ1 computer, while DAQ2 generally only saves digitized traces from its multichannel digitizer. These traces (up to 16) are stored in ASCII and similarly transferred to cloud-based backup systems each day.

2.4 Data Analysis Software

Data collected during experimental runs with the AIS are both analyzed in situ and after collection and storage using secondary programs. The in situ analysis occurs to provide information that is required during the experiment or to analyze the information more coarsely while being collected for ease of operation. As with the operational programs, this analysis is performed in LabVIEW. Post-experimental analysis is done in MATLAB and is used to perform more time intensive analysis of the data and is much more varied in function. Individual analysis of data in MATLAB is discussed in subsequent chapters as it pertains to each experiment.

2.4.1 In Situ Analysis

As detailed in the above sections, the ability to spectrometrically characterize single particles while they oscillate within the NET is a key feature of certain operational modes of the apparatus. This analysis therefore must be fast enough to be performed while the particle maintains a stable trapping trajectory, and the rate of this analysis helps determine the throughput of the apparatus. The key features of the program that enables this in situ analysis are: a digitization of a set number of oscillations from ICD2, fast analysis of particle oscillation frequency and velocity, rapid calculation and implementation of the LINAC timing sequence, and tracking of the particle position within the trap for proper ejection.

The digitizer used for collection of ICD2 information operates with a timing determined by the program loaded onto its companion FPGA. This digitizer is capable of operating with a baseclock frequency of 40 MHz however, the digitizer on the AIS typically operates with a data acquisition rate of 500 kHz, which is chosen to be significantly faster than critical features of the ICD2 waveform (the rising and falling edge) while still allowing some iterative calculations to be performed on the FPGA for each cycle. The typical oscillation frequency of submicron particles in the NET is ~500 Hz. In order to get a representative set of particle oscillations, ~100 ms (or ~50 oscillations) of oscillation data from ICD2 is digitized and transferred from the FPGA/digitizer to DAQ1. This timing sequence is chosen to acquire multiple waveforms to average together, but still kept short enough to operate the apparatus at as fast a throughput as possible. After this information has been transferred, the particle continues to oscillate in the NET while DAQ1 calculates the LINAC timing sequence.

In order to calculate both the mass-to-charge ratio and velocity of the particle, the frequency of the oscillation is calculated from the digitized data. A fast Fourier transform (FFT) of the data is performed with the digitized data (LabVIEW, FFT Spectrum Mag-Phase VI). This FFT has a frequency resolution of ~8 Hz, which is improved upon by fitting a Gaussian peak to the FFT spectrum produced. The peak of this Gaussian is taken as the oscillation frequency of the particle in the trap and used to calculate the particle mass-to-charge ratio as indicated in Equation 2.1. In addition to the mass-to-charge calculation, this frequency is used to divide the digitized waveform into single pass waveforms which are averaged together to create a waveform averaged over the trapping cycle (as in Figure 2.8). From the averaged ICD waveform, both the peak amplitude (charge) and width (velocity) are calculated. In order to accurately determine the amplitude and width of the single square wave the discharge through

the detector must be considered when comparing the falling and rising edges of the waveform. As noted earlier, the amplitude of the waveform is equal relative to the baseline on both the rising and falling edges, but each edge height has a different maximal point and different baseline level. In order to account for this, the height of the waveform is independently measured on both edges and averaged together. Velocity likewise is measured using the 60% maximal point on each edge independently.

After the velocity and mass-to-charge ratio of the particle have been calculated, this information is used to calculate the transit time of the particle through the LINAC. Using Equations 2.2 and 2.3, for a given particle mass-to-charge ratio, initial velocity, and energy applied to the LINAC the transit time is calculated at every point 'x' along the axis of the LINAC. After getting times at every axial point in the LINAC, the centers of each LINAC element are compared, and the transit time between them is calculated. The particle experiences an acceleration from the LINAC's electric field when passing between the elements, so the transit time between centers is used for the pulse sequence since there is little to no field experienced at element centers. Each time is stored and transmitted back to the FPGA/digitizer which controls the LINAC high voltage switches.

In order to properly inject the particle from the NET into the LINAC, the 'exit' mirror potential (towards the LINAC) must be lowered so it does not affect the particle velocity. To accomplish this timing, the FPGA/digitizer tracks the position of the particle during each oscillation within the trap. Although the signal presented in Figure 2.10 would allow easy identification of each peak, when working with particles with fewer charges, the signal-to-noise ratio can be significantly smaller. In order to facilitate particle tracking in the NET, a filter is

applied to the signal. The chosen filter is modeled after the cross-correlation filter applied in Thomas et. al.[16] to detect dust grain signals from an image charge detection device. In brief, this filter produces a correlation between the signal being fed into it and the expected shape of the signal. This correlation allows magnification of signals of similar frequencies and shape, and significant reduction to high/low frequency noise (Figure 2.21). The storage and queue system required for this filter are all implemented on the FPGA/digitizer connected to ICD2. Signal from ICD2 is referenced to the cross-correlation signal as the data are generated, producing a parallel filtered signal. The cross-correlation filter introduces a controlled offset from the window size of the filter. The first points of data fed into the filter need to occupy the averaging window until it is saturated, the filter does not output information until this is complete. These initial point make signals output from the cross-correlation filter lag slightly behind the raw signal. This offset does not significantly affect the operation of the AIS because it is much smaller than the period of oscillation for a particle within the trap and only needs to be rigorously accounted for upon particle release. For every oscillation within the NET the particle entering and exiting ICD2 is recorded by thes FPGA (using the circles in Figure 2.21) and the direction/state of the particle is tracked through all oscillations. When the timing sequence for the LINAC is transmitted to the FPGA/digitizer, the program delays the lowering of the exit mirror until the particle is determined to be moving away from the LINAC through ICD2. This is done to prevent the change in mirror voltage from affecting the particle trajectory. As the particle oscillates back through ICD2 the LINAC acceleration sequence is triggered (with a delay accounting for transit time in the trap).

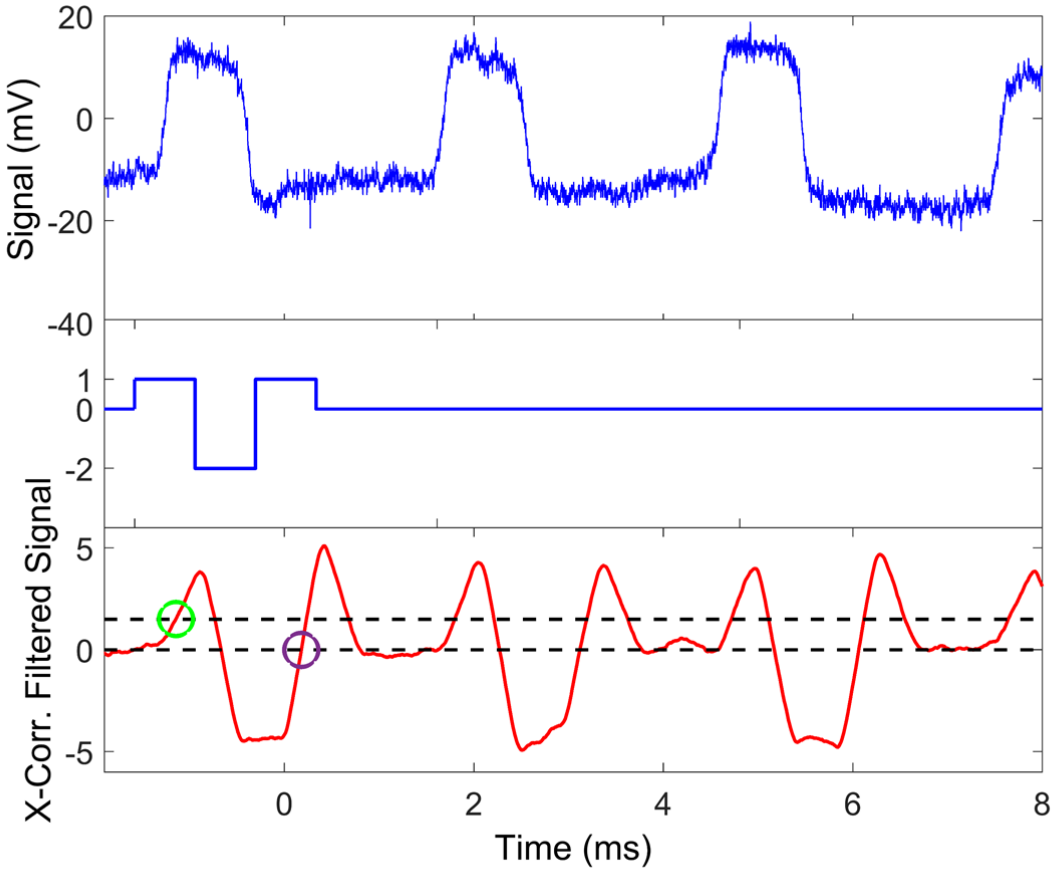

Figure 2.21: *Cross-correlation filter with example signal and output. An example signal from ICD2 is shown on top, the filter window for the cross-correlation (single filter window) is shown in the middle frame, and the resulting filtered signal is shown in the bottom frame. In AIS the entrance and exit of the particle from ICD2 is marked with the green and purple circles on the cross-correlation signal offset by the size of the filter.*

2.5 Spectrometer Calibration

Calibration of the detector response for a high fidelity charge measurement is one of the critical parameters that affects the resolution of a CDMS technique. In the AIS this calibration is performed in two discrete phases: an initial detector characterization with a known particle species followed by detector re-calibration and electrical response on individual particle trapping cycles. In the image charge detection circuit (detailed in Appendix A) of ICD2, a test capacitor is connected directly from the input of the FET to a voltage pulse generator (Agilent 33220A). This capacitor (of nominal value C_{test}) is used to put a discrete amount of charge onto the detector, from which a response amplitude can be measured on the detector output. The value of the capacitor used (in addition to the line capacitance) must be determined as accurately as possible to know the precise amount of charge being applied for a given detector response. As such, listed values of capacitance and measurements made with a capacitance meter are insufficiently accurate to get a precise value (in the case of this experiment ~1 pF or below). In order to get as accurate a measurement of capacitance as possible, a known species of particle is loaded into the AIS for CDMS analysis. The initial calibration of the AIS was done with 990 nm polystyrene latex spheres (PSLs) as detailed in [17]. These monodisperse particles were are repeatedly trapped in the NET and a distribution of mass-to-charges ratios is collected. The waveform for each particle is also collected and the detector response is measured on an individual particle basis. The distribution of particle mass-to-charge ratios and particle peak heights is then fit to the predicted mass of the calibration species using:

$$m_{species} = \frac{m}{z} * V_{signal} * F_{calibration} \tag{2.5}$$

where the mass of the homogenous species used ($m_{species}$) is compared to the measured mass-to-charge ratio ($\frac{m}{z}$) determined by the oscillation frequency, the response of ICD2 (V_{signal}), and adjusted to linearly fit with the calibration factor $F_{calibration}$.

This calibration value is equivalent to measuring the true detector response to a given amount of charge (dependent on the feedback capacitor, the operational amplifier, and FET used in the circuit). With this factor determined, a voltage test pulse applied to the test capacitor can be correlated to a true value of charge being applied to the detector to allow measure of $F_{calibration}$ at any time using the following equation:

$$C_{test} = \frac{V_{signal} * F_{calibration}}{V_{test-pulse}} \tag{2.6}$$

where the voltage applied to the test capacitor, $V_{test-pulse}$, is applied with the function generator. With an accurate value of the test capacitance measured, $F_{calibration}$ can be measured by applying a test pulse to the detector and measuring the voltage signal produced. Recalibration of ICD2 specifically was implemented to account for change in the supply voltage delivered to the ICD2 electronics, which results in a change in detector response. It was found that the supply voltage changes over the course of days due to the draining of the batteries used to supply the detector's power. By fitting the calibration factor to the known mass of the test species, accurate mass measurements can be made on subsequent particles without a homogenous mass distribution.

2.6 Conclusion

The above sections detail the form and function of key components and systems in the AIS. The main function of the apparatus is to create single, charged particles, of known energy and observe each particle's interaction with a variety of surfaces and detectors. This is accomplished by using an electrospray ionization source to charge and aerosolize particles before being injected into vacuum via an aerodynamic lens. Individual particles are energetically selected, and injected into a mass spectrometer where their mass, charge, and velocity is characterized using charge detection mass spectrometry. Each particle is then ejected into a linear accelerator where its final energy is determined by potentials applied during acceleration. The impact and characterization of these particles is then examined by a variety of detectors, the form and function of which are detailed in the remaining chapters of this dissertation.

Acknowledgements

Chapter 2 uses a figure (2.10) as it appears in Adamson, B.D.; Miller, M.E.C.; Continetti, R.E. The aerosol impact spectrometer: a versatile platform for studying the velocity dependence of nanoparticle-surface impact phenomena. *European Physical Journal, Techniques and Instrumentation,* 2017, 4 (2). The dissertation author is coauthor and the dissertation advisor is the corresponding author.

Figure 2.10 is reproduced under Creative Commons Attribution License 4.0.

2.7 References

(1) Adamson, B. D.; Miller, M. E. C.; Continetti, R. E. The Aerosol Impact Spectrometer: A Versatile Platform for Studying the Velocity Dependence of Nanoparticle-Surface Impact Phenomena. *EPJ Tech. Instrum.* **2017**, *4* (1), 2. https://doi.org/10.1140/epjti/s40485-017-0037-6.

(2) Bischoff, L.; Mair, G.; Mair, A.; Ganetsos, T.; Akhmadaliev, C. The Mass Spectrum of a Tin Liquid Metal Ion Source. *Nucl. Instruments Methods Phys. Res. Sect. B Beam Interact. with Mater. Atoms* **2004**, *222* (3–4), 622–626. https://doi.org/10.1016/j.nimb.2004.03.070.

(3) Barney, B. L.; Pratt, S. N.; Austin, D. E. Survivability of Bare, Individual Bacillus Subtilis Spores to High-Velocity Surface Impact: Implications for Microbial Transfer through Space. *Planet. Space Sci.* **2016**, *125*, 20–26. https://doi.org/10.1016/J.PSS.2016.02.010.

(4) Shu, A.; Collette, A.; Drake, K.; Grün, E.; Horányi, M.; Kempf, S.; Mocker, A.; Munsat, T.; Northway, P.; Srama, R.; Sternovsky, Z.; Thomas, E. 3 MV Hypervelocity Dust Accelerator at the Colorado Center for Lunar Dust and Atmospheric Studies. *Rev. Sci. Instrum.* **2012**, *83* (7), 75108. https://doi.org/10.1063/1.4732820.

(5) Daly, R. T.; Kerby, J. D.; Austin, D. E. Electrospray Charging of Minerals and Ices for Hypervelocity Impact Research. *Planet. Space Sci.* **2013**, *75* (1), 182–187. https://doi.org/10.1016/j.pss.2012.11.012.

(6) Fenn, J. B.; Mann, M.; Kai Meng, C.; Fu Wong, S.; Mann, M.; Fu WONG, S.; Whitehouse, C. M. Electrospray Ionization for Mass Spectrometry of Large Biomolecules. *Sci. New Ser.* **1989**, *246* (4926), 64–71.

(7) Liu, P.; Ziemann, P. J.; Kittelson, D. B.; McMurry, P. H. Generating Particle Beams of Controlled Dimensions and Divergence: I. Theory of Particle Motion in Aerodynamic Lenses and Nozzle Expansions. *Aerosol Sci. Technol.* **1995**, *22* (3), 293–313. https://doi.org/10.1080/02786829408959748.

(8) Wang, X.; McMurry, P. H. A Design Tool for Aerodynamic Lens Systems. *Aerosol Sci. Technol.* **2006**, *40* (5), 320–334. https://doi.org/10.1080/02786820600615063.

(9) Zeman, H. D. Deflection of an Ion Beam in the Two-Dimensional Electrostatic Quadrupole Field. *Rev. Sci. Instrum.* **1977**, *48*, 1079. https://doi.org/10.1063/1.1135188.

(10) Shelton, H.; Hendricks, C. D.; Wuerker, R. F. Electrostatic Acceleration of Microparticles to Hypervelocities. *J. Appl. Phys.* **1960**, *31*, 1243. https://doi.org/10.1063/1.1735813.

(11) Auer, S.; Grün, E.; Srama, R.; Kempf, S.; Auer, R. The Charge and Velocity Detector of the Cosmic Dust Analyzer on Cassini. *Planet. Space Sci.* **2002**, *50*, 773–779.

(12) Benner, W. H. A Gated Electrostatic Ion Trap To Repetitiously Measure the Charge and m/z of Large Electrospray Ions. *Anal. Chem* **1997**, *69* (20), 4162–4168.

(13) Smith, J. W.; Siegel, E. E.; Maze, J. T.; Jarrold, M. F. Image Charge Detection Mass Spectrometry: Pushing the Envelope with Sensitivity and Accuracy. *Anal. Chem.* **2011**, *83* (3), 950–956. https://doi.org/10.1021/ac102633p.

(14) Fontanese, J.; Clark, G.; Horányi, M.; James, D.; Sternovsky, Z. Microchannel Plate Efficiency to Detect Low Velocity Dust Impacts. *J. Geophys. Res. Sp. Phys.* **2018**, *123* (12), 9936–9940. https://doi.org/10.1029/2018JA025577.

(15) Gemer, A. J.; Sternovsky, Z.; James, D.; Horanyi, M. The Effect of High-Velocity Dust Particle Impacts on Microchannel Plate (MCP) Detectors. *Planet. Space Sci.* **2020**, *183* (December 2018), 104628. https://doi.org/10.1016/j.pss.2018.12.011.

(16) Thomas, E.; Auer, S.; Drake, K.; Horányi, M.; Munsat, T.; Shu, A. FPGA Cross-Correlation Filters for Real-Time Dust Detection and Selection. *Planet. Space Sci.* **2013**, *89*, 71–76. https://doi.org/10.1016/j.pss.2013.09.004.

(17) Adamson, B. D.; Miller, M. E. C.; Continetti, R. E. The Aerosol Impact Spectrometer: A Versatile Platform for Studying the Velocity Dependence of Nanoparticle-Surface Impact Phenomena. *EPJ Tech. Instrum.* **2017**, *4* (2). https://doi.org/10.1140/epjti/s40485-017-0037-6.

Chapter 3. Coefficient of Restitution Studies of Polystyrene Latex Spheres

3.1 Introduction

Impact dynamics of a particle striking a surface can be expressed in a variety of forms and measurements. A commonly used metric for these collisions is to measure particle energy loss during collision, expressed as the coefficient of restitution (CoR). By measuring the ratio of the rebound velocity of a particle from a surface to the incident velocity, the elastic and inelastic processes of the collision can be summarized in a single term.[1] Decoupling the variety of processes within this measurement continues to be the subject of models[2–5] and experimental examinations[6–9] of particle-surface systems. Experimental observation of particle CoR for use in modeling and understanding these dynamics is typically confined to particle sizes that can be observed optically as many velocity measurement techniques rely on direct observation of particle trajectories to determine velocity. Understanding of smaller systems remains challenging without additional techniques for measuring particle interactions with surfaces at smaller scales. The AIS was developed to perform measurements of particle dynamics below the optical detection limit.

In order to demonstrate the functionality of the AIS a particle species that was both previously studied in impact dynamics measurements and homogenous in mass was desired. A commonly used and widely reference used in aerosol research are polystyrene latex spheres or PSLs. These spheres are available in well-defined and homogenously sized solutions with a

variety of coatings and surface layers to facilitate ionization. More importantly, foundational research[2,10,11] into impact dynamic studies of small spheres measured the CoR of PSLs over a wide range of velocities. As such, PSLs were selected to perform the calibration described in Chapter 2, and to compare the functionality of the AIS charge-based detection mechanism to previously experimental methods.

3.2 Experimental Methods

In order to calibrate the mass spectrometer used in the AIS, two different, homogenously-sized PSL species were characterized. Solutions of 510 nm and 990 nm (Polyscience #07307 and #07310) PSL particles were prepared in a 1:1 mixture of 25 mM ammonium acetate in water and HPLC grade methanol. The solution's number densities were 3e10 particles per mL for the 510 nm solution, and 4.1e8 particles per mL for the 990 nm solution. These solutions were sprayed using the AIS electrospray ionization source into vacuum at a flow rate of 0.26 mL/h and an electrospray voltage of ~5 kV. Positive potential was used to create positively charged particles with 1000s – 10000s of fundamental charges. Particles were injected into vacuum through a drying tube heated to ~185°C to desolvate the aerosolized solutions. After drying, the particle beam was collimated using an aerodynamic lens and the beam was sampled using a quadrupole deflector. After passing through the deflector, particle flux was sufficiently reduced to allow individual particle detection on image charge detectors. Deflector settings were selected to balance the expected particle mass with the measured particle velocities by comparing the kinetic energy of the particle expected charge

of the particle to the voltage applied to the quadrupole deflector (energy-per-charge selection). The expected charge of each diameter PSL was calculated using the Rayleigh limit[12,13] of the solution. This is a commonly used limit in ESI that predicts the maximum amount of charge you can put on a liquid sphere before coulombic explosion of the droplet takes place (as a function of droplet surface tension). The limit for the solid particles used here pertains to the liquid suspension they are initially created in and how much charge that can sustain while evaporating off of the particles (mathematical description can be found in Chapter 8). Trends in the amount of charge on each particle was measured for a quadrupole deflector setting between 100-1000 V using a post-deflector image charge detection tube as shown in Figure 3.1. The Rayleigh limit[12,13] for the two PSL species was observed to be achievable in the deflector scans used to measure particle charge.

After passing through the quadrupole deflector individual particles were trapped in the nanoparticle electrostatic trap (NET) for spectrometric analysis. A large ensemble of each sized PSL species was sequentially trapped and charge detection mass spectrometry (CDMS) was used to collect mass information to calibrate the mass spectrometer as outlined in Chapter 2. Sample mass spectra collected with the calibrated mass spectrometer are shown in Figure 3.2.

After trapping single particles in the NET and measuring their mass-to-charge ratio (m/z), a nine stage linear accelerator (LINAC) was programmed to accelerate/decelerate particles over a wide energy range. The LINAC was programmed individually for each particle's unique m/z measurement in real time as outlined in Chapter 2. Briefly, the particle's unique m/z was used with a SIMION simulation of the LINAC's electric field to calculate individual particle transit times through the acceleration electrodes. This timing was used to

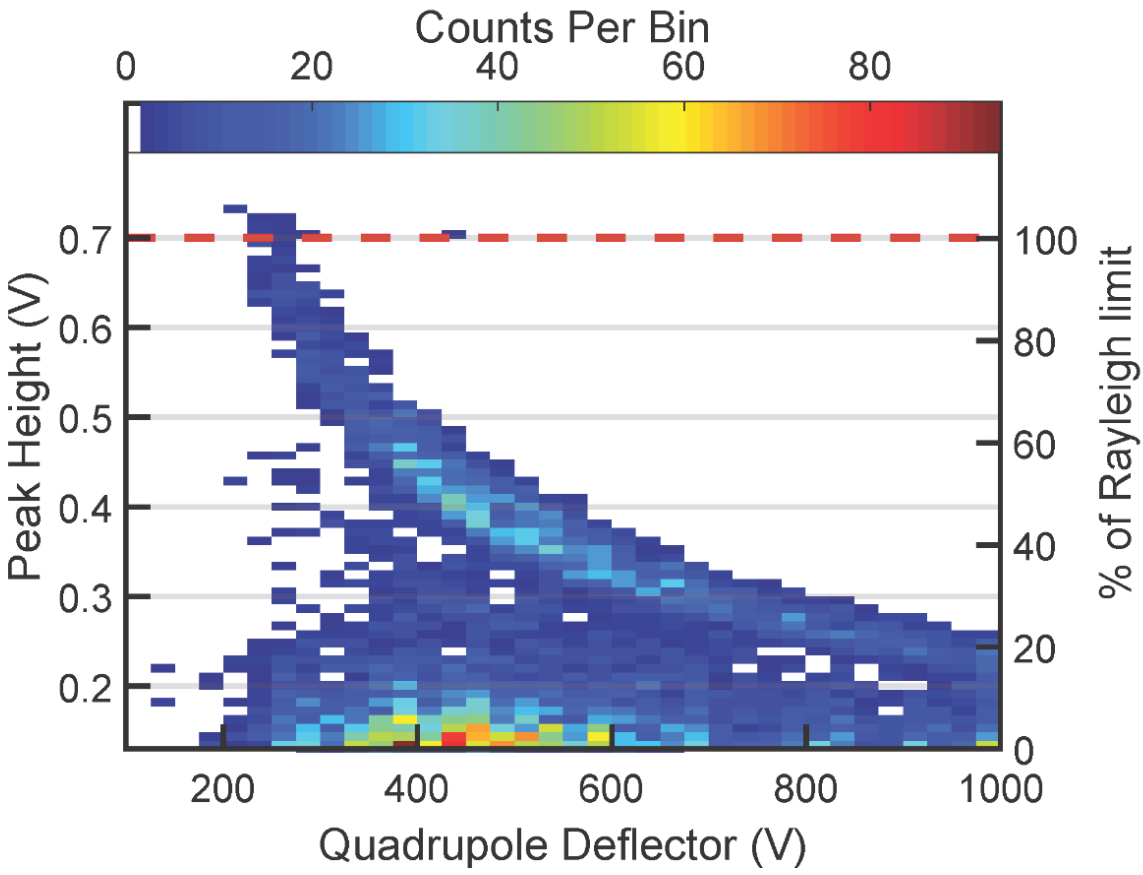

Figure 3.1: *Quadrupole deflector charge distribution for 990 nm PSL particles. The QD was scanned over a variety of voltages (200-1000 V) and the resulting distribution of particle charges (displayed as image charge detector output voltage) selected by the deflector was measured for each setting. The distribution that appears as a crescent shape moving from 0.7 V to 0.25 V from QD setting of 250V to 1000 V corresponds to PSL particle passing through the deflector. The detector voltage as a percentage of the Rayleigh limit is shown on the right with the Rayleigh limit for 990 nm PSLs plotted as a red dashed line. This figure is reproduced from ref. 16.*

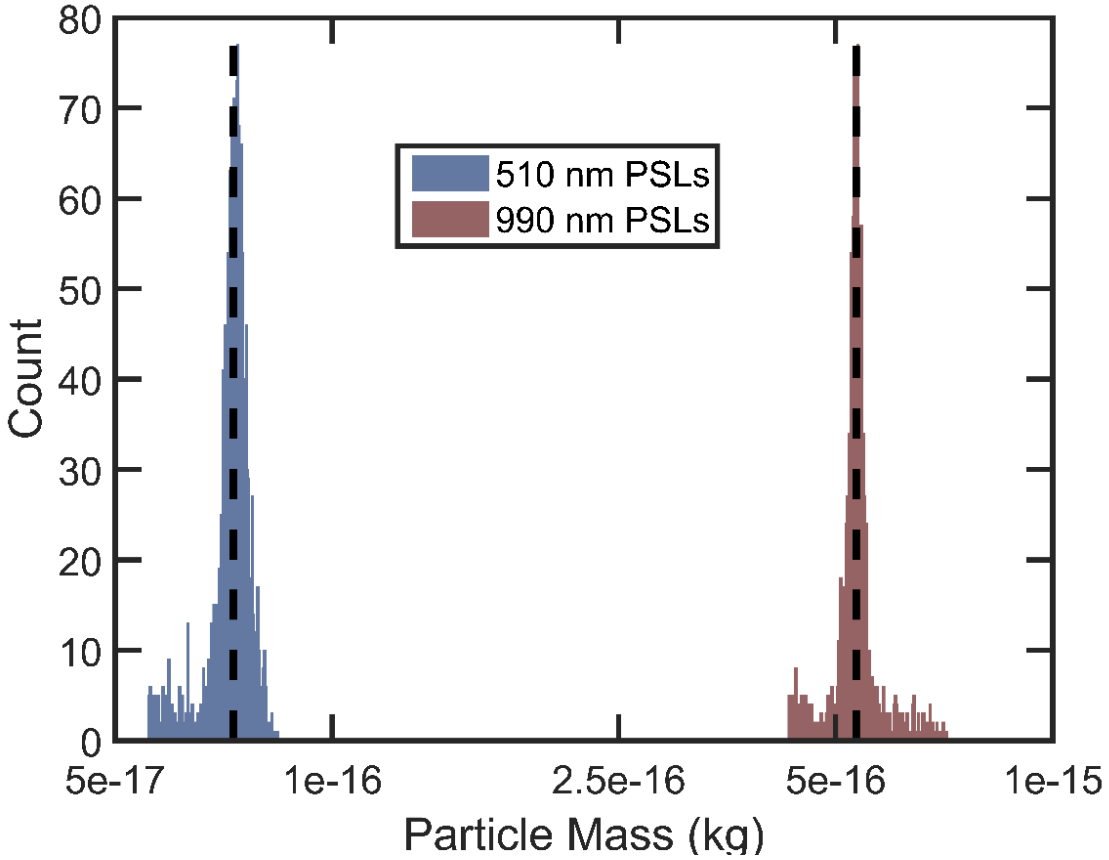

Figure 3.2: *CDMS spectra of 510 nm and 990 nm PSL particles post-calibration. The black dashed lines correspond to the expected masses of the sphere sizes injected. Masses within 0.8*σ of each data set are displayed, others are rejected. This figure is reproduced from ref. 16.*

program two high voltage switches in a sequence to either accelerate or decelerate individual particles. The LINAC was operated with negative potentials from 0 V to -45 kV to accelerate particles and positive potentials of 0 V to +383 V to decelerate particles (only 990 nm PSLs were decelerated). The final velocity achieved by individual particles was measured using a simple image charge detection tube (as outlined in Chapter 2) to measure the transit time through the simple tube geometry.

After acceleration, particles pass through an image charge detection tube before directly impacting a piece of single crystal silicon wafer, ~20 mm square, located ~25 mm from the back of the ICD tube. The surface roughness of the wafer was minimized to reduce any effect from uneven contact the homogenous spheres would experience. The wafer was mounted perpendicular to the incident particle beam using a cylindrical mounting block seated on an alignment rail to square the target face with the particle beam axis (Figure 3.3). After impacting the silicon wafer target, if a particle rebounded along the incident beam axis the rebound velocity was measured using the same image charge detector that measured the incident velocity. This was repeated for many particles at each LINAC potential and particle ensembles of like incident velocity were averaged to calculate the CoR.

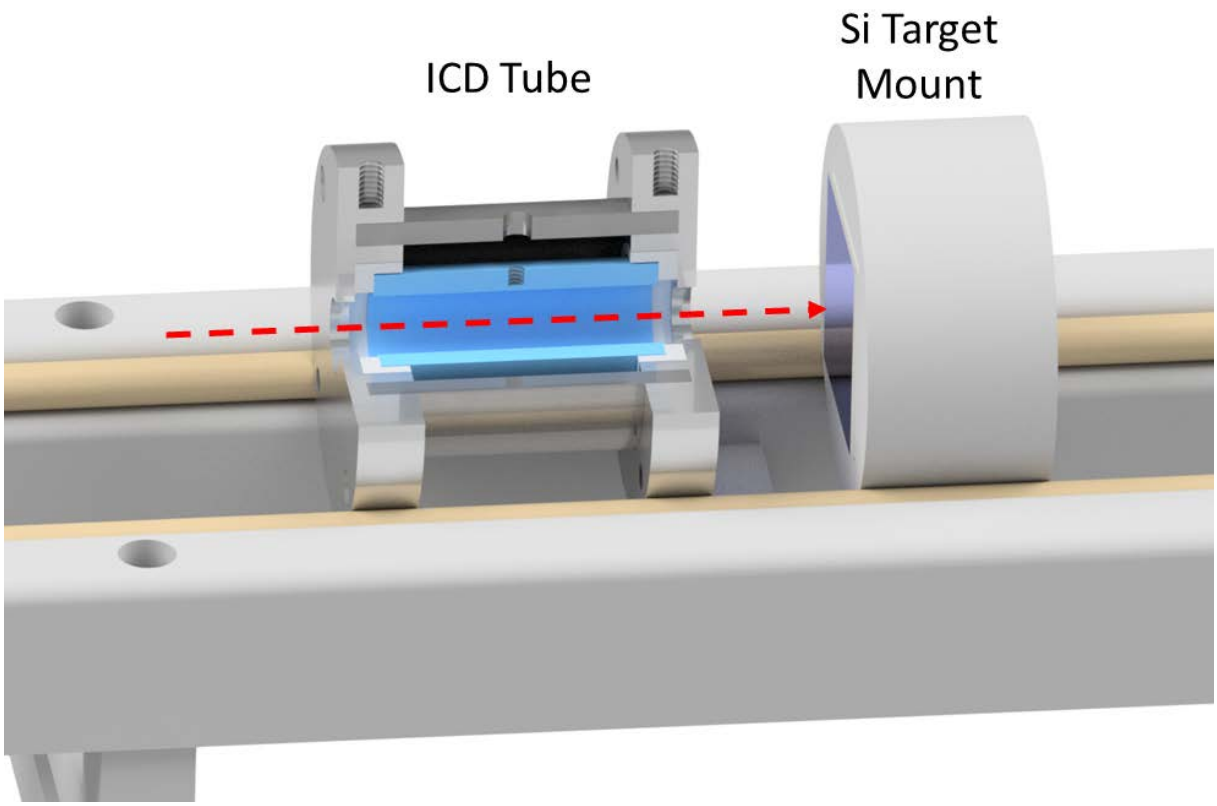

Figure 3.3: *ICD and target diagram for PSL CoR measurements. Incident particle trajectory is shown in red.*

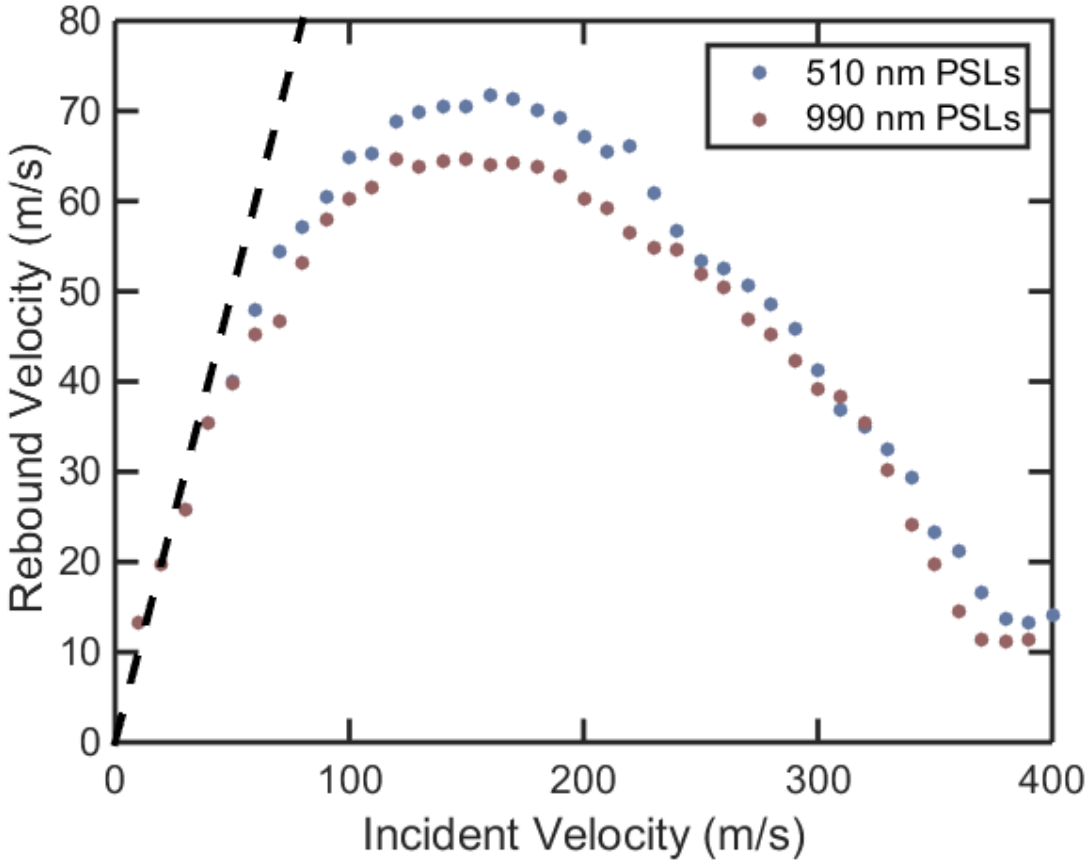

Figure 3.4: *Average rebound velocity for 510 nm and 990 nm PSL particles on a silicon target. The 1-1 velocity is represented with a dashed black line. Velocity data is grouped in 10 m/s incident velocity bins with the average rebound velocity of each bin represented on the y-axis.*

3.3 Results and Discussion

In order to compare the current results to past studies, the velocity range of interest was chosen to match that examined by Dahneke[2], ranging from 10 m/s to 400 m/s. Although Dahneke measured particle velocities below 10 m/s, the defocusing introduced by the LINAC's deceleration field made collection of information about velocities below 10 m/s very difficult. The velocity range studied for the two different PSL sizes used in this experiment was similar, however deceleration was only performed on the 990 nm sized spheres. The average rebound velocity of both 510 nm and 990 nm PSL particles is presented in Figure 3.4

At lower velocities (< 60 m/s) particle rebound velocities were found to be very similar to incident velocities. The 1-1 velocity line plotted in Figure 3.4 indicates minimal inelasticity in the collision. As the incident velocity increases, a maximal rebound velocity is achieved at ~150 m/s before decaying to near zero at 400 m/s. The local maxima of these curves reflect the change in impact dynamics where the collisions become dominated by inelasticity. After this point, with increasing incident velocity progressively more energy is lost to inelastic processes until above 400 m/s particles stop rebounding from the surface.

The behavior of the two particle species measured here compares well to that measured by Dahneke. A comparison between the data collected here and Dahneke is presented in Figure 3.5. The general trend of all three data sets compares well with a slight offset between Dahneke and the data presented here. This is likely due to differences in materials used and differences in acceleration/detection techniques. Dahneke impacted PSL particles onto a polished quartz surface with the use of a pressure differential accelerator. The difference in impact target will

have an effect on the collision as noted by Dahneke and others,[2,4,14] although this effect is minimized by the use of polished material significantly harder than the particle species.[3] The highly charged nature of the PSL particles used in this experiment also potentially can affect the particle-surface interaction.[15] However the effect of this interaction should become less significant at higher velocities. The comparison shown here indicates the difference shown here is maximal at higher velocities. Additionally, the PSLs produced using the electrospray ionization source here may still maintain a small layer of solvent even after the electrospray drying process. Although this fluid layer is most likely minimal as complete drying of the particles is expected, it cannot be ruled out as a possible source of difference in comparing the two measurements. Finally, the detection methods for recording velocity could introduce differences in the data from errors associated with the measurement. Dahneke used two light beams crossed with the PSL particle beam to measure when particles crossed those beams with photomultiplier tubes. The transit time between the two light beams was measured and the time-of-flight was used to calculate the particle velocity. This differs from the image charge detection technique used here. Difference in exactly how the signal width and travel distance are related could introduce systematic error in velocity measurements in both experiments and it is very likely that this at least partially contributes to the difference in the two data sets. Although there are many possible explanations for the differences observed in the data, the three sets generally follow the same trend and behavior establishing the methodology used here as a valid measure for particle CoR, and showing that there is no significant size-dependence in the impact dynamics for PSLs in this size range.

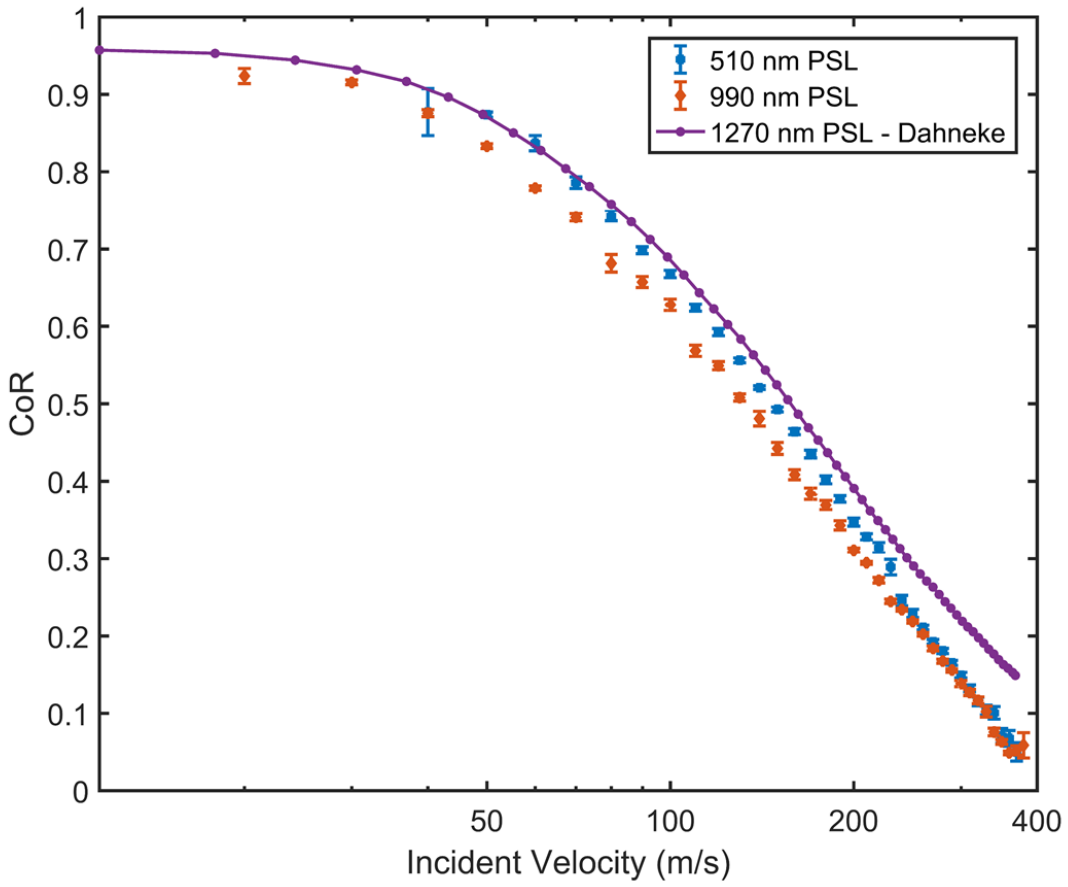

Figure 3.5: *Comparison of PSL CoR data to Dahneke (1975). The error bars ascribed to the 510 and 990 nm data are derived from the 95% confidence interval of a normal distribution. 510 and 990 nm PSL data is grouped into 10 m/s incident velocity bins with the average CoR of that bin represented on the y-axis. The data from Dahneke is extracted from the published figure.*

3.4 Conclusions

Particle generation, characterization, energetic control, and CoR characterization has been demonstrated with PSL particles. The CoR data collected in these experiments were compared to previous work and found to show good agreement The demonstration of the AIS as an experimental platform to perform impact measurements with a potential wide variety of particle species open exciting opportunities to expand experimental understanding of particle-target interactions. Future experiments will explore the effect of different particle species and targets as well as expand different detection capabilities in addition to measuring particle CoR. Additional discussion of the experiment presented here can be found in ref. [16].

Acknowledgements

Chapter 3 uses figures (3.1 and 3.2) as they appear in Adamson, B.D.; Miller, M.E.C.; Continetti, R.E. The aerosol impact spectrometer: a versatile platform for studying the velocity dependence of nanoparticle-surface impact phenomena. *European Physical Journal, Techniques and Instrumentation*, 2017, 4 (2). The dissertation author is coauthor and the dissertation advisor is the corresponding author.

3.5 References

(1) Dahneke, B. Particle Bounce or Capture—Search for an Adequate Theory: I. Conservation-of-Energy Model for a Simple Collision Process. *Aerosol Sci. Technol.* **1995**, *23* (1), 25–39. https://doi.org/10.1080/02786829508965292.

(2) Dahneke, B. Further Measurements of the Bouncing of Small Latex Spheres. *J. Colloid Interface Sci.* **1975**, *51* (1), 58–65. https://doi.org/10.1016/0021-9797(75)90083-1.

(3) Wall, S.; John, W.; Wang, H.-C.; Goren, S. L. Measurements of Kinetic Energy Loss for Particles Impacting Surfaces. *Aerosol Sci. Technol.* **1990**, *12* (4), 926–946. https://doi.org/10.1080/02786829008959404.

(4) Tsai, C.-J.; Pui, D. Y. H.; Liu, B. Y. H. Capture and Rebound of Small Particles Upon Impact with Solid Surfaces. *Aerosol Sci. Technol.* **1990**, *12* (3), 497–507. https://doi.org/10.1080/02786829008959364.

(5) Cai, Y.; Tay, K.; Zheng, Z.; Yang, W.; Wang, H.; Zeng, G.; Li, Z.; Keng Boon, S.; Subbaiah, P. Modeling of Ash Formation and Deposition Processes in Coal and Biomass Fired Boilers: A Comprehensive Review. *Appl. Energy* **2018**, *230*, 1447–1544. https://doi.org/10.1016/j.apenergy.2018.08.084.

(6) Sommerfeld, M.; Huber, N. Experimental Analysis and Modelling of Particle-Wall Collisions. *Int. J. Multiph. Flow* **1999**, *25*, 1457–1489.

(7) Schöner, C.; Rennecke, S.; Weber, A. P.; Pöschel, T. Introduction of a New Technique to Measure the Coefficient of Restitution for Nanoparticles. *Chemie-Ingenieur-Technik* **2014**, *86* (3), 365–374. https://doi.org/10.1002/cite.201300132.

(8) Hassani-Gangaraj, M.; Veysset, D.; Nelson, K. A.; Schuh, C. A. Melt-Driven Erosion in Microparticle Impact. *Nat. Commun.* **2018**, *9* (1), 5077. https://doi.org/10.1038/s41467-018-07509-y.

(9) Hassani-Gangaraj, M.; Veysset, D.; Nelson, K. A.; Schuh, C. A. In-Situ Observations of Single Micro-Particle Impact Bonding. *Scr. Mater.* **2018**, *145*, 9–13. https://doi.org/10.1016/j.scriptamat.2017.09.042.

(10) Dahneke, B. The Capture of Aerosol Particles by Surfaces. *J. Colloid Interface Sci.* **1971**, *37* (2), 342–353. https://doi.org/10.1016/0021-9797(71)90302-X.

(11) Dahneke, B. Measurements of Bouncing of Small Latex Spheres. *J. Colloid Interface Sci.* **1973**, *45* (3), 584–590.

(12) Rayleigh, Lord. XX. On the Equilibrium of Liquid Conducting Masses Charged with Electricity. *Philos. Mag. Ser. 5* **1882**, *14* (87), 184–186.

https://doi.org/10.1080/14786448208628425.

(13) Fenn, J. B.; Mann, M.; Kai Meng, C.; Fu Wong, S.; Mann, M.; Fu WONG, S.; Whitehouse, C. M. Electrospray Ionization for Mass Spectrometry of Large Biomolecules. *Sci. New Ser.* **1989**, *246* (4926), 64–71.

(14) Rennecke, S.; Weber, A. P. Charge Transfer to Metal Nanoparticles Bouncing from Conductive Surfaces. *Aerosol Sci. Technol.* **2014**, *48* (10), 1059–1069. https://doi.org/10.1080/02786826.2014.955566.

(15) John, W. Particle-Surface Interactions: Charge Transfer, Energy Loss, Resuspension, and Deagglomeration. *Aerosol Sci. Technol.* **1995**, *23* (1), 2–24. https://doi.org/10.1080/02786829508965291.

(16) Adamson, B. D.; Miller, M. E. C.; Continetti, R. E. The Aerosol Impact Spectrometer: A Versatile Platform for Studying the Velocity Dependence of Nanoparticle-Surface Impact Phenomena. *EPJ Tech. Instrum.* **2017**, *4* (2). https://doi.org/10.1140/epjti/s40485-017-0037-6.

Chapter 4. Impact Dynamic Studies with a Tapered Image Charge Detector

4.1 Introduction

Image charge detection devices have been reported for applications in mass spectrometry[1,2] and hypervelocity particle impact studies of astrophysical dust behavior in space environments.[3] Image charge detectors (ICDs) have been fabricated in a variety of geometries to suit application-specific needs including the common cylindrical electrode design,[4,5] planar electrode detectors,[6] and wire-grid detectors.[7–9] Particles with sufficient charge can interact with image charge electrodes of varying geometries to provide spatial information that, when combined with time-resolved measurements, allows the determination of the particle trajectory. Previously reported wire-grid detectors are capable of examining incident particle trajectories, as reported in refs. [7] and [8]. With an appropriate electrode geometry and charge-detection instrumentation, the rebound trajectory of a single scattered particle as a function of incident energy can be determined. Measuring rebound trajectories using an ensemble of single particles allows the determination of scattering angular distributions and dynamical information including the inelasticity of the particle-surface interaction. This method of detection is well suited to characterize the dynamics of particles difficult to detect optically because of their size or speed, but still capable of carrying high amounts of charge in addition to enabling the examination of charge-transfer phenomena occurring during particle impacts. In the present study, a new type of multiplexed image-charge-based particle detector is described and applied to measurements of mass- and energy-selected submicron particle scattering. The detector is

based on a series of cylindrical electrodes of increasing diameter, and is referred to as the tapered ICD, or TICD.

The TICD was developed to examine angular distributions for the scattering of energy-selected micron and sub-micron particles using the Aerosol Impact Spectrometer (AIS).[10] The AIS uses an electrospray ionization source coupled with an aerodynamic lens, a linear nanoparticle electrostatic trap (NET), and a linear accelerator to direct mass- and charge-resolved particles onto a target surface. The initial studies with the AIS[10] measured the coefficient of restitution (CoR) for submicron polystyrene latex spheres (PSLs) by detecting particles rebounding in a narrow range of angles around the surface normal using a single cylindrical ICD. The TICD described here has a wide acceptance angle for scattered particles that can be easily changed by varying the detector-target distance. This allows the multiplexed detection of particle scattering angle and velocity distributions.

In the following sections, the AIS configuration used in this study is briefly reviewed followed by a more detailed discussion of the TICD. Polystyrene latex spheres are used as a test species to demonstrate the functionality of the detector. Additionally, experiments using tin metal nanoparticles are presented and used to compare the fidelity of TICD measurements to previous detector designs. The measurement of particle coefficient of restitution, a measurement of the velocity loss of single particle collisions, is used to compare the two detector designs (as the previously used detector design was made expressly to measure particle CoR). CoR measurements are useful for experimental examination and characterization of particle-surface interactions in addition to being a commonly examined metric of longstanding impact dynamics models.[11,12] This measurement of CoR not only establishes the detector

functionality but also constitutes the first experimental measurements of charged metal nanoparticle impact dynamics in the plastic regime. Finally, the angular distribution for tin particle scattering at 150 m/s from polished Mo is reported and compared to a random desorption distribution to demonstrate the capability of this detector to examine particle scattering over a wide range of rebound angles.

4.2 Experimental Methods

The TICD is housed within a grounded stainless steel cylinder designed to fit with a pre-existing ion optics rail as well as shield the electronics and detection surfaces of the TICD. Within the shielding, the detector consists of 6 stainless steel ring-shaped electrodes stacked within a retaining PEEK cylinder, an endcap for mounting the detector electronics, and two retaining shields on either end to enclose the assembly (Figure 4.1). The ring electrode stack design is detailed in the supplementary material.

The electrodes individually act as ICDs and can be isolated from one another or coupled together. In the experiments presented here, sets of two rings were coupled together to create three separate detection elements from the six ICD electrodes (see Figure 4.1). The electronics for the detectors are instrumented with a FET (J-FET, PMBFJ309.215) and feedback resistor/capacitor (R_F = 10 GΩ, C_F = 0.1 pF) circuit as close to the electrodes as possible to reduce noise and increase detector sensitivity. The signals from these circuits are fed to external charge-sensitive pre-amplifiers (Amptek A-250) with a baseline correcting operational

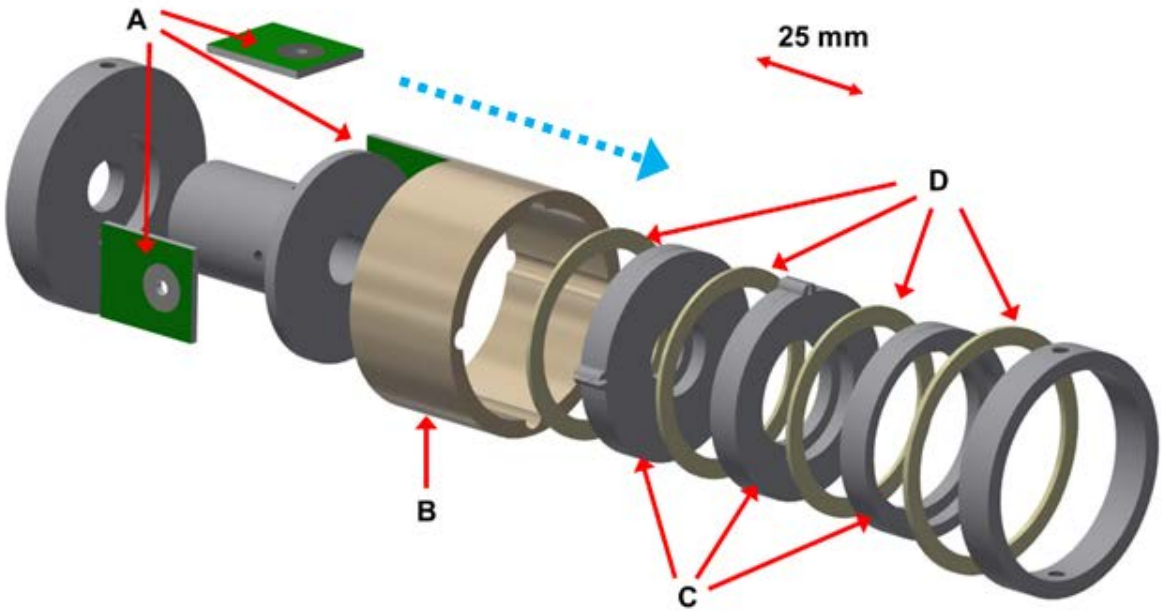

Figure 4.1: *Expanded view of the tapered image charge detector (TICD). Entire assembly is housed in a grounding shield (not shown here). Direction of incident particle travel shown in blue. A) Printed circuit boards for the three image charge detection circuits. B) PEEK insulator that retains the detector element stack. C) Three detection elements of current detector configuration. D) Teflon spacers for isolation of individual detection elements.*

amplification circuit. The physical separation of the preamplifier from the FET and feedback circuit is modeled after the GeFRO preamplifier circuit design.[13]

As implemented in the AIS, a grounded stainless steel tube is used to fix the distance of a similarly instrumented conductive target from the TICD. This collision analysis target (CAT) is mounted on the ion optics rail using an aluminum cylinder. On the cylinder the target is centered using a stainless steel plate and held electrically isolated from the plate with a 3-D printed mounting platform (FormLabs Form 2 printer, methacrylic acid esters and photoinitiator) (Figure 2). The target is held flat with a steel retaining ring insulated with a Teflon spacer, exposing the central area of the target through an opening in the ring. A 5x5 mm molybdenum mirror (II-VI Infrared) with a 20 nm surface finish was used as the target in the experiments reported here. The polish of the mirror was chosen to minimize the effect of target surface asperity on particle scattering. It has been previously noted that surface asperity has a significant effect on lower velocity impact measurements (<10 m/s, before bulk yielding of the impact).[12] Low velocity measurements are not the focus of this study, however surface roughness is minimized to reduce any possible effect. An ICD circuit of the same design as those used in the TICD is mounted behind the target and a connection is made through a push-pin contact in the target mount.

The three signals from the TICD and the signal from the CAT are fed into a high-speed 16 channel digitizer front end of a FPGA module (National Instruments, NI 5751B and PXIe-7961R) for recording and data processing. This module runs in tandem with the data acquisition system used on the AIS to generate the particles under study. A cylindrical ICD located directly

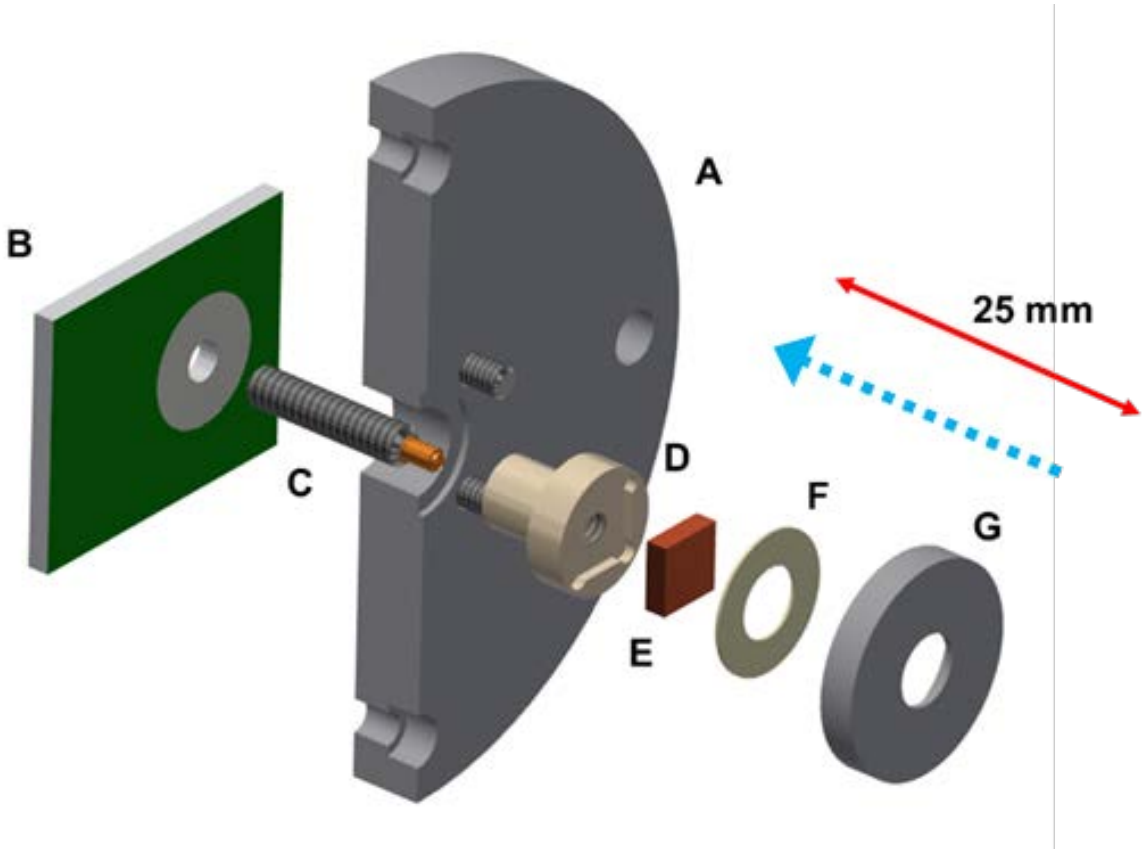

Figure 4.2: *Expanded view of the collision analysis target (CAT). Direction of incident particle travel shown in blue. A) Stainless steel plate for the target mount (halved), connected to Al mounting cylinder (not shown). B) Image charge detection circuit printed circuit board connected to the target with a screw/spring pin assembly. C) Spring pin contact with target. D) 3-D printed mounting piece for the target. E) 5x5 mm impact target. F) Teflon retaining ring for isolating target. G) Mounting ring to hold target in place.*

before the TICD generates a trigger upon detection of an incident article that initiates acquisition of the TICD and CAT signals (Figure 4.3).

The measurable angular ranges using the TICD and CAT detector are determined by 5 detector geometry parameters, as shown in Figure 4.4: the axial distance of the target from the innermost detection element (a), the axial step size of each element (Δa), the radial distance of the target center from the innermost element (r), the radial step size of each element (Δr), and the exposed radius of the impact target (r_t). Four of these parameters ($\Delta a, r, \Delta r$ and r_t) are inherent to the detector design, but the fifth parameter a is designed to be easily varied by changing the distance of the CAT from the TICD. This allows for a variety of angular ranges to be accessed depending on the distance of the CAT from the TICD.

In the initial characterization of the detector, the nominal parameters used are listed in Table 4.1 (with a spacer used between CAT and TICD). The angular ranges of each element listed in Table 4.1 overlap due to uncertainty in the particle impact position on the target and can be decreased by reducing the exposed area of the target (see Supplementary Material). In the experiment presented here particle signals measured on the CAT cannot be assigned an exact impact location smaller than the exposed face of the target. The uncertainty of the position of impact on the target is the largest contribution to error in the angular measurements discussed below. A more detailed description of the calculations used to determine angular ranges from the parameters as well as a more thorough treatment of error in these calculations can be found in the Supplementary Material.

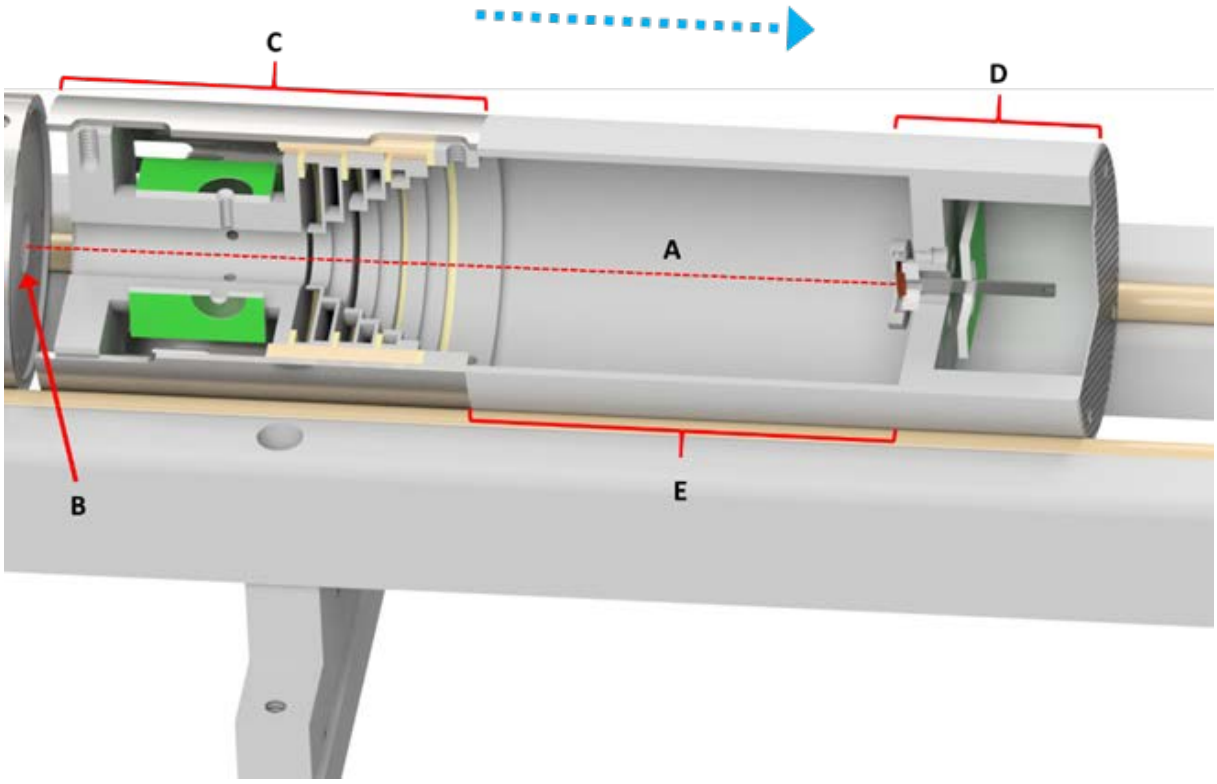

Figure 4.3: *Detector setup for scattering measurements with the TICD. The detector, target, and tube sit on an ion optics rail that allows isolation of the individual elements. Direction of incident particle travel shown in blue. A) Centerline of the detection system (dashed line). B) Image charge detector that triggers acquisition of TICD/CAT data. C) TICD. D) CAT. E) Spacing tube between TICD and the CAT.*

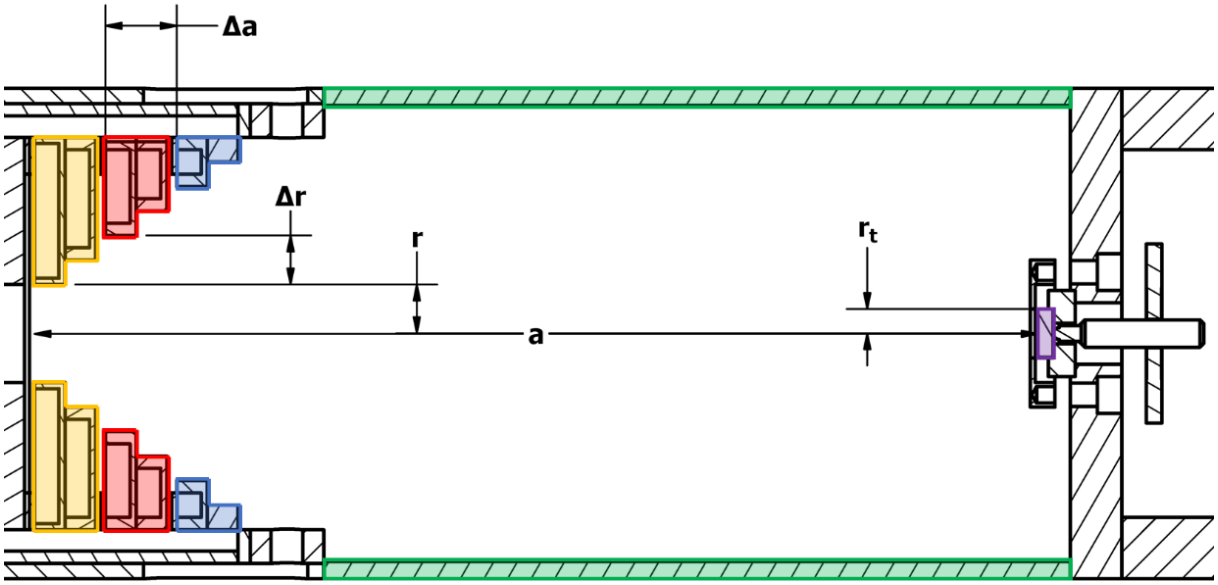

Figure 4.4: *Axial geometry of TICD (slice) configured with three detector elements (highlighted in yellow, red, and blue), the CAT (purple), and spacer (green). Key parameters of the TICD/CAT design are noted:* $\boldsymbol{a}$, $\boldsymbol{\Delta a}$, $\boldsymbol{r}$, $\boldsymbol{\Delta r}$, *and* $\boldsymbol{r_t}$. *The target is secured with a mounting ring (Figure 4.2G) seen around the target here. Parameter a is measured from the target face, not this ring.*

Table 4.1: *List of parameters used for detector characterization*

TICD Parameters:	$\boldsymbol{a = 104\ mm}$	$\boldsymbol{r = 5.1\ mm}$	$\boldsymbol{r_t = 2.5\ mm}$
	$\boldsymbol{\Delta a = 7.4\ mm}$	$\boldsymbol{\Delta r = 5.1\ mm}$	
Angular Ranges:	$Element\ 1 = 1.4° - 7.5°$	$Element\ 2 = 4.6° - 11.3°$	$Element\ 3 = 8.2° - 15.6°$

4.3 Calibration and Analysis

The detector was tested using highly charged (~18000 e) 990 nm polystyrene latex spheres (PSLs, Polyscience #07310) produced using electrospray ionization. Particles were accelerated to a final energy of ~16.7 MeV, resulting in a final particle velocity of ~100 m/s. Incident particle velocity after acceleration was measured using a cylindrical ICD located before the TICD and CAT.

The signal on each detector element is produced from the charge on the particle inducing a current pulse on the electrode. The preamplifier circuit attached to each electrode amplifies the current pulse and produces a voltage signal. These signals are analyzed using an independent analysis program (developed in MATLAB) to characterize the variety of different signal shapes and types (see Figure 4.5 and Figure 4.6). The magnitude and shape of the signal is dependent on the particle distance from each detection element, time spent in the detection region, and shielding from other nearby elements. Incident particles pass through all three detection elements before impacting the target producing a signal of differing magnitude on each element sequentially: the first and strongest signal (yellow) is produced on the detector closest to the particle's path (the innermost detector), the second signal (red) is produced on the detector in the center of the TICD stack, and the third, weakest signal (blue) is produced on the outermost detector of the stack. When a particle impacts the target (purple) a strong sharp peak is produced on the CAT. This peak is significantly narrower than the peaks observed on the TICD due to the smaller interaction time between the particle and the target; the CAT detector is a flat surface while the TICD detectors are cylinders with a larger detection region. The preceding four signals all follow the same pattern for events that can be characterized by this

Figure 4.5: *Example signal waveforms generated by the TICD and CAT. TICD signals (yellow, red and blue) and the CAT (purple) are analyzed. A) Particle rebounds from target and impacts the outermost element of the TICD. B) Particle rebounds from target and impacts the middle element of the TICD and bounces back towards the target. C) Particle rebounds from target and impacts the innermost element of the TICD and bounces back towards the target. D) Particle rebounds from target and passes through the TICD without impact indicating a near zero angle scattering trajectory. E) Particle impacts the target and rebounds at a scattering angle greater than that detectable by TICD. F) Particle passes through TICD but does not strike the target.*

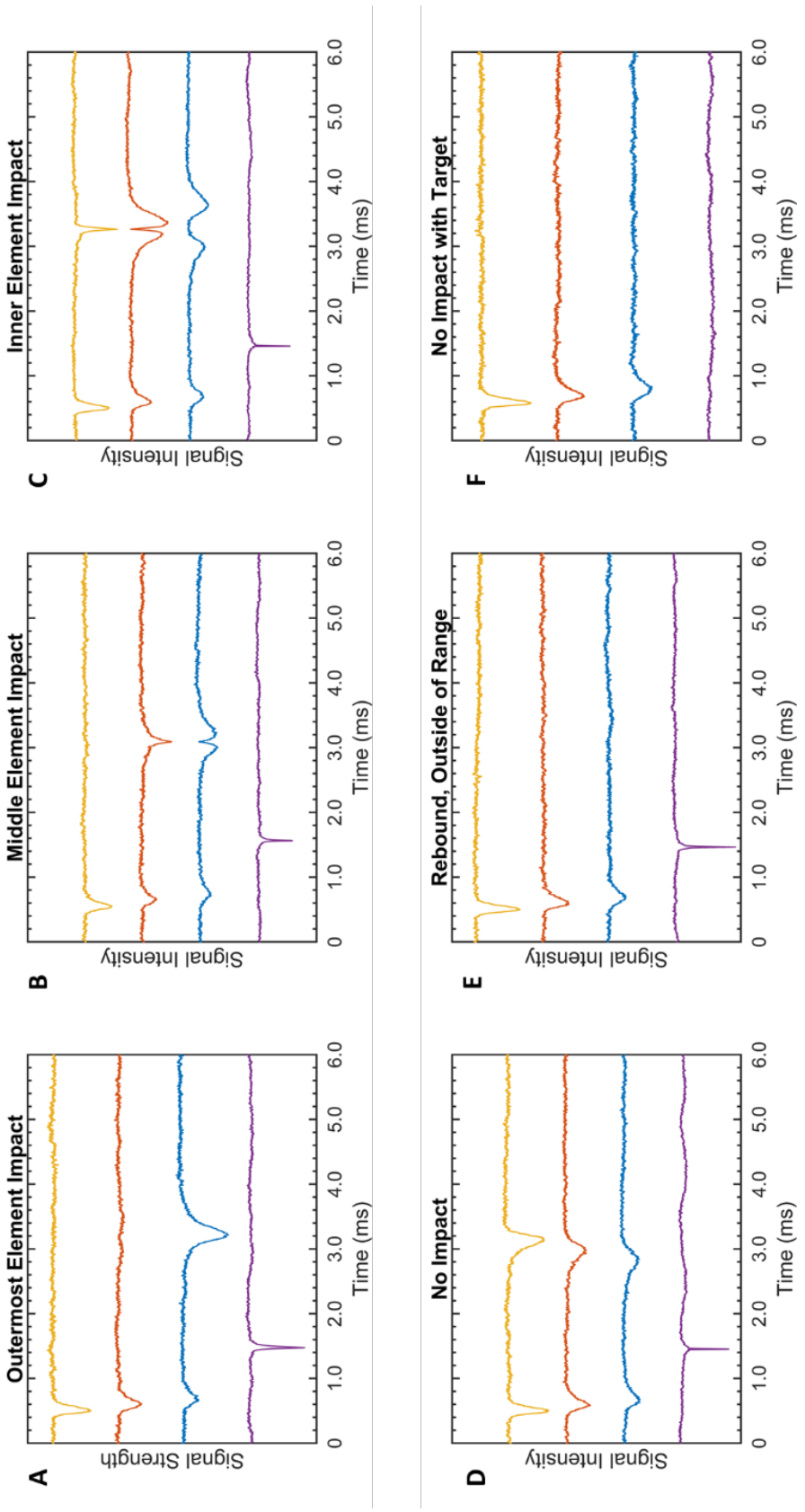
A
Outermost Element Impact
Signal Strength
B
Middle Element Impact
Signal Intensity
C
Inner Element Impact
Signal Intensity
D
No Impact
Signal Intensity
E
Rebound, Outside of Range
Signal Intensity
F
No Impact with Target
Signal Intensity
0
1.0
2.0
3.0
4.0
5.0
6.0
Time (ms)

detector. If there is deviation from this behavior (see Figure 4.5F) the particle trajectory is not analyzed.

After impact with and rebound from the target, the signals can be sorted into 5 different types of events (Figure 4.5A-E). Figures 4.5A-C show when a rebounding particle impacts one of the detection elements of the TICD. In each case the rebounding particle is seen interacting either with only one detector in the stack (Figure 4.5A) or with sequential elements multiple times indicating a change in direction (Figures 4.5B-C). In both Figure 4.5B and 4.5C the signal from the impacted element is significantly narrower than in Figure 4.5A. The width of the impact peak is not indicative of an impact itself, but rather indicative of where on the detection element the particle is striking. In 4.5A the rebounding particle penetrates the detection region of the outer element, the region in which the individual detector element responds to induced charge, before striking that element and bouncing away. However, in 4.5B and 5C the rebounding particle does not significantly penetrate the detection region of the middle and inner elements respectively and interacts only with the target-side face of each element to produce the observed signal (much like the signal seen from the impact target face). In addition to the impact signals in Figures 4.5B and 4.5C, a correlated anti-signal peak is observed in the previous element (blue for 4.5B and red for 4.5C) as a sharp return to baseline. This behavior resembles that of previously reported position sensitive ICD designs,[7–9] and is due to the quenching of image charge signal on other elements as a particle impinges on a single element. The charge of the particle impacting a single element is effectively screened by the surface charge of that element, shielding the image charge signal from other detectors. Figure 4.5D shows a set of signals corresponding to the rebounding particle scattering back along the incident trajectory with no impact on TICD elements. A notable feature of this trace is the

clipped return to baseline of the final element signal (yellow). This peak is less symmetric than those of other elements due to the presence of a grounded shield immediately behind the stack, at the entrance to the TICD. This grounded element shields the detector from the particle image charge once it leaves the detection region, resulting in an asymmetric peak shape. Finally, particle rebound outside of the angular acceptance range of the TICD produces a signal as shown in Figure 4.5E. The particle impacts the target and is not seen on any other detection element within the acquisition time frame.

In addition to the detection of various impact and rebound events, particle deposition can readily be identified by the TICD and CAT (Figure 4.6). When a charged particle approaches a detector element the signal induces charge flow through a feedback circuit with a characteristic time determined by the feedback resistor and capacitor used. In the signals shown in Figure 4.6, the discharge time is significantly longer than the observed signal due to the short amount of time a scattered particle spends in the vicinity of a given detector element. Discharge of the signal can be attributed to either the particle sticking to the surface or complete charge transfer from the particle to the element surface upon impact. For the insulating PSL particles used, complete charge transfer to the surface after collision is not expected at the velocities measured.[14] The characteristic discharge is therefore identified as being a signature of particle deposition onto a detector element.

The long discharge times observed in Figure 4.6A (blue), 4.6B (yellow), 4.6C (blue), and 4.6D (purple) are examples of particle deposition onto detection elements of the TICD, with discharge times characteristic of the resistor-capacitor feedback circuit.

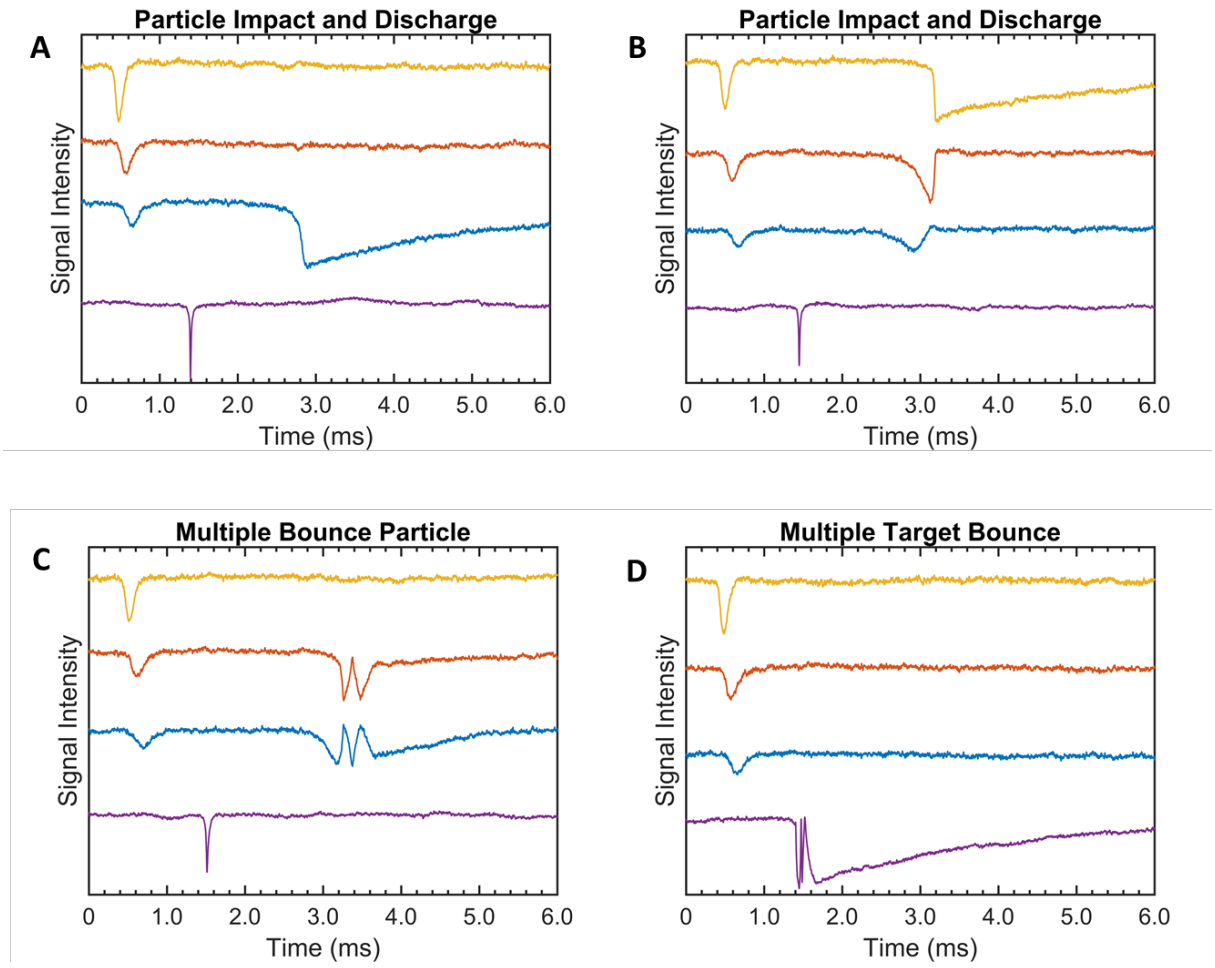

Figure 4.6: *Signatures of particles impacting and discharging through the elements. This discharge is indicative of a particle sticking to the surface and depositing charge. A) Particle rebounds into the outer detection element with subsequent discharge through the outer element circuit. B) Particle rebounds into the inner detection element with subsequent discharge through the inner element circuit. C) Particle rebounds and impacts the middle detection element. After initial impact the particle bounces between the middle and outer elements twice before sticking to the outer element and subsequent discharge through the circuit. D) Particle impact with the CAT. The particle after impact appears to bounce between the mounting ring and the target twice before sticking to the target with subsequent discharge. Particle deposition directly onto the target (without bouncing) is not shown because at the energy measured (16.7 MeV) PSL particles did not stick to the target upon initial impact.*

For all events where rebound from the CAT was detected an angular range can be assigned as shown in Table 4.1. In addition to particle rebound angle, the rebound velocity of an individual particle can also be calculated from the same four signal channels. This is done by measuring the time between the particle passing through each element of TICD and the time that the particle impacts the CAT. This timing information, in conjunction with the distance of the center of each detection element from the impact target, is used to calculate both the incident and rebound velocity for each particle. When a particle passes through all three elements after impacting the target, this measurement is performed in triplicate and averaged to calculate the CoR, the ratio of the particle's rebound velocity to incident velocity. The geometry and time dependent signals used in this calculation are demonstrated in Figure 4.7, and a sample calculation is provided in Table 4.2. For other types of events, varying levels of redundant CoR calculations can be performed based on the number of detector elements a given particle interacts with.

The average CoR obtained with 990 nm PSLs was compared to a previously reported CoR measurement with a simpler ICD design.[10] This was found to be in good agreement for similar velocities: 0.53 at 105 m/s with the TICD and 0.57 at 104 m/s with previously reported techniques. A more complete comparison over a larger range of velocities was performed between the two detection methods using 500 nm tin dust particles (US Research Nanomaterials Inc. #US1131M). Particles were produced and characterized using the same methodology as the 990 nm PSL particles (detailed above), starting with a colloidal suspension of nominally 500 nm tin powder (with thin oxide layer) in methanol/water (HPLC-grade methanol with 25

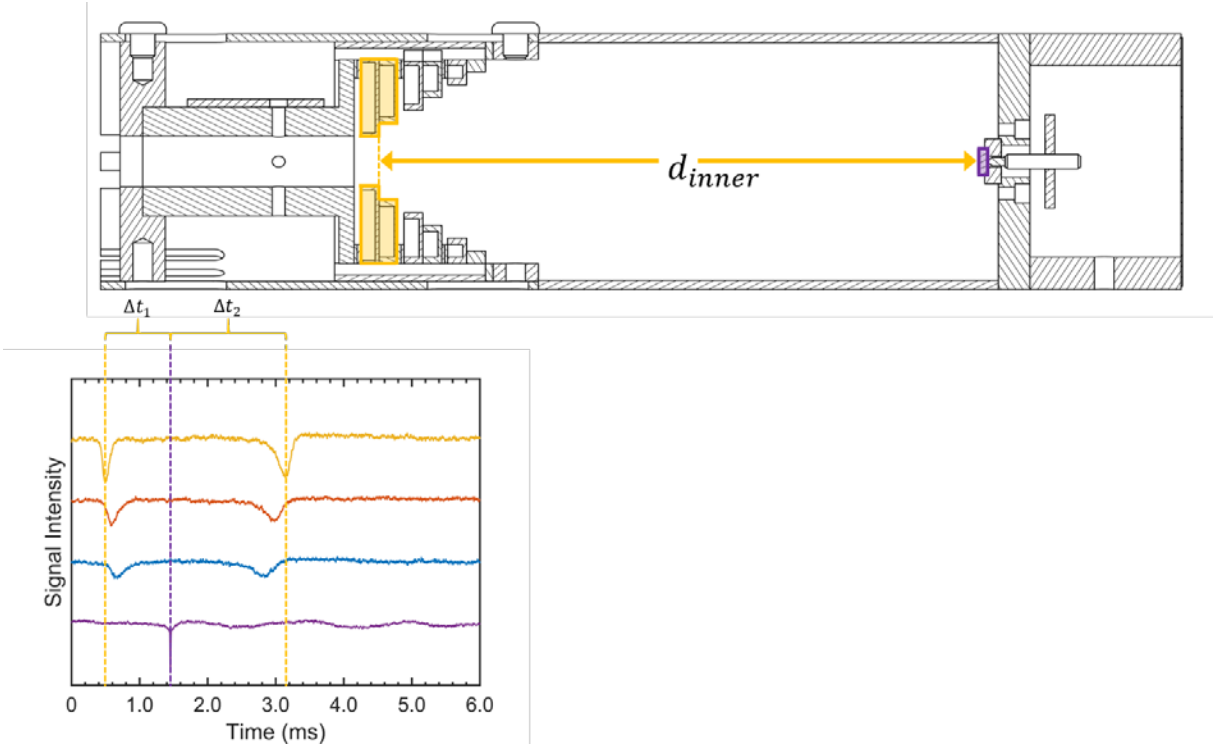

Figure 4.7: *Geometry for measuring CoR of particles using the TICD and CAT. By measuring the time it takes for particles to cross the distance (d) between the target and the center of each detector element (Δt_1 and Δt_2), the incident and rebound velocity can be measured. Parameter d_{inner} is calculated by subtracting $\Delta a/2$ from a (with a small correction for the spacer used in the detector). Values for d_{middle} and d_{outer} are calculated by subtracting Δa from d_{inner} and d_{middle} respectively. Depending on how the particle rebounds this measurement can potentially be made up to three times for a single particle (one time for each detector element with particle signal).*

***Table 4.2**: Example CoR calculations performed for the signals in Figure 4.7*

	Yellow– Inner	**Red – Middle**	**Blue - Outer**
Δt_1	940 µs	875 µs	782 µs
Δt_2	1699 µs	1530 µs	1388 µs
d	101 mm	93.5 mm	86 mm
$v_i = d/\Delta t_1$	107 m/s	107 m/s	110 m/s
$v_r = d/\Delta t_2$	59 m/s	61 m/s	62 m/s
$CoR = v_r/v_i$	0.55	0.57	0.56

mM aqueous ammonium acetate). Previous CoR measurements of 500 nm tin had been made over the velocity range of 50 – 500 m/s using a single ICD tube, and this data set was used to compare the CoR data collected using TICD. Data measured with the TICD captures particles that not only rebound through the detector completely but also those that impact one of the TICD detection elements. A comprehensive subset of velocities was examined and the two CoR data sets are in good agreement, as shown in Figure 4.8. This demonstrates that the CoR measurement functionality of a single ICD tube is maintained in the new detector design, while also allowing more complex scattering measurements, trajectory analysis, and charge transfer related to particle deposition. An assumption here is that there is no angular dependence to the CoR as these results are averaged over a range of recoil angles. This assumption will be examined with a larger dataset in the future.

In addition to the CoR information presented in Figure 4.8, the scattering angular distribution was measured for tin/tin oxide particles at an incident velocity of 150 m/s as shown in Figure 4.9. The experiment was performed without a spacer between the TICD and the CAT in order to access a larger angular acceptance range. The a value used to calculate the angles reported in Figure 4.9 was measured to be 26.6 mm; the other parameters ($r, \Delta r, \Delta a,$ and r_t) were kept the same as reported in Table 4.1. This parameter change increases the angular acceptance of the TICD to a maximum detectable rebound angle of 79° relative to the surface normal. Signal waveforms like those in Figure 4.5 and Figure 4.6 were visually sorted and assigned a scattering angular range based on the first detector element impacted by the particle following rebound from the CAT. When no subsequent impact on the TICD was detected, the particles either rebounded back in the incident direction, with a waveform like that in Figure 4.5D, or rebounded at an angle larger than the angular acceptance of the detector (> 79° relative

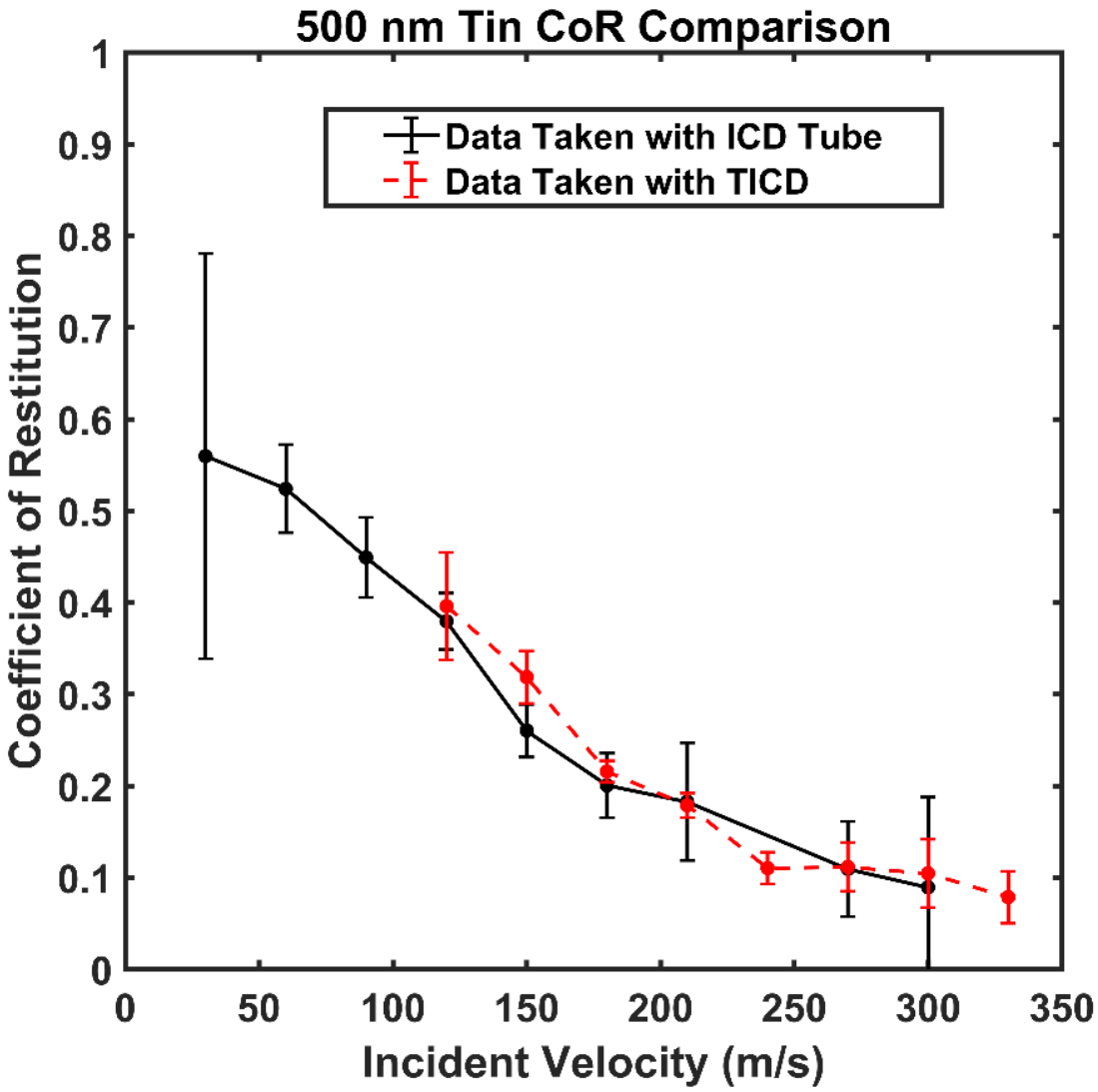

Figure 4.8*: CoR comparison between previously acquired data (black) and newly acquired data with TICD (red). The two datasets are in good agreement. The incident velocity data is grouped into 30 m/s bins where the error bars are the 95% confidence interval of a normal distribution for the CoR within each bin. Lines have been added between points to guide the eye and only connect points with no fitting.*

to the surface normal) as in Figure 4.5E.

The angular distribution peaks in the <15.9° bin around the surface normal, showing that most particles rebound backwards along the incoming particle trajectory. These results can be compared with a cos(θ) distribution expected in random desorption of particles from a surface as shown in Figure 4.9. The measured distribution is more strongly peaked along the surface normal, indicating a tendency towards more specular reflection. These results provide several interesting directions to pursue. The tin/tin oxide particles are non-spherical and can be expected to exhibit increasing inelasticity as incident particle energy is increased. Effects of this inelasticity on rebound trajectories can thus be measured with this detector. Additionally, the effect of surface roughness on the deviation of rebound trajectories from normal can be explored by changing the impact target. In the present experiments, a Mo mirror with a 20 nm surface finish was used, minimizing any effect from surface roughness, but rougher targets can be examined with the same instrumentation. To improve the angular resolution of the device for future measurements, the incident particle beam collimation will be improved. This will allow the CAT target to be reduced in area and the angular resolution of the apparatus increased significantly.

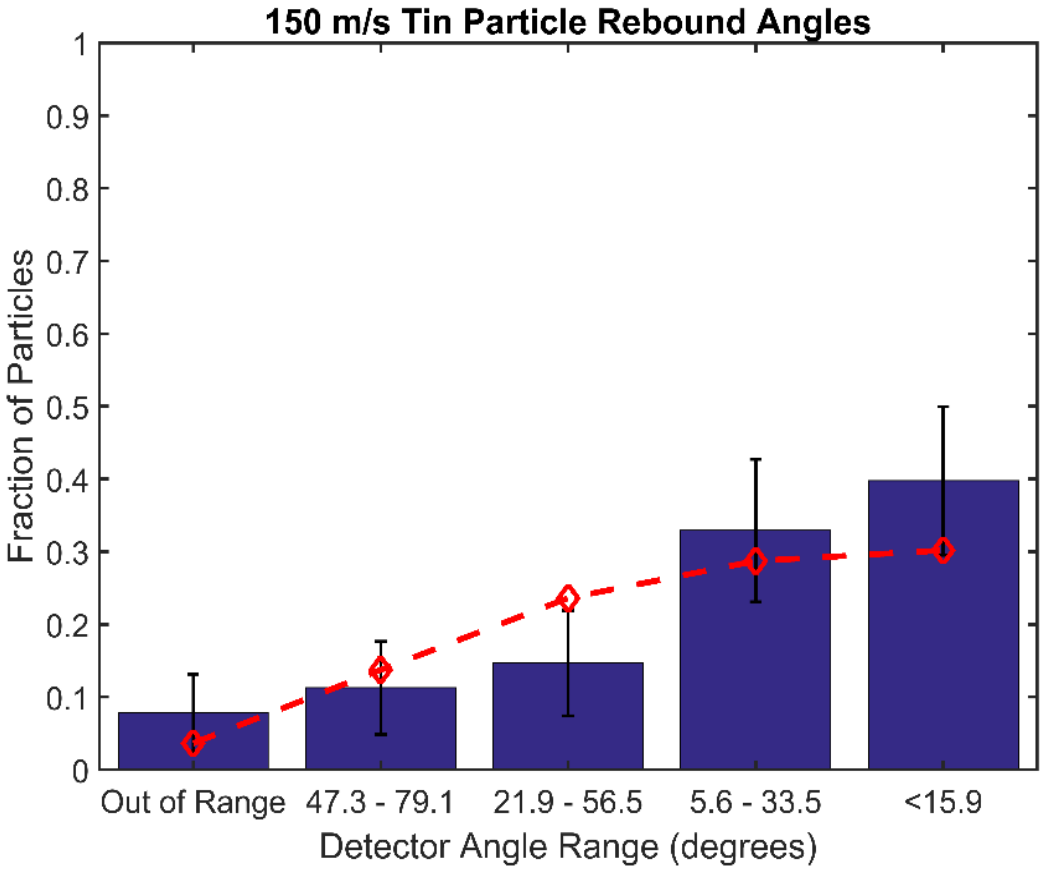

***Figure 4.9**: Analysis of tin particle rebound trajectory for particles with an incident velocity of 150 m/s (30 m/s bin). 84 particles that impacted the target were visually sorted by their rebound traces and assigned a rebound angle. The fraction of each rebound angle range is presented here with the error bars calculated as the 95% confidence of the Wilson score interval. Additionally, a normalized cosine distribution is shown (dashed red) for comparison to random desorption.*

4.4 Conclusions

A new angle-resolved ICD for charged submicron particles is reported. The detector is composed of radially symmetric elements in a tapered pattern for measuring scattered particle dynamics and is equipped with an image-charge-instrumented metallic target for detecting particle impacts. The detector has been tested using charged PSL spheres and submicron tin/tin oxide particles. Analysis of the data is presented, demonstrating measurement of particle scattering angles after impact and the determination of the CoR for energy and size-selected incident particles. Comparison to previous studies has been performed to confirm fidelity of these measurements. The ease of analysis and the variable angular ranges accessible with this flexible detector design facilitate application to studies of the impact dynamics of highly charged particles on conducting surfaces. Application of the detector to studies of the CoR of charged submicron metal particles, as presented here, constitutes the first reported examination of such species in the plastic deformation impact regime and also demonstrates the ability to measure scattering angle distributions by analysis of the post-impact trajectories. This new detection scheme builds on novel image charge detection devices previously described[21] as well as wire grid trajectory analysis detectors.[22,23] The ability to control particle composition and incident energy provided by the AIS will allow new experimental information to be collected for charged particle impact dynamics with the TICD for the evaluation of particle impact models.

Acknowledgements

Chapter 4, in full, is a reprint of the material as it appeared in Miller, M.E.C.; Mezher, M.; Continetti, R.E., Tapered image charge detector for measuring velocity distributions of submicrometer particle scattering. *Review of Scientific Instruments* 2020**,** 96 (6), 063305. The dissertation author is the primary author and the dissertation advisor is the corresponding author.

4.5 References

(1) Benner, W. H. A Gated Electrostatic Ion Trap To Repetitiously Measure the Charge and m/z of Large Electrospray Ions. *Anal. Chem* **1997**, *69* (20), 4162–4168.

(2) Keifer, D. Z.; Jarrold, M. F. Single-molecule Mass Spectrometry. *Mass Spectrom. Rev.* **2017**, *36*, 715–733. https://doi.org/10.1002/MAS.21495.

(3) Srama, R.; Srowig, A.; Rachev, M.; Grün, E.; Kempf, S.; Moragas-Klostermeyer, G.; Srowig, A.; Conlon, T.; Harris, D.; Grün, E.; Auer, S.; Glasmachers, A.; Helfert, S.; Linnemann, H.; Tschernjawski, V. Development of an Advanced Dust Telescope. In *Modern Meteor Science An Interdisciplinary View*; Hawkes, R., Mann, I., Brown, P., Eds.; Springer Netherlands: Dordrecht, 2005; pp 211–220. https://doi.org/10.1007/1-4020-5075-5_22.

(4) Gamero-Castaño, M. Induction Charge Detector with Multiple Sensing Stages. *Rev. Sci. Instrum.* **2007**, *78*, 43301. https://doi.org/10.1063/1.2721408.

(5) Doussineau, T.; Yu Bao, C.; Clavier, C.; Dagany, X.; Kerleroux, M.; Antoine, R.; Dugourd, P. Infrared Multiphoton Dissociation Tandem Charge Detection-Mass Spectrometry of Single Megadalton Electrosprayed Ions. *Rev. Sci. Instrum.* **2011**, *82* (8), 84101. https://doi.org/10.1063/1.3628667.

(6) Barney, B. L.; Daly, R. T.; Austin, D. E. A Multi-Stage Image Charge Detector Made from Printed Circuit Boards. *Rev. Sci. Instrum.* **2013**, *84* (84), 114101.

(7) Northway, P.; Auer, S.; Drake, K.; Horanyi, M.; Mocker, A.; Munsat, T.; Shu, A.;

Sternovsky, Z.; Thomas, E.; Xie, J. Characteristics of a New Dust Coordinate Sensor. *Meas. Sci. Technol. Meas. Sci. Technol* **2012**, *23* (23), 105902–105906. https://doi.org/10.1088/0957-0233/23/10/105902.

(8) Auer, S.; Grün, E.; Kempf, S.; Srama, R.; Srowig, A.; Sternovsky, Z.; Tschernjawski, V. Characteristics of a Dust Trajectory Sensor. *Rev. Sci. Instrum.* **2008**, *79* (127), 84501. https://doi.org/10.1063/1.2960566.

(9) Auer, S.; Grün, E.; Srama, R.; Kempf, S.; Auer, R. The Charge and Velocity Detector of the Cosmic Dust Analyzer on Cassini. *Planet. Space Sci.* **2002**, *50*, 773–779.

(10) Adamson, B. D.; Miller, M. E. C.; Continetti, R. E. The Aerosol Impact Spectrometer: A Versatile Platform for Studying the Velocity Dependence of Nanoparticle-Surface Impact Phenomena. *EPJ Tech. Instrum.* **2017**, *4* (1), 2. https://doi.org/10.1140/epjti/s40485-017-0037-6.

(11) Wall, S.; John, W.; Wang, H.-C.; Goren, S. L. Measurements of Kinetic Energy Loss for Particles Impacting Surfaces. *Aerosol Sci. Technol.* **1990**, *12* (4), 926–946. https://doi.org/10.1080/02786829008959404.

(12) Tsai, C.-J.; Pui, D. Y. H.; Liu, B. Y. H. Capture and Rebound of Small Particles Upon Impact with Solid Surfaces. *Aerosol Sci. Technol.* **1990**, *12* (3), 497–507. https://doi.org/10.1080/02786829008959364.

(13) Cassina, L.; Cattadori, C.; Giachero, A.; Gotti, C.; Maino, M.; Pessina, G. GeFRO : A New Charge Sensitive Amplifier Design for Wide Bandwidth and Closed-Loop Stability Over Long Distances. *IEEE Trans. Nucl. Sci.* **2014**, *61* (3), 1259–1268.

(14) John, W.; Reischl, G.; Devor, W. Charge Transfer to Metal Surfaces from Bouncing Aerosol Particles. *J. Aerosol Sci.* **1980**, *11*, 115–138. https://doi.org/10.1016/0021-8502(80)90029-4.

Chapter 5. Impact Dynamics of Submicron Tin Particles

5.1 Introduction

Both in nature and manufacturing, particles below 1 μm diameter have important uses in and a significant effect on a variety of processes. These include the effects of environmental aerosols on cloud formation and weather, the degradation of materials in space from micro-meteorite impacts, and dust contaminants in clean rooms that lead to manufacturing defects. One such contamination process occurs in extreme ultraviolet (EUV) photolithographic manufacturing where tin metal contaminants introduced from a laser-produced plasma[1] degrade sensitive systems and optics. Designing mitigation strategies for this debris requires understanding of tin particle dynamics when bouncing and sticking to surfaces within the apparatus at velocities of 150-500 m/s. In order to acquire fundamental information regarding the physics of submicron particle scattering the Aerosol Impact Spectrometer (AIS) was used to study the scattering of individual charged submicron tin particles as a function of incident velocity.

The experimental technique used provides an approach to understanding the dynamics and material properties that affect particle sticking to and rebounding from surfaces, something that has been an area of interest for a wide range of applications. Examination of the scattering dynamics, particularly for submicron particles has mostly been theoretical, without consistent experimental validation of proposed models and systems. Experimental observation of impact dynamics has proven challenging for particles below optical detection thresholds and many

studies that record in situ behavior do so for species > 1 μm in size.[2–5] Particle rebound behavior is often described by the coefficient of restitution (CoR) of a collision, defined as the ratio of the rebound and incident velocities. Indirect observations of impact behavior at the nanoscale have also been reported using extrapolations and modeling to determine particle velocities that are otherwise challenging to detect.[6–8] Previous work and modeling at the nanoscale is particularly focused on understanding the effects of nanoscale properties on collisions normally described with continuum mechanics. Therefore, most of these studies have been confined to collisions of particles < 100 nm in diameter where deviations from bulk material properties have been noted.[9,10] Examination of particles in the 100-1000 nm diameter range provides information about the transition from a bulk description of particle properties down into the nanoscale. In this work we demonstrate the use of the AIS[11] to characterize the dynamics of submicron tin particle impacts of varying size and incident energies as relevant to contamination in industrial processes. The inelasticity of these collisions as a function of incident energy and size is examined in addition to the average scattering angle from a polished molybdenum target surface. A simple model is applied to the CoR data to extrapolate a size-dependent material property effect that matches the effects previously seen in nanoparticles of different size ranges. An empirical size-dependent scaling for the CoR and angular distributions of particle rebounds is also presented, normalizing the size dependence in terms of ratio of the incident kinetic energy and the nanoparticle impact contact area.

5.2 Experimental Methods

The operation of the AIS to produce, characterize, and accelerate particles is detailed in Chapter 2 and ref. [11], and is briefly reviewed here for application to tin particles. Electrospray ionization (ESI) is used to aerosolize and charge individual tin particles of diameters 150-500 nm. Powders of 150 nm, 300 nm, and 500 nm tin particles (Millipore Sigma and US Research Nanomaterials Inc.) were suspended in 1:1 mixtures of 25 mM aqueous ammonium acetate and HPLC-grade methanol, with final particle densities of 4.1e10, 9.5e9, and 3.2e9 particles-per-milliliter, respectively. Once injected, the particles pass through a heating chamber at ~10 Torr, heated to 250°C to desolvate the particles, then pass through an aerodynamic lens to focus and collimate the beam. The resulting charged particle beam is energy selected with a quadrupole deflector, deflecting particles of a selected kinetic energy-per-charge into a linear electrostatic ion beam trap[12] for characterization.

In the linear electrostatic ion beam trap, single particles typically holding thousands of fundamental charges (positive) oscillate between two electrostatic mirrors in vacuum (~μTorr). The oscillation of single particles is detected with an image charge detector (ICD) and the mass and charge of each particle is determined using charge detection mass spectrometry (CDMS). In addition to in situ analysis of individual particles used in this characterization, samples of particles injected into the apparatus were collected using strips of carbon tape and analyzed for composition and oxide layer. For particles collected within the apparatus, a thin (~10 nm) oxide layer was observed along with significant variation in particle size for each nominal powder size. Because of the heterogeneity in the initial tin powder samples, the mass information obtained with CDMS is used to select for specific particle diameters with an assumption of the

bulk tin density. Individual particles of each selected diameter (150, 300, and 500 nm) are released and accelerated using a linear accelerator (LINAC). A range of potentials on the LINAC allowed particles to be accelerated to velocities between 125-450 m/s (0 to 55 keV acceleration potentials).

5.3 Results

Accelerated particles are impacted onto a highly polished (< 20 nm surface finish) molybdenum target (5x5 mm square), a material of interest in the EUV photolithographic light source. The incident velocity of single particles was measured using two different ICDs located before the target: a tubular ICD (as in ref. 11) was used with 150 nm tin particles and a tapered ICD (as in ref. [13]) was used with 300/500 nm tin particles. The rebound velocity of all three species was recorded for particles rebounding through the same ICD, and angle-resolved measurements of particle rebound trajectories were recorded for 300/500 nm particles using the tapered ICD. The measurements made with these two types of detectors has previously been shown to be in agreement.[13]

The CoR of each collision was measured and an ensemble average of each particle size was produced from the single-particle data. These data are summarized in Figure 5.1 with the average CoR for each particle size grouped by incident velocity. As previously observed in different particle materials within this velocity range,[3,5,11,14] as incident velocity increases the average CoR decreases until particles cease rebounding from the surface. This trend is consistent with the particle losing a greater fraction of the incident kinetic energy at higher impact velocities. As particle velocity increases, the likelihood of rebounding from the impact

target decreases progressively until no rebounds are detected, seen here for particles with incident velocities > 425 m/s. On average, the CoR curves decrease as the incident particle mass increases, with less significant difference at higher impact velocity.

In addition to CoR data collected for 150 nm, 300 nm, and 500 nm diameter tin particles, additional scattering angle information was collected for the two larger particle diameters. The fraction of particles that rebound as a function of velocity is plotted for different rebound angular ranges in Figure 5.2. For both 300 nm and 500 nm particles there is a critical velocity range where particles begin to stick and discharge through the target. Again, there is a difference in the behavior of the two particle diameters, significantly in the cases of frame b and f. The onset of particles sticking to the target occurs at higher velocity for the smaller 300 nm particles. The significance of the size-dependent differences noted in both the angular rebound behavior and the CoR is explored in more detail in the following section.

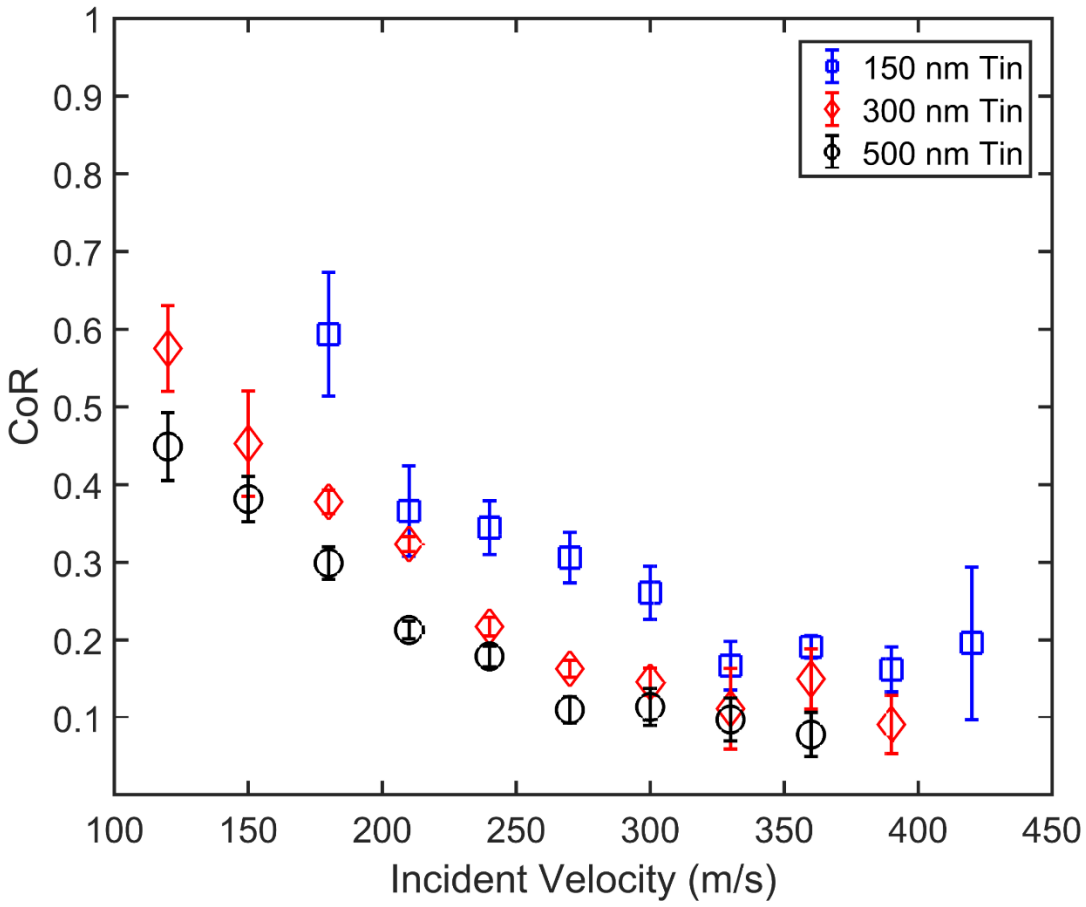

Figure 5.1: *CoR measurements of 150, 300, and 500 nm diameter tin particles. Incident velocity is grouped into 30 m/s bins, with the average CoR within that velocity range marked by a point. The error bars constitute the 95% confidence interval for the CoR measured in each velocity bin. The minimum number of particles in each bin is 2. The total number of events collected for each particle size is as follows: 150 nm – 75, 300 nm – 675, and 500 nm – 464.*

Figure 5.2: *Measurement of particle rebound trajectory as a function of incident velocity for 300 nm and 500 nm tin particles. a) Fraction of particles that rebound through the TICD without hitting a detector element. b) Fraction of particles that rebound and impact the inner detector element. c) Fraction of particles that rebound and impact the middle detector element. d) Fraction of particles that rebound and impact the outer detector elements. e) Fraction of particles that rebound outside of the outer element detection limit. f) Fraction of particles that impact and stick to the target, discharging through the target detector.*

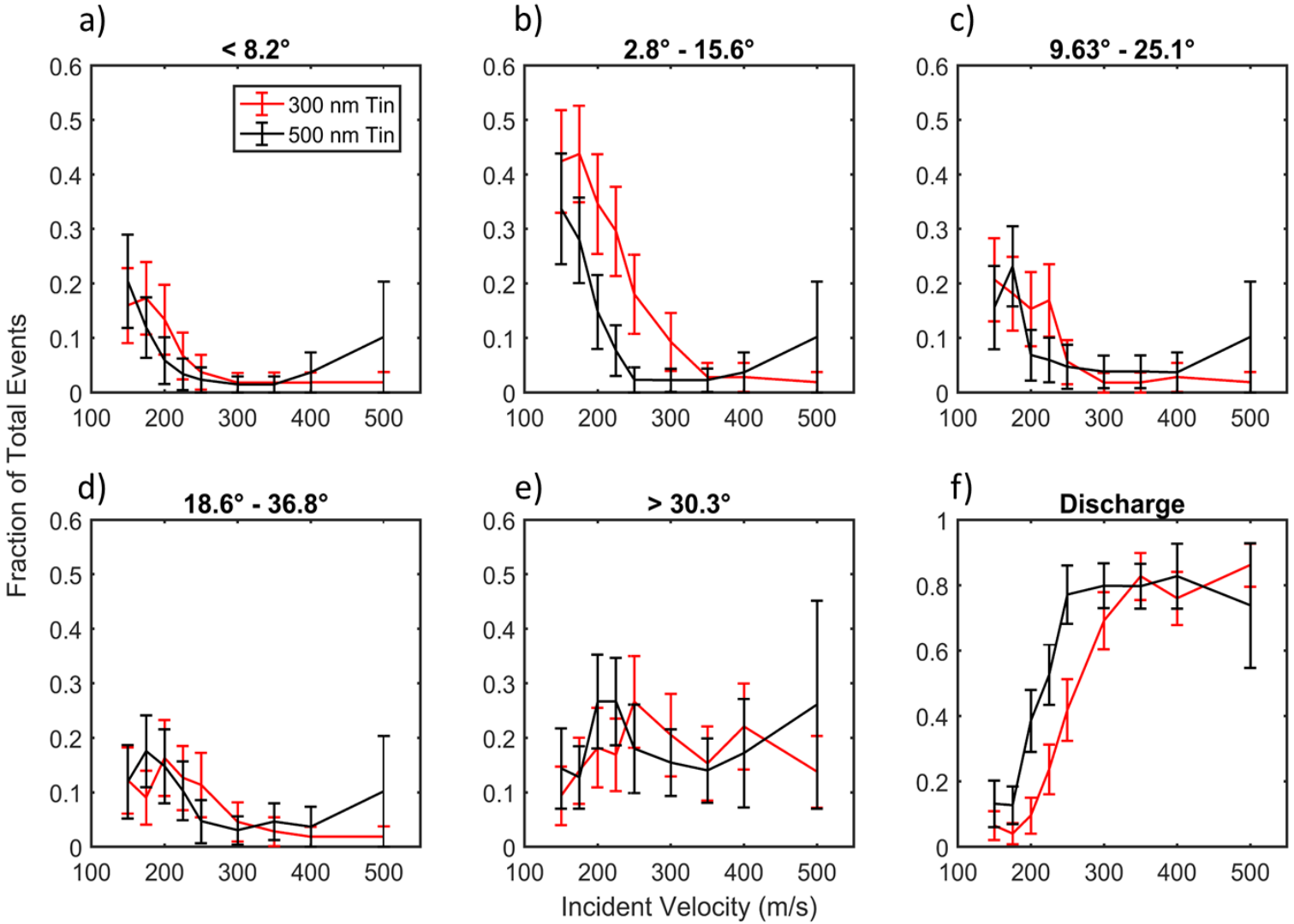
a)
< 8.2°
b)
2.8° - 15.6°
c)
9.63° - 25.1°
d)
18.6° - 36.8°
e)
> 30.3°
f)
Discharge
300 nm Tin
500 nm Tin
Fraction of Total Events
Incident Velocity (m/s)

5.4 Discussion

In the following sections, a model is applied to extract material properties from the CoR data collected, specifically the size dependent yield strength of the tin metal nanoparticles. Additionally, the post-impact behavior of the tin particles is scaled using an empirically determined scaling factor. This factor is based on particle energy and contact area and scales the differences in sticking observed for particles on the impact target as well as the CoR data.

5.4.1 Modeling of CoR Data

In order to understand the CoR measurements collected for the three sizes of tin metal particles a model based on the elastic component of the scattering was applied to the data. This model is referred is an application of Hertzian contact model, and has previously been applied to a particle-surface interactions.[3,15] The model allows the CoR to be represented by three material parameters of the system: Young's modulus (of both the particle and target), the Poisson ratio that governs material deformation (of both the particle and the target), and the yield strength (of the particle). Generally, the yield strength of either the particle or surface is selected based on which is more likely to deform first. In the analysis presented here the more plastic material, tin, the particle with lower bulk value for yield strength compared to the target molybdenum was selected. The model represents the CoR as:

$$CoR = \left(1 - \frac{K_L}{K_i}\right)^{\frac{1}{2}} \tag{5.1}$$

Here, K_L is the kinetic energy change due to loss mechanisms in the system and K_i is the initial kinetic energy of the particle. At lower velocities a variety of factors have a significant effect on the kinetic energy loss in the system and many models exist for aspects of this behavior.[16] However, at the relatively high velocities used in the system under study, plastic deformation becomes the dominant mechanism of inelasticity. Therefore we can define K_L as being equal to K_P (the loss of kinetic energy due to plastic deformation).

Bitter[17] defined K_P in terms of the initial kinetic energy of the system (K_i) and a critical yield velocity (v_y) representing the onset of plastic deformation:

$$K_P = \left[\left(K_i - \frac{K_y}{16}\right)^{\frac{1}{2}} - \left(\frac{15K_y}{16}\right)^{\frac{1}{2}}\right]^2 \tag{5.2}$$

Here, K_y is the kinetic energy associated with the critical velocity, $K_y = \frac{1}{2}m_p v_y^2$. As shown in Bitter, the critical velocity is defined from the limit of a Hertzian treatment of a purely elastic impact:

$$v_y = \left(\frac{2\pi}{3K}\right)^2 \left(\frac{2}{5\rho}\right)^{\frac{1}{2}} Y^{\frac{5}{2}} \tag{5.3}$$

Here $K = 4/3\left(\kappa_p + \kappa_t\right)$ where $\kappa_i = (1 - v_i^2)/\xi_i$, where v_i is the Poisson ratio of both the particle and target, ξ_i is the Young's modulus of both the particle and the target, ρ is the density of the particle, and Y is the yield strength of the particle. With this model it is possible to calculate the CoR as a function of incident particle energy, the yield strength of the particle, the Young's modulus of both the particle and the target, the Poisson ratio of both the particle and the target, and the density of the particle.

The CoR data measured for each particle size can be compared to the predictions of the Hertzian model to allow the extraction of material properties of the submicron tin particles. The incident kinetic energy for each individual particle was calculated from the measured particle incident velocity and mass. The nominal masses for particles in these size ranges are as follows: 150 nm, 1.29e-17 kg; 300 nm, 1.03e-16 kg; and 500 nm, 4.77e-16 kg. The mass for each size particle was calculated using the bulk density for alpha tin,[18] 7.29 g/cm^3, which is also used for particle density in Equation 5.3. Although the individual mass was measured for every particle trapped in the linear electrostatic trap, at the time of this study individual particles could not be correlated to individual impact events recorded on the tapered image charge detector. The masses above are a good measure of the ensemble average mass for particles studied since the masses were selected by CDMS to correspond to diameters within 10% of 150, 300, and 500 nm particles. In addition to the CoR information and incident kinetic energy for each particle impact, several bulk materials parameters were used in the model. The bulk values of Young's modulus (330 GPa) and the Poisson ratio (0.32) for molybdenum[19] were selected as the target material parameters. The material properties of the submicron tin particles within this experiment are of primary interest. Previous work has demonstrated that bulk Young's modulus of materials is applicable to particles as small as ~20 nm.[20] This consistent Young's modulus (and by extension the Poisson ratio) is in stark contrast to previous studies of size dependence in particle yield strength for materials less than a micron in size.[9,10,15,21,22] Most studies have examined material yield strength with traditional loading tests that induce strain over long time scales unlike those involved in high velocity impact systems, with the exception of Rennecke and Weber.[15] In high velocity impacts, quantifying the yield strength of the materials involved becomes more challenging as this property become dynamic with the high strain rates involved

in a collision ($> 10^6$ s^{-1}).[5,23] The effect of these dynamic processes is challenging to account for with the simple model presented here, therefore the yield strength calculations presented measure an effective material yield strength for the collisions, comparable to the work of Rennecke and Weber.[15]

Initial fitting of the model to Equation 5.1 (using Equations 5.2 and 5.3) was performed using the CoR data measured for all three diameters of tin particles. A non-linear least squares algorithm implemented in MATLAB[24] was used to fit the model with particle yield strength, Poisson ratio, and Young's modulus as free parameters. Although the Poisson ratio and Young's modulus were used as free parameters to allow the best fit possible to the data, tight constraints were placed on these two parameters so as not to deviate significantly from bulk values while yield strength was examined over a broad range. Specifically, Young's modulus was constrained between 40 and 50 MPa, the Poisson ratio was constrained between 0.3 and 0.4, and the yield strength was constrained between 0.01 and 100 GPa. Values found for Young's Modulus and the Poisson ratio for each particle size all compare well with each other and are very close to the expected bulk values (45 MPa and 0.33).[19] It was found that the best-fit values of yield strength differed significantly for each size particle: 150 nm, 16.1 GPa; 300 nm, 13.4 GPa; and 500 nm, 12.0 GPa. Results of the fit are listed in Table 5.1 and plotted in Figure 5.3.

The fits performed using the model described above are compared to the measured CoR data for each particle size in Figure 5.3. With this model a full understanding of the impact dynamics and various contributions to energy loss during the collision is not feasible. Theoretical investigations and modeling of different impact effects including inelastic processes such as thermal, surface, and frictional effects have been carried out and generalized

for a wide variety of particle sizes.[4,16,25,26] In addition to these effects, material properties that may be size-dependent are needed to accurately apply these models. The Hertzian model applied here consistently under-predicts the inelasticity (higher CoR) at velocities greater than ~200 m/s and over-predicts inelasticity at velocities less than ~200 m/s for the three particles sizes. However, the model is useful as it allows for the extraction of an approximate yield strength for each particle size that best fits the measured CoR data. The physical significance of the yield strength calculated here is most useful for quantifying size-dependent trends in particle behavior, rather than an absolute value for the stress and strain the particle experiences during collision. Yield strength is known to be dynamic in high-strain situations[23] and the values calculated here represent a trend characterization of the behavior for each particle size under the high-strain of an impact. In addition to being useful for characterizing the size-dependent behavior observed here, previous modeling of nanoscale (<100 nm) platinum and silver metal particle impacts at similar velocities has used a similar approach for calculating the yield strength,[15] allowing a comparison across three different metal types of submicron particles: tin, platinum, and silver. Critical velocity in these experiments was extracted from changes in charge deposition, rather than measures of CoR.

Examination of the dependence of the best-fit yield strength on particle size is plotted in Figure 5.4. A trend line for the three sizes of tin measured was fit, and the particle diameter scaling was determined to be $\sim d^{-0.24}$. Previous work examining the size dependence of material yield strength in sub-micron systems[9,10,15,21] has found different diameter-based dependency in yield strength depending on the measurement technique used. The experimental techniques used have included indentation testing applied to the nanoscale and observed with electron microscopy (SEM and TEM),[9,10] axial straining of nanopillars under TEM observation,[21] as

***Table 5.1**: Results of model fit to CoR data for each particle size.*

Particle Size	Yield Strength	Young's Modulus	Poisson Ratio
150 nm	16.1 GPa	44.5 MPa	0.33
300 nm	13.4 GPa	44.7 MPa	0.33
500 nm	12.0 GPa	44.7 MPa	0.33

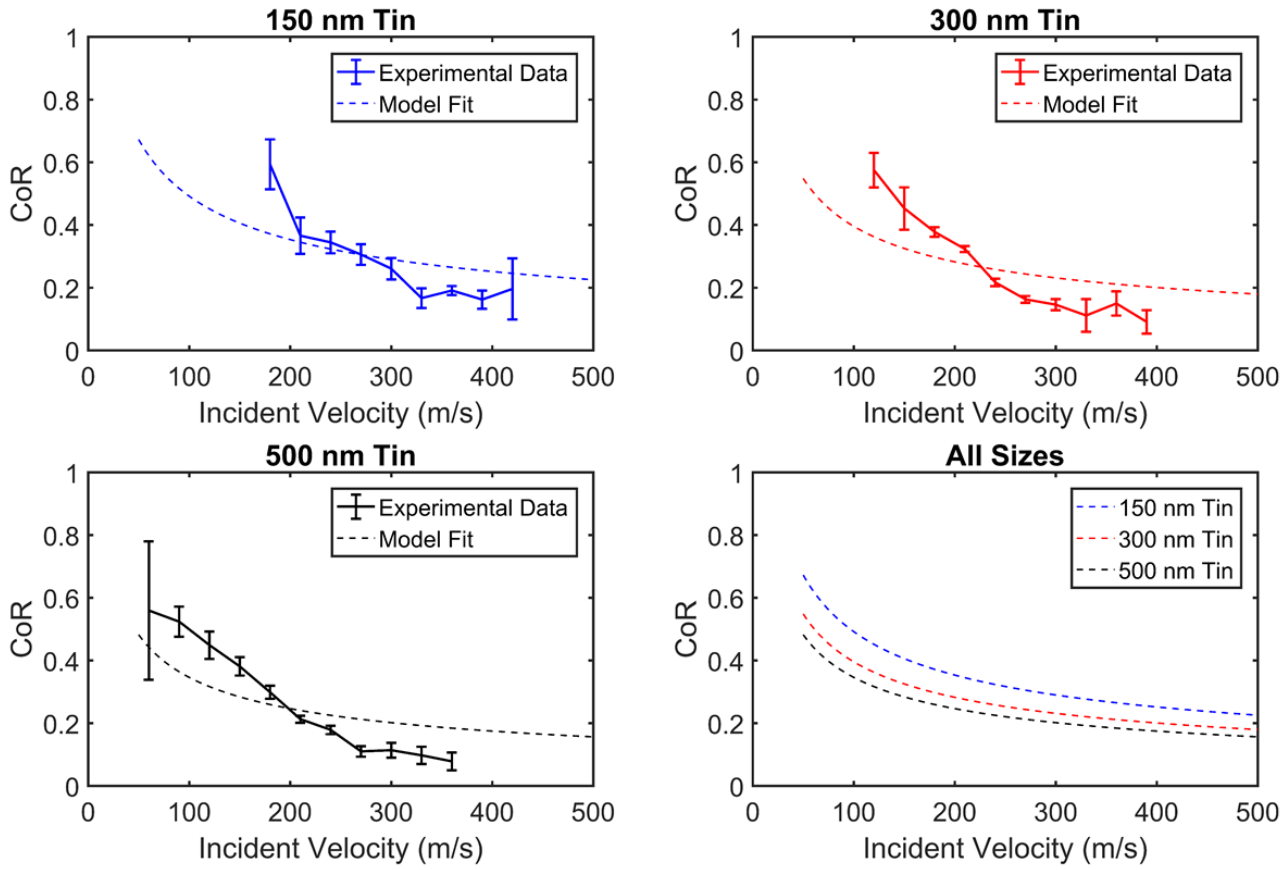

Figure 5.3: *CoR trends fit with Hertzian contact model for 150 nm, 300 nm, and 500 nm diameter tin particles. Least squares fits made by varying Young's modulus, the Poisson ratio, and yield strength was performed for each particle size.*

well as measurements derived from nanoparticle impacts with a surface.[15] Traditional indentation testing and axial strain systems involve the slow application of strain to the system and are unable to account for the high strain rates experienced during a collision. The calculations performed by Rennecke and Weber on platinum and silver however, are similarly derived from collisional experiments and are therefore comparable to the measurement described here for tin. Rennecke and Weber used measurements of charge transfer in nanoparticles accelerated in a single-stage-low-pressure-impactor to determine particle critical velocity. The critical velocity observation was used to then calculate the yield strength Equation 5.3 assuming bulk values for Poisson ratio and Young's modulus. The yield strengths of their nanomaterial systems are not only on the same order as the yield strength measured here, but also follow a similar diameter scaling trend ($\sim d^{-0.25}$). Comparison of the behavior observed by Rennecke and Weber and this work is presented in Figure 5.4 where the trend lines are extrapolated to overlap the distinct size regimes of their experiments on platinum and silver and the current experiments on tin. The two methodologies employed to calculate yield strength of the materials (measurements of CoR with fitting and measurements of critical velocity through charge transfer) produce very similar trends. Consistency between the two methods employed and the two size regimes studied indicates that future experiments can use multiple methods to extract this material property. Additionally, the scaling of all metals measured is consistent from nanomaterials to submicron material sizes allowing extrapolation of material properties from one size regime to the other.

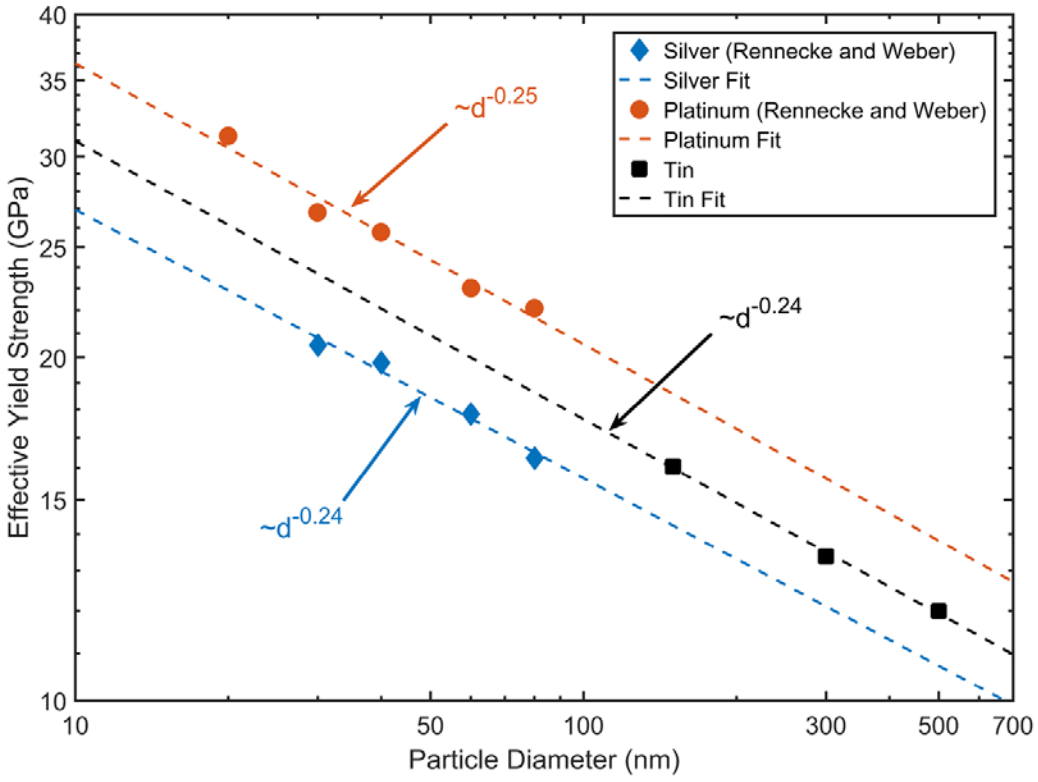

***Figure 5.4**: Comparison of the size dependent fit of particle yield on tin and the study in ref. 15 on Pt and Ag.*

5.4.2 Scaling Particle Rebound Angular Measurements

In addition to the CoR measurements analyzed in the above section, angular scattering information was collected for two different diameter tin particles. To the best of our knowledge no exist studies of the scattering behavior of submicron metal particles rebounding from normal incidence onto a surface, thus the information collected here is unique. Within the angular distribution data, it is of particular note that the two diameter tin particles examined appear to follow a similar trend, but distinctly offset in rebound angular behavior. This is most readily observed in Figure 5.2b and 5.2f. In order to examine the progression of this difference for the velocities measured, integrated bounce and sticking behavior for 300 nm and 500 nm tin are plotted in Figure 5.5. For particles rebounding from the target (Figure 5.2a-e), the total fraction of 300 nm particles is compared to the total fraction of 500 nm particles in Figure 5.5.

The two different particle sizes converge to an asymptotic behavior at higher velocities but are distinctly offset for the majority of the velocity range measured. At higher velocities neither particle size always sticks to the target, but rather both converge to an ~80% probability of sticking to the target. Most events that do not stick to the target at higher velocities rebound with a high angle relative to the detector centerline or are otherwise not detected by the image charge detector (events described in Figure 5.2e). It is hypothesized that these high velocity events correspond to the particles beginning to break apart, behavior observed for large micron-sized tin particles at higher velocities.[4] Upon fragmentation, individual fragment charges may be below the limit of detection with the image charge detector. At high velocity significant

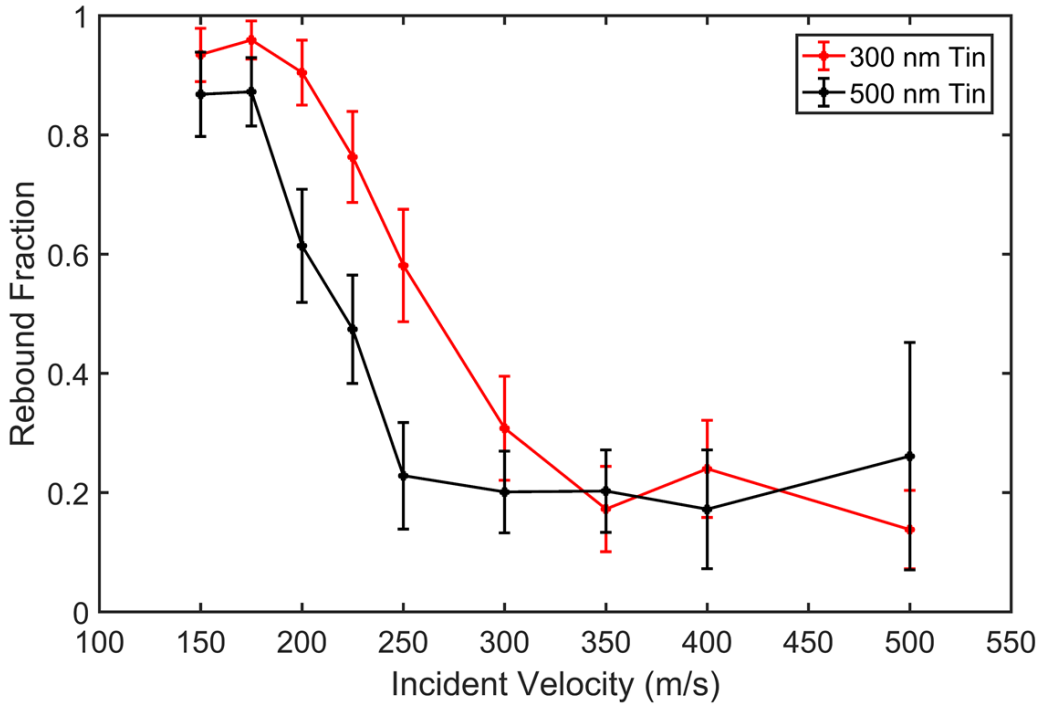

Figure 5.5*: Comparison of rebound behavior for 300 nm and 500 nm tin particles plotted as a function of incident particle velocity. The sticking fraction (the other possible behavior observed) is the inverse of this plot.*

deformation of the particle is expected and the rebound behavior of a non-spherical deformed particle may lead to increased high angle scattering.

Previous studies of larger particles (~10 μm) have explored the capture mechanism on a surface. As observed optically with high speed imaging by Xie et al. and Hassani-Gangaraj et al., progressive flattening of the material eventually leads to capture by the surface. This flattening is indicative of the dynamic changes within the material during the collision where large regions of plasticity (localized melting) in the particle become the primary contributor to inelastic rebounds. Hassani-Gangaraj et al.[4] examined the post-impact shape and behavior of ~10 μm tin metal particles. With these larger species, capture of the particles by a surface was observed between 300-500 m/s. The primary mechanism for particle capture was observed to be melting of the sphere from partial conversion of the impact energy to heat. This heat drives the initially spherical particle into a half-ellipsoid shape with a contact area of $A_C = \pi d^2/2$, where d is the initial diameter of the particle. A variety of behaviors were observed around this impact velocity regime including scattering from the surface at lower velocities, sticking to the surface, and material splashing at higher velocities.

The striking size dependence in the rebound angular distributions for 300 and 500 nm diameter tin, as well as the CoR data in the 150-500 nm diameter size range is something previously unobserved for metals in this size regime. Hertzian contact modeling provides a rationalization for the size dependence of the CoR, but extension of that model to the rebound angular and fractional sticking results reported here are beyond the scope of this work. However, an empirical normalization of the size dependence of these observables is found in the data. Instead of plotting the observables as a function of the incident velocity, in Figure 5.6 they are plotted in terms of the incident kinetic energy divided by the predicted final contact

area assuming complete deformation ($\pi d^2/2$). This empirical scaling rule not only normalizes the fractional behavior of particle rebound and sticking between 300 nm and 500 nm tin particles, but also scales all three diameter CoR measurements to statistically similar values as shown in Figure 5.6. If the incident kinetic energy of the particle is divided by the predicted final contact area, as done in Figure 5.6a, the rebound fraction (and therefore also the sticking fraction) of the two particle sizes converge together to become statistically identical. The rebound behavior observed here has a finite range over which rebound fractions decreases. This range is nearly identical when scaled by incident kinetic energy/contact area for the 300 and 500 nm diameter tin particles, reaching a minimum fraction of rebounding events at ~40 J/m^2. Although this scaling works remarkably well for the submicron particle sizes measured here, it does not appear to apply to larger particles. In the work of Hassani-Gangaraj et al. a measured sticking velocity of ~375 m/s for 9 μm diameter tin particles would correspond to ~1540 J/m^2. The use of contact area to normalize the behavior of submicron particles rebounding from a surface provides a simple way to model the inelastic processes in particle-surface collisions. As noted earlier, these inelastic processes include heating, melting and fragmentation, and for submicron tin particles these phenomena are complicated by the fact that the 10 nm tin oxide surface layer becomes an increasingly important fraction of the total volume of the particle as the size decreases. Nonetheless, it can be seen in Figure 5.6b that this same scaling applies well to the CoR measurements including particles down to a 150 nm diameter. Further investigation of this phenomenon in other metals will be of interest as universal models for submicron particle scattering are developed.

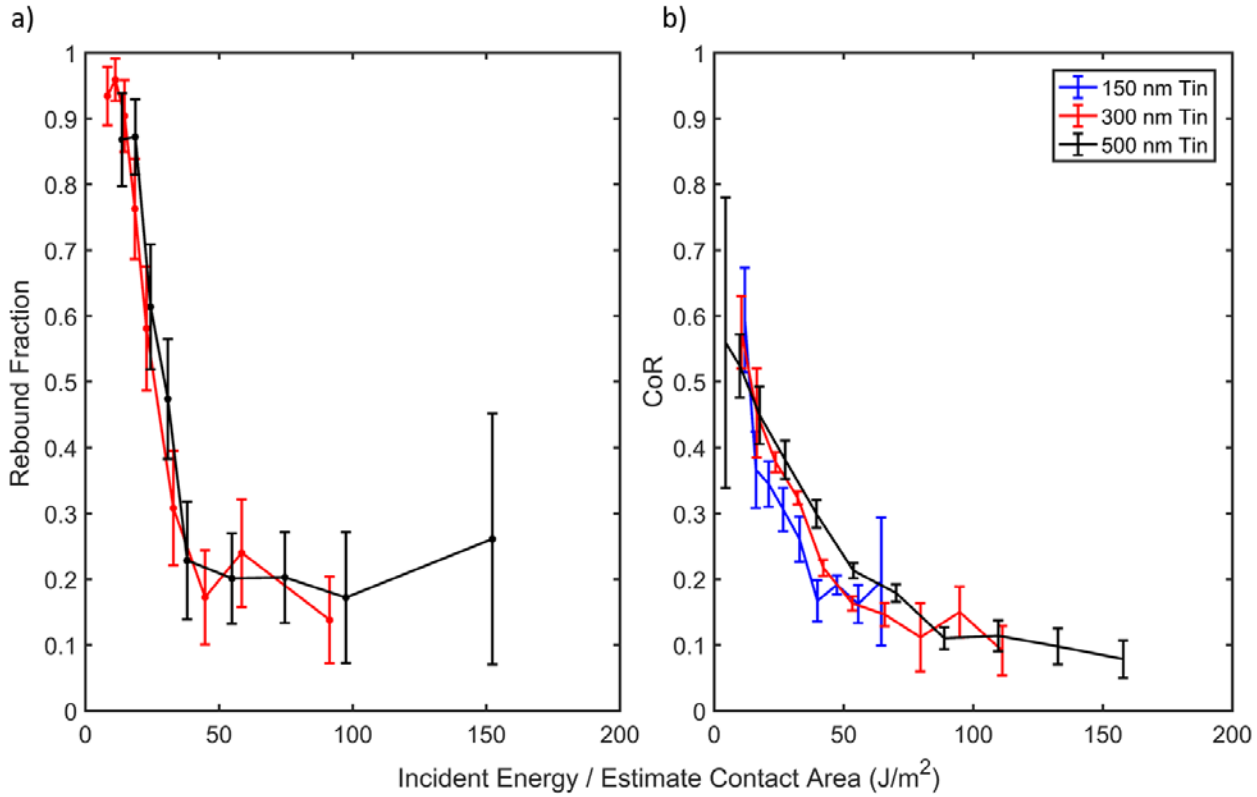

Figure 5.6: *Empirical normalization of the size dependence of particle rebound, sticking and CoR data as a function of the incident kinetic energy divided by the predicted final contact area. a) Fraction of 300-500 nm diameter particles that bounce from the target. b) Particle CoR in the 150, 300 and 500 nm diameter size range.*

5.5 Conclusion

The Aerosol Impact Spectrometer equipped with an angle-resolved image charge detector has allowed the CoR and rebound angular distributions for tin particles of 150, 300 and 500 nm diameter to be measured over an impact velocity range of 50 – 450 m/s. The size-dependent behavior observed in the CoR data has been attributed to differences in particle impact yield strength using a simple Hertzian model. Additionally, the rebound behavior of two different sizes of tin particles has been examined and a scaling in terms of incident kinetic energy-per-contact-area has been shown to normalize the rebound and CoR data over the submicron size range investigated here. The experiments reported here constitute the first reported measurements of submicron metal particle rebound dynamics with scattering angle sensitivity. With the methods outlined here, further examination of particle properties can be performed from microns to hundreds of nanometer in size where the transition from bulk properties to microscopic properties becomes important. The measure of effective impact yield strength for a given target-particle pair provides insight into the inelastic dynamics of particles upon collision with a surface. Additionally, the observation of a sticking velocity significantly lower than previously seen for larger metal particles and identification of a scaling method to rationalize the size-dependent scattering dynamics of submicron particles demonstrates the difference in behavior across an order of magnitude in size across the submicron regime. The versatile electrospray ionization particle source used in the Aerosol Impact Spectrometer allows for the extension of measurements examining the onset of particle sticking in other particle/target material pairs in the submicron particle range. The study here allows for more

accurate modeling and prediction of the transport of particulate contamination in complex industrial processes such as EUV lithography.

Acknowledgements

Chapter 5 is a manuscript in preparation with authors Miller, M.E.C.; Mezher, M.; De Dea, S.; Continetti, R.E., with the working title Size-dependent Coefficient of Restitution Phenomena for Submicron Tin Particles. The dissertation author is the primary author and the dissertation advisor is the corresponding author.

5.6 References

(1) Brandt, D. C.; Fomenkov, I. V.; Lercel, M. J.; La Fontaine, B. M.; Myers, D. W.; Brown, D. J.; Ershov, A. I.; Sandstrom, R. L.; Bykanov, A. N.; Vaschenko, G. O.; Böwering, N. R.; Das, P.; Fleurov, V. B.; Zhang, K.; Srivastava, S. N.; Ahmad, I.; Rajyaguru, C.; De Dea, S.; Dunstan, W. J.; Baumgart, P.; Ishihara, T.; Simmons, R. D.; Jacques, R. N.; Bergstedt, R. A.; Porshnev, P. I.; Wittak, C. J.; Woolston, M. R.; Rafac, R. J.; Grava, J.; Schafgans, A. A.; Tao, Y. Laser Produced Plasma EUV Sources for Device Development and HVM. *Extrem. Ultrav. Lithogr. III* **2012**, *8322* (March 2012), 83221I. https://doi.org/10.1117/12.916521.

(2) Dahneke, B. The Capture of Aerosol Particles by Surfaces. *J. Colloid Interface Sci.* **1971**, *37* (2), 342–353. https://doi.org/10.1016/0021-9797(71)90302-X.

(3) Wall, S.; John, W.; Wang, H.-C.; Goren, S. L. Measurements of Kinetic Energy Loss for Particles Impacting Surfaces. *Aerosol Sci. Technol.* **1990**, *12* (4), 926–946. https://doi.org/10.1080/02786829008959404.

(4) Hassani-Gangaraj, M.; Veysset, D.; Nelson, K. A.; Schuh, C. A. Melt-Driven Erosion in Microparticle Impact. *Nat. Commun.* **2018**, *9* (1), 5077. https://doi.org/10.1038/s41467-018-07509-y.

(5) Xie, W.; Alizadeh-Dehkharghani, A.; Chen, Q.; Champagne, V. K.; Wang, X.; Nardi, A. T.; Kooi, S.; Müftü, S.; Lee, J.-H. Dynamics and Extreme Plasticity of Metallic Microparticles in Supersonic Collisions. *Nat. Sci. Reports* **2017**, *7*, 5073. https://doi.org/10.1038/s41598-017-05104-7.

(6) Ayesh, A. I.; Brown, S. A.; Awasthi, A.; Hendy, S. C.; Convers, P. Y.; Nichol, K. Coefficient of Restitution for Bouncing Nanoparticles. *Phys. Rev. B - Condens. Matter Mater. Phys.* **2010**, *81* (19). https://doi.org/10.1103/PhysRevB.81.195422.

(7) Rennecke, S.; Weber, A. P. The Critical Velocity for Nanoparticle Rebound Measured in a Low Pressure Impactor. *J. Aerosol Sci.* **2013**. https://doi.org/10.1016/j.jaerosci.2012.12.007.

(8) Schöner, C.; Rennecke, S.; Weber, A. P.; Pöschel, T. Introduction of a New Technique to Measure the Coefficient of Restitution for Nanoparticles. *Chemie-Ingenieur-Technik* **2014**, *86* (3), 365–374. https://doi.org/10.1002/cite.201300132.

(9) Kim, J. Y.; Greer, J. R. Tensile and Compressive Behavior of Gold and Molybdenum Single Crystals at the Nano-Scale. *Acta Mater.* **2009**, *57* (17), 5245–5253. https://doi.org/10.1016/j.actamat.2009.07.027.

(10) Nowak, J. D.; Beaber, A. R.; Ugurlu, O.; Girshick, S. L.; Gerberich, W. W. Small Size Strength Dependence on Dislocation Nucleation. *Scr. Mater.* **2010**, *62* (11), 819–822. https://doi.org/10.1016/j.scriptamat.2010.01.026.

(11) Adamson, B. D.; Miller, M. E. C.; Continetti, R. E. The Aerosol Impact Spectrometer: A Versatile Platform for Studying the Velocity Dependence of Nanoparticle-Surface Impact Phenomena. *EPJ Tech. Instrum.* **2017**, *4* (1), 2. https://doi.org/10.1140/epjti/s40485-017-0037-6.

(12) Benner, W. H. A Gated Electrostatic Ion Trap To Repetitiously Measure the Charge and m/z of Large Electrospray Ions. *Anal. Chem* **1997**, *69* (20), 4162–4168.

(13) Miller, M. E. C.; Mezher, M.; Continetti, R. E. Tapered Image Charge Detector for Measuring Velocity Distributions of Submicrometer Particle Scattering. *Rev. Sci. Instrum.* **2020**, *91* (6), 063305. https://doi.org/10.1063/1.5142207.

(14) Dahneke, B. Further Measurements of the Bouncing of Small Latex Spheres. *J. Colloid Interface Sci.* **1975**, *51* (1), 58–65. https://doi.org/10.1016/0021-9797(75)90083-1.

(15) Rennecke, S.; Weber, A. P. Charge Transfer to Metal Nanoparticles Bouncing from Conductive Surfaces. *Aerosol Sci. Technol.* **2014**, *48* (10), 1059–1069. https://doi.org/10.1080/02786826.2014.955566.

(16) Tsai, C.-J.; Pui, D. Y. H.; Liu, B. Y. H. Capture and Rebound of Small Particles Upon Impact with Solid Surfaces. *Aerosol Sci. Technol.* **1990**, *12* (3), 497–507. https://doi.org/10.1080/02786829008959364.

(17) Bitter, J. G. A. A Study of Erosion Phenomena Part I. *Wear* **1963**. https://doi.org/10.1016/0043-1648(63)90003-6.

(18) Harrison, P. G. *Chemistry of Tin*; Blackie, 1989.

(19) Committee, A. I. H. *ASM Handbook, Volume 2 Properties and Selection: Nonferrous Alloys and Special Prupose Materials*, Second.; ASM International: Materials Park, OH, 1991.

(20) Armstrong, P.; Peukert, W. Size Effects in the Elastic Deformation Behavior of Metallic Nanoparticles. *J. Nanoparticle Res.* **2012**, *14* (12), 1–13. https://doi.org/10.1007/s11051-012-1288-4.

(21) Kiener, D.; Minor, A. M. Source-Controlled Yield and Hardening of Cu(1 0 0) Studied by in Situ Transmission Electron Microscopy. *Acta Mater.* **2011**, *59* (4), 1328–1337. https://doi.org/10.1016/j.actamat.2010.10.065.

(22) Richter, G.; Hillerich, K.; Gianola, D. S.; Mönig, R.; Kraft, O.; Volkert, C. A. Ultrahigh Strength Single Crystalline Nanowhiskers Grown by Physical Vapor Deposition. *Nano Lett.* **2009**, *9* (8), 3048–3052. https://doi.org/10.1021/nl9015107.

(23) Chen, Q.; Alizadeh, A.; Xie, • Wanting; Wang, X.; Champagne, V.; Gouldstone, • Andrew; Lee, J.-H.; Sinan, •; Ftü, M.; Müftü, S.; Edu, M. High-Strain-Rate Material Behavior and Adiabatic Material Instability in Impact of Micron-Scale Al-6061 Particles. *J Therm Spray Tech* **2018**, *27*, 641–653. https://doi.org/10.1007/s11666-018-0712-4.

(24) Inc., T. M. Trust Region Reflective, MATLAB Curve Fitting Toolbox. Natick, Massachusetts, United States.

(25) Fauchais, P.; Montavon, G. Thermal and Cold Spray: Recent Developments. *Key Eng. Mater.* **2008**, *384*, 1–59. https://doi.org/10.4028/www.scientific.net/KEM.384.1.

(26) Cai, Y.; Tay, K.; Zheng, Z.; Yang, W.; Wang, H.; Zeng, G.; Li, Z.; Keng Boon, S.; Subbaiah, P. Modeling of Ash Formation and Deposition Processes in Coal and Biomass Fired Boilers: A Comprehensive Review. *Appl. Energy* **2018**, *230*, 1447–1544. https://doi.org/10.1016/j.apenergy.2018.08.084.

Chapter 6. Bombardment of Freestanding Thin Films

6.1 Introduction

Extreme ultra-violet (EUV) 13.5 nm photolithography has become the leading technology in the production of sub 10 nm transistor architecture led by the production company ASML. Of the wide variety of components within the complex machines required for this patterning, perhaps the most important interface is the photolithographic mask that patterns the silicon chips after light production. At this mask, the light is focused through the mask pattern to create the transistor architecture on the silicon used for chip manufacturer. Maintaining the integrity of the photomask is of the upmost importance as any error or perturbation of the light through the mask can affect millions of dollars of transistor chips during manufacture. A variety of potential contaminants in the form of dust produced during the photolithographic process or from the manufacturing process have the ability to affect the photomask. A significant source of this potential contamination comes from the tin plasma light source, which produces the light for photolithographic patterning. The light source uses droplets of tin excited into a plasma with a high powered CO_2 laser.[1] Significant tin metal debris is created during this process[2] and has the ability to propagate to the mask as a dust. Between this primary dust source within the apparatus, a thin film, just above the focal plane of the lithographic mask is commonly used to protect the mask from debris.[3,4] The film, known as a pellicle, must be designed to transmit the patterning light without significant absorption and this becomes particularly challenging at shorter wavelengths.[5] In order to allow transmission of high energy (13.5 nm) photons, films

as thin as ~10 nm must be employed. Large films used in manufacturing can have freestanding film areas of 150 cm^2 with a thickness of only 50 nm.[6] Depending on the contaminants it is exposed to, high energy particles can potentially punch through such a thin film, destroying its protective ability. In order to assess the durability of these thin films, it is possible to directly examine films under bombardment in the laboratory with a controlled particle source. The AIS is capable of creating well-characterized particles of a controlled energy on demand, and was used to test the durability of sample pellicle films.

For EUV-relevant pellicles, the AIS is capable of producing debris analogues on demand, specifically 500 nm tin particles. This, paired with the energetic control of the LINAC, allows ready measure of whether a sample film can survive under different velocity impacts. For this study, the films used were manufactured and supplied by ASML for testing in AIS. In addition to testing these films, broader interest in thin film and other freestanding material durability can be examined with the experimental procedures outlined here. Microparticle impacts are particularly well suited for examining thin films and other fragile structures expected to withstand debris and other particle impacts in industrial processes[7] or space-flight applications.[8] A common metric for material performance is to measure the ballistic limit of materials, the velocity at which a projectile can reliably perforate a material. Classically applied to high stress systems, such as body armor,[9] the ballistic limit for microparticle impact[10] is relevant for protective coating applications and is challenging to study without a controlled particle source such as the AIS. The studies in this work assess EUV-relevant pellicle thin film durability and demonstrate how more extensive testing can be performed for measuring ballistic limits.

6.2 Experimental Methods

In order to test the durability of thin films in the AIS, two different particle materials were used: 990 nm polystyrene latex sphere particles (PSLs) and 500 nm tin metal particles. Both particle species were produced with electrospray ionization using the same methodologies outlined in Chapters 3 and 5. The AIS was operated in per-particle analysis mode for both particle types with progressively higher potentials on the LINAC. PSLs were produced with velocities between 20 m/s and 260 m/s using a maximal deceleration potential of +250 V and a maximal acceleration potential of -15 kV. 500 nm tin particles (with a full-width-half-max spread in size of ~30 nm) were produced with velocities between 30 m/s and 760 m/s using a maximal deceleration potential of +630 V and a maximal acceleration potential of -72 kV.

The post-acceleration region of the AIS was configured to allow detection of particle velocities, electrostatic gating of incorrect particle velocities, and optical access to each pellicle mounted in the beamline (Figure 6.1). Image charge detectors were placed both before and after the pellicle film. Upon entering the post-acceleration chamber, particles initially passed through an ICD (labeled ICD3) to measure post-acceleration velocity. The signal from ICD3 is digitized using the digitzer/FGPA configured with DAQ1 (See Chapter 2). The FPGA of DAQ1 is programmed to measure the particle velocity passing through ICD3. This is done with a simple trigger to detect the particle entering and exiting the tube of ICD3. This time difference was used to approximately determine the particle velocity passing through the tube. This approximate velocity determined when to lower the potential on an electrostatic deflector mounted after ICD3. This deflector provided protection of the pellicle from errant or unexpected velocity impacts by using a potential higher than the total acceleration potential.

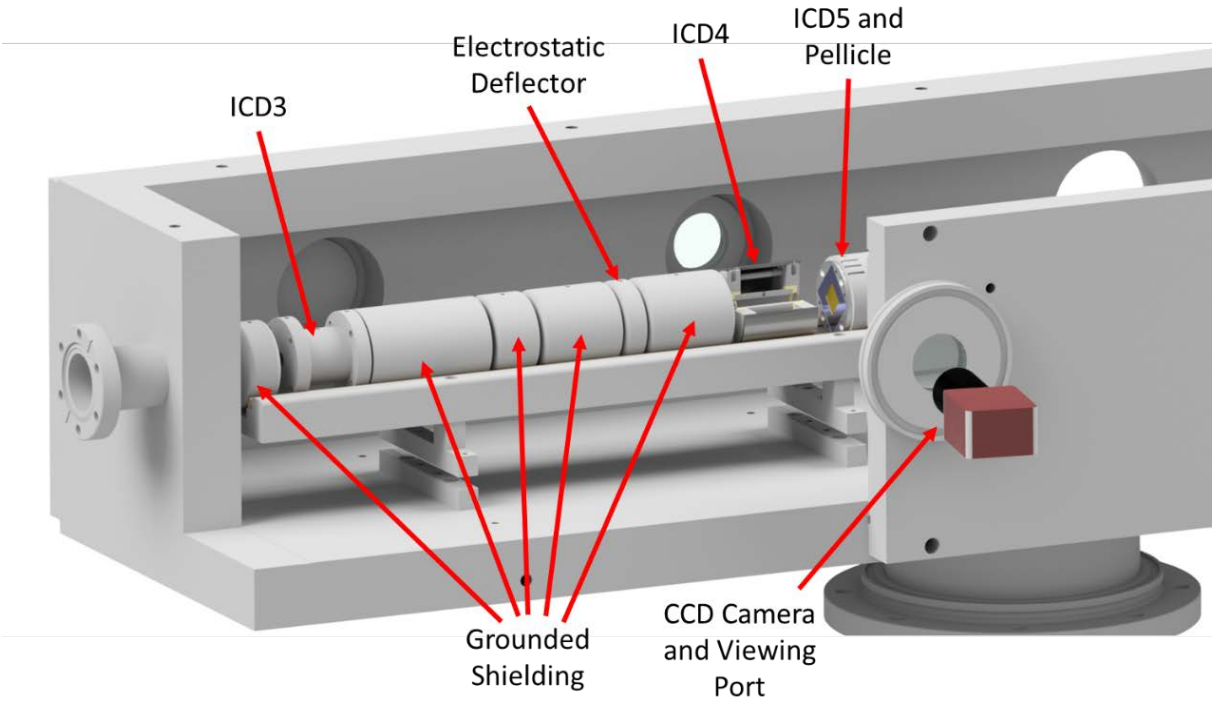

Figure 6.1: *Pellicle impact region setup with key components labeled.*

This was limited by how much potential (below 4 kV) could be applied to the single element deflector. At acceleration potentials that exceeded 4 kV, all accelerated particles impacted the pellicle.

After the electrostatic gate, two ICDs (ICD4 and ICD5) were mounted with a small gap (~23 mm) between them. The pellicle film was mounted in a specialized chuck between the two ICDs using two spring clips fastened to the film's retaining scaffold (Figure 6.2). The 100 mm^2 films (with larger retaining scaffold) fastened to the chuck were mounted on the front face of ICD5 normal to the incident particle beam. ICD4 was used to calculate final particle velocity before impact and detect any particles rebounding from the film. ICD5 was placed to measure any possible particles punching through the film without optically apparent film destruction. The small gap between the two detectors allowed a white light lamp external to the chamber to illuminate the pellicle face through a viewport window. Through a viewport window on the opposite side of the chamber a CCD camera was used to monitor film status and observe catastrophic film failure (Figure 6.3). After a particle was recorded passing through ICD3 at the correct velocity, the protective electrostatic deflector would lower and the particle would pass through ICD4 before hitting the pellicle. With a sufficient delay the camera was triggered to acquire an image of the pellicle after impact which was then transmitted to DAQ1 through a USB interface on the camera. This image was observed for every particle and the program on DAQ1 would pause until the experimental operator continued particle bombardment. In order to measure film destruction, the acceleration potential was progressively increased until catastrophic destruction of the film was observed in the CCD image. No particles in any experimental trial were observed on ICD5.

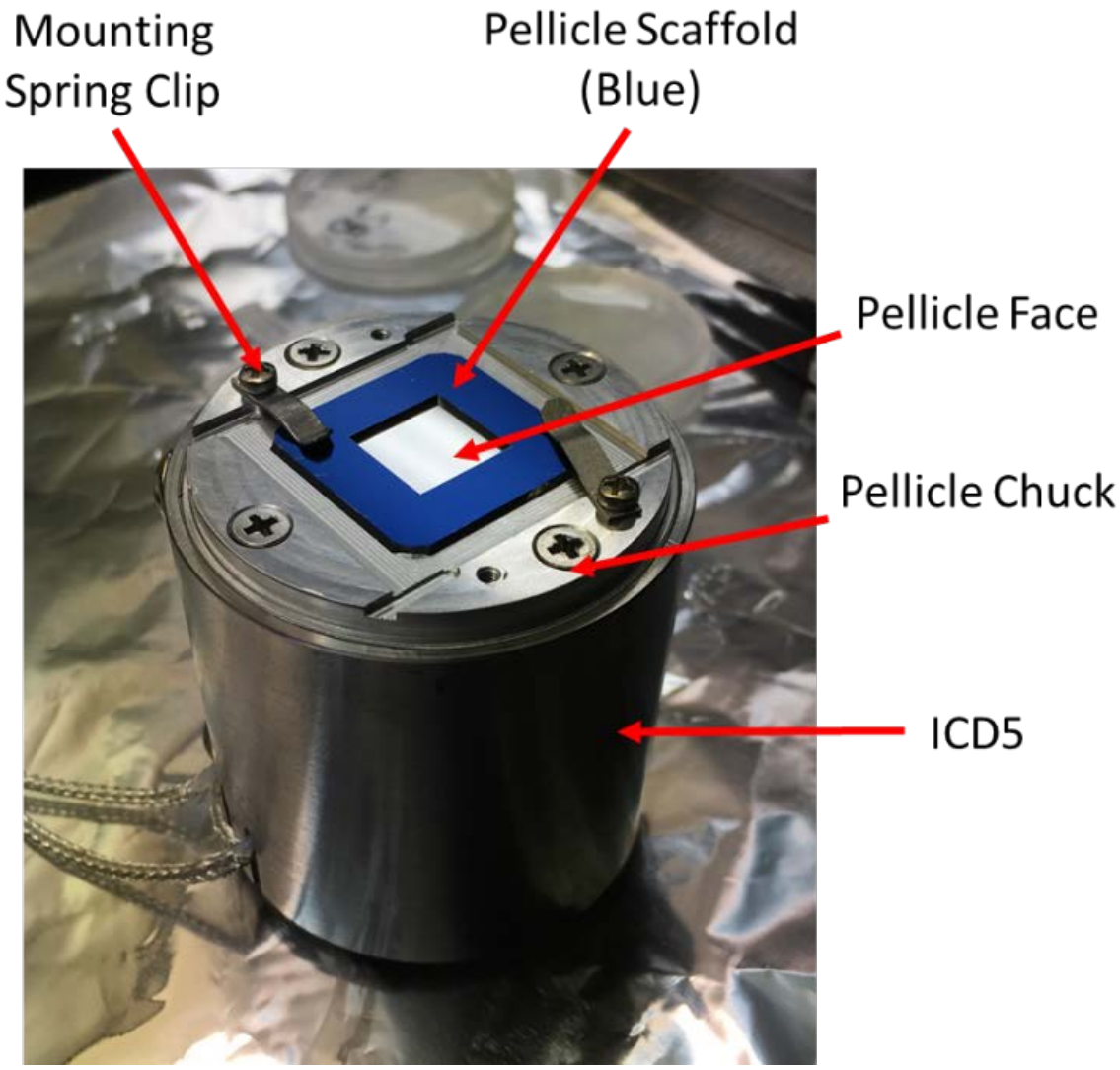

Figure 6.2: *Pellicle with scaffolding mounted in chuck on ICD5.*

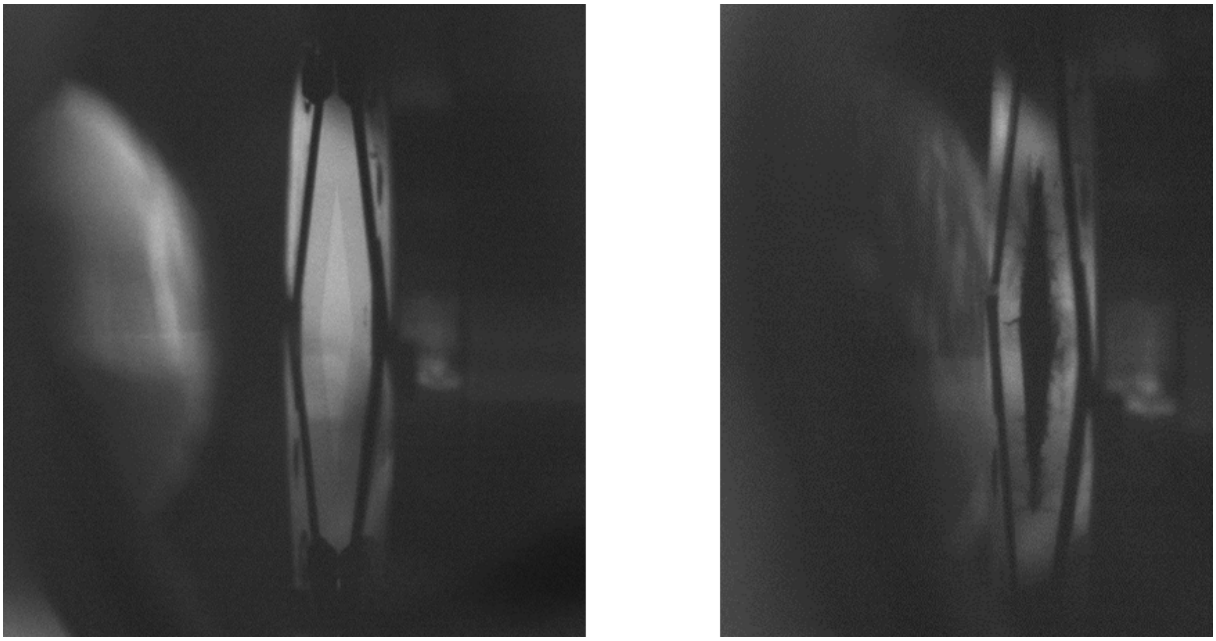

Figure 6.3: *CCD camera images of installed pellicles. (Left) Intact pellicle as observed from external CCD camera. Bright diamond in image center is the pellicle film. (Right) Pellicle after destruction. Debris and a distinct lack of film observed during failure.*

6.2.1 Film Provenance

The pellicles used in this experimental evaluation were scaled down in area as compared to those used in manufacturing. These films were supplied by the ASML Pellicle Group. The composition and thickness of the pellicles that were tested are summarized along with relevant impact data in Table 6.1. Further details regarding the exact manufacturing technique and structure of each film are unknown. The films supplied to UCSD were primarily single composition films. Films used in EUV manufacturing processes are typically composed of several layers with a polysilicon core and capping layers on either side to protect against oxidation.[6] Film production is typically done with physical vapor deposition of the required layers onto the scaffolding. Two classes of films were delivered to UCSD: films with a potentially variable amount of strain already applied and films without significant strain applied. The films without strain were readily identifiable by their diaphanous behavior and heterogeneous surface. Both film types were explored in these experiments, but no information about the pre-strain of the material was provided making the exact characterization of material properties challenging. Consequently, only generalized description of the observed phenomena and demonstration of experimental feasibility are presented here as the significant outcomes of this experiment.

6.2.2 Film Installation

Ultrathin freestanding films were found be extremely fragile and careful handling was required to not erroneously break films during installation. After a film was carefully installed

on the mounting chuck (Figure 6.2), the entire assembly was put into the test chamber as in Figure 6.1. Initial rough vacuum in this chamber was provided by a dry vacuum pump (Osaka DSP 500) that was run through a manual angled vacuum valve. This valve was opened as slowly as possible to evacuate the experimental chamber at approximately one decade of pressure every 5 minutes. Once a pressure of less than 10 mTorr was achieved, the valve was opened completely and the turbomolecular pump was operated normally to evacuate the chamber to 1e-7 Torr. This procedure, coupled with careful handling of the film, was required to not damage the film prior to particle impact studies.

6.3 Results and Discussion

A total of 11 films of varying composition and thickness were successfully studied in these experiments. Some films were examined only at lower energies and were shown to be capable of withstanding low energy particle impact while others were impacted with progressively higher energy particles until film destruction. A summary of the materials, thicknesses, experimental outcome, and other relevant parameters is provided in Table 6.1. For each pellicle tested, incident particles were progressively accelerated to higher velocities with 1-10 particles recorded within each expected velocity range. A representative experimental data set is shown in Figure 6.4 where the velocity of every particle incident on a 40 nm polysilicon pellicle was recorded up to a particle velocity of 760 m/s. If the particle was recorded to have rebounded back through ICD4, the velocities (incident and rebound) are recorded as a pair of symbols (▷ and ◁).

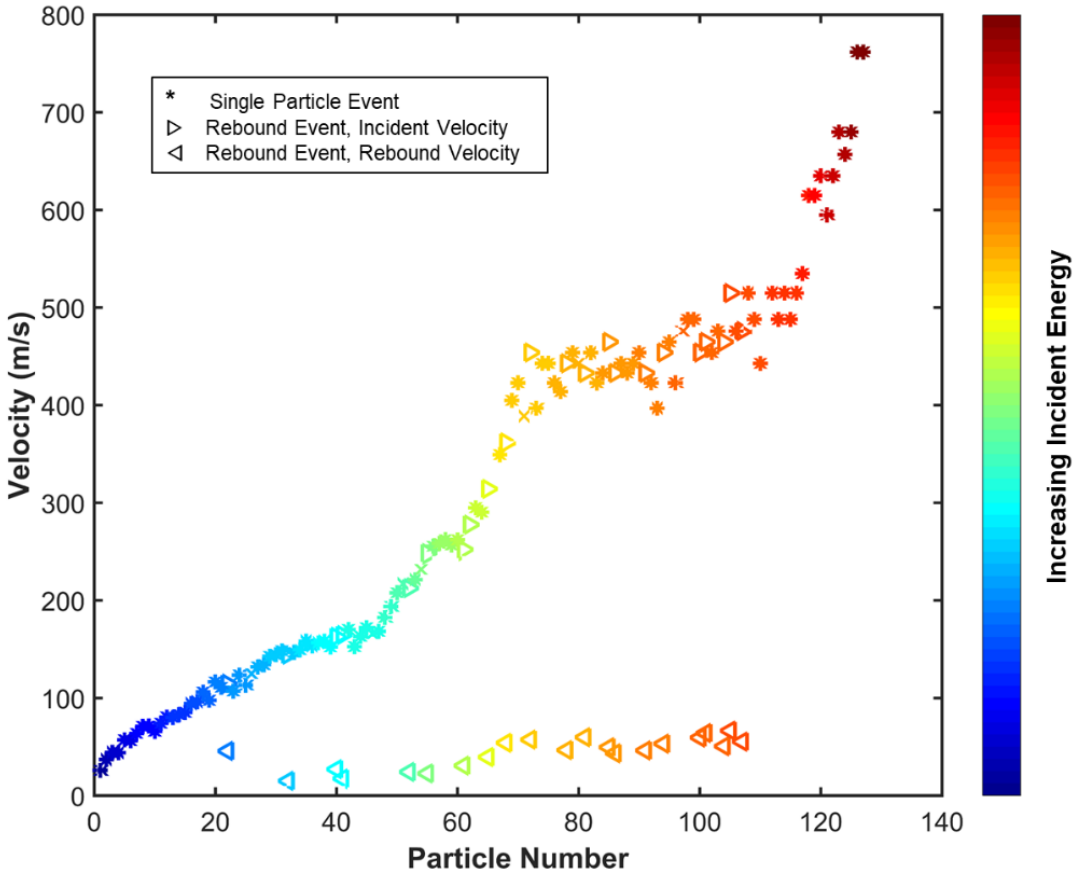

Figure 6.4. *Typical pellicle bombardment dataset. Velocity of 500 nm tin particles used to bombard a 40 nm thick polysilicon pellicle. Each particle was progressively accelerated using the LINAC until reaching final velocity of the experiment. This pellicle was unbroken by the repeated bombardment.*

In addition to the catastrophic failure observations observed in 5 of the 11 pellicles, coefficient of restitution data (CoR) were collected on every pellicle trial for both 990 nm PSL and 500 nm tin particles. These measurements were performed with ICD4, in the same manner as the experiment detailed in Chapter 3. The CoR measurements presented here were performed in more limited velocity ranges and with fewer particles subject to the testing conditions of the pellicle films, but comparison to previous work is striking. The CoR measurements deviate sharply from the previously observed trends in both PSL and tin metal particles. CoR results for particles impacting strained pellicles are compared to the hard target impacts (detailed in Chapters 3 and 5) for PSL and tin particles in Figure 6.5. The raw CoR data is averaged in 30 m/s incident velocity bins and the error bars correspond to the 95% confidence interval for each velocity bin in all plots. As compared to previously collected data, both PSL and tin particle behave radically different when rebounding from the thin film pellicles. It is particularly of interest that the results for both particle species are more consistent with each other than with the previous measurements of impact on hard targetss. In the previous analysis in Chapter 5, attention was paid to the material properties of the impacting particle that resulted in a size-dependent CoR. Here, the two dissimilar material particles are very consistent and the common element in this case is the strained thin-film impact target. Although several different pellicle material compositions were used to generate Figure 6.5, the differences in these materials has much less of an impact on the CoR of the two particle species than the differences between the thin film and bulk targets. The aspect ratio of the thin film thickness to the particle size used (the ratio of the film thickness to particle diameter) in these experiments is less than 1. When compared to the previous experiments, this is decades smaller since the bulk target and particle aspect ratios usually exceeded 1000.

Figure 6.5 C*omparison of CoR for pellicle and bulk targets. 30 separate tin particle CoR measurements were made with the pellicle target and 117 separate PSL particle CoR measurements were made with the pellicle targets. Each averaged bin consists of at least 2 different CoR measurements. (Top Left) PSL CoR on pellicles is compared to PSLs impacting a silicon target presented in Chapter 3. (Top Right) Tin CoR on pellicles is compared to tin particles impacting a molybdenum target presented in Chapter 5. (Bottom) The two particles impacting pellicles are compared.*

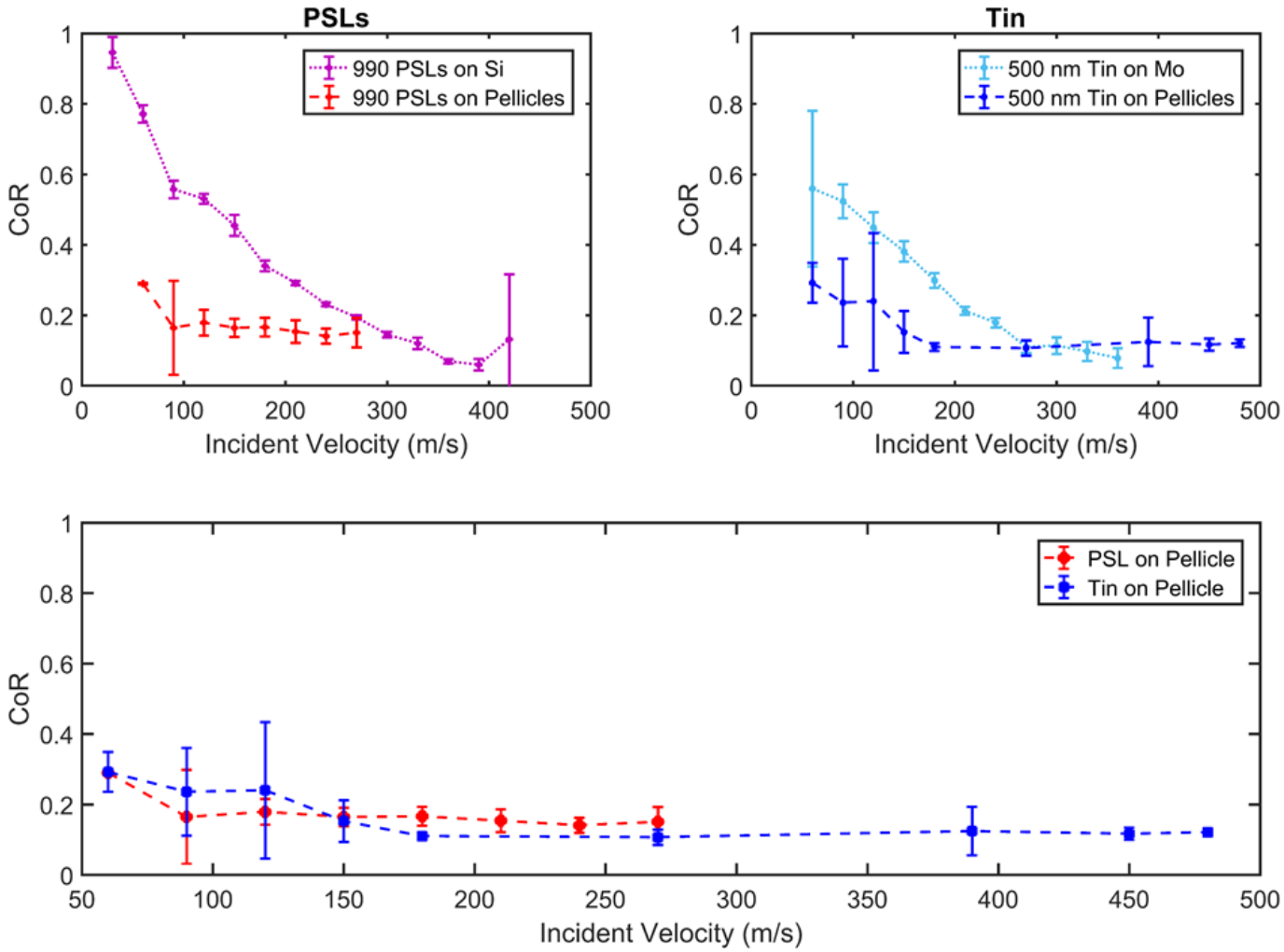
PSLs
990 PSLs on Si
990 PSLs on Pellicles
CoR
Incident Velocity (m/s)
Tin
500 nm Tin on Mo
500 nm Tin on Pellicles
CoR
Incident Velocity (m/s)
PSL on Pellicle
Tin on Pellicle
CoR
Incident Velocity (m/s)

The difference in aspect ratio changes the ability of the target material to yield under impact and the capacity to deform under high velocity impacts before eventually fracturing.[10] Yielding of the pellicle target appears to homogenize the rebound behavior of the two different particle types across a wide range of velocities. The influence of the strained target on the rebound dynamics is emphasized by the observations on the 500 nm tin particles at very high velocity as shown in Figure 6.5. Previous studies of 500 nm tin particle impacts on bulk molybdenum targets did not record any measurable rebounds for incident velocities > 400 m/s. Particle impact on the pellicles at incident velocities in excess of 400 m/s yielded many rebound events compared to bulk targets.

Although the CoR measurements across the different pellicles are relatively uniform, the destruction velocities measured were found to scale with the film thickness examined. Target thickness is known to have effect on penetration and post-impact behavior in studies of macroscopic projectiles[11] where aspect ratios can be ~1. This effect has also been demonstrated for microparticle impacts on thin films.[10,12] For the 5 pellicles destroyed in this study, the destruction velocity is plotted versus the film thickness in Figure 6.6. Chen et. al. developed a model of thin film failure that scales velocity and film thickness with the thermal, yielding, and elastic energy distribution mechanisms and predicts this scaling to be non-linear, but a more careful application of that model here is challenging without more detailed film composition information. Two different materials were used to measure pellicle destruction in Figure 6.6 complicating any application of material dependent modeling. An outlier to this trend is the 40 nm polysilicon pellicle bombarded with particles up to 760 m/s but still survived. It is unknown if the pre-stress in this film's manufacturing process was different than that of the other 40 nm polysilicon films destroyed at lower velocities, but initial stress in the material is expected to

change film response to impact. This variable in the film manufacturing process would help dictate the film survivability and needs to be balanced with the optical flatness required to effectively transmit EUV photons.[6]

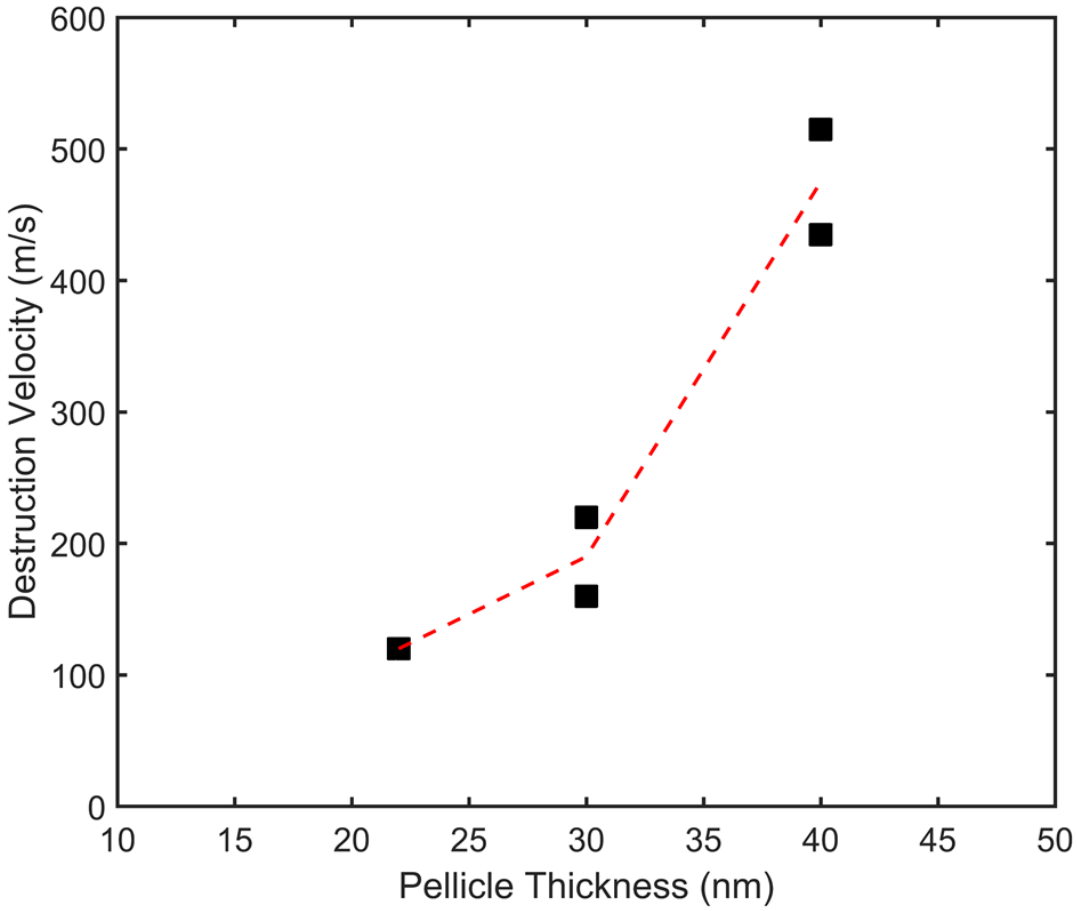

Figure 6.6 *The destruction velocity as a function of film thickness for the 5 pellicles measured. The dashed red line is added to guide the eye for the average destruction velocity of each pellicle thickness.*

Table 6.1: *Summary of pellicle impact experiments*

Composition	**Thickness (nm)**	**Film Stress**	**Particle Species**	**Impact Velocity Range**	**Maximal Impact Kinetic Energy (J)**	**Film Destroyed?**
Polysilicon with Silicon Nitride layer and Yttrium/Boron	45	Diaphanous	PSLs	30-475	6.0e-11	No
Molybdenum Disilicide	22	Strained	PSLs	20-120	3.8e-12	Yes
Polysilicon	40	Strained	PSL/Tin	30-260 (PSLs), 30-760 (Tin)	1.4e-10	No
Polysilicon	40	Strained	PSLs	30-260	1.8e-11	No
Polysilicon with Yttrium/Boron Coating	42 (2 nm coating)	Strained	PSLs	30-260	1.8e-11	No
Polysilicon with Yttrium/Boron Coating	42 (2 nm coating)	Strained	PSLs	30-260	1.8e-11	No
Polysilicon with Silicon Nitride layer and Yttrium/Boron	45	Strained	PSLs	30-260	1.8e-11	No
Molybdenum Disilicide	30	Strained	Tin	30-220	1.2e-11	Yes
Molybdenum Disilicide	30	Strained	Tin	70-160	6.1e-12	Yes
Polysilicon	40	Strained	Tin	30-515	6.3e-11	Yes
Polysilicon	40	Strained	Tin	70-435	4.5e-11	Yes

6.4 Conclusion

The AIS has been used to test industrially relevant pellicle thin films under particle bombardment. Pellicle destruction was measured in 5 separate films of three separate thicknesses. A general trend in the film durability is observed and the coefficient of restitution for particles rebounding from the pellicle films is reported. The differences noted in comparing CoR measurements in pellicle targets with those of harder, thicker targets demonstrates the radically different behavior in systems where significant yielding/deformation of the target is expected. Future measurements on freestanding thin films will aim to use more well characterized and consistently produced films to isolate the dynamics that affect film destruction and particle rebound behavior. The single particle production and bombardment can also be applied to thin film coatings and other hard structures to apply microparticle bombardment experiments to a wider variety of materials research options.

6.5 References

(1) Brandt, D. C.; Fomenkov, I. V.; Lercel, M. J.; La Fontaine, B. M.; Myers, D. W.; Brown, D. J.; Ershov, A. I.; Sandstrom, R. L.; Bykanov, A. N.; Vaschenko, G. O.; Böwering, N. R.; Das, P.; Fleurov, V. B.; Zhang, K.; Srivastava, S. N.; Ahmad, I.; Rajyaguru, C.; De Dea, S.; Dunstan, W. J.; Baumgart, P.; Ishihara, T.; Simmons, R. D.; Jacques, R. N.; Bergstedt, R. A.; Porshnev, P. I.; Wittak, C. J.; Woolston, M. R.; Rafac, R. J.; Grava, J.; Schafgans, A. A.; Tao, Y. Laser Produced Plasma EUV Sources for Device Development and HVM. *Extrem. Ultrav. Lithogr. III* **2012**, *8322* (March 2012), 83221I. https://doi.org/10.1117/12.916521.

(2) van de Kerkhof, M. A.; van Empel, T.; Lercel, M.; Smeets, C.; van de Wetering, F.; Nikipelov, A.; Cloin, C.; Yakunin, A.; Banine, V. E. Advanced Particle Contamination Control in EUV Scanners. In *Proceedings of SPIE*; 2019; p 27. https://doi.org/10.1117/12.2514874.

(3) Asbach, C.; Fissan, H.; Kim, J. H.; Yook, S. J.; Pui, D. Y. H. Technical Note: Concepts for Protection of EUVL Masks from Particle Contamination. *J. Nanoparticle Res.* **2006**, *8* (5), 705–708. https://doi.org/10.1007/s11051-006-9080-y.

(4) Amemiya, M.; Ota, K.; Taguchi, T.; Suga, O. Evaluation of Particle Protection Capability of Extreme Ultraviolet Lithography Mask Carrier in Vacuum Transfer by Experiment and Calculation. *Jpn. J. Appl. Phys.* **2011**, *50* (9 PART 1). https://doi.org/10.1143/JJAP.50.096701.

(5) Wurm, S. EUV Lithography: Progress, Challenges, and Outlook. *30th Eur. Mask Lithogr. Conf.* **2014**, *9231* (May), 923103. https://doi.org/10.1117/12.2076766.

(6) Susanna Licheri. Offline Study of next Generation EUV Pellicle Materials and Performances., KTH Royal Institute of Technology, Stockholm, 2019.

(7) Fauchais, P.; Montavon, G. Thermal and Cold Spray: Recent Developments. *Key Eng. Mater.* **2008**, *384*, 1–59. https://doi.org/10.4028/www.scientific.net/KEM.384.1.

(8) Stübig, M.; Schäfer, G.; Ho, T. M.; Srama, R.; Grün, E. Laboratory Simulation Improvements for Hypervelocity Micrometeorite Impacts with a New Dust Particle Source. *Planet. Space Sci.* **2001**, *49* (8), 853–858. https://doi.org/10.1016/S0032-0633(01)00035-6.

(9) Johnson, T. H.; Freeman, L.; Hester, J.; Bell, J. L. A Comparison of Ballistic Resistance Testing Techniques in the Department of Defense. *IEEE Access* **2014**, *2*, 1442–1455. https://doi.org/10.1109/ACCESS.2014.2377633.

(10) Chen, S. H.; Souna, A. J.; Soles, C. L.; Stranick, S. J.; Chan, E. P. Using Microprojectiles to Study the Ballistic Limit of Polymer Thin Films. *Soft Matter* **2020**,

16 (16), 3886–3890. https://doi.org/10.1039/d0sm00295j.

(11) Bobbili, R.; Paman, A.; Madhu, V.; Gogia, A. K. The Effect of Impact Velocity and Target Thickness on Ballistic Performance of Layered Plates Using Taguchi Method. *Mater. Des.* **2014**, *53*, 719–726. https://doi.org/10.1016/j.matdes.2013.06.005.

(12) Bizao, R. A.; Machado, L. D.; De Sousa, J. M.; Pugno, N. M.; Galvao, D. S. Scale Effects on the Ballistic Penetration of Graphene Sheets. *Sci. Rep.* **2018**, *8* (1), 6750. https://doi.org/10.1038/s41598-018-25050-2.

Chapter 7. Particle Beam Characterization with a Microchannel Plate Detector

7.1 Introduction

Microchannel plate detectors (MCPs) are charged particle detectors with widespread use in time-of-flight mass spectrometry, photoelectron spectroscopy and ion imaging applications.[1,2] In this chapter, the application of MCPs to the detection of submicron highly charged particles is investigated, a realm that has received only minimal investigation previously.[3,4] The function of an MCP is to amplify the electrons produced by high energy photons, charged particles, and high energy neutrals.[5,6] MCPs consist of an array of glass capillary channels, typically with an angular offset relative to incident particles or photons, and have been shown to be extremely versatile in applications ranging from molecular physics to image intensifiers used in night vision.[7] Amplification of incident electrons by factors on the order of 10^4 per MC is routinely achieved. Incident charged particles, or high energy neutrals that generate secondary electron emission result in an amplification cascade down a single channel within a plate. The electrons of the detector are replenished with an external voltage source across the channels within a plate and serial plates offer signal multiplication of up to 70 dB.[5]

Generation of the electron cascade within an MCP capillary and subsequent detection with a variety of charge sensitive detectors is critical to MCP operation. Without the initial cascade, no amplification can occur and an incident signal will not register. As such, understanding the

efficiencies of MCP plates to effectively start this cascade has been an area of study across different detector applications.[5,6,8–10] Previous work to predict theoretical efficiencies of MCP detectors has primarily focused on the detection efficiencies of small molecular ions, electrons, and high energy photons,[11] however MCPs in space flight applications have been shown capable of measuring interactions with significantly larger particles, the efficiency of which is not well understood.[12] Contemporary work[3,4] has been able to characterize MCP detector efficiencies with large, micron and submicron metal particles. The work presented here offers additional information regarding detector efficiencies coupled with analysis of the detector performance as it applies to the Aerosol Impact Spectrometer (AIS). Liquid charged particles produced by electrospray ionization and subsequently frozen under vacuum are characterized and accelerated with the AIS directly into an MCP detector with a phosphor screen. The resulting patterns/efficiencies are analyzed to characterize the width of the post-accelerator particle beam and demonstrate MCP function with large particles (~100 GDa).

7.2 Experimental

In order to examine the MCP detector response to particles generated in the AIS a liquid solution for particle generation was used. The solution was the solvent commonly used in the AIS electrospray ionization (ESI) source, a 1:1 mixture of aqueous 25 mM acetic acid and HPLC grade methanol, which was sprayed and characterized for acceleration. The heater of the AIS ESI injection region was not used since vacuum freezing of the liquid droplets was desired. The AIS was operated in the per-particle analysis mode, trapping individual particles in an electrostatic ion trap for spectrometric characterization before accelerating them into the detector. The MCP and

phosphor screen detector were mounted normal and in-line with the accelerated particle beam (Figure 7.1), and the configuration was also equipped with a pre-MCP image charge detector (ICD). Optical access to the phosphor screen was provided by an angled mirror located behind the stack allowing observation of the screen from an external CCD camera (FLIR Grasshopper).

Particles generated with the solvent solution had a mean mass of ~115 GDa (standard deviation of 20 GDa), and carried between 10000-30000 positive charges (e). Freezing of the particles during the hundreds of millisecond transit times through the apparatus before impacting the MCP is expected from rapid evaporative cooling in each droplet.[13] Particles were accelerated to velocities of 700-1000 m/s using an acceleration potential of 36 kV before impacting the MCP detector. Beam characterization and efficiency calculations were performed for varying detector geometries.

The MCP detector characterized in this study was a chevron stack (Beam Imaging Solutions BOS-25) detector with P-43 phosphor screen. The MCPs have channels 10 μm in diameter (with a 40:1 aspect ratio), spaced 12 μm apart, with a 12° bias angle. The phosphor screen generates light from the intense charge transmitted by the MCP stack positioned directly in front of it. A phosphorescent spot indicates where the initial signal was produced spatially on the plane of the MCP. Operation of the MCP typically used a front plate voltage between 1.3-1.8 kV and a back plate voltage between 3.2-3.6 kV. The phosphor screen was operated between 5.5-6 kV. In addition to measurements using the open face of the detector, a grounded wire mesh and grounded semicircle covering were fashioned for the detector to test different response and examine possible signal generation mechanisms. A pre-MCP ICD (Figure 7.1) was mounted to trigger the acquisition data produced by the detector only when an accelerated particle passes through the ICD and directly onto the MCP face.

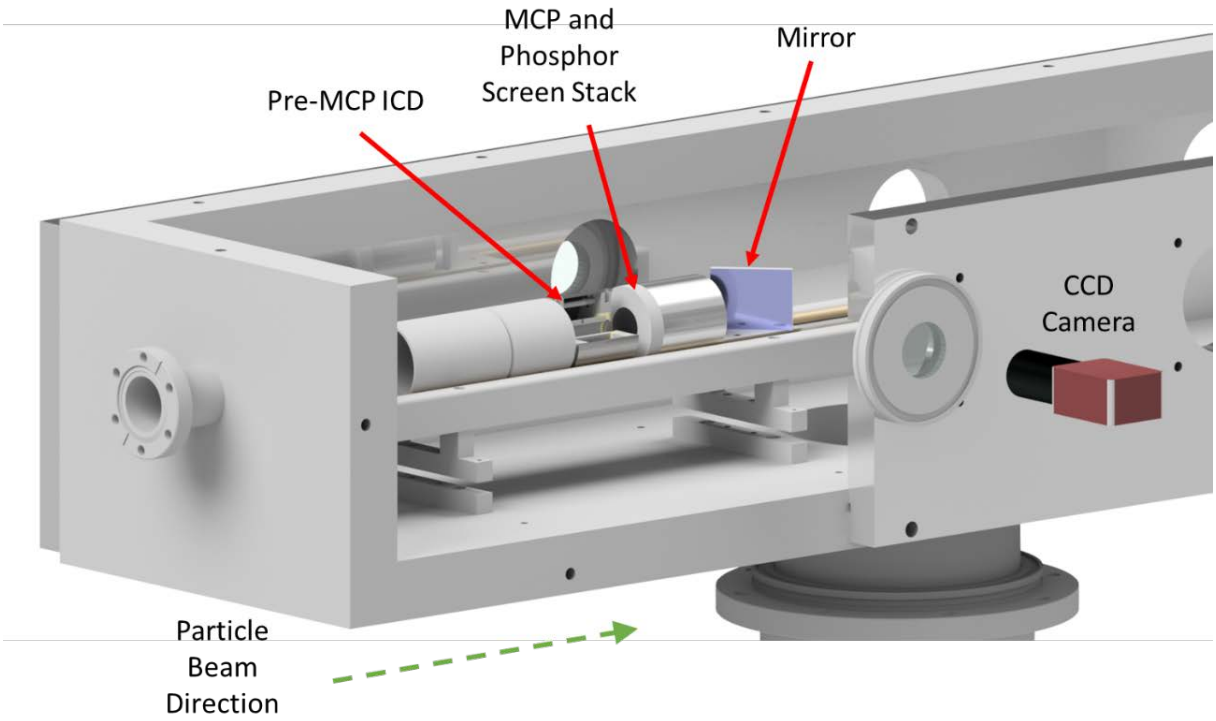

Figure 7.1: *Experimental setup of MCP impact measurements with major components labeled.*

7.3 Results and Discussion

Single image frames recorded using the CCD camera of the phosphor screen were digitally stored after a particle impact was recorded with the pre-MCP ICD. These images were then exported into MATLAB for analysis. Each frame from the CCD was converted into a binary image and individual spots on the screen were identified. For images with one or more spots the centroid of the fragments was identified. It is proposed that this centroid more accurately represents the initial impact location since any fragments/ejecta that propagate from the initial impact location should do so randomly. In order to profile the particle beam, measurements of many particle fragment centroids were combined together and an ensemble plot generated. These images were then overlaid with the geometrically limited size of the particle beam restricted by the inner diameter of the pre-MCP ICD as shown in Figure 7.2 for particles directly impacting the exposed face of the MCP detector. By looking at the centroids of each image, it is apparent that all particles fell within the maximal beamline diameter (with one exception), showing that the analysis method provides physically consistent data. Particles impacting within this diameter are at maximal concentration in the center, but appear distributed throughout the geometrically allowed diameter, indicating that the particle beam was not tightly focused along the beam centerline. Lack of focus in the particle beam is most likely the result of imperfect injection into the LINAC, determined by the particle trajectories in the nanoparticle electrostatic trap (NET) used for injection and errors associated with the precise timing of the LINAC. Timing errors can come from a variety of possible error sources including error in the initial velocity measurement, the particle mass-to-charge ratio measurement, and the exact ejection timing from the NET.

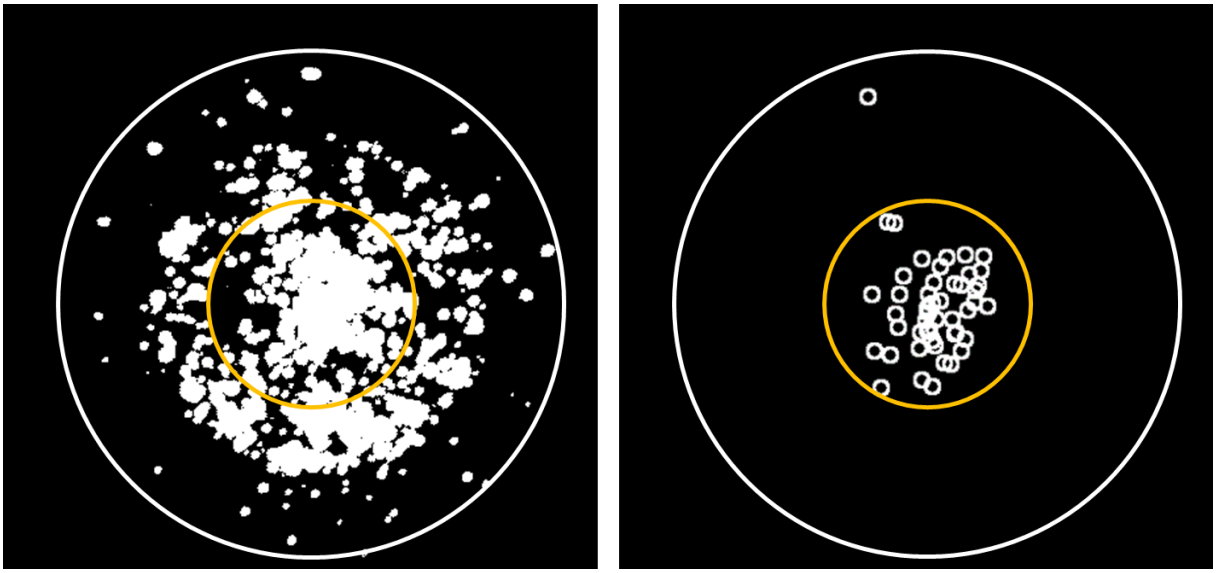

Figure 7.2: *Overlay of binary phosphor screen images from particles impacting an MCP detector with open face. The outer diameter of the phosphor screen (25 mm) is shown as a white circle and the maximal beamline diameter (~10 mm) is shown as an orange circle. (Left) Overlay of 49 images with varying numbers of events. (Right) Overlay of centroids of all 49 images. The front plate voltage of the MCP was operated at 1.8 kV and the phosphor screen was operated at 6 kV.*

In addition to particles impacting the bare-faced MCP detector, impacts on the MCP with a grounded wire mesh placed ~3.8 mm from the face were also measured. Originally installed to reduce potential noise from background ions within the vacuum chamber, the wire mesh on the detector altered the fragmentation patterns and centroids observed in the beamline. An overlay of these images is displayed in Figure 7.3. The centroid pattern of this image deviates significantly from the allowed diameter dictated by the pre-MCP ICD. This behavior was surprising since initial impact locations or impacts with a fragmentation pattern radially distributed around the initial impact site should have a centroid confined by the pre-MCP ICD diameter. In order to explain this observed behavior, the centroids in the image were colorized by the number of spots used to make them. Blue rings correspond to fewer spots increasing to red rings with most spots used to make the centroid. A pattern can be observed where most event centroids outside of the allowed diameter are created from images with the fewest number of spots in them (Figure 7.4). Centroids made from image frames with four or more spots are confined to the allowed diameter indicating that the high spot count centroids more accurately predict where the particle beam is impacting. It is possible that the low count centroids are only produced from wide angle secondary ejecta (electrons or particle fragments) resulting from interaction of the incident particles with the grid, leading to a deviation in the incident trajectories. Compared to the tighter distribution observed with the uncovered MCP detector it is also possible that the difference in electric field uniformity of the mesh-covered MCP detector allows ejecta from the initial impact to stray farther from the initial impact site with single events. The electric field lines of the uncovered detector would tend to pull negatively charged species ejected from the plate toward the center at further distances from

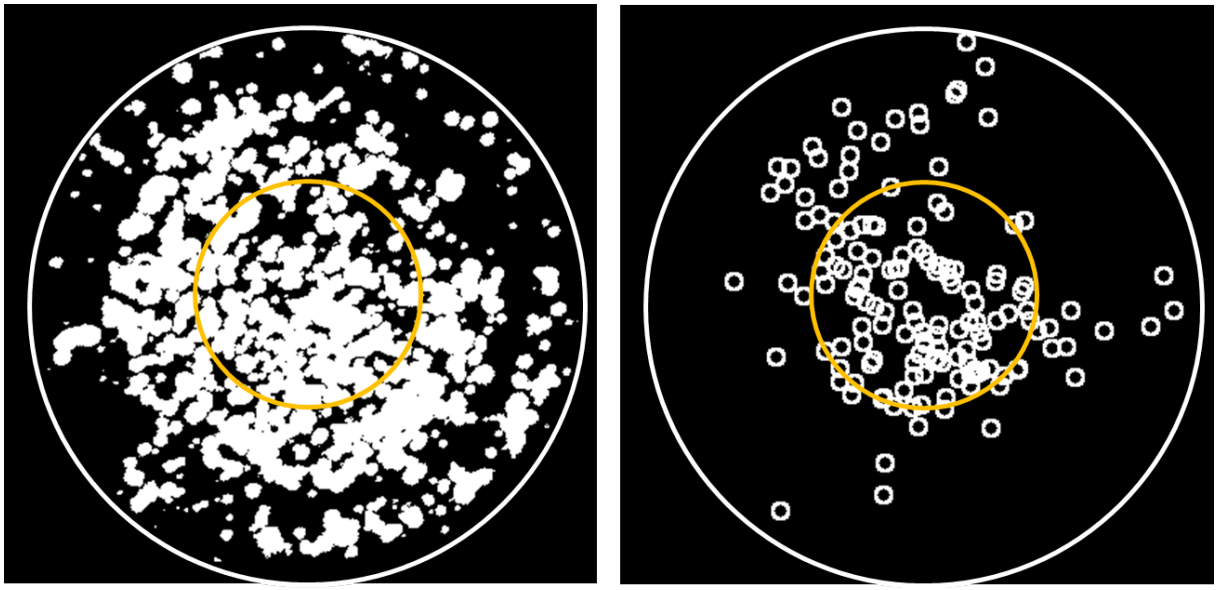

Figure 7.3: *Overlay of binary phosphor screen images from particles impacting an MCP detector with mesh covering. The outer diameter of the phosphor screen (25 mm) is shown as a white circle and the maximal beamline diameter (~10 mm) is shown as an orange circle. (Left) Overlay of 149 images with varying numbers of events. (Right) Overlay of centroids of all 149 images. The front plate voltage of the MCP was operated at 1.38 kV and the phosphor screen was operated at 5.6 kV.*

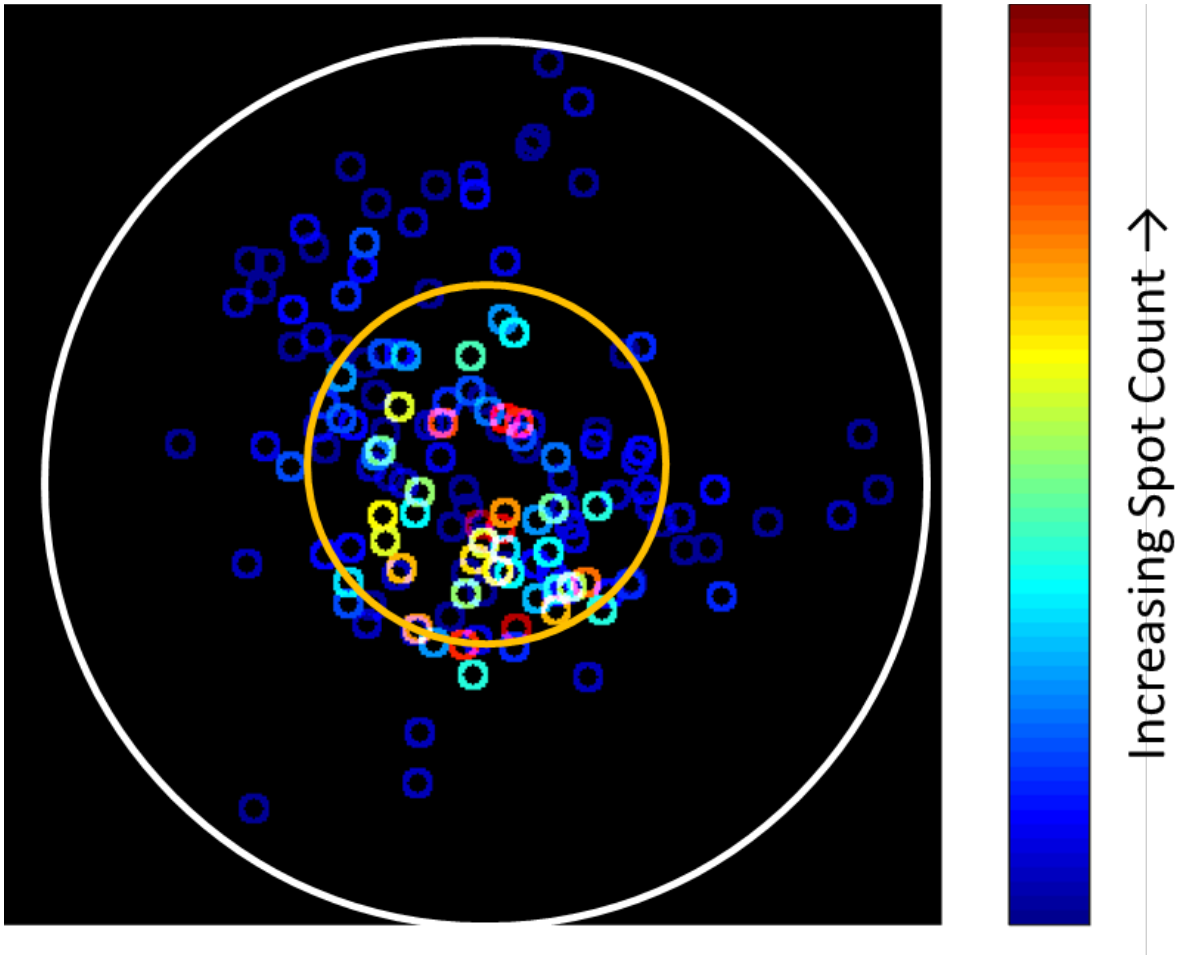

Figure 7.4: *Centroid image in Figure 7.3 colorized to indicate number of spots used to produce centroid. Blue rings are made with low numbers of particles (1-3 spots in the image), while other colors indicate higher spot counts used to make the centroid.*

the MCP face (Figure 7.5), whereas the grounded mesh creates a much more uniform electric field region. This is expected to affect only secondary ejecta as the original particle is of like-charge to the face of the MCP and of significantly higher energy.

In order to test the focusing effect of the bare-faced MCP and to determine the efficiency of detecting ejecta, half of the MCP face was blocked with a grounded metal plate (Figure 7.6). Unlike the grid, the metal plate did not allow incident particle and ejecta to pass through it, and the open face side of the MCP would still be expected to experience the focusing effect of the completely bare face MCP. Particles of same energy as in previous tests were accelerated onto the half-exposed MCP face with nominally half of the beam centerline impacting the detector and half impacting the metal plate. The resulting images are compiled together with their centroids in Figure 7.7.

The vast majority of spots produced on the phosphor screen occur in the exposed face of the MCP, but do not fall within the allowed area determined by the pre-MCP ICD. Additionally the high density cluster that can be observed in the centroids (Figure 7.7) occurs outside of the allowed area. This indicates that the majority of signal (at least in this observation) does not directly come from the incident particle impact, but rather mostly from secondary ejecta. The perturbed field from the half-faced MCP therefore is able to focus secondary ejecta to the center of that exposed area. It is notable that this focus appears much tighter than the uncovered MCP face. When fully uncovered, direct particle impacts (if measured) are more likely to contribute to the signal measured on the MCP face (something that is not focused by the front plate voltage), whereas in the half-covered face the majority of signal appears to come from secondary ejecta that are more readily focused by the MCP electric field. The increase in focus is also attributable to

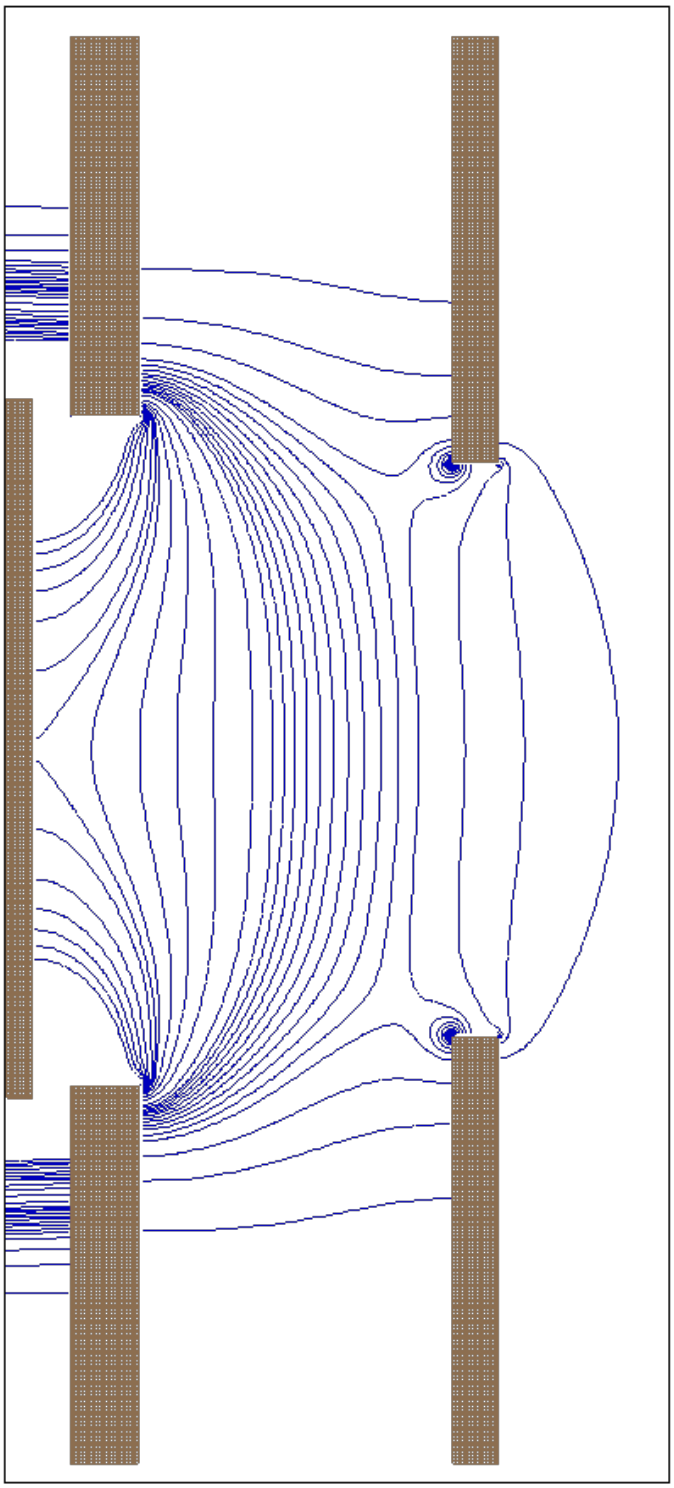

Figure 7.5: *SIMION simulation of the bare faced MCP geometry. Positive electric field lines are marked in blue. The face of the MCP (far left) is held at positive potential, while the MCP mount and pre-MCP ICD shield are held at ground.*

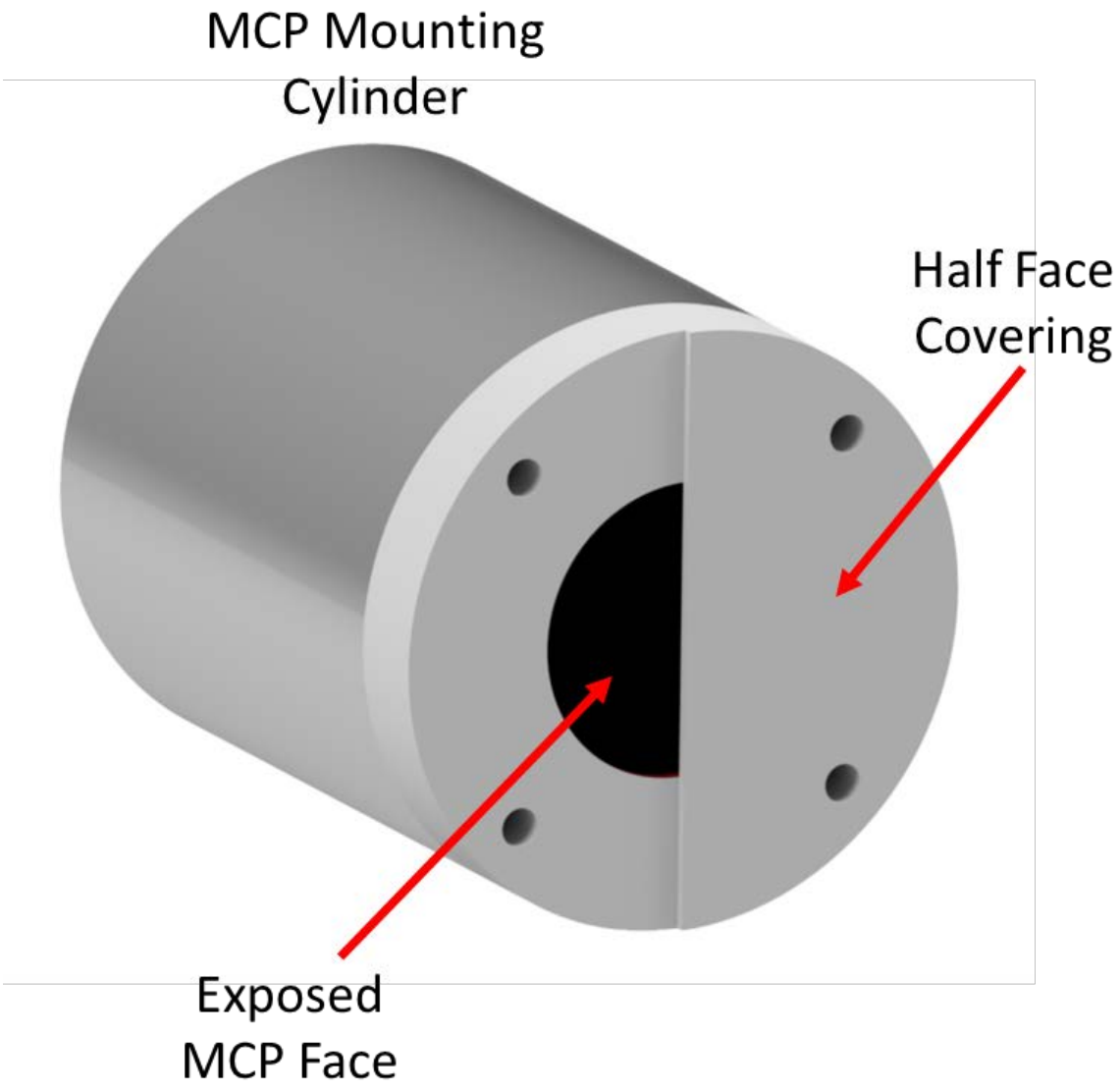

Figure 7.6: *MCP stack configured with half of the detector covered. Major components labeled.*

the smaller active area of the half covered MCP, resulting in sharper field lines to the detector center and a stronger focusing effect.

In addition to characterizing the patterns produced by the varying detector geometries, efficiency measurements were performed for all of the experiments previously discussed. Efficiency calculations are performed by comparing the number of incident particles (as recorded by the pre-MCP ICD) with the number of frames observed to contain signal from the phosphor screen. A summary of these efficiencies is recorded in Table 7.1 including a 95% confidence interval (CI) measurement. The Wilson Score[14,15] was used to calculate this confidence interval using the following form:

$$p = \frac{n_{true} + \left(\frac{z^2}{2}\right)}{n_{total} + z^2} \tag{7.1}$$

$$\sigma = \frac{z}{n + z^2}\sqrt{\frac{n_{true} * n_{false}}{n_{total}} + \left(\frac{z^2}{4}\right)} \tag{7.2}$$

where p is the calculated efficiency of the detector, σ is the confidence interval, n_{true} is the number of frames with signal, n_{total} is the total number of incident particles, $n_{false} = n_{total} - n_{true}$, and z is the z-score for the 95% confidence interval (1.96).

The uncovered detector and detector with mesh have a statistically similar detection efficiency but have very different patterns to the detected images. Difference in the electric focusing of the two detectors contributes to the difference in the image patterns. The slightly increased efficiency of the uncovered detector could also be attributed to the much smaller attractive region of the mesh-covered detector. Electric field lines of the MCP with mesh only

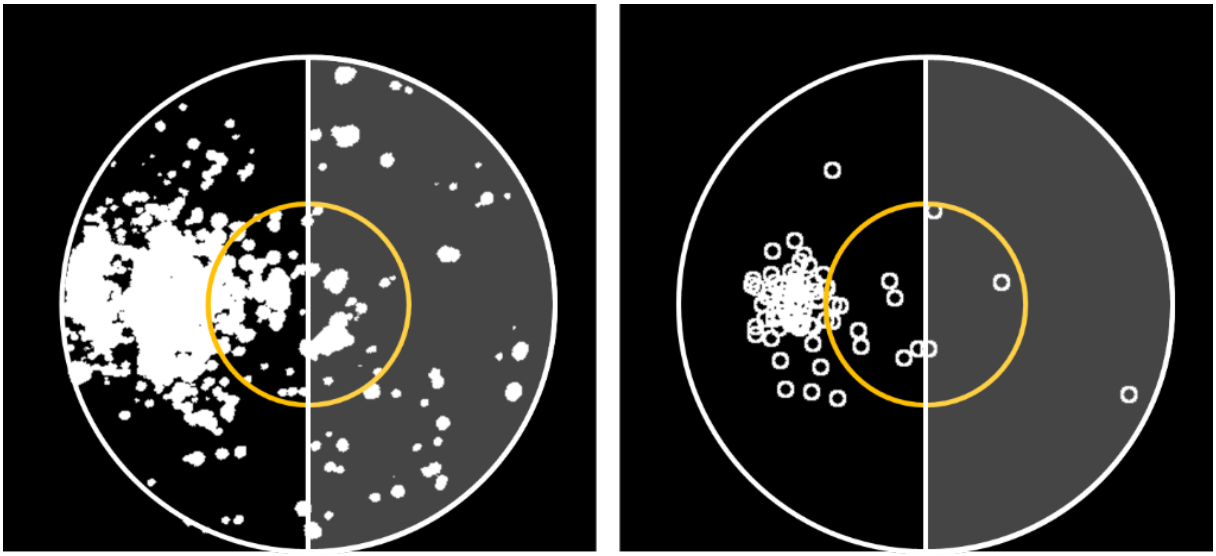

Figure 7.7: *Overlay of binary phosphor screen images from particles impacting an MCP detector with half-face cover. The outer diameter of the phosphor screen (25 mm) is shown as a white circle and the maximal beamline diameter (~10 mm) is shown as an orange circle. The covered area of the detector is shaded (right side). (Left) Overlay of 77 images with varying numbers of events. (Right) Overlay of centroid of all 77 images. The front plate voltage of the MCP was operated at 1.6 kV and the phosphor screen was operated at 6 kV.*

Table 7.1: *Efficiencies of different MCP configurations*

Description	Total Events	Signals	Efficiency (%)	95% CI (%)
Uncovered	305	49	16.5 %	4.1 %
With Mesh	1018	149	14.8 %	2.2 %
With Half Cover	397	77	19.7 %	3.9 %

extend ~3.8 mm from the front face before terminating at the grounded mesh, potentially restricting the ability of the detector to re-capture energetic ejecta after impact.

The higher (although still statistically similar) efficiency of the half-covered MCP suggest that the majority of measured signal from all geometries of the MCP are attributable to secondary ejecta rather than direct measurement of particle impact. Direct measurements of particle impact are most likely occurring in all geometries observed, but the initial sites of impacts appear to be obscured by multiple secondary signals. In the case of the half-exposed MCP these signals are more numerous than the direct measurements, leading to a centroid focus outside of the allowed impact region caused by electrical focusing from the front plate.

Contemporary work[3,4] has also measured the efficiencies of MCPs operating with particles of a similar mass and charge (iron pellets) at both higher and lower velocities. Lower velocity measurements (< 300 m/s) performed in Fontanese et. al. found an MCP detector efficiency of 6% (with a proposed error of 1%). Higher velocity measurements (> 2 km/s) performed in Gemer et. al. measured a significantly higher detector efficiency of 96%. The work of Fontanese et. al., Gemer et. al., and the experiments presented here show a trend of increasing efficiency with higher impact velocities even for these large submicron charged particles across a range of different particle compositions and experimental setups.

7.4 Conclusion

High velocity methanol/water ice particles impacted onto an MCP plate detector equipped with a phosphor screen have demonstrated the ability of using these detectors with high energy, large (>100 GDa) particles. These measurements are consistent with other contemporary work measuring MCP detector response with like-charge and similar mass species of a different composition, but extend charged particle detection techniques to much larger analytes than previously reported. Characterization of the post-acceleration beam in the AIS has been performed with image analysis of the resulting MCP detector signals. The MCP with phosphor screen detector presented here will be used in future measurements to improve the collimation of the post-accelerated particle beam. Future work will focus on creating a tighter beam using new injection optics and tighter initial beam size produced with the aerodynamics lens. Additional higher velocity measurements with similarly sized particles will also be performed to record MCP efficiencies up to space-relevant velocities where MCP detectors are applied for measurements of smaller particles.

7.5 References

(1) Schulte, P.; Arnold, F. Detection of Upper Atmospheric Negatively Charged Microclusters by a Rocket-Borne Mass Spectrometer. *Geophys. Res. Lett.* **1992**, *19* (23), 2297–2300. https://doi.org/10.1029/92GL02631.

(2) Burch, J. L.; Gombosi, T. I.; Clark, G.; Mokashi, P.; Goldstein, R. Observation of Charged Nanograins at Comet 67P/Churyumov-Gerasimenko. *Geophys. Res. Lett.* **2015**, *42* (16), 6575–6581. https://doi.org/10.1002/2015GL065177.

(3) Fontanese, J.; Clark, G.; Horányi, M.; James, D.; Sternovsky, Z. Microchannel Plate Efficiency to Detect Low Velocity Dust Impacts. *J. Geophys. Res. Sp. Phys.* **2018**, *123* (12), 9936–9940. https://doi.org/10.1029/2018JA025577.

(4) Gemer, A. J.; Sternovsky, Z.; James, D.; Horanyi, M. The Effect of High-Velocity Dust Particle Impacts on Microchannel Plate (MCP) Detectors. *Planet. Space Sci.* **2020**, *183* (December 2018), 104628. https://doi.org/10.1016/j.pss.2018.12.011.

(5) Wiza, J. L. Microchannel Plate Detectors. *Nucl. Instruments Methods* **1979**, *162*, 587–601. https://doi.org/10.1016/0029-554X(79)90734-1.

(6) Barat, M.; Brenot, J. C.; Fayeton, J. A.; Picard, Y. J. Absolute Detection Efficiency of a Microchannel Plate Detector for Neutral Atoms. *Rev. Sci. Instrum.* **2000**, *71*, 2050. https://doi.org/10.1063/1.1150615.

(7) Sinor, T. W.; Bender, E. J.; Chau, T.; Estrera, J. P.; Giordana, A.; Glesener, J. W.; Iosue, M. J.; Lin, P. P.; Rehg, S. New Frontiers in 21st Century Microchannel Plate (MCP) Technology: Bulk Conductive MCP-Based Image Intensifiers. In *Image Intensifiers and Applications II*; Johnson, C. B., Ed.; SPIE, 2000; Vol. 4128, p 5. https://doi.org/10.1117/12.405876.

(8) Fehre, K.; Trojanowskaja, D.; Gatzke, J.; Kunitski, M.; Trinter, F.; Zeller, S.; Schmidt, L. P. H.; Stohner, J.; Berger, R.; Czasch, A.; Jagutzki, O.; Jahnke, T.; Dörner, R.; Schöffler, M. S. Absolute Ion Detection Efficiencies of Microchannel Plates and Funnel Microchannel Plates for Multi-Coincidence Detection. *Rev. Sci. Instrum.* **2018**, *89* (4), 045112. https://doi.org/10.1063/1.5022564.

(9) Straub, H. C.; Mangan, M. A.; Lindsay, B. G.; Smith, K. A.; Stebbings, R. F. Absolute Detection Efficiency of a Microchannel Plate Detector for Kilo-Electron Volt Energy Ions. *Rev. Sci. Instrum.* **1999**, *70* (11), 4238–4240. https://doi.org/10.1063/1.1150059.

(10) Goruganthu, R. R.; Wilson, W. G. Relative Electron Detection Efficiency of Microchannel Plates from 0-3 KeV. *Rev. Sci. Instrum.* **1984**, *55* (12), 2030–2033. https://doi.org/10.1063/1.1137709.

(11) Fraser, G. W. The Ion Detection Efficiency of Microchannel Plates (MCPs). *Int. J. Mass*

Spectrom. **2002**, *215* (1–3), 13–30. https://doi.org/10.1016/S1387-3806(01)00553-X.

(12) Burch, J. L.; Gombosi, T. I.; Clark, G.; Mokashi, P.; Goldstein, R. Observation of Charged Nanograins at Comet 67P/Churyumov-Gerasimenko. *Geophys. Res. Lett.* **2015**, *42* (16), 6575–6581. https://doi.org/10.1002/2015GL065177.

(13) Zhang, Z.; Gao, J.; Zhang, S. Heat and Mass Transfer of the Droplet Vacuum Freezing Process Based on the Diffusion-Controlled Evaporation and Phase Transition Mechanism. *Sci. Rep.* **2016**, *6* (1), 35324. https://doi.org/10.1038/srep35324.

(14) Wilson, E. B. Probable Inference, the Law of Succession, and Statistical Inference. *J. Am. Stat. Assoc.* **1927**, *22* (158), 209–212. https://doi.org/10.1080/01621459.1927.10502953.

(15) Brown, L. D.; Cai, T. T.; Dasgupta, A. Interval Estimation for a Binomial Proportion. *Stat. Sci.* **2001**, *16* (2), 101–133. https://doi.org/10.1214/ss/1009213286.

Chapter 8. Enceladus Ice Particle Analog Production

8.1 Introduction

The Cassini-Huygens interplanetary mission advanced our understanding of the Saturn system with more than a decade-long residence around the planet and its moons. During this mission a large plume of icy particles were found emanating from the southern pole of Enceladus, a moon of Saturn.[1,2] This observation and subsequent studies of this plume have shown strong evidence for a global subsurface ocean being the origin of the icy ejecta.[3] The sampling of this plume has both geologic and astrobiologic implications with the convenience of being able to probe this information from orbit. Using the instruments available aboard Cassini, a series of studies[4–7] to examine particle composition were performed identifying a variety of grain types including evidence of complex high-mass organic components in certain grains.[8] Spectrometric resolution to study high mass constituents was limited and therefore future missions to probe the Enceladus plume have become a significant focus in the exploration of ocean worlds.[9]

An essential element of planning for future missions is the evaluation of instrumentation proposed for characterization of the ejecta plume. This builds on the effort to produce and experimentally characterize laboratory analogs to the constituents of the plume used to understand the data by Cassini, and it continues to be an area of considerable focus.[10,11] Ice particles previously observed in the Enceladus plume are primarily composed of water and 100

nm to 10 μm in diameter.[4,10,12] Other components including salts and high mass organics are of key interest to understanding the origins and environments that produce the ejected aerosols. Creation of laboratory analog particles like those found previously by Cassini is possible with the AIS by spraying liquid water that is subsequently vacuum frozen. The ESI source used by the AIS uses solutions that can be created to simulate different concentrations of secondary components within these ice particles. Particles produced with the AIS can be accelerated to high velocities and injected into vacuum-compatible instruments to test instrument efficacy in identifying particle components and response to single particle impacts. Future missions have the potential to achieve a wide variety of interaction velocities with plume-based particles. The orbital velocity of the space craft is usually significantly greater than the initial velocity achieved by the particles exiting the moon.[13] Creating particles over a wide range of potential interaction velocities allows the AIS to examine a variety of different interactions that could occur in future missions.

In addition to providing an experimental platform for testing instrument response in the laboratory, the impact dynamics of the ice particles produced by the AIS have been examined. Experimental measurements of the scattering, fracture and adherence of ice particles in collisions with surfaces can aid in the design of particle collectors in sampling instruments. This analysis is demonstrated for a subset of particle impact velocities using the AIS. Micron- to submicron-sized ice particles have been impacted onto a hard target and the post impact dynamics measured using image charge detection techniques, such as those applied in Chapter 5, with additional analysis for the assessment of particle fragmentation thresholds. Previous investigations of large ice particle impacts have noted velocity dependent behavior in the fractionation and post-fragment behavior of ice particles impacting a hard target.[14] The

experiments performed here are compared to predictions made from studies of the impact of much larger ice particles. These experiments not only demonstrate the production of ice grains with the AIS for use in space-relevant instrument qualifications, but also the impact dynamics of these submicron- to micron-sized ice particles.

8.2 Experimental Methods

Ice particle generation was performed using the AIS ESI source. In order to create pure water-ice, solutions of deionized water were sprayed into vacuum. Freezing of these particles in vacuum was desired, so no post-injection heating was used in the particle source. Changes in the voltage (between 2-3.5 kV) and location of the electrospray needle (5-15 mm away from orifice) have been used to control the size distribution of water-ice particles. Particle size distributions of the ice particles were calculated from ensembles of individual particle mass measurements taken in the NET. Two different diameter particle distributions are shown in Figure 8.1.

Upon injection into vacuum, rapid evaporative cooling of the liquid droplets is expected to occur. Modeling[15] and experiments[16] examining the freezing rate of water droplets on the order of 10 μm in vacuum have both shown that droplet freezing happens < 10 ms in pressures higher than those in most regions of the AIS. Before being trapped for spectrometric characterization in the NET, particles travel ~1.75 m from initial formation in the electrospray.

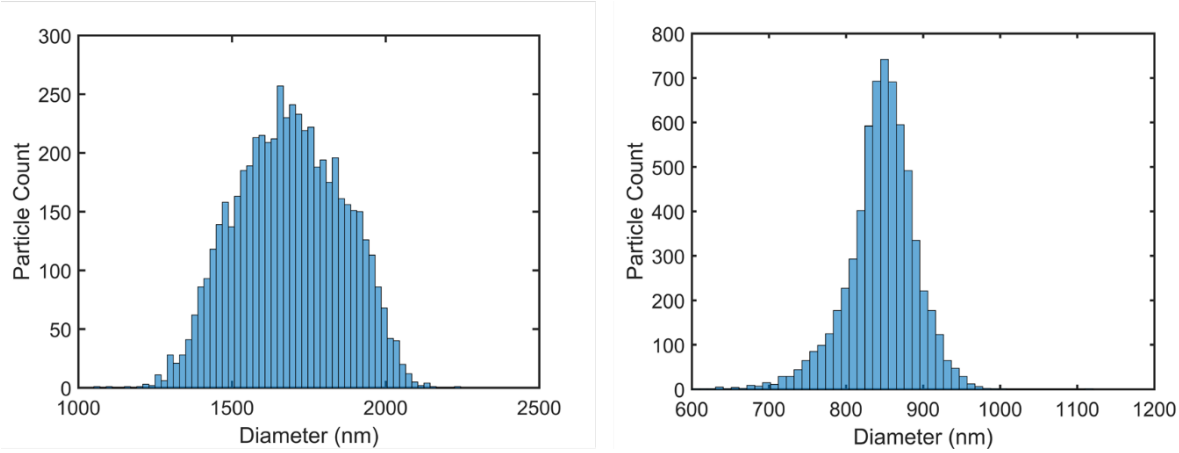

Figure 8.1: *Two different ice particle diameter distributions produced using different ESI conditions. (left) Distribution of ice particles with a mean diameter of ~1700 nm. (right) Distribution of particles with a mean diameter of ~850 nm.*

Particle velocities measured in the NET for the two diameters presented above averaged 83 m/s for the larger diameter particles and 98 m/s for the smaller diameter particles (both with a full-width-half-max < 6 m/s). These velocities are representative of particle velocity as they traverse the instrument, as velocities are not expected to change significantly in the relatively high-pressure aerodynamic lens. Before entering the NET, particles will therefore have already spent more than 15 milliseconds traveling through vacuum and are expected to be frozen. When operating in per-particle analysis mode (PPAM, see Chapter 2), particles spend an additional ~300 ms oscillating in the NET, allowing additional time for freezing before acceleration. The creation of frozen particles is additionally supported by the impact experiments reported in the Results and Discussion Section below that show particles readily rebounding from a hard impact target at velocities > 100 m/s, whereas liquid water particles have been shown to stick and spread upon surfaces.[17]

Both PPAM and Mode-D operational modes have been used to accelerate ice particles in the AIS (see Chapter 2). PPAM has been used to characterize particle impact dynamics paired with individual particle spectrometric information, while Mode-D has been used to demonstrate the highest accelerated velocities achieved in the AIS. When examining the impact dynamics of the ice particles studied here, the impact detector setup detailed in Chapter 4 and 5, the TICD and CAT, was used. Ice particles of velocities 50 – 900 m/s were impacted onto a highly polished molybdenum target, and their post impact behavior and trajectories were measured.

8.3 Results and Discussion

The particles generated in this experiment were used characterize the impact dynamics of micron sized ice particles over a wide velocity range. However, these velocities are less than what is needed for the production of ice particle analogs with realistic velocities. The following section details what is required to achieve the desired velocities followed by a discussion of the ice particle behavior observed over a lower velocity range.

8.3.1 Reaching Desired Ice Particle Velocity

In order to accelerate particles to the analogous velocity conditions expected in future orbital missions, final velocities of ~5 km/s are desired. In order to achieve higher velocities with the AIS LINAC, additional acceleration stages have been added to increase the limit of total energy applied to a particle during acceleration. Current electrical hardware permits each stage of the LINAC to operate at potentials up to 10 kV. The final velocity of a particle after acceleration with the LINAC can be calculated using the following:

$$v_f = v_i \sqrt{\frac{nV_L + V_{init}}{V_{init}}} \tag{8.1}$$

where v_f is the final velocity, v_i is the initial velocity, n is the number of acceleration elements used, V_L is the potential applied to each element of the LINAC (the potential applied to the particle per-charge), and V_{init} is the initial kinetic energy per charge of the particle. Initial

kinetic energy per charge is easily determined in these experiments by the potential applied to the quadrupole deflector. Maximal post-acceleration velocity with the current LINAC configuration is achieved when the number of elements in the LINAC is maximized and the initial kinetic energy per charge of the particles is minimized. In order to increase the number of stages used, a 20 element LINAC was installed with an additional 20 stages planned for further expansion. The 20 element LINAC has been shown to be capable of accelerating 850 nm ice particles up to velocities of ~2.5 km/s. The ice particles generated at this diameter have an initial kinetic energy per charge of ~250 eV/q and initial velocity of ~98 m/s. The final velocities achieved are slightly lower than the velocity predicted by Equation 8.1 (~2.75 km/s). This overprediction stems from drop in the amplitude of the pulse train produced for the LINAC across the 20 pulse sequence of ~15% when operating at 9 kV.

A 40 element LINAC would bring particles of similar properties to velocities of ~3.9 km/s. In order to achieve a velocity of 5 km/s, additional reduction of the ice particle kinetic energy per charge is desired. This potential is determined by:

$$V_{init} = \frac{m v_i^2}{2q} \tag{8.2}$$

where m is the mass of the ice particle and q is the particle charge. From the combination of Equations 8.1 and 8.2, and since $nV_L \gg V_{init}$, the final velocity is approximately:

$$v_f \approx \sqrt{\frac{2qnV_L}{m}} \tag{8.3}$$

In order to maximize v_f by changing the particle, the mass can be lowered, and the charge increased. However, when creating charged particles with electrospray ionization, an upper

limit for the amount of charge that can be deposited on a single aerosolized particle is governed by the Rayleigh limit, a size dependent phenomenon:[18]

$$q < 8\pi\sqrt{\epsilon_0 \gamma a^3} \tag{8.4}$$

where ϵ_0 is the permittivity of vacuum, γ is the surface tension of the liquid being used, and a is the particle radius. The amount of charge on an ESI-produced droplet is expected to be less than this limit which is governed by the surface tension of the liquid, otherwise Coulombic fission of the droplet will occur and charge will be removed with material until this limit is satisfied. In order to attain minimal initial electric potential, droplets with $\sim 8\pi\sqrt{\epsilon_0 \gamma a^3}$ amount of charge are desired. When combining Equations 8.3 and 8.4, it becomes evident that $v_f \sim a^{-3/4}$ when calculating mass from material density and particle volume $\left(\frac{4}{3}\pi a^3\right)$. Therefore, smaller sized particles yield higher final velocities. In order to calculate the particle size required to achieve ~5 km/s acceleration with a 40 stage accelerator, and 400 kV total acceleration potential, the density of water (~1000 kg/m^3), and surface tension of water in vacuum (~0.073 N/m)[19] can be used with Equations 8.3 and 8.4 to determine a resulting diameter of ~575 nm. Future work with the 40 stage LINAC will focus on producing particles of this size and demonstrating 5 km/s final velocities.

8.3.2 Impact Dynamics of Ice Particles

In addition to direct instrument characterization, the AIS can examine how ice particles will interact with collector surfaces. These measurements include how particles bounce off surfaces at low velocities, and how particles fragment. For the two particle sizes shown in Figure 8.1, individual particle measurement of the CoR was performed between 30-300 m/s. The velocity-dependent average CoR generated from this data is shown in Figure 8.2. The two particle diameters are statistically similar at every point where the CoR was measured. Observations of rebound behavior above this limit are explored for the water-ice examined in this experiment by measuring the distribution of charge among an array of detectors after initial particle impact. The detector used in this experiment is the same four-channel detector introduced in Chapter 4, with three concentric rebound charge detectors, and a charge-sensitive target. Using this detector arrangement, three different post-impact behaviors were identified for the ice particles: rebound from the target, impact and sticking to the target, impact and fragmentation. An overview of signals measured for each type of behavior is presented in Figure 8.3.

The primary signal of interest for determining the post-impact behavior of the ice particles studied here is from the impact target. The shape of the target signal, post impact, is indicative of the velocity of a particle rebounding from the target, where sharp peaks indicate a faster rebound (moving away from the target more quickly), broader peaks indicate a slower rebound, and a long slow tail indicates discharge through the target circuitry (characteristic to detector electronics), consistent with the particle sticking to the target. In Figure 8.3A, signal on the target is a sharp peak associated with the particle rapidly approaching the face of the

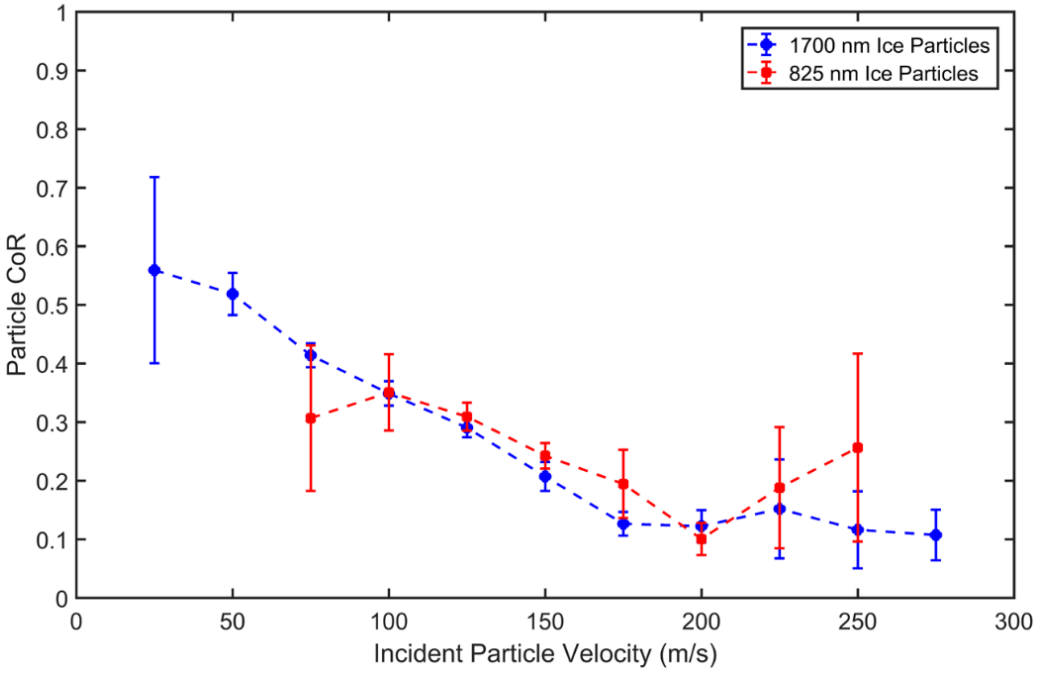

Figure 8.2: *Average CoR for 1700 nm and 850 nm ice particles. Incident velocity is grouped into bins of 25 m/s. The error bars of each bin are determined from the 95% confidence interval of each bin CoR measurements. Each bin contains at least 3 events.*

Figure 8.3: *TICD (blue, red, and yellow) and CAT (purple) temporal signals for water-ice particles. A) Temporal signals of ice particle impacting the CAT and rebounding on a low-angle trajectory back through the TICD. B) Temporal signals for ice particle impacting the CAT and sticking, discharging through the target. C) Temporal signals ice particle impacting the CAT, breaking apart, with some fragment sticking to the target, and some fragment rebounding back through the TICD before returning to the target. D) Temporal signals for ice particle impacting the CAT, breaking apart, with some fragment sticking to the target, and some fragment rebounding into the TICD. Note the three separate signals on the CAT signal after initial impact, consistent with formation of multiple fragments.*

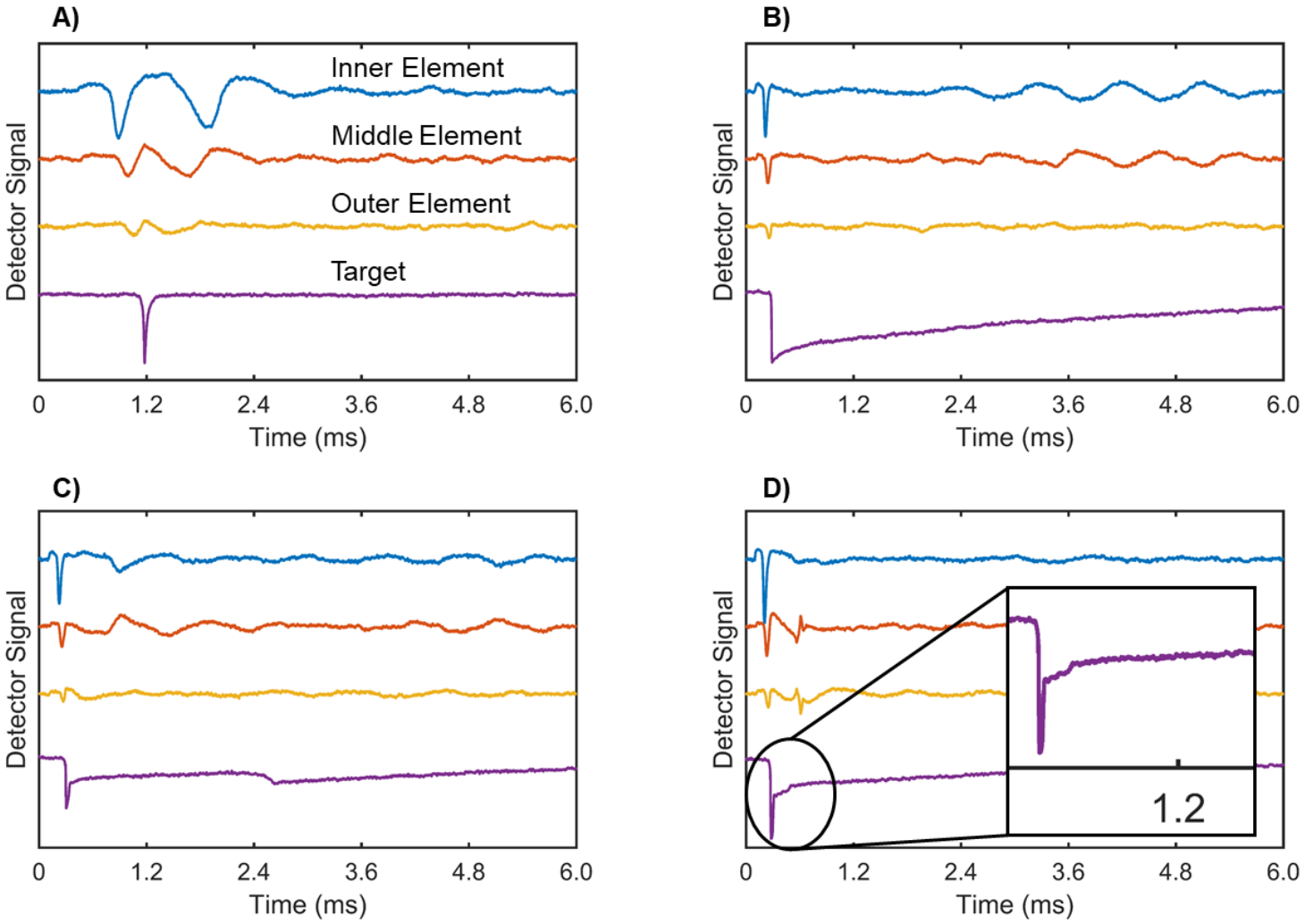
A)
Inner Element
Middle Element
Outer Element
Target
Detector Signal
0
1.2
2.4
3.6
4.8
6.0
Time (ms)
B)
Detector Signal
Time (ms)
C)
Detector Signal
Time (ms)
D)
Detector Signal
1.2
Time (ms)

target, impacting, and bouncing back away from the target. The particle is observed for a second time on the three elements of the TICD after it has impacted the target. The rebound signal on the TICD elements is roughly equal in magnitude compared to the incident signal and occurs in the reverse time order because the direction of the particle travel has changed. In Figure 8.3B the particle impacts the target and fully discharges through the feedback circuitry of the target detector, seen as a low frequency return to baseline. This signal is not accompanied by a fast return to baseline, which is indicative of charge leaving the target, but rather all charge that impacts the target is discharged through the target detector. The two waveforms described in Figure 8.3A and 8.3B have previously been examined in Chapter 4 and ref [20], but are included to highlight the differences found in Figure 8.3C and 8.3D.

Figure 8.3C demonstrates evidence for particle fragmentation after impact with the target. The initial impact of the particle is followed by a partial return of the output signal to detector baseline at 0.4 ms. This is only a partial return to baseline, where the sharp peak occurs in concert is with a lower amplitude long slow tail similar to that observed in Figure 8.3B (sticking to the target). In this case, only part of the incident charge is deposited on the target, and the remaining charge bounces away. The rebounding partial charge can been seen as a broad low amplitude signal on both the middle and inner elements between 0.8-1.6 ms (the signal amplitude is too low to be detected on the outer element). This charge carrier bounces back through to the inner element, impacting that element, and bouncing again before returning to the target at 2.6 ms, depositing the remaining charge. This signal demonstrates the tracking of two separate charge carriers created after impact with the target, and is evidence of particle fragmentation after impact where each fragment is a charge carrier. Another signal categorized in the same manner is shown in Figure 8.3D. The initial impact of the particle is followed by

three separate signal features: a sharp peak that partially returns to baseline indicative of some charge carrier rebounding from the target, a lower amplitude slow tail that extends to 0.6 ms where a break is observed. This is consistent with a partial charge carrier rebounding slowly from the target and is followed by another feature of a long slow tail consistent with discharge a fraction of the initial charge onto the target. These three distinct temporal signatures on the target and the post-impact partial charge signals detected on the middle and outer elements of the TICD are also indicative of the particle breaking apart upon impact and producing multiple charge carriers that either stick or rebound. A detailed analysis of these fragmentation events will require a more complex multiplexed detector with higher angular resolution than the detector used in this study.

In addition to the signal analysis presented for Figure 8.3C and D, particle fragmentation detection from the TICD and CAT is supported by the velocity dependence shown by these events. In Figure 8.4 the three major event types outlined in Figure 8.3 (particle rebound from the target, particle sticking to the target, and particle fragmentation after impact) are measured for over 1000 impacts, using 850 nm ice particles, with impact velocities between 40 and 880 m/s. The fraction of each event type is displayed for each 40 m/s incident velocity bin. Particle rebound from the target only occurs at lower velocities and these rebounds produce the CoR measurements recorded in Figure 8.2. A small number of events that rebound between 280 and 360 m/s are not shown in the CoR measurements in Figure 8.2 as these events appear to rebound with high-angle trajectories outside of the detection range of the TICD. At slightly higher velocities, the vast majority of particles stick to the impact target and fully discharge through the target feedback circuitry. Finally, as particle incident velocity increases above 300 m/s, the number of fragmentation events increases until it becomes the dominant event at the highest

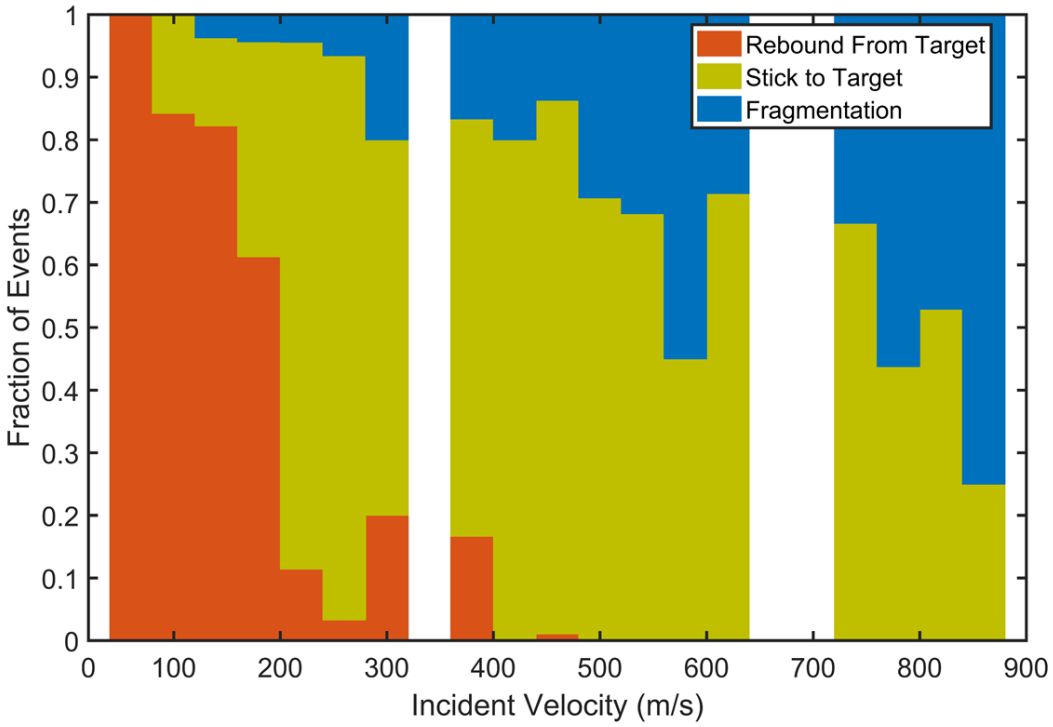

Figure 8.4: *Post-impact behavior of 850 nm ice particles. Each bar contains at least 5 events from a total event amount of ~1040 particles and is grouped into 40 m/s incident velocity bins.*

velocities measured here. Areas of the chart left blank indicate that insufficient data were collected in those velocity ranges, whereas all other velocity bins have a minimum of 5 events total.

The events like those displayed in Figure 8.3 are possibly not capturing every fragmentation event that is occurring after impact. If all charge carriers impact the same detector or travel with similar velocities into the same detector, the signal created by the TICD and CAT could not be differentiated from a single particle with the same trajectory. Additionally, if fragments are created without a significant amount of charge, the uncharged species are invisible to this charge-sensitive technique. Although these other possible behaviors can occur, from these measurements it is possible to assign coarse fragmentation limits for comparison to previous work. Above ~400 m/s the fragmentation events noted on the TICD and CAT begin to make up a significant fraction (> 20 %) of total events and eventually become the dominant event above ~700 m/s. Previous studies examining the fragmentation limits of larger (> 10 μm) ice particles have noted a size dependent behavior for fragmentation thresholds.[14] Hauk optically characterized ice particle fragmentation limits for particles 30 μm to 3.5 mm in size after impacting a rigid surface. The particles studied were aerodynamically accelerated to velocities that induced fragmentation for each particle size. Three different fragmentation modes were noted by Hauk: minor fragmentation where the particle loses up to 20 % of its original volume as fragments(s); major fragmentation where the particle loses between 20-50% of its original volume as fragment(s); and catastrophic fragmentation where the particle loses > 50% of its original volume as fragment(s). The fragmentation limit observations proposed by Hauk are extrapolated down to the 850 nm diameter particles studied by the AIS in Figure 8.5. The limit above which all particles fragment (minor, major, and

catastrophic) as extrapolated from Hauk is ~300 m/s. A second limit proposed by Hauk occurs when particles exclusively undergo major/catastrophic fragmentation. When extrapolated to an 850 nm diameter particle, this occurs at 640 m/s. The limits created by Hauk agree well with the limits observed in Figure 8.4 where above 300-400 m/s particles cease rebounding from the impact target and clear fragmentation events on the CAT begin to become significant and above ~700 m/s fragmentation events begin to dominate the total fraction of events. Many of the sticking events observed between 300-700 m/s could be producing smaller fragments, like the minor fragmentation noted by Hauk, but without significant charge being lost from those fragments. The major fragmentation limit has a higher likelihood of carrying away significant amounts of charge as the fragments produced are significantly larger (in total volume) and can therefore be more readily identified by the charge-sensitive detection techniques demonstrated here. Future studies will examine this behavior for other particle sizes in the AIS and expand the velocity range to include all space-relevant velocities up to 5 km/s.

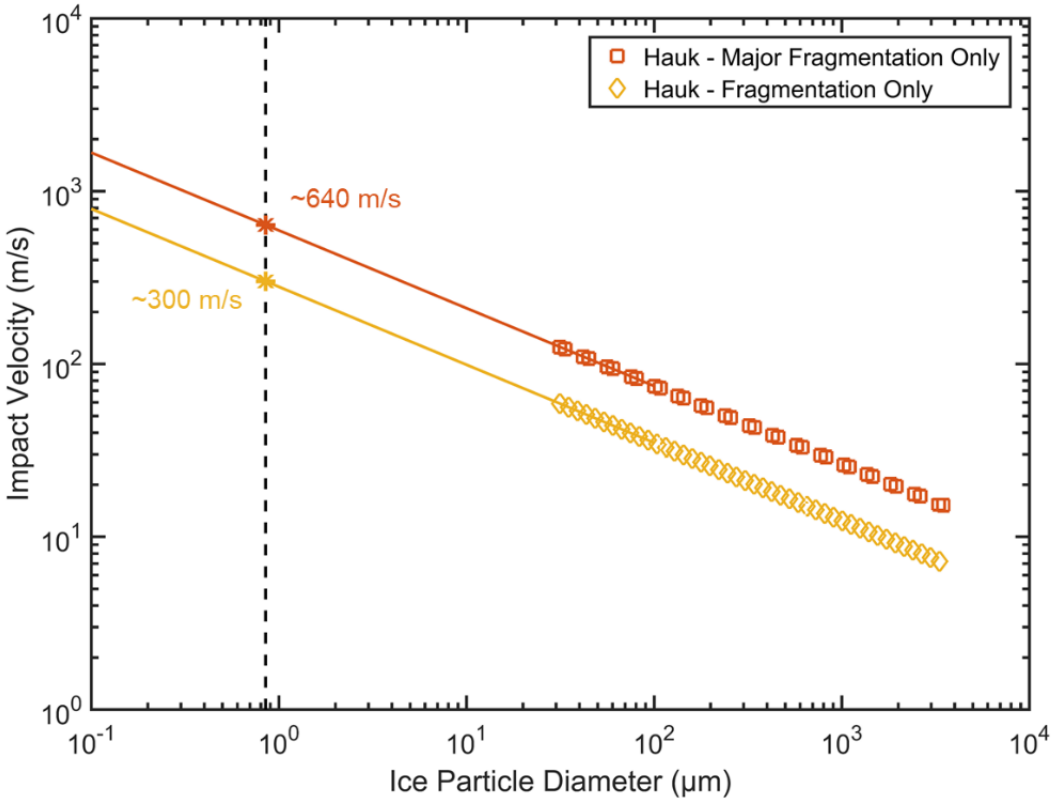

Figure 8.5: *Thresholds of fragmentation extracted from Hauk. Points (red squares and yellow diamonds) are extracted from trendlines in Hauk and fitted with extrapolating lines (solid red and yellow) to lower particle diameters. Limits at particle sizes of 850 nm (dashed line) are shown with stars.*

8.4 Conclusion

Production of ice grains analogous in size to those previously observed in space-flight missions has been demonstrated in the AIS. The capacity for making particles of varying composition with ESI and having single particle characterization makes the AIS well suited to test future mission equipment with laboratory ice particle analogs. Demonstration of the AIS feasibility for generating hypervelocity particles up to ~5 km/s has been shown and lower velocity impacts of particles have been characterized. Application of the unique measurement capabilities of the TICD and CAT for the study of particle-surface impact and fragmentation dynamics were demonstrated and compared to previous studies of water-ice particle impacts. Future work will explore reaching significantly higher energy impact velocities up to 5 km/s with an expanded LINAC, and the fragmentation observation capabilities of the TICD and CAT will be applied to higher velocities.

Acknowledgements

Chapter 8 is a manuscript in preparation with authors Miller, M.E.C.; Burke, S.; Continetti, R.E., with the working title Impact Studies of Hypervelocity Micron Water-Ice. The dissertation author is the primary author and the dissertation advisor is the corresponding author.

8.5 References

(1) Porco, C. C.; Helfenstein, P.; Thomas, P. C.; Ingersoll, A. P.; Wisdom, J.; West, R.; Neukum, G.; Denk, T.; Wagner, R.; Roatsch, T.; Kieffer, S.; Turtle, E.; McEwen, A.; Johnson, T. V.; Rathbun, J.; Veverka, J.; Wilson, D.; Perry, J.; Spitale, J.; Brahic, A.; Burns, J. A.; DelGenio, A. D.; Dones, L.; Murray, C. D.; Squyres, S. Cassini Observes the Active South Pole of Enceladus. *Science (80-.).* **2006**, *311* (5766), 1393–1401. https://doi.org/10.1126/SCIENCE.1123013.

(2) Hansen, C. J.; Esposito, L.; Stewart, A. I. F.; Colwell, J.; Hendrix, A.; Pryor, W.; Shemansky, D.; West, R. Enceladus' Water Vapor Plume. *Science* **2006**, *311* (5766), 1422–1425. https://doi.org/10.1126/science.1121254.

(3) Collins, G. C.; Goodman, J. C. Enceladus' South Polar Sea. *Icarus* **2007**, *189* (1), 72–82. https://doi.org/10.1016/J.ICARUS.2007.01.010.

(4) Postberg, F.; Kempf, S.; Hillier, J. K.; Srama, R.; Green, S. F.; McBride, N.; Grün, E. The E-Ring in the Vicinity of Enceladus: II. Probing the Moon's Interior—The Composition of E-Ring Particles. *Icarus* **2008**, *193* (2), 438–454. https://doi.org/10.1016/J.ICARUS.2007.09.001.

(5) Jones, G. H.; Arridge, C. S.; Coates, A. J.; Lewis, G. R.; Kanani, S.; Wellbrock, A.; Young, D. T.; Crary, F. J.; Tokar, R. L.; Wilson, R. J.; Hill, T. W.; Johnson, R. E.; Mitchell, D. G.; Schmidt, J.; Kempf, S.; Beckmann, U.; Russell, C. T.; Jia, Y. D.; Dougherty, M. K.; Waite, J. H.; Magee, B. A. Fine Jet Structure of Electrically Charged Grains in Enceladus' Plume. *Geophys. Res. Lett.* **2009**, *36* (16), L16204. https://doi.org/10.1029/2009GL038284.

(6) Teolis, B. D.; Perry, M. E.; Magee, B. A.; Westlake, J.; Waite, J. H.; Teolis, C. : Detection and Measurement of Ice Grains and Gas Distribution in the Enceladus Plume by Cassini's Ion Neutral Mass Spectrometer. *J. Geophys. Res* **2010**, *115*, 9222. https://doi.org/10.1029/2009JA015192.

(7) Yaroshenko, V. V.; Ratynskaia, S.; Olson, J.; Brenning, N.; Wahlund, J.-E.; Morooka, M.; Kurth, W. S.; Gurnett, D. A.; Morfill, G. E. Characteristics of Charged Dust Inferred from the Cassini RPWS Measurements in the Vicinity of Enceladus. *Planet. Space Sci.* **2009**, *57* (14–15), 1807–1812. https://doi.org/10.1016/J.PSS.2009.03.002.

(8) Postberg, F.; Khawaja, N.; Abel, B.; Choblet, G.; Glein, C. R.; Gudipati, M. S.; Henderson, B. L.; Hsu, H.-W.; Kempf, S.; Klenner, F.; Moragas-Klostermeyer, G.; Magee, B.; Nölle, L.; Perry, M.; Reviol, R.; Schmidt, J.; Srama, R.; Stolz, F.; Tobie, G.; Trieloff, M.; Waite, J. H. Macromolecular Organic Compounds from the Depths of Enceladus. *Nature* **2018**, *558* (7711), 564–568. https://doi.org/10.1038/s41586-018-0246-4.

(9) Hendrix, A. R.; Hurford, T. A.; Barge, L. M.; Bland, M. T.; Bowman, J. S.; Brinckerhoff, W.; Buratti, B. J.; Cable, M. L.; Castillo-Rogez, J.; Collins, G. C.; Diniega, S.; German, C. R.; Hayes, A. G.; Hoehler, T.; Hosseini, S.; Howett, C. J. A.; McEwen, A. S.; Neish, C. D.; Neveu, M.; Nordheim, T. A.; Patterson, G. W.; Patthoff, D. A.; Phillips, C.; Rhoden, A.; Schmidt, B. E.; Singer, K. N.; Soderblom, J. M.; Vance, S. D. The NASA Roadmap to Ocean Worlds. *Astrobiology* **2019**, *19* (1), 1–27. https://doi.org/10.1089/ast.2018.1955.

(10) Postberg, F.; Kempf, S.; Schmidt, J.; Brilliantov, N.; Beinsen, A.; Abel, B.; Buck, U.; Srama, R. Sodium Salts in E-Ring Ice Grains from an Ocean below the Surface of Enceladus. *Nature* **2009**, *459* (7250), 1098–1101. https://doi.org/10.1038/nature08046.

(11) Klenner, F.; Postberg, F.; Hillier, J.; Khawaja, N.; Stolz, F. Analogue Spectra for Impact Ionization Mass Spectra of Water Ice Grains Obtained at Different Impact Speeds in Space. In *EPSC-DPS 2019*; 2019; Vol. 13, pp 564–568.

(12) Postberg, F.; Schmidt, J.; Hillier, J.; Kempf, S.; Srama, R. A Salt-Water Reservoir as the Source of a Compositionally Stratified Plume on Enceladus. *Nature* **2011**, *474* (7353), 620–622. https://doi.org/10.1038/nature10175.

(13) Teolis, B. D.; Perry, M. E.; Hansen, C. J.; Waite, J. H.; Porco, C. C.; Spencer, J. R.; Howett, C. J. A. Enceladus Plume Structure and Time Variability: Comparison of Cassini Observations. *Astrobiology* **2017**, *17* (9), 926–940. https://doi.org/10.1089/ast.2017.1647.

(14) Hauk, T. Investigation of the Impact and Melting Process of Ice Particles, Technischen Universität Darmstadt, Darmstadt, 2016.

(15) Zhang, Z.; Gao, J.; Zhang, S. Heat and Mass Transfer of the Droplet Vacuum Freezing Process Based on the Diffusion-Controlled Evaporation and Phase Transition Mechanism. *Sci. Rep.* **2016**, *6* (1), 35324. https://doi.org/10.1038/srep35324.

(16) Shin, H. T.; Lee, Y. P.; Jurng, J. *Spherical-Shaped Ice Particle Production by Spraying Water in a Vacuum Chamber*.

(17) Willem Visser, C.; Tagawa, Y.; Sun, C.; Lohse, D. Microdroplet Impact at Very High Velocity. https://doi.org/10.1039/c2sm26323h.

(18) Rayleigh, Lord. XX. On the Equilibrium of Liquid Conducting Masses Charged with Electricity. *Philos. Mag. Ser. 5* **1882**, *14* (87), 184–186. https://doi.org/10.1080/14786448208628425.

(19) Zhang, Y.; Feller, S. E.; Brooks, B. R.; Pastor, R. W. Computer Simulation of Liquid/Liquid Interfaces. I. Theory and Application to Octane/Water. *J. Chem. Phys.* **1995**, *103* (23), 10252–10266. https://doi.org/10.1063/1.469927.

(20) Miller, M. E. C.; Mezher, M.; Continetti, R. E. Tapered Image Charge Detector for

Measuring Velocity Distributions of Submicrometer Particle Scattering. *Rev. Sci. Instrum.* **2020**, *91* (6), 063305. https://doi.org/10.1063/1.5142207.

Appendix A. Circuit Diagrams

A.1 Apparatus Control

To control the variety of high voltage switches, function generators, and other peripherals operating during experiments on the AIS, most control signals are produced using the FPGA/digitizer on DAQ1. The digitizer (NI 5731) has 12 digital input/output ports that are used to control the various parts of a given experiment. In order to partially isolate and buffer the digitizer during operation, a configurable buffering circuit is used to mediate these digital ports when required to output signal. This is particularly desired when the logical pulses produced are used to control high voltage switching where the possibility of arcing or feedback could destroy an unprotected line and the switch circuits required use much higher currents than the digital outputs of the NI 5731 are capable of delivering. Figure A.1 shows the circuit diagram for an individual digital port, that with a selectable jumper receives a direct input, or outputs a signal that is buffered and polarity reversible with an external toggle switch. A high speed MOSFET driver (TC4426) is used to buffer the signal (internal diagram not shown) with delays ~40 ns. Being able to rapidly re-configure the polarity of a logical output line allows easy polarity reversal of both acceleration and trapping switches using only hardware changes. 12 of the circuits displayed in Figure A.1 are combined onto a single custom printed circuit board (PCB), the design of which is shown in Figure A.2. This PCB is mounted into a chassis equipped with 12 coaxial input ports, and 12 coaxial output ports.

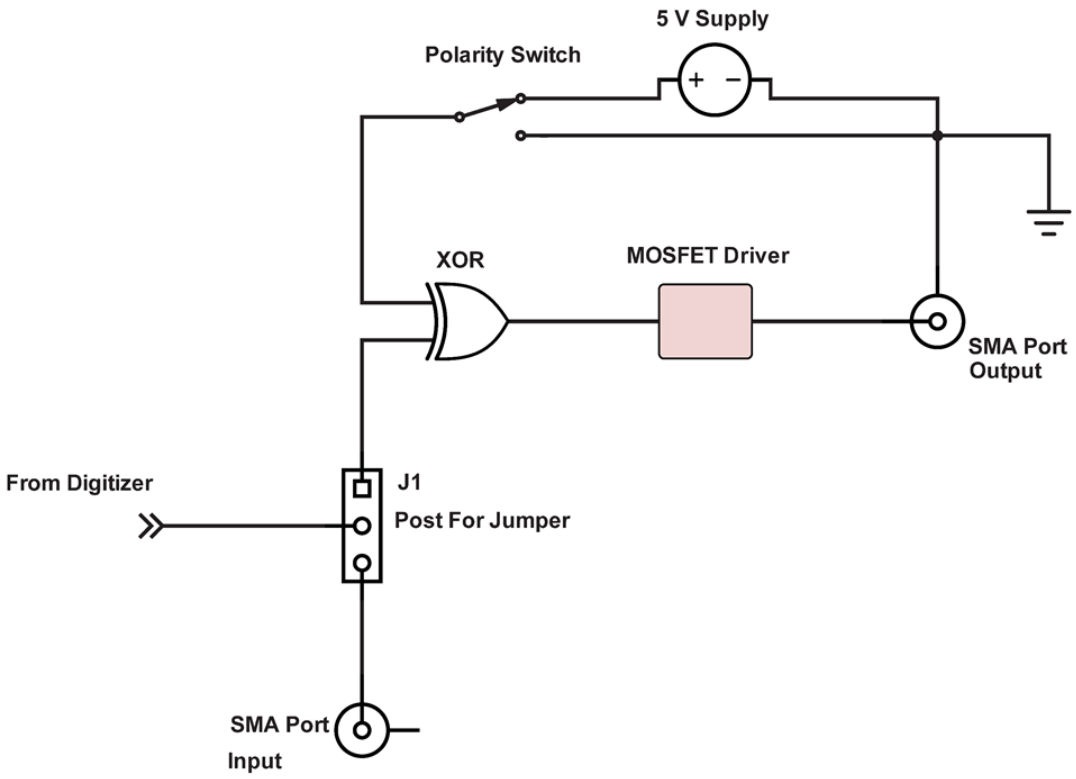

Figure A.1: *Diagram of digital port buffer.*

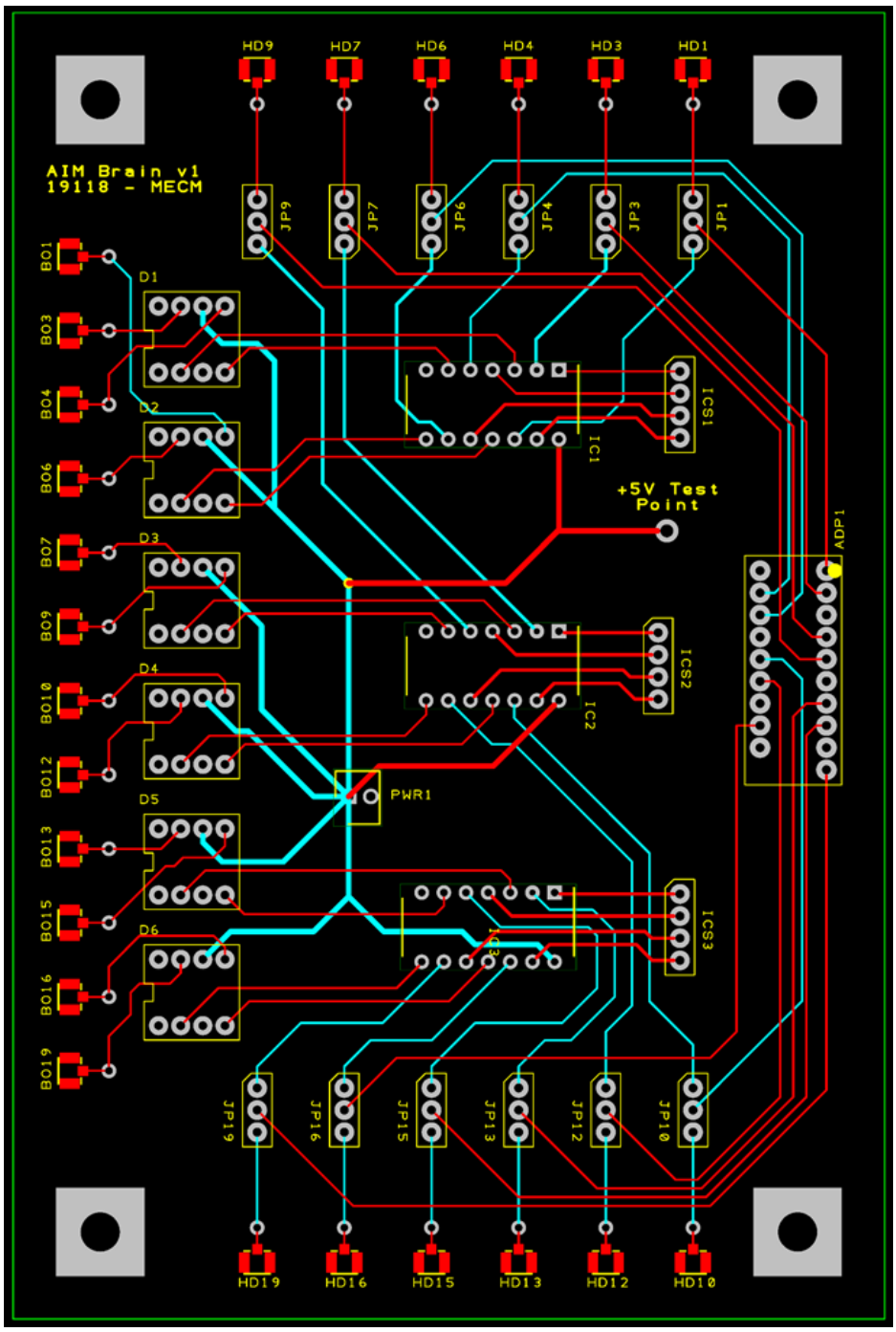

Figure A.2: *Diagram of custom buffer PCB. Color key: silkscreen – yellow, top copper – red, bottom copper – blue, pads – silver. Free space in board contains copper fill on top and bottom (not pictured) as grounding plane. Three x4 XOR gates (SN74AHC86N) are used, and six x2 fast MOSFET drivers (TC4426CPA) are used. Input is a small break-out board (Chip Quik, CN0002) for an HDMI plug connector and connections to box-mounted SMA connectors are facilitated with surface mounted ultra-miniature coax connectors(HD#, BO#).*

A.2 NET Circuitry

The NET is a linear electrostatic trap consisting of two electrostatic mirrors with an image charge detector between them. The are 7 mirror plates within each stack are positioned 4.75 mm apart between two grounded end caps. Each plate has a thickness of 1.5 mm and is electrically isolated with nylon spacers. The assembly is aligned using three holes symmetrically positioned near the plates outer edge. Each hole allows a 3.8 mm alumina rod to pass through all plates within a stack that is pressure fit into holes in each end cap. A 4.75 mm nylon spacer is mounted over each rod between each plate in the stack. Electrical connections to each plate are made with a small tab machined onto the edge of each plate where a ring connector can be affixed with a screw and nut. Within the 7 mirror stack 4 plates are connected to a switched voltage divider to create a potential ramp that facilitates particle oscillation, 2 are grounded, and 1 is held at a constant potential to act as an einzel lens. The voltage divider is constructed from a set of 4 potentiometers external to the NET vacuum chamber and attached through a multipin feedthrough. A diagram of the NET mirrors is presented in Figure A.3.

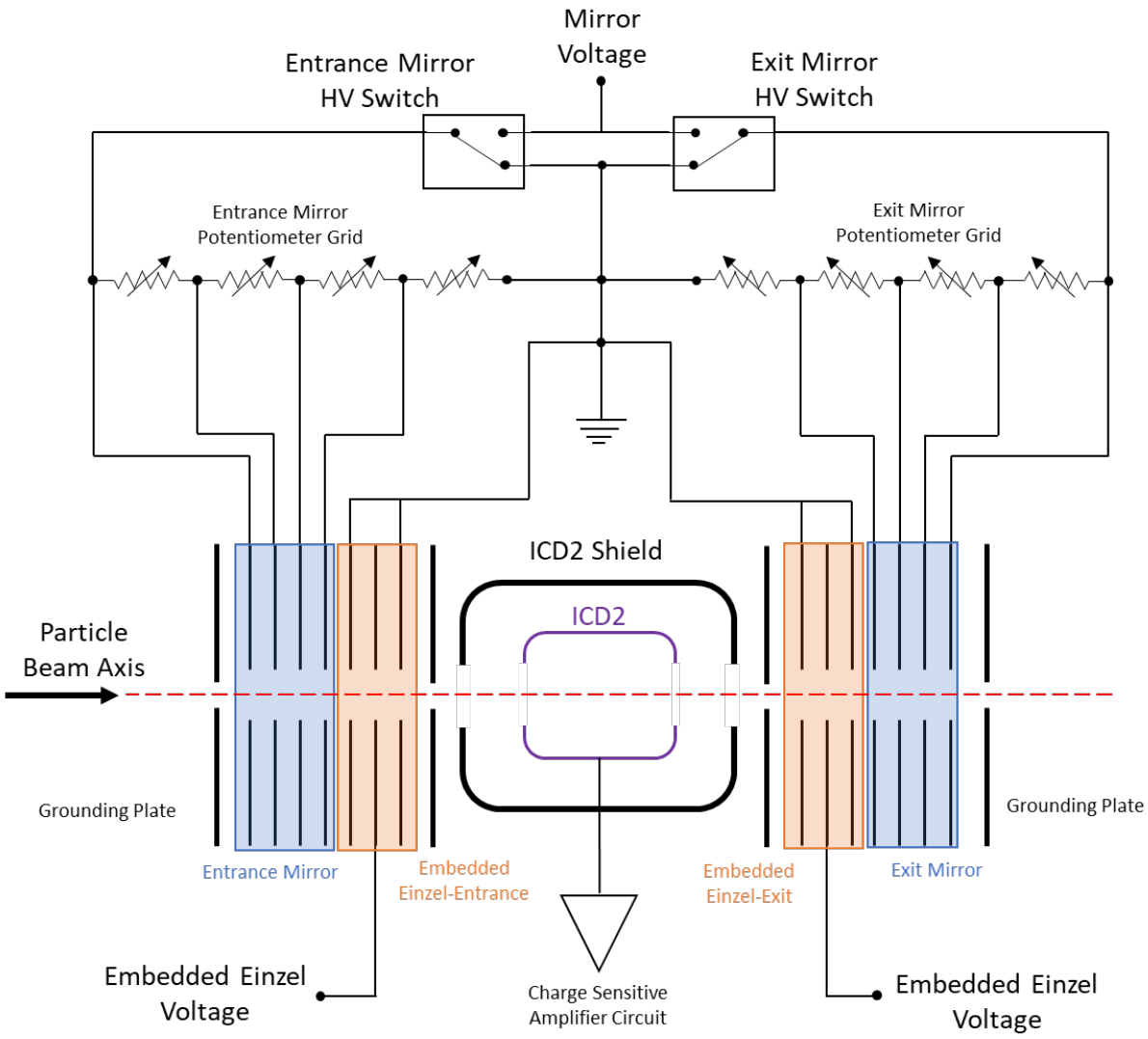

Figure A.3: *Diagram of the NET circuit and related components. The potentiometer voltage divider is external to the chamber and allows modification to the ramping potential of each NET mirror. The einzel lenses are directly connected to a power supply. ICD2 is shielded by a grounded enclosure in the center of the trap, electrical connections to this detector are detailed in section A.5.*

A.3 LINAC High Voltage Circuitry

When operating with 2-20 elements in the LINAC, two high voltage switches are used to control the acceleration potentially. These switches are manufactured by Behlke and are 30 kV rated push-pull mosfet switches (HTS 301-03-GSM). To operate, voltage is supplied to two separate poles of the switch, for the AIS one of these poles is grounded. Positive particles are generally created in the AIS, and negative acceleration potentials are used to accelerate these particles. The high voltage power supplied to the negative terminal of each switch is buffered with two capacitor banks, a shared larger capacitance bank, and smaller individual bank for each switch. Resistors are also used in-line with the power supply to prevent reflection along the power line potentially damaging the high voltage power supply. The power supply used to power the accelerator is a 20 kV, 15 mA, reversible polarity supply (XP Power, PS/FR20R15.0). This supply is operated manually to change the acceleration potential applied. The power-side circuit of the LINAC is detailed in Figure A.4.

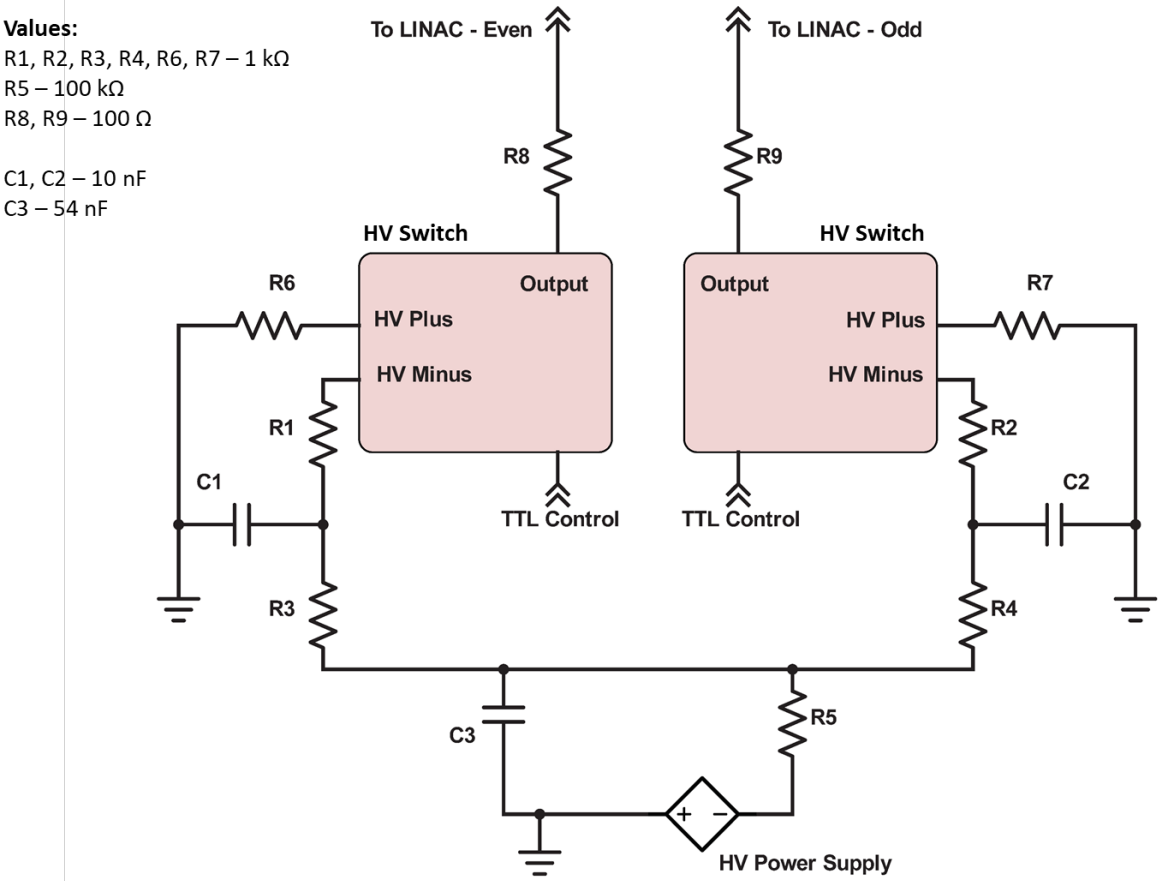

Figure A.4: *Diagram of the high voltage circuit used to switch the LINAC. Typical values for the passive components used are listed in the top left corner. HV switch is controlled by a logic board detailed in the next section.*

A.4 LINAC Logic Circuit

To operate the high voltage switches of the LINAC, logical pulses from the DAQ1 digitizer are output through the circuitry in section A.1. In addition to the buffering capability supplied by the circuit in A.1, a decoupling circuit for the logical pulses is used. This circuit contains two key components to isolate the logical pulses used to trigger the switch. Pulses from DAQ1 are initially coupled through a high speed optocoupler (HPCL2611) which has a common mode rejection of 10 kV/μs. The HPCL2611 output is regulated using a photo-detector logic gate on the output-side FET. This signal is run through an additional buffer circuit (MOSFET driver TC4426) before triggering the HV switches. This buffer also has the same delay of 40 ns as the MOSFET driver in the initial buffering circuit (A.1). This decoupled and buffered signal is used to control the switch output through the switch logical interface. A simplified circuit is displayed in Figure A.5, and a detailed circuit diagram is shown in Figure A.6.

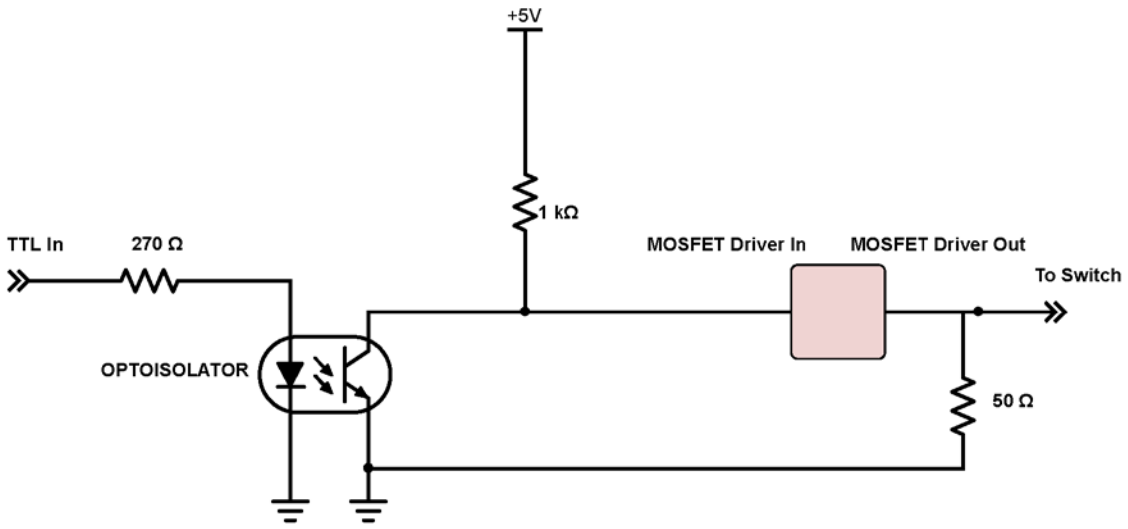

Figure A.5: *Diagram of the logic circuit used to switch the LINAC. TTL from the DAQ1 digitizer is coupled to the switch using the above circuit.*

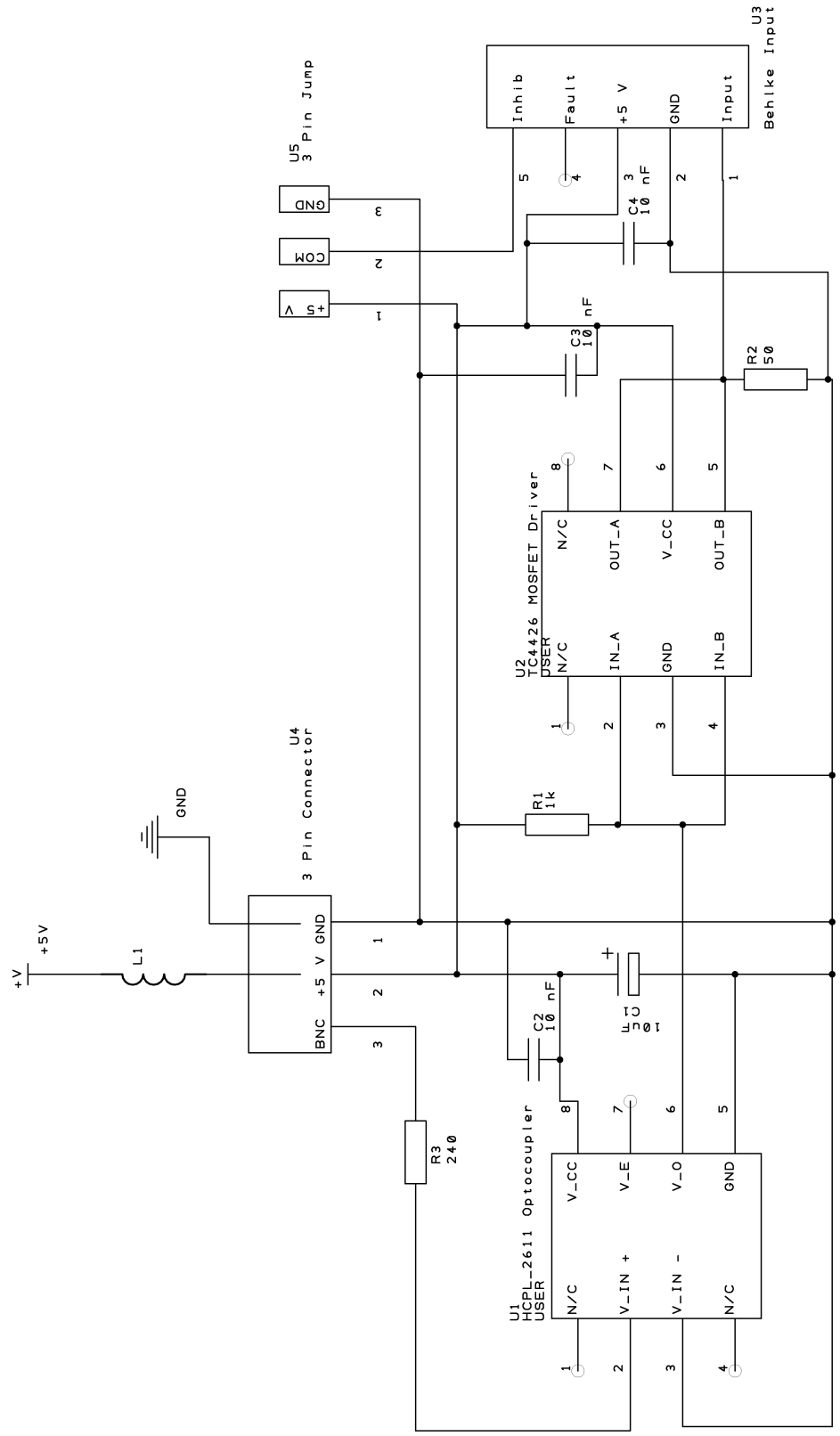

Figure A.6: *Circuit diagram detailing the circuit in Figure A.5. The input labeled BNC is the logical signal transmitted from DAQ1*

A.5 Remote FET Configuration for Image Charge Detector

Image charge detection circuits take small current signals from an image charge detection element and amplify these signals using the combination of a FET and amplifier. The image charge detectors operated throughout the AIS are configured to allow remote operation of the amplifier, external to the vacuum chamber. The JFET (PMBFJ309) used to interface with the ICD detector element and produce the initial signal from the particle image charge is mounted as close as possible to the detector element to reduce noise. The feedback resistor and capacitor (C_F and R_F in Figure A.7) are mounted with this FET on a small PCB directly attached to the image charge detection tube with a screw. The feedback capacitor partially determines the gain of the ICD detector and is minimized (~0.1 pF) to maximize gain. The feedback resistor shapes the pulses produced from the detector with higher values reducing the discharge of the signal as the particle passes through the ICD tube (see Figure 2.8, typical values on the AIS are 1-10 GΩ). In addition to the feedback circuit, a test capacitor can be optionally mounted on this board to allow calibration of the detector response. This capacitor can be pulsed with potential to apply a set amount of charge to the detector in order to measure the entire circuit response. External to the vacuum chamber, an Amptek A250 amplifier is used to amplify signal from the FET board into the voltage signals output by each detector. This is interfaced to the FET PCB using a coaxial feedthrough connected to ports ‘FET’ and ‘FB’ on each board. The A250 is mounted and its power stabilized with a series of capacitors. A diagram of these two circuits is shown in Figure A.7. The internal circuitry of the A250 is not shown.

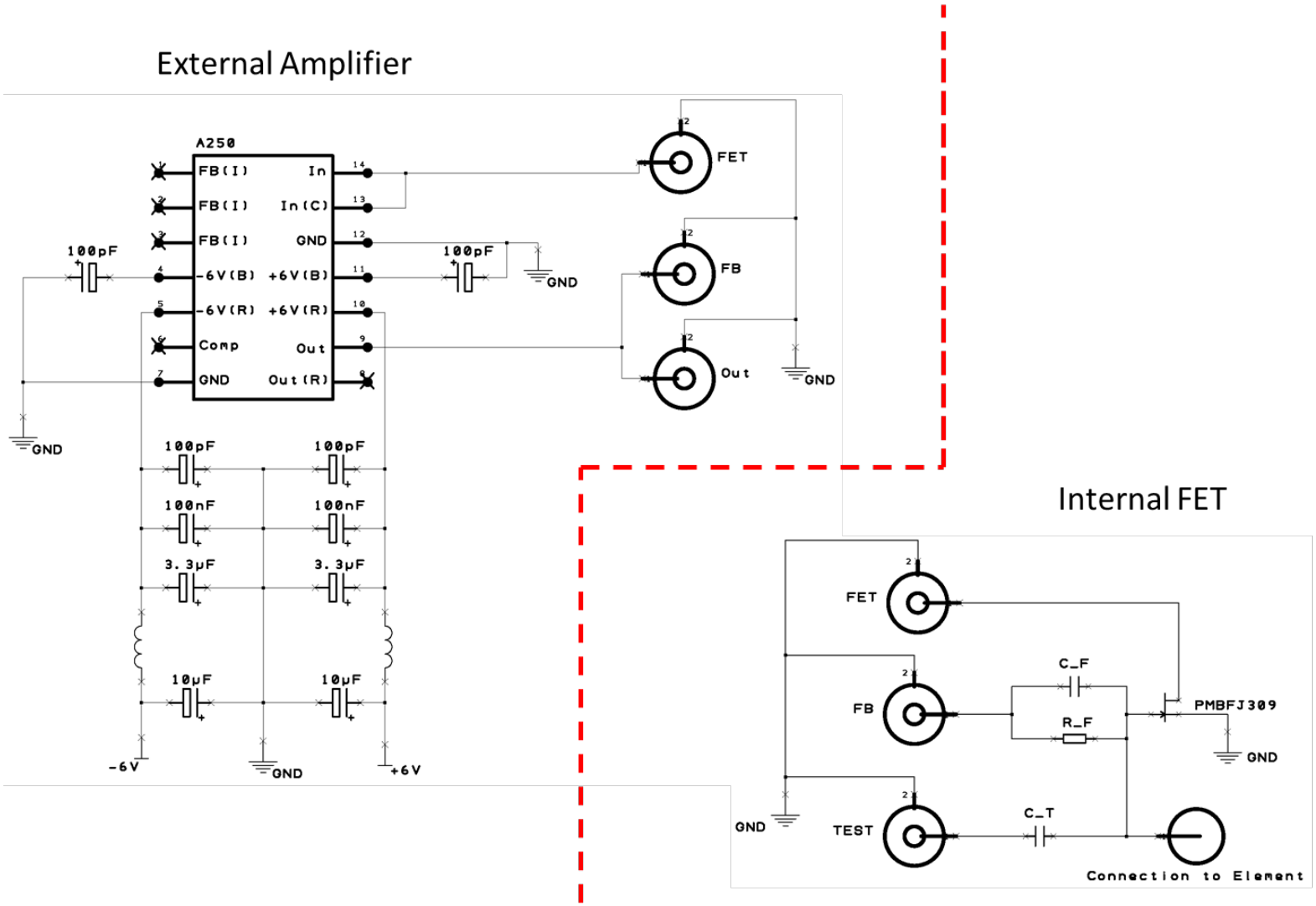

Figure A.7: *The two circuits used for operating ICDs. The Internal FET circuit operates in vacuum connected to the External Amplifier circuit through coaxial feedthroughs*